Simulation of Variability in the Tropical Western Indian Ocean

Majuto Clement Manyilizu

Thesis Presented for the Degree of

DOCTOR OF PHILOSOPHY

in the Department of Oceanography,

UNIVERSITY OF CAPE TOWN

December 2013

Supervisors

Prof. Chris J. Reason

Department of Oceanography, University of Cape Town, Cape Town, South Africa

Dr. Pierrick Penven

Institut de Recherche pour le Developpement, Laboratoire de Physique des Oceans (UMR 6523, CNRS, IFREMER, IRD, UBO), Centre IRD de Bretagne, France

Dr. Francois Dufois

CSIRO Marine and Atmospheric Research,
Private Bag 5,
Wembley WA 6913, Australia

Declaration

I, **Majuto Clement Manyilizu**, declare that this thesis is my own unaided work, both in concept and execution, and that apart from the normal guidance from my supervisors; I have received no assistance except as acknowledged. Neither the substance nor any part of this thesis has been submitted in the past, or is being at any other university.

Publication in review based on the present work:
Manyilizu, M., F. Dufois, P. Penven, and C. Reason, 2013: Interannual Variability in the Tropical Western Indian Ocean. *African Journal of Marine Science*, Manuscript submitted for publication.

The scholarship for this study was provided by the Carnegie-IAS Regional Initiative in Science and Education (**RISE**) through the Western Indian Ocean Regional Initiative in Marine Science and Education (**WIO-RISE**) network. In addition, the International Centre for Education, Marine and Atmospheric Science over Africa (**ICEMASA**) in collaboration with Institut de Recherche pour le Developpement (**IRD**) provided financial support towards the submission of this thesis.

Abstract

The oceanic circulation and properties in the Tanzanian shelf region in the tropical western Indian Ocean have been studied in this thesis using a regional ocean model. The study investigated the influences of the Northeast Madagascar Current (NEMC) in the Tanzanian shelf waters at the annual cycle. Furthermore, the thesis examined the interannual variability of the sea surface temperature (SST) in the Tanzanian shelf region, and compares it with that offshore or with subsurface temperature. At the annual cycle, the westward-flowing NEMC advects relatively warm and fresh waters from the north of Madagascar towards the Tanzanian shelf region by interrupting the upwelled water from the Seychelles-Chagos ridge. At interannual timescales, the weakest interannual SST variations, which lie over the weak subsurface waters variations, occur in the coastal waters off Tanzania, where its variance is shared with waters to the north of Madagascar. Such SST variations are dominated by variability at about five year periods. The strongest interannual SST variations, which lie over the strongest subsurface temperature variations, occur offshore, being dominated by two periods, one at about 2.7 and the other near five years. The interannual variability of the region seems to be linked to El Niño-Southern Oscillation (ENSO) and Indian Ocean Dipole (IOD) events, which induce changes in the thermocline and surface forcing in the region. Local surface heat flux exchanges driven by the anomalous shortwave radiation dominate the weakest interannual SST variability in the Tanzanian shelf region, with some contribution by the advection of heat anomalies from the NEMC. Further offshore, the strongest interannual variability of the SST is dominated by the thermocline variations induced by local Ekman pumping from local wind stress curl and by remote forcing from large-scale climate modes.

Acknowledgements

I would like to express my gratitude to my supervisors: Prof. Chris Reason, Dr. Pierrick Penven and Dr. Francois Dufois. Their guidance has been an instrumental in helping me throughout this degree. I am particularly grateful to Dr. Pierrick Penven for his constantly invaluable support, guidance and encouragement during this study. His positive attitude to me and my research has been a key element to completion of this PhD.

I am grateful to staff and students in the Department of Oceanography, University of Cape Town, who have supported me through the duration of this thesis. Special thanks to Dr. Nicolas Rascle, Yonss José, Jerome Guiet, Vicent Guri and Obadias Cossa for their academic and social support during this PhD journey.

I am appreciative of the financial assistance received from the WIORISE network and ICEMASA/IRD as well as the study leave from the University of Dodoma.

I would like to express my profound gratitude to my family, relatives and friends who have been encouraging me, tolerating my moods and long absence, all while believing I could finish this thesis. I am extremely grateful to my parents, my father Nyelu Clement Manyilizu and my mother Kashindye Musili Shiganga for their unconditional support and sacrifice in my academic career and life. Special thanks to my wife, Joyce and our daughters, Nina and Alfrida. I also extend my warm gratitude to my mother-in-law, Alfrida Muhoja, father-in-law, Joseph Maping’wa, my brothers and my sisters as well as all my friends. I love all of them very much. Their support in my academic career and my debt to them are beyond measure.

Above all, I thank Almighty God for granting me the wisdom, health and strength to undertake this research and enabling me to successful completion.

Dedication

I dedicate this Doctoral thesis to my parents, my father Nyelu Clement Manyilizu and my mother Kashindye Musili Shiganga for their unconditional support and sacrifice in my academic career and life.

Table of Contents

List of Figures

List of Tables

Chapter 1

Introduction

1.0 Background

The Tanzanian shelf region plays a vital role in socio-economic development of Tanzania and its neighbouring countries. Fishing is the main food source and commercial activity in the coastal communities contributes to the country's gross domestic product (GDP) by about 2.1-5.0% for Mainland Tanzania and 2.2-10.4% for Zanzibar (Jiddawi and öhman, 2002). Marine and coastal shipping through four major ports in the shelf region, Dar es Salaam, Zanzibar, Tanga and Mtwara, also contributes significantly to the country's trade and income. These ports provide transport services to local communities as well as transit goods to land-locked countries such as Uganda, Rwanda, Burundi, Democratic Republic of Congo, Zambia and Malawi. Furthermore, the current discoveries of oil and gas, important resources, below the ocean off Mtwara in the southern Tanzanian shelf are expected to boost the country's economy in addition to tourism and recreation. Most importantly, because the Tanzanian shelf region is a part of the western Indian Ocean, its variability of the sea surface temperature (SST) greatly influences the rainfall distribution, especially the October-December rains over the region (e.g. Mutai and Ward, 2000; Ogallo et al., 1988; Mapande and Reason, 2005). Such rainfall patterns affect the country's economy as drought leads to shortage of food and energy (hydroelectric power), and flooding causes disease outbreak (e.g. malaria and cholera) as well as loss of life and property. In short, marine goods and services in the Tanzanian shelf are of critical importance to the development of Tanzania and the neighbouring countries. Thus, physical structure and oceanic processes in the shelf that relate to aforementioned socio-economic activities have been the focus for the last few decades.

The economic and environmental importance of the Tanzanian shelf region for local and international trades relies on its physical structure and convenient geographical location. The shelf is characterized by a slightly extended coastline that stretches from the Kenyan border in the north (4^{o}S) to the south ($10^{0}5$'S) at the Mozambican border (Figure 1.1). The coastline

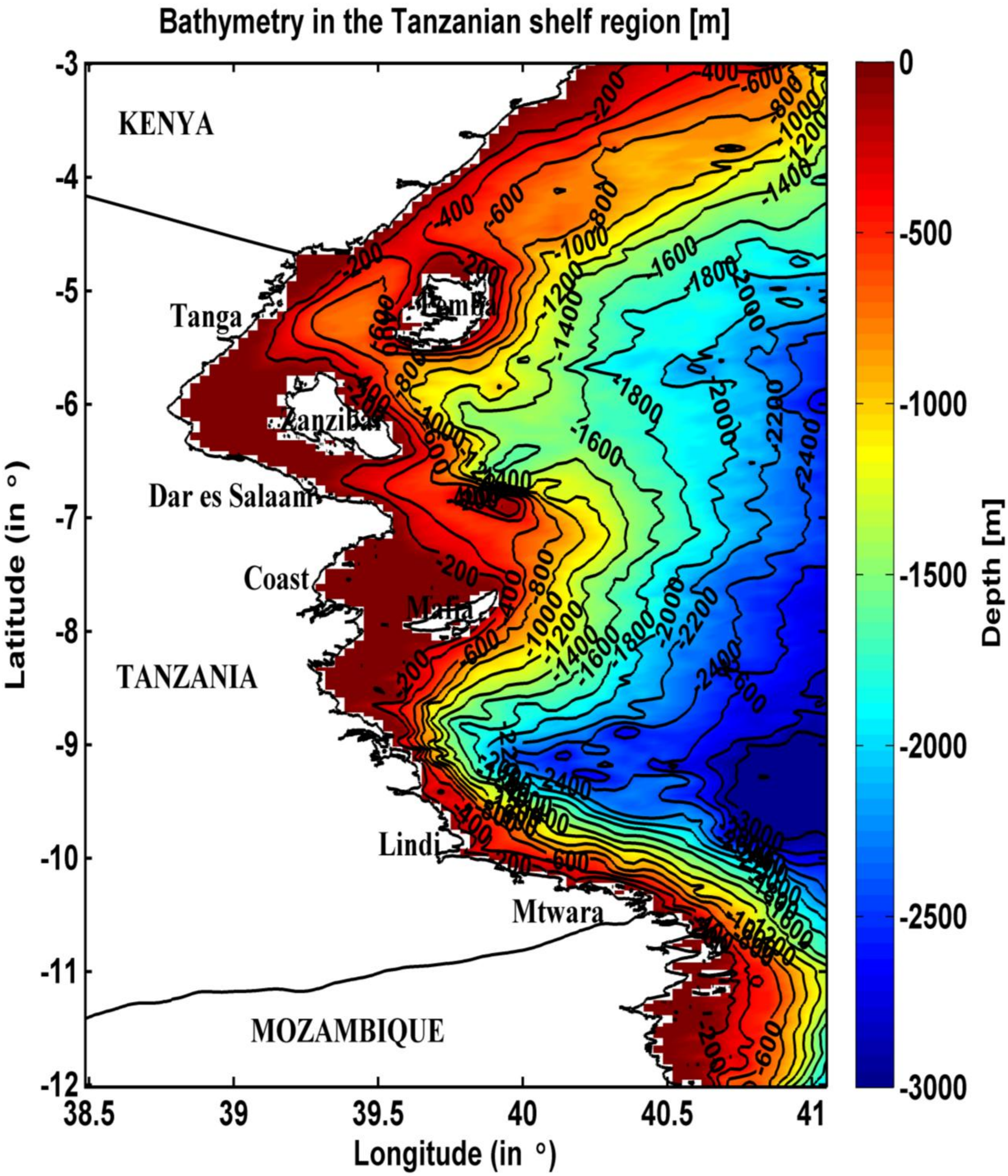

Figure 1.1: The physical structure with bathymetry distribution (m) with 200 m contour intervals derived from ETOPO2V2C (www.ngdc.noaa.gov) and administrative regions in the Tanzanian shelf region. (Positive values are for latitudes in the Northern hemisphere and longitudes in the East, respectively).

encompasses five administrative regions, namely, Tanga, Coast, Dar es Salaam, Lindi and Mtwara (Figure 1.1). Sandy open beaches as well as extensive mangrove forests in the riverine estuarine and delta environments bound the coastline with some cliff out-cropping in the south of the region. The shelf is generally narrow with sea-grass, fringing coral reef and island habitats. It consists of three major islands, Unguja (commonly known as Zanzibar), Pemba and Mafia (Figure 1.1), as well as numerous small islands such as Latham, Tutia, Songosongo, Mbuya, Pangavini, Kendwa, Inner and Outer Nyakatombe, Inner and Outer Sinda. The shelf deepens sharply after the 60 m depth with different distances from the coast. The 200 m depth occurs at about 2 km from the coast in the narrowest region in the southern Tanzania and 80 km in the widest region in the northern Tanzania (Figure 1.1). The location, size and shape of the Tanzanian shelf are very convenient for the fishing, ports, tourism and recreation as well as for strong ocean variability in the upper ocean circulation and properties.

The seasonal variability of the upper ocean circulation and properties in the Tanzanian shelf region respond to the monsoon winds with the East African Coastal Current (EACC) dominating the surface circulation. The surface monsoon winds blow generally from the southeast in austral winter (June-September) and from the northeast in austral summer over the shelf (Ngusaru and Mohammed, 2002) with two transition periods, austral autumn in April/May and austral spring in October/November. The austral winter is characterized by the coolest SST (~24^{o}C) due to strong winds and surface heat fluxes, and the warmest SST (~28-30^{o}C) occurs during the transitions when the surface winds and fluxes are weak (McClanahan, 1988). The seasonality varies the discharges of permanent rivers into the shelf such as Pangani, Wami, Ruvu, Rufiji, Matandu, Mbemkuru, Lukuledi and Ruvuma. These rivers discharge more freshwater into the shelf during rainy seasons (March-May and September-October) resulting in low surface salinity (34 and 35.2 psu in April-June), whereas high salinity occurs in the austral summer (Nyandwi et al., 2001). The EACC dominates the surface circulation, being supplied by the North East Madagascar Current (NEMC). During the austral winter, the EACC is strengthened (to ~2 m/s) by the wind, and it extends northward to form the Somali Current (SC) (Newell, 1957; Dubi, 2000; Schott and McCreary., 2001; Julius, 2005). In the austral summer, the southward SC and winds weaken the EACC (to ~0.2 m/s) as the EACC and SC meet and confluence eastward to form the eastward South Equatorial Counter-Current (SECC) (Newell, 1957; Dubi, 2000). In general, the monsoon winds over the Tanzanian shelf region drive the strong seasonal variability in the upper ocean circulation and properties which affect the socio-economic activities in the country.

Large scale climate modes (such as El Niño-Southern Oscillation, ENSO and Indian Ocean Dipole, IOD) change the conditions in the Tanzanian shelf region at an interannual time scale. Significant changes in the shelf waters occur on the SST and sea surface height (SSH) as well as on the coral reefs. Evidence shows that interannual variability of the SST in the tropical western Indian Ocean strongly influences the regional rainfall variability (e.g. Reason et al., 2000; Annamalai and Murtugudde, 2004; Yamagata et al., 2004; Schott et al., 2009). For example, during the positive IOD or El Niño events (e.g.1997/1998), strong warming of the tropical Indian Ocean was associated with severe floods in parts of East Africa (Schott et al., 2009). The warm SST anomalies and the rise in sea level in the Tanzanian shelf during the 1997/98 event also negatively affected coral reefs by increasing the level of coral mortality to about 50-60% (Obura et al., 2002). Severe drought and cold SST anomalies in the Tanzanian shelf can occur during negative IOD or La Niña events (e.g.1999/2000; Schott et al., 2009). In short, large scale climate events have strong impacts on SST, SSH, rainfall variability and coral reefs in the Tanzanian shelf region. Consequently, these events greatly affect social-economic activities (such as fisheries, tourism, recreation as well as marine and coastal shipping), and ultimately, the country's economy.

Variability of the ocean in the Tanzanian shelf region has significant socio-economic importance for Tanzania and the neighbouring countries, and thus, its understanding is crucial. The variability of the upper ocean (e.g. SST, salinity, waves, current and SSH) in the shelf affects economic activities such as fisheries, coastal shipping, tourism and recreation at seasonal and interannual time scales. Therefore, a better understanding of the ocean processes related to the environmental and social-economic activities in the shelf region at seasonal and interannual scales is important. Along with gaining more insight into the variability in the Tanzanian shelf region, such knowledge will improve planning and management of climate sensitive activities in Tanzania.

1.1 Motivation

Despite the critical importance of the Tanzanian shelf region for the development of Tanzania and its neighbouring countries, not much work has been published on the area. Some progress has been made in various observational studies (e.g. Newell, 1957; Swallow et al., 1988; Dubi, 2000; Julius, 2005) but to date, there has been little modeling activity (e.g. Mayorga-Adame, 2007). The impacts of the circulation on the ocean properties in the shelf are not well understood. This is evident from a lack of clear systematic research on the relative effects of the NEMC and EACC on the spatial inhomogeneity of the properties in the shelf. The comparison and relationship of the variability of the upper ocean temperature between the Tanzanian shelf waters and further offshore are not well documented. There is relatively poor understanding on the relationship of the shelf SST with that offshore or with subsurface temperature. Thus, filling in the gaps of understanding of the variability in the Tanzanian shelf region and further offshore using numerical studies is a main motivation for this study. A need for more effort using modeling is very important as numerical simulations may provide insight into the ocean processes throughout the water column and can be used to investigate sensitivities to various forcing mechanisms.

This study deploys a modeling approach to investigate the variability in the Tanzanian shelf region in relationship to further offshore in the tropical western Indian Ocean. It focuses on the impacts of the ocean circulation (the NEMC and EACC) on the ocean properties in the Tanzanian shelf at seasonal time scale. The study also addresses the relationship between the SST in the Tanzanian shelf and further offshore as well as that at the subsurface temperature at an interannual scale. Therefore, the thesis attempts to fill the gaps of the existing knowledge in the Tanzanian shelf region through the following questions:

1. How does the Northeast Madagascar Current (NEMC) contribute to the volume, heat and salt transport and budgets in the coastal waters of Tanzania?
    i. What is the mean flow and seasonality of the Northeast Madagascar Current in the north of Madagascar? Is this seasonality in phase with the East African Coastal Current (EACC) in the Tanzania shelf region?

    ii. How does advection from the NEMC influence the heat content of the upper ocean in the Tanzanian shelf waters?
    iii. How does advection from the NEMC influence the salinity in the Tanzanian shelf waters?

2. How large is the interannual variability of the sea surface temperature in the tropical western Indian Ocean compared to the annual cycle? What drives this inter-annual variability?
    i. How large are the seasonal variations in the tropical western Indian Ocean compared to the interannual variability?
    ii. Does the SST variability differ in the coastal waters in the Tanzanian shelf region from further offshore?
    iii. Does the Northeast Madagascar Current (NEMC) contribute to the SST variability in coastal waters in the Tanzanian shelf region?
    iv. How sensitive is the SST to the local surface heat fluxes and to lateral remote influences?
3. How does the upper ocean temperature vary in the Tanzanian shelf region and offshore in the tropical western Indian Ocean? How sensitive is it to the local surface or lateral remote forcing?
    i. What are the characteristics of the upper ocean temperature in the Tanzanian shelf region compared to offshore in the tropical western Indian Ocean?
    ii. Does the subsurface temperature near and below the thermocline depth vary in the same way as the SST in the Tanzanian shelf region and offshore?
    iii. How does the upper ocean temperature in the Tanzanian shelf region and further offshore respond to the local surface heat fluxes?
    iv. How does the upper ocean temperature in the Tanzanian shelf region and further offshore respond to the lateral remote influences?

1.2 Thesis Organization

The thesis is organized as follows: This introductory chapter (Chapter 1) is followed by literature review in Chapter 2. The methodology applied and datasets used in this study are described in Chapter 3. Chapter 4 deals with the evaluation of the performance of the regional model in the tropical western Indian Ocean. The mean and seasonal impacts of the upper ocean circulation on the properties in the Tanzanian shelf region are investigated in Chapter 5. The interannual variability in the tropical western Indian Ocean with a focus on the Tanzanian shelf region is presented in Chapter 6. Chapter 7 focuses on the analysis of the subsurface ocean with SST interannual variability in the Tanzanian shelf region and further offshore. The last chapter (Chapter 8) summarizes the results of the aforementioned chapters, and suggests some applications as well as the scope for future work.

Chapter 2

Literature review

2.0 Introduction

This thesis focuses on a numerical investigation of the seasonal and interannual variability of the Tanzanian shelf waters and offshore in the tropical western Indian Ocean. In this region, much research efforts on *in situ* observations, satellite measurements and model simulations seemed to be carried out after the 1997/98 El Niño/Indian Ocean Dipole event, a strong motivation for studies of regional climate variability (e.g. Saji et al., 1999; Schott and McCreary, 2001; Annamalai and Murtugudde, 2004; Hermes and Reason, 2008; Schott et al., 2009). These studies aimed to understand the seasonal and interannual variability of the tropical Indian Ocean, and its influences on climate variability in the region and other parts of the globe. To conduct a thorough literature review on the Tanzanian shelf waters and offshore in the tropical western Indian Ocean, it is more useful to divide the literature review into seasonal and interannual components. The first part of the literature review (2.1) deals with the seasonality of the atmospheric circulation, upper ocean circulation and upwelling processes as well as the upper ocean properties, and the second part reviews work on interannual variability (2.2). The last part of this chapter gives a summary.

2.1 Seasonality

2.1.1 Atmospheric Circulation

The atmospheric circulation over the tropical western Indian Ocean shows a number of unique regional features associated with thermal, geographical and topographical characteristics. In this region, the wind direction north of 10^{o}S reverses twice a year during austral winter and summer seasons (Pickard et al., 1990; Krishnamurti, 1996; Gadgil, 2003; Schott et al., 2009). The temperature contrasts between the Asian landmass and the adjacent Indian Ocean drive the monsoonal reversals of the wind (e.g. Halley 1686; Krishnamurti, 1971a and b; Webster, 1987; Li and Yanai, 1996). As a result, seasonal variation of the large-scale atmospheric systems located in the Arabian high (ridge) and the Mascarene high (east or south of Madagascar) in the Northern and Southern Hemisphere, respectively. Within the region, the surface winds blow from or to either the Asian landmass. However, the effects of the Coriolis acceleration deflect the surface winds, and the East African highlands channel them along the western Indian Ocean coast.

During austral summer (December to March), high surface pressure over the Asian landmass causes a north-south pressure difference (barely exceeds 6 hPa) from the Indian subcontinent to the South Indian Ocean (Tomczak et al., 1994). Thus, the surface winds in the North Indian Ocean are forced from the Indian subcontinent towards Madagascar, but due to effects of Coriolis acceleration, northeasterly winds blow from the Asian landmass towards the tropical western Indian Ocean. The winds are channelled by the East African highlands over the tropical western Indian Ocean. These surface winds are known the North East or winter monsoon (Figure 2.1a).

During austral winter (June to September), low surface pressure over the Asian landmass causes a north-south pressure gradient of about 22hPa from Madagascar to Arabia (Tomczak et al., 1994). The pressure gradient force combined with effect of Coriolis acceleration and channelling effect of the East African highlands causes southwesterly winds to blow from the western Indian Ocean and Arabian Sea towards the Asian landmass. These surface winds are known as the South West or summer monsoon (Figure 2.1b). The region between 10^{o}S and the equator over the tropical western Indian Ocean experiences southeasterly wind flow; some authors name these winds the South East monsoon (SE) (McClanahan, 1988). The surface winds during this season peak in July-August, and fade away in September-October (Rao and Ram, 2005). The South West monsoon is considered to be a continuation across the equator of the southeast trades, concentrated in a narrow low-level jet called the Findlater or Somali Jet (Findlater, 1969 and 1978; Pickard et al., 1990).

The monsoon transition periods occur for about four to six weeks during April through May for austral autumn, and October through November for austral spring. During both transition periods, the zonal component of winds nearly vanishes at the equator, and thus, there is no sustained easterly wind along the equator as in other oceans (Schott et al., 2009). The surface winds become weaker and a westerly component appears to dominate along the equator (Schott et al., 2009) as shown in Figure 2.1c and d.

The South West monsoon and the North East monsoon display differences in strength and spatial scale as well as regional weather and climate patterns. The South West monsoon is stronger than the North East monsoon; it dominates the annual mean wind pattern which looks like a weaker version of the South West monsoon. In the southern tropical Indian Ocean, the southeast trades dominate throughout the year, being strongest and closest to the equator during the South West

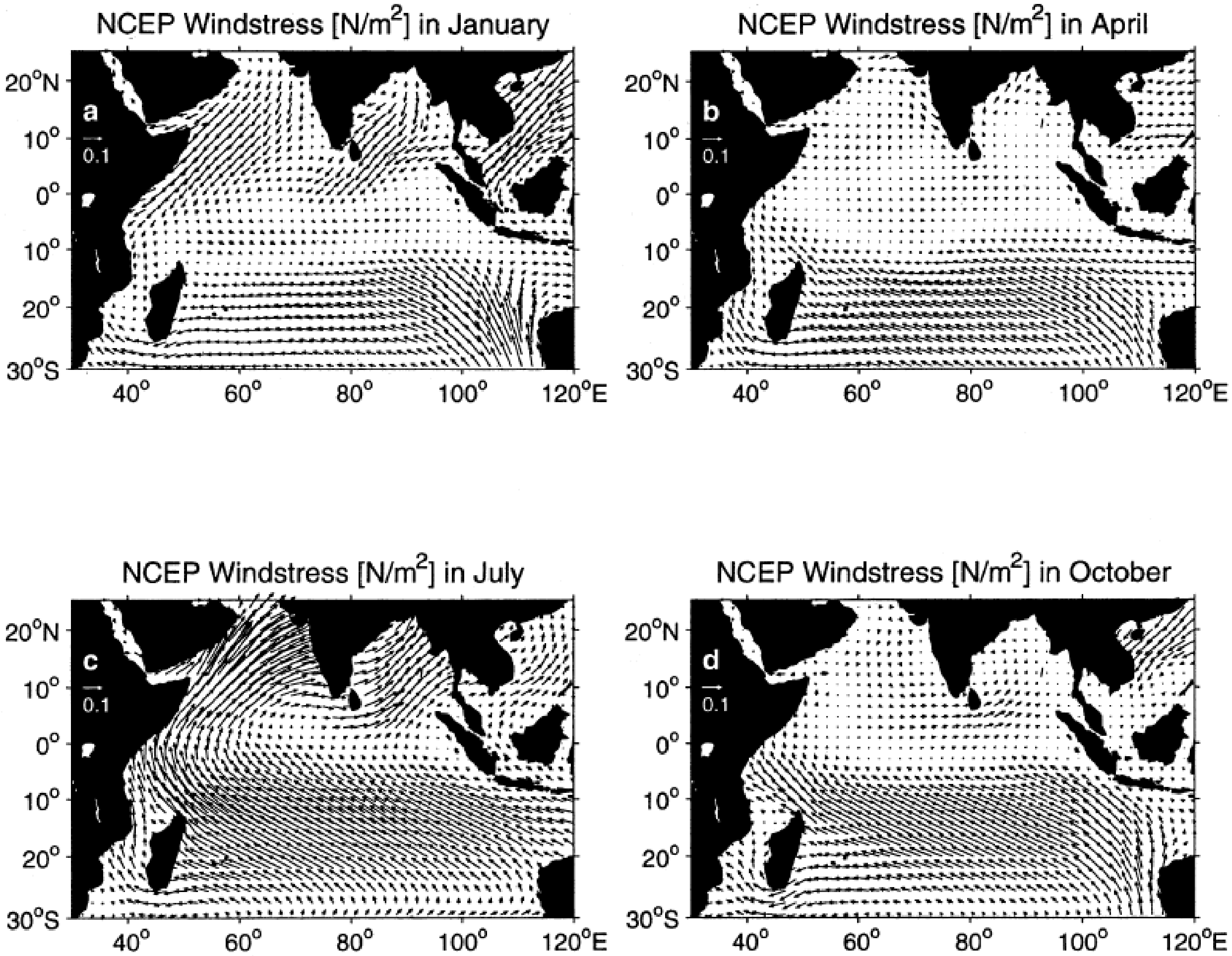

Figure 2.1: Monthly mean wind stress (Nm^{-2}) from NCEP climatology (a) January – North East monsoon, (b) April- Spring, (c) July – South West monsoon, and (d) October - Autumn (Schott and McCreary, 2001).

monsoon and vice versa in the North East monsoon. Xie et al. (2002) found that the southeast trade winds peak between 15 and 20^{o}S. The monsoons determine the climate of the tropical western Indian Ocean and countries surrounding it. The South West monsoon is characterized by high cloud cover, rainfall and wind over the North Indian Ocean and vice versa during the North East monsoon. The East African region experiences two rainy seasons during the transition periods between these monsoons; namely, during March-May and October-December.

The seasonal rainfall variability over the East African region is associated with the north-south migration of the Inter-Tropical Convergence Zone (ITCZ) (e.g. Griffiths, 1959; Ogallo, 1989). During October and April, the ITCZ is at 2^{o}S, moving southwards and northwards, respectively. By the end of December, it reaches 12^{o}S followed by its southernmost location at the end of January/February, before it starts moving northward over eastern Africa. The ITCZ lags about four to six weeks behind the time of the sun's maximum elevation (EAMDb, 1963). The area from the tropical western Indian Ocean to the East African interior, especially northern Tanzania and southern Kenya, receives bimodal rainfall shortly after equinoxes i.e. vernal equinox in 20/21 March and autumnal equinox 22/23 September (McClanahan, 1988). The East African interior receives long rains called Masika during March through May (MAM) and short rains called Vuli during October to December (OND) (e.g., Mpeta, 1997). Northern East Africa experiences bimodal dry seasons during both summer and winter solstices (McClanahan, 1988); it dries during June, July and August because the ITCZ migrates north over India and Southeast Asia which receive rainfall at that time. During the North East monsoon, the winds pass over the drier Somali land, and thus, only a small rainfall peak is received over the coastal areas (McClanahan, 1988). Southern Tanzania is near the southernmost location of the ITCZ, and thus, it experiences only one rainy season from November to April, peaking from January to February (EAMD, 1963a and b; Alusa et al., 1973; Mpeta, 1997).

In general, the tropical western Indian Ocean experiences strong seasonal variability of atmospheric circulation fields as shown by the surface winds and rainfall. Strong seasonality of the surface winds and rainfall in the region drives corresponding reversing surface ocean circulation and upwelling as well as ocean properties like temperature and salinity. The seasonal upper ocean circulation and upwelling processes in the region are described in Section 1.2, followed by the upper ocean properties (Section 1.3).

2.1.2 Upper Ocean Circulation and Upwelling Processes

The tropical Indian Ocean is characterized by strong seasonal reversing surface circulation and upwelling processes over the coastal and open oceans (Schott et al., 2009). The surface ocean circulation is strongly seasonally reversed in the northern tropical Indian Ocean (north of 12^oS), and either strengthened or weakened to the southern tropical Indian Ocean, by the seasonal reversals in surface winds (Schott et al., 2009). Within the southern tropical Indian Ocean, the southeast trade winds drive the South Equatorial Current (SEC). The path of the SEC is more irregular due to the underlying topography and Rossby waves (Maltrud et al., 1998; Gordon and McClean, 1999). The SEC is located between 10 and 20^oS (Cutler and Swallow, 1984; Shenoi et al., 1999) with velocities that rarely exceed 0.3 ms^{-1} (Tomczak et al., 1994).

The SEC branches at the eastern coast of Madagascar landmass (about 18^oS) into the Northeast Madagascar Current (NEMC) and the Southeast Madagascar Current (SEMC), flowing northwestward and southward, respectively (Figure 2.2). The SEMC transports about 20Sv to the southern tip of Madagascar, where it dissolves into a sequence of eddies and dipoles that migrate to the African coast (de Ruijter et al., 2004; Quartly et al., 2004). The NEMC transports about 29.60±8Sv annual mean (Swallow et al., 1988; Schott et al., 2009) with 0.7 ms^{-1} near-surface speed that decreases monotonically to a depth of 1000 m (Schott and McCreary, 2001). Near the African coast (at about 10^oS), the NEMC splits into the southward eddy-dominated flow through the Mozambique Channel and the northward permanent flow as the East African Coastal Current (EACC) (Pickard et al., 1990; Tomczak et al., 1994). The annual mean volume transported through the Mozambique Channel, which occurs in migrating anti-cyclonic eddies, has been estimated as 17Sv from a multiyear moored array and hydrographic section analysis (de Ruijter et al., 2002; Donohue and Toole, 2003). This volume matches earlier inverse model results of 15 ± 5Sv (Ganachaud et al., 2000). The SEC, NEMC and EACC in the southern tropical Indian Ocean are permanent flows, but are strengthened during the South West monsoon and weakened in the North East monsoon.

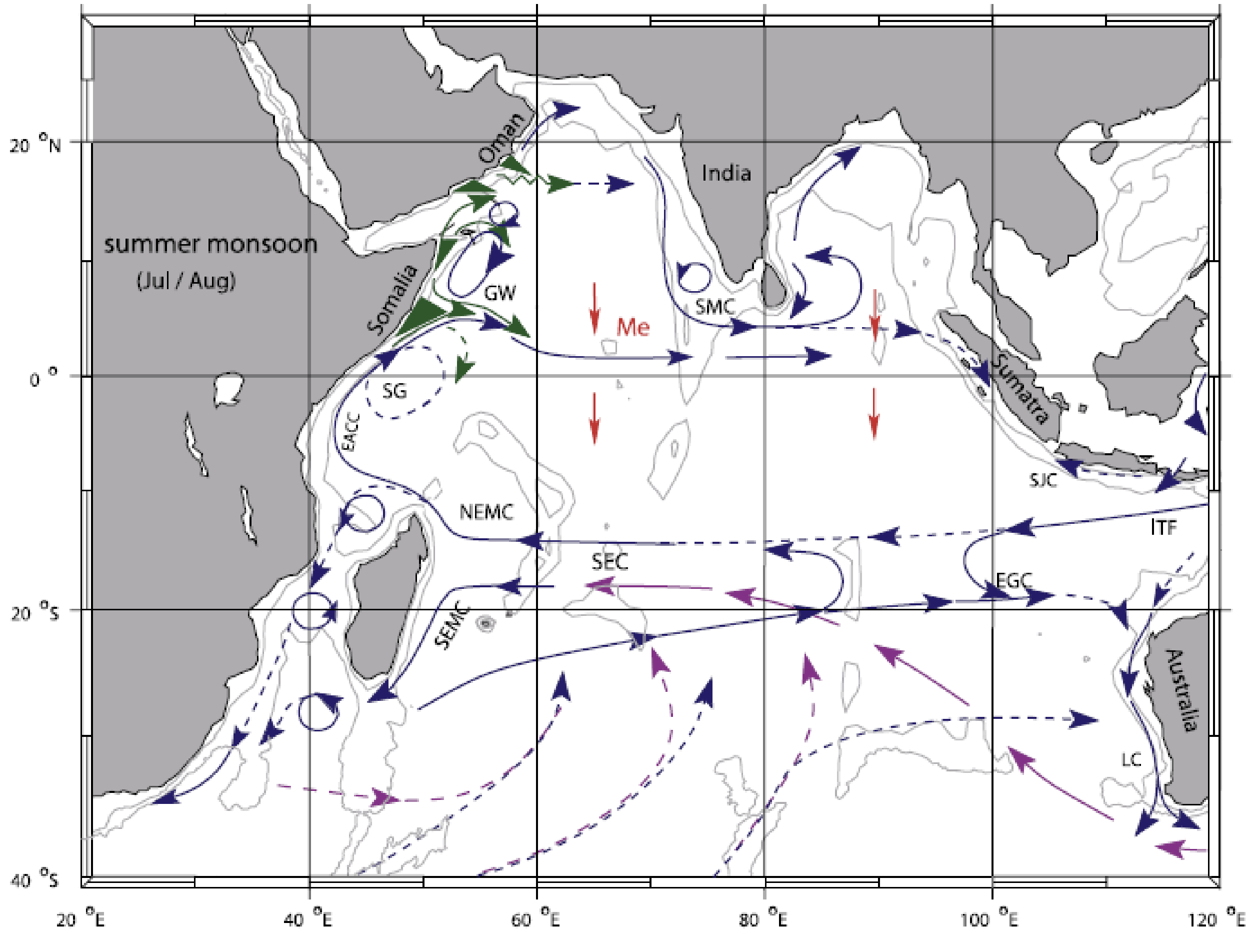

Figure 2.2: Schematic diagram of the Indian near surface ocean circulations, the subsurface return flow of the supergyre (in magenta) and red vectors (Me) show directions of meridional Ekman transports during the South East (summer) monsoon (Schott et al., 2009).

During the South West monsoon, the southeast trade winds along the East African coast strengthen the EACC to a velocity of up to 2 ms^{-1} from April through October (Newell, 1957; Dubi, 2000; Julius, 2005). Similar speeds of about 2.0 ms^{-1} with a transported volume of 15Sv in the top of 100 m were reported in the Indian Ocean Experiment (INDEX-1976-1979) during April and May of 1979 (Leetmaa et al., 1982; Schott and McCreary, 2001). The upper ocean circulation occuring during the South West monsoon in the tropical Indian Ocean is shown in Figure 2.2. The EACC supplies the northward flowing Somali Current which flows across the equator, showing different cells and gyres, depending on the time of the season and the driving wind field (Schott et al., 2009). After crossing the equator, part of the low-latitude Somali

Current turns offshore to the east near 4^oN with a width of order 50-100km, generating an upwelling process of cooler, nutrient-rich waters (Pickard et al., 1990; Schott and McCreary, 2001; Schott et al., 2009) further north off the East African coast (Düing and Schott, 1978; Smith and Codispoti 1980; Leetmaa et al., 1982). The remaining part of the Somali Current recirculates across the equator forming the Southern Gyre (SG) (Schott et al., 2009) which varies in strength from year to year (Schott et al., 1990). Further north at $4\text{-}10^oN$, the Great Whirl (GW) forms as a result of very strong anti-cyclonic wind stress curl generated offshore from the Somali coast; it causes another cold wedge at $10\text{-}12^oN$ (Schott and McCreary, 2001). The Great Whirl is almost completely closed in the late South West monsoon season from August to September, which has very small exchanges with the offshore flow. Another smaller recurrent eddy known as the Socotra Gyre (or Eddy) is formed at about 12^oN (Pickard et al., 1990; Schott and McCreary, 2001). During this season, the seasonal Southwest Monsoon Current (SMC) is formed in the northern Indian Ocean, flowing eastward to the south of Sri Lanka before turning northward; it carries saltier Arabian Sea water into the Bay of Bengal (Jensen, 2003; Schott et al., 2009).

During the North East monsoon, the northern edge of the weakened SEC shifts southward from its location between $10\text{-}20^oS$ during the South West monsoon as the southeast trades do (Schott et al., 2009). The northeasterly winds channeled by the East African highlands along the western Indian Ocean drive the southward flowing Somali Current (also known as the Somali Counter Current, SCC). The southward limit of the SCC can reach to 4^oS before it turns off the coast, where the northeasterly winds are stronger (Johnson et al., 1982). The northeasterly winds and the Somali Counter Current along the East African coast are in an opposite direction to the EACC during this period. As a result, the EACC is weakened to average velocities of less than $0.2ms^{-1}$ during November through March (Newell, 1957; Dubi, 2000; Julius, 2005). Its weakest velocities are reported in February (Tomczak et al., 1994), when the North-East monsoon is fully developed. The surface ocean circulation in the tropical Indian Ocean during the North East monsoon is portrayed in Figure 2.3.

The northward flowing EACC and the Somali Counter Current meet in a confluence zone ranging between 2 and 4^oS during the North East monsoon (Swallow et al., 1991; Schott et al.,

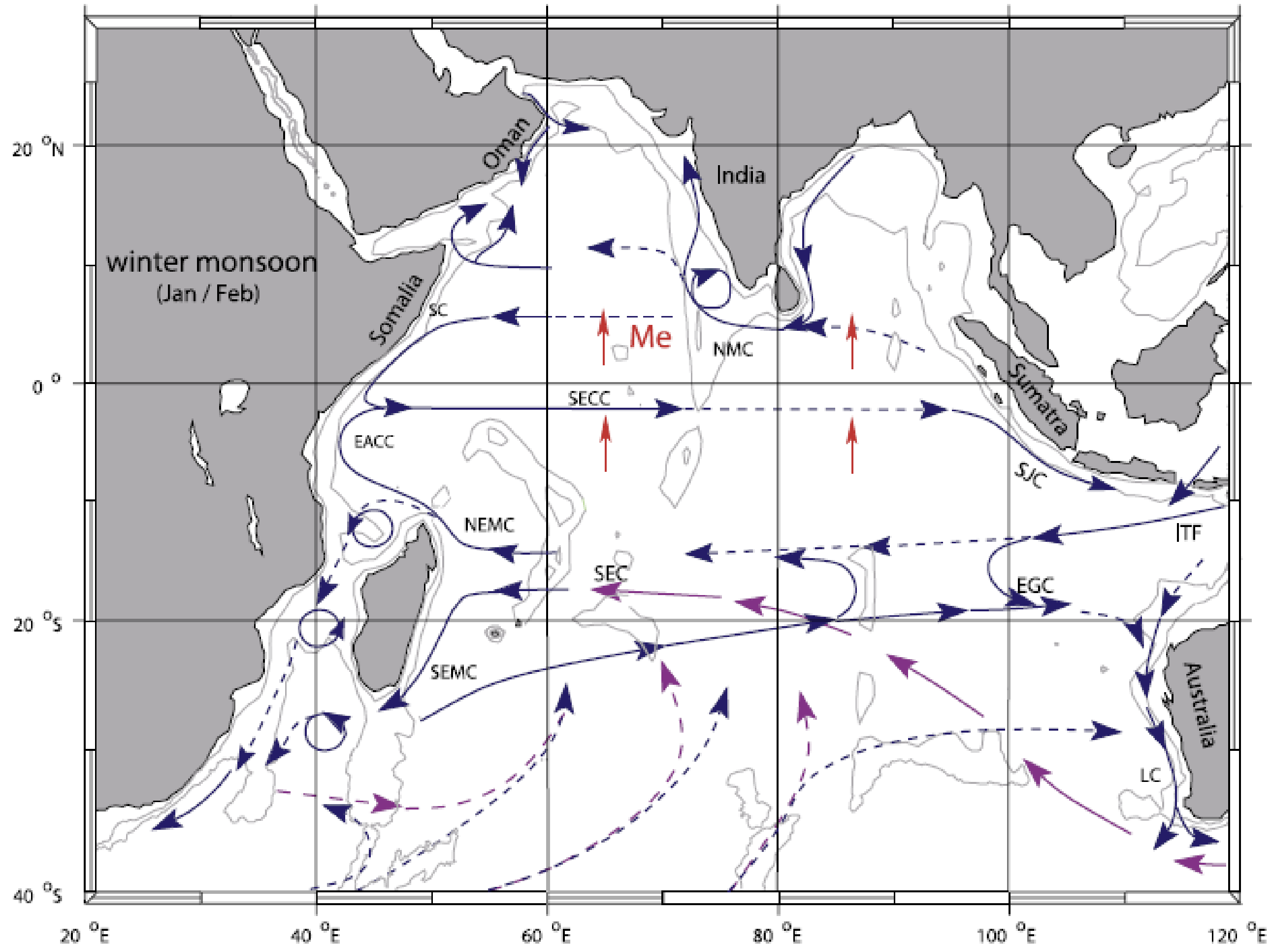

Figure 2.3: As Figure 2.2 but in the North East (winter) monsoon.

2009). The confluence of the EACC and Somali Counter Current results in an eastward offshore flow between 2 and 4°S known as the South Equatorial Counter Current (SECC) (Düing and Schott, 1978; Schott and McCreary, 2001). Kabanova (1968) suggested that when the SECC leaves the coast, it may cause a slight upwelling off the northern Kenyan coast. However, since then, not much work supporting that suggestion has been carried out on this region. The SECC is attributed to the merging of the westward flowing currents which cause the geostrophic balance with meridional density contrast in the Seychelles-Chagos thermocline ridge region (Hermes and Reason, 2008; Yokoi et al., 2008). The SECC does not go beyond 70°E in January, being opposed in the east by a weak westward flow. It is best developed in February when it forms a continuous band across the Indian Ocean, causing high sea level in the east (Morrow and Birol, 1998). The velocities of the SECC are between 0.5-0.8ms^{-1} in the west but weaker in the east.

The SECC is masked by overlying westward Ekman currents during the South West monsoon (McCreary et al., 1993; Song et al., 2004; Schott et al., 2009). The northern Indian Ocean experiences the Northeast Monsoon Current (NMC) which is prominent in January and March when the North East monsoon is fully developed. The NMC carries fresher water from the Bay of Bengal into the Arabian Sea (Schott et al., 2009). Moreover, the fresher water from the Bay of Bengal is indicated by several studies to cross the equator in the eastern basin during this season (Han and McCreary, 2001; Jensen, 2003).

During the monsoon transition periods (April/May and October/November), the Indian Ocean equatorial region experiences eastward flowing equatorial currents driven by the relative strong westerly winds along the equator that produce Ekman convergence there (McPhaden et al., 2009). These are the strong eastward surface jets estimated to have the strength of about $1ms^{-1}$ (Schott and McCreary, 2001) and they differentiate the Indian Ocean from Pacific and Atlantic Oceans. They are known as the Equatorial or Wyrtki Jets, after Wyrtki who firstly identified them (Wyrtki, 1973). Model studies forced with two different realistic wind data by Anderson et al. (1993), Jensen (1993) and Han et al. (1999) showed that the Wyrtki Jets are weaker in autumn than in spring.

The Wyrtki Jets play an important role in the seasonal heat balance of the Indian Ocean basin (McPhaden et al., 2009). In supporting the above, Schott and McCreary (2001) observed that two months after the onset of the Wyrtki Jets, upper surface waters are transported from west to east. They decrease the thermocline and mixed layer, sea surface level and surface temperature in the west while increasing them in the east. The eastern equatorial Indian Ocean becomes warmer with more atmospheric convective activities that cause more rainfall and drainage from the land thus, lowering salinity than in the west (Vinayachandran et al., 2009).

The impacts of the Wyrtki Jets are extended beyond the Indian Ocean equatorial region by oceanic dynamic processes driven by remote forcing such as Rossby and Kelvin waves (Schott et al., 2009). This occurs when currents arrive at the end of the basin in the east, where some of the transported waters are reflected towards the west to propagate as Rossby waves as observed in the 2-layer model by O’Brien and Hurlburt (1974). Some waters reflect poleward as packets of coastal Kelvin waves which impact the Bay of Bengal (Schott and McCreary, 2001). The reflected equatorial waves were also explored in a comparison of interactions of model analysis and observations with directly wind-forced waves generating the seasonal cycle of the equatorial regime by Yuan and Han (2006).

The tropical Indian Ocean is also characterized by an eastward Equatorial Undercurrent (EUC) when the winds have an easterly component, typically February to June (Schott et al., 2009). However, It has been reported that the westward flowing Equatorial Undercurrent can be only observed consistently during austral autumn (Schott and McCreary, 2001) and at different depth and locations along the equatorial Indian Ocean (e.g. Taft, 1967; Swallow, 1967; Knox, 1976; Leetmaa and Stommel, 1980; Reppin et al., 1999). Reppin et al. (1999) suggested that the EUC can appear in other seasons as well but only when anomalous easterlies occur. Using a numerical model, Jensen (1991) showed the westward undercurrent begins in May and persists throughout the South West monsoon. Nevertheless, Leetmaa and Stommel (1980) confirmed the existence of the EUC which meanders more than 100 km south of the equator.

The tropical Indian Ocean is characterized by two shallow meridional overturning circulations that carry cool water within the thermocline to upwelling regions namely, Cross-Equatorial-Cell (CEC) and Subtropical Cell (STC). The CEC is supplied by the recirculation within the subtropical gyre, the Indonesian Throughflow and from subduction regions of the southeastern subtropics, carries cool water at thermocline level to northern upwelling regions (Schott et al., 2009). The CEC transports about 6Sv and plays a significant role in heat exchange between the Northern and Southern Hemispheres (Schott et al., 2004). The STC transports about 8Sv from southern subduction, recirculation and inflow from the ITF to the upwelling from 5-10^{o}S (Schott et al., 2009).

The southwest tropical Indian Ocean (SWTIO) exhibits an oceanic thermal dome located near the Republic of Seychelles termed Seychelles dome (SD) by Yokoi et al. (2008) and Seychelles-Chagos thermocline ridge (SCTR) by Hermes and Reason (2008). In the SWTIO, the main upwelling peaks near 7-8^{o}S and 60^{o}E, which it may shift meridionally and zonally throughout the year ranging between 70 and 80 m. Thus, sometimes the minimum thermocline in the main upwelling links to another minimum thermocline around 11^{o}S, 90^{o}E, near Chagos. This linkage leads to ridge form rather than dome, the name suggested by Hermes and Reason (2008). The main upwelling region is dominated by semiannual signal with two minima upper heat content which correspond to mature season of the SCTR in June and December-January (Hermes and

Reason, 2008; Yokoi et al., 2008). Hermes and Reason (2008) and Yokoi et al., (2008) show the semiannual signal are associated with local Ekman pumping in the region due to due to the beta effect and zonal wind stress driven by the change in wind direction resulting into downwelling (upwelling) during boreal summer (boreal winter). Furthermore, the wind stress curl between the southeasterly trades and the equatorial monsoon winds lead to annual cycle with strong upwelling occurring during boreal summer and autumn (Yokoi et al., 2008).

The upwelling in the SWTIO does not show signature in the SST but it strongly influences the overlying SST which in turn impacts the climate conditions in various regions, and regional biological and physical activities. The rainfall distribution over eastern Africa is determined by SST patterns in the upwelling region in the SWTIO (Hermes and Reason, 2009). The above normal SST anomalies in the upwelling region delay the ITCZ to move into the Indian subcontinent, leading to delay of the onset of the Indian summer monsoon by 6-7 days (Annamalai et al., 2005). Thus, Izumo et al. (2008) suggested that the spring SST in the main upwelling region to be a potential predictor for the Indian summer monsoon rainfall. The tropical cyclones are closely related to the thermocline depth in the upwelling region (Xie et al., 2002). More (less) tropical cyclone days tend occur in the Southwest Indian Ocean with deeper (shallower) thermocline depth during austral summers (Hermes and Reason, 2009). Xie et al. (2002) showed the presence of high biological productivity in the ridge due to upwelling of nutrient-rich water. Furthermore, owing to the location of the SCTR on the path of the Indonesian throughflow, it influences the stratification and air-sea heat flux in the Indian Ocean as shown by Song et al. (2004). In short, the SCTR plays significant roles climate variability in eastern Africa and Asian, and in regional ocean biological and physical activities.

2.1.3 Upper Ocean Properties

The tropical Indian Ocean displays a strong seasonal reversal in upper ocean properties as the response to the strong surface wind reversals. In association with the surface wind reversals, strong seasonal variability is observed in the surface heat fluxes, sea surface temperature (SST), sea surface salinity (SSS) and mixed layer depth. However, studies of relationships of the SST and the mixed layer depth over the tropical Indian Ocean have been focused on the North Indian

Ocean, particularly, in the Arabian Sea and Bay of Bengal (e.g. Udaya Bhaskar et al., 2006 and 2007; Sreenivas et al., 2008; PrasannaKumar et al., 2005). Strong seasonal variability of the upper ocean properties has been noted in the tropical western Indian Ocean and in the Arabian Sea and Bay of Bengal due to response to response of the seasonally reversing monsoon circulation (Schott et al., 2002; Vissa et al., 2013).

The surface heat fluxes over the tropical Indian Ocean play a major role in heating and cooling of the upper surface ocean. Different authors have studied the spatio-temporal variability of the net heat fluxes over the tropical and equatorial Indian Ocean (e.g. Rao et al, 1989, Godfrey et al., 1995; Rao and Sivakumar, 2000; Rao et al., 2005). Rao et al. (1989) found that the tropical South Indian Ocean gains heat during the austral summer and loses it in the austral winter, and most of the equatorial Indian Ocean gains heat throughout the year. They found that net surface heat fluxes of more than 100 Wm^{-2} occur over the north-western and western Indian Ocean (north of 10^{o}S) during March-April and off Somalia and Arabia during September-October. Heat loss of about 40 Wm^{-2} from south of 10^{o}S occurs in May to August (Rao et al., 1989). Godfrey et al. (1995) showed that there is a positive annual heat flux north of 15^{o}S which ranges in magnitude by 0.5-1.0 $x10^{15}$ Wm^{-2}. Rao and Sivakumar (2000) showed that during the North-East monsoon, cold dry north-easterly winds originating from the Asian landmass cause strong cooling off the North Indian Ocean, especially in the northwest of both Arabian Sea and Bay of Bengal. Moreover, the influence of light winds and clear sky conditions in the pre-South West monsoon season may results in a high net surface heat gain that warms the ocean region north of 20°S, with increasing amplitude toward the north. A remarkable cooling over the entire tropical Indian Ocean, and particularly over the south-west, results mainly from the net surface heat loss that occurs during the South West monsoon season. However, coastal wind-driven upwelling off Somalia and Arabia leads to cooler SST there. During the post-South West monsoon season, the net surface heat flux warms the entire Arabian Sea with maximum value in the south-western region, where the insolation is high, and the evaporation is low because of the presence of cold upwelled waters at the surface.

The net upper-ocean heat flux in the north-south direction across the equator in the Indian Ocean has a strong semi-annual component while the heat transport and storage indicate a strong annual component (Chirokova and Webster, 2006). The cross-equatorial heat transport reaches maximum absolute values in January (about 1.2PW) and July (about -1.6 PW); the North Indian Ocean heat storage peaks at 1.9 PW in March and minimum value of -1.4 PW occurs in June. The net surface heat flux peaks in March and October with positive values 1.0 and 0.8 PW, respectively, while minimum values occur in January (-0.6 PW) and June (-0.15 PW). There is a large southward heat transport (about -1.5 to -2 PW) from spring through autumn and a northward transport (+1.5 to +2 PW) during the rest of the year (winter and summer) with maximum transport between 10 and 15^{o}S. The Indian Ocean shows latitudinal commonality in the heat transport signs i.e. if the transport is anomalously southward at the equator, it is anomalously southward at all latitudes (Chirokova and Webster, 2006). The Ekman transport influences the variability of the heat transport while winds and cloudy conditions, which govern shortwave radiation intensity, influence the net surface heat flux distribution in the North Indian Ocean.

The seasonal cycle of the sea surface temperatures of the tropical Indian Ocean is mainly influenced by surface heat fluxes and Wyrtki Jets. The Wyrtki Jets during the transitional periods transport warm surface water along the equatorial Indian Ocean eastward, resulting in a deeper thermocline in the east than in the west. As a consequence, there is an east-west asymmetric distribution of the SST over the ocean basin with the warm SST in the eastern side and cooler one in the western side (Vinayachandran et al., 2009). The influence of the surface heat fluxes on the sea surface temperature over the coastal waters of the East Africa is clearly pointed out by MacClanahan (1988). He found that the SSTs in the East African coastal waters decrease by lagging behind air temperature during the South West monsoon due to increased cloud cover and decreased air temperatures. Further quantitative studies of the coastal waters off East Africa have shown that the SST ranges between 26-28^{o}C in February, 28°C in May, between 24-26°C in August, 27°C in November (United Nations Environmental Program (UNEP), 1985; Mahongo, 1999) and between 25-26^{o}C in June and July (Nyandwi et al., 2001). Rao et al. (2005) stated that the SST at 10^{o}S varies from about 29^{o}C in March-April to about 26^{o}C in August whereas further north, the SST increases from about 28^{o}C in the west to more than 29^{o}C in the eastern part during January-February.

Further description of the temperatures of the coastal waters off East Africa can be found in Newell (1959); Dubi (2000); Francis et al. (2000); Nyandwi et al. (2001) and Julius (2005).

Newell (1959) and Julius (2005) pointed out that during the monsoonal transition months of March and April, when the North East monsoon ends, the maximum SST of 28-30^{o}C occurs shortly after the maximum air temperatures has been reached over the East African coastal ocean. The minimum SST of 24^{o}C on average occurs in June-September during the South West monsoon. These quantitative SST studies match with the monthly surface water temperatures off the Tanzanian coast for three sampling periods 1975, 1969 and 1955-56 (McClanahan, 1988). Available studies of SST variability in relation to the mixed layer depth have been conducted in the north of the Indian Ocean with a greater focus over the Arabian Sea where the mixed layer is deepened and shoaled during both monsoons and transitions respectively (Udaya Bhaskar et al., 2006 and 2007; Sreenivas et al., 2008; and PrasannaKumar et al., 2005). In the Arabian Sea, the SST cools during the South West and North East monsoons when the mixed layer is deeper and warms in inter-monsoon periods when the mixed layer is shallow. The Wyrtki jets around the

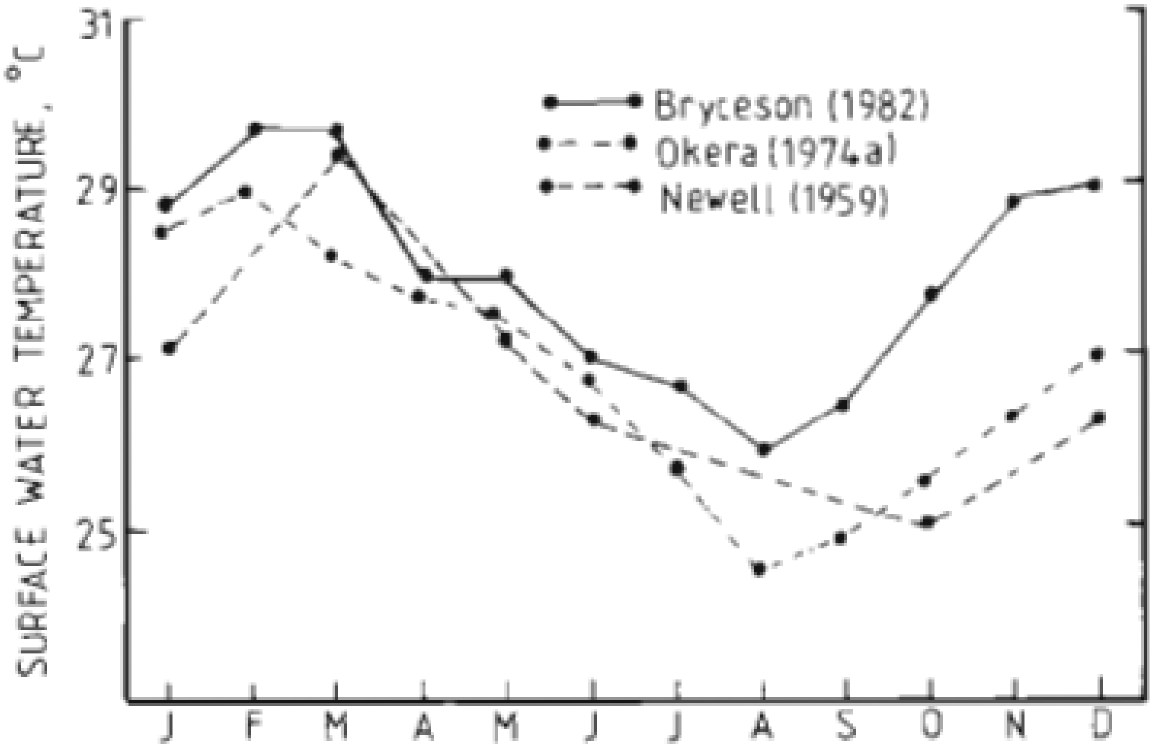

Figure 2.4: Monthly surface water temperatures off the Tanzanian coast for three sampling periods (1975, 1969, 1955-56) (McClanahan, 1988).

equatorial Indian Ocean which occur in the transition periods create a download gradient of the mixed layer from west to east (Keerthi et al., 2012). Foltz et al. (2010) showed that seasonal cycle of the mixed layer in the south-western Indian Ocean results from wind stirring effect and buoyancy fluxes as well as wind influence on thermocline depth.

Salinity variability has not been widely studied since salinity observations are sparse, both temporally and spatially in the tropical oceans and up to now there are no clear satellite salinity measurements (Subrahmanyam et al., 2011). However, a few authors have conducted studies on variability of salinity, relying on sparse observational data over the East African coastal ocean (e.g. Bryceson, 1982; Nyandwi et al., 2001). The salinity of the coastal waters off East Africa is influenced by upper ocean mixing, upwelling, river discharge, precipitation and runoff. The upper ocean mixing, river discharge and runoff are sources of phosphorus and nitrate over the coastal waters off Tanzania and southern Kenya while mixing and upwelling are sources off northern Kenya and Somalia (McGill, 1973; Smith and Codispoti, 1980).

Salinity in the East African coastal ocean shows seasonality mainly depending on river discharge. Minimum salinity occurs at the onset of the South West monsoon when river discharge, cloud cover and precipitation are high along the coast of East Africa. During this time, freshwater discharge from major rivers such as the Ruvuma, Mbemkulu, Rufiji, Ruvu and Pangani, after the MAM rainy season plays a great role in lowering the salinity of the coastal ocean. The Rufiji river, which is one of the largest rivers in Africa, is noted to discharge about 2000-3000m^3/s into the Tanzanian coastal ocean (Dubi, 2000; Shaghude, 2003; and Julius, 2005). The influence of discharge of the major rivers such as the Tana and Sabaki on coastal waters off northern Kenya is also noted shortly after the inland rainy season in both seasons, MAM and OND. In contrast to this, the highest salinity in the coastal waters off East Africa occurs during the North East monsoon when air temperatures and solar insolation are high, and the rainfall and river discharges are low. Nyandwi et al. (2001) found 34 and 35.2 psu as the

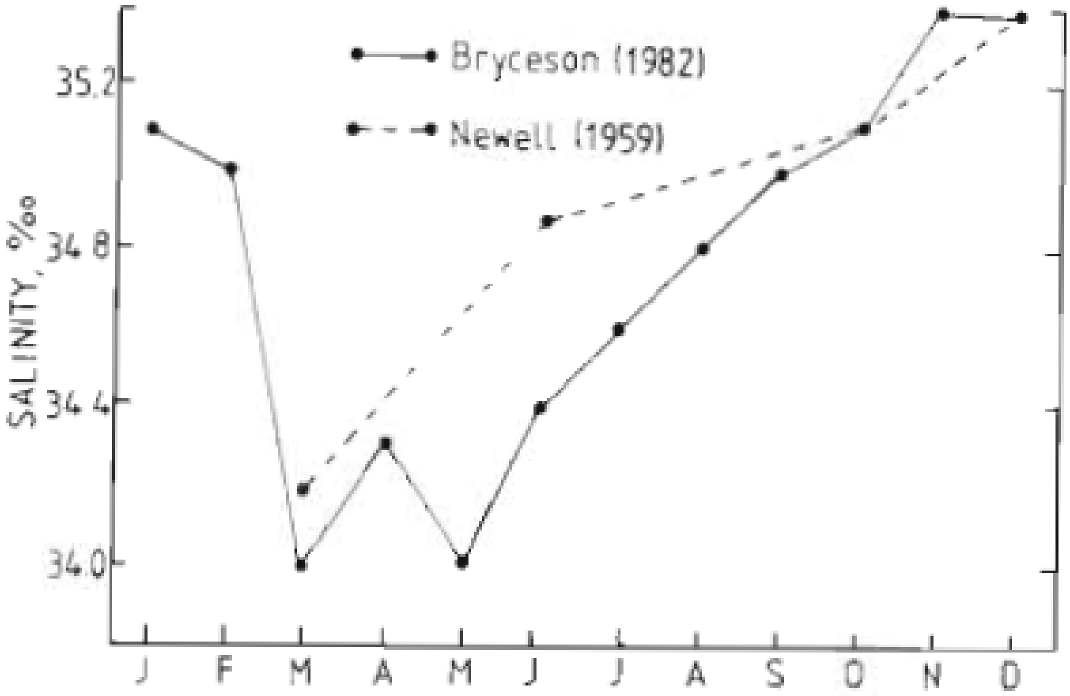

Figure 2.5: Salinity changes off the Tanzanian coast during two years (McClanahan, 1988).

typical sea surface salinity values between April and June on the East African coastal waters off Tanzania.

The tropical Indian Ocean indicates a strong seasonal cycle in the atmospheric circulation fields, upper ocean circulation, properties and upwelling. This seasonal cycle may differ from year to year due to considerably at interannual climate moderation. Thus, the following section deals with the interannual variability in the region.

2.2 Interannual Variability

The 1997/98 climatic event triggered several studies of interannual variability in ocean-atmosphere interactions especially in the tropical Indian Ocean. Different studies of interannual variability have been conducted in the tropical Indian Ocean based on observations, satellite-derived data and model simulations since then (e.g. Chambers et al., 1999; Murtugudde and Busalacchi, 1999; Behera et al., 2000; Reason et al., 2000; Annamalai and Murtugudde, 2004; Yamagata et al., 2004; McPhaden et al., 2009; Schott et al., 2009). These studies concluded that the interannual variability of the tropical Indian Ocean basin is mainly influenced by the El Niño-Southern Oscillation (ENSO) that originates over the equatorial Pacific Ocean, and the Indian Ocean Dipole (IOD). Therefore, the review of the interannual variability related to the Tanzanian shelf region in the tropical Indian Ocean focuses on the ENSO and IOD phenomena.

2.2.1 El Niño-Southern Oscillation (ENSO)

The ENSO is a strong coupled ocean-atmosphere mode in the tropical Indo-Pacific Ocean, characterized by occurrence of anomalously cold (warm) SST anomalies in the central and eastern equatorial Pacific Ocean during La Niña (El Niño), and changes in the zonal pressure atmospheric gradient (the Southern Oscillation) across the equatorial Pacific (Schott et al., 2009). Any El Niño evolution involves an anomalous increase of the SST and sea surface height (SSH) in the eastern tropical Pacific Ocean and the opposite in the west. Composite analysis using the Hadley Centre SST (HadSST) dataset from 1950–2006 by Rayner et al. (2006) shows that the ENSO mechanism is phase-locked to the annual cycle; the ENSO-induced SST anomalies develop over the Pacific during austral winter, peak in austral summer and decay in the following austral autumn (Figure 2.6; Schott et al., 2009). The change in zonal atmospheric pressure gradient over the tropical Pacific Ocean leads to a large-scale shift in the atmospheric convection that increases the angular momentum which remotely modifies the atmospheric circulation in both the tropics and extratropics (Alexander et al., 2002; Liu and Alexander, 2007). As a consequence, ENSO impacts the global atmospheric circulation. The climatic characteristics of the impacts of ENSO events on a region depend on the pre-existing climate and local characteristics of a particular region (Marchant et al., 2006).

The tropical Indian Ocean basin slowly warms during an El Niño event peaking in austral autumn (March-May) following the El Niño onset year (Figure 2.6; Klein et al., 1999; Reason et al., 2000; Liu and Alexander, 2007; Schott et al., 2009). This warming is attributed to ENSO-induced changes in the surface heat fluxes, especially wind-induced latent heat and cloud-induced heat fluxes (Klein et al., 1999; Reason et al., 2000). However, downwelling Rossby waves induced by ENSO anomalous winds in the southeastern Indian Ocean warms the western tropical South Indian Ocean instead of the ENSO-induced heat flux (Xie et al., 2002). The downwelling Rossby waves in the southeastern Indian Ocean are favoured by the simultaneous presence of an upwelling and a shallow themocline (Xie et al., 2002). It also has been noted that midlatitude South Indian Ocean cools during El Niño (Reason et al., 2000).

Strong interannual SST variability occurs in the Southwest Indian Ocean due to changes of the thermocline ridge between 5 and 10°S forced by the Rossby waves from the southeastern Indian Ocean (Murtugudde and Busalacchi, 1999; Murtugudde et al., 2000; Behera et al., 2000). During December when El Niño matures, strong anomalous anti-cyclonic wind stress curl forms in the tropical southeastern Indian Ocean which forces downwelling Rossby waves westward (Chambers et al., 1999). The Rossby waves deepen the thermocline between 5 and 10°S in the southwest Indian Ocean, and consequently, warm the SST (Murtugudde and Busalacchi, 1999; Murtugudde et al., 2000; Behera et al., 2000; Xie et al., 2002). As a result, the region over the thermocline ridge appears to have maximum interannual SST variability in April-July with standard deviation of about 0.4-0.5°C (Schott et al., 2009). The ENSO-induced ocean warming in the tropical Indian Ocean persists until the following austral winter impacting the regional atmospheric weather and climate.

The tropical Indian Ocean and countries surrounding it experience profound changes in the atmospheric weather and climate characteristics during ENSO events that can lead to severe socio-economic problems. Great changes in precipitation occur in the region with heavy rainfall taking place over East Africa, and severe drought occurring over Indonesia and southern Africa during El Niño events (e.g. Chambers et al., 1999; Reason et al., 2000; Yamagata et al., 2004; McPhaden et al., 2009; Schott et al., 2009). The opposite conditions typically occur during La Niña events. The most recent very strong El Niño event is that of 1997/1998 which caused devastating floods in East Africa and severe drought over Indonesia during October-November. During that event, the severe flooding in the East African region caused several deaths and outbreak of diseases such as malaria and cholera as well as displacement of many people (Schott et al., 2009). In contrast, severe droughts took place over Indonesia that caused wild fire outbreaks on several of its islands resulting in smoke and haze which caused serious health problems. This very strong 1997/1998 event triggered and motivated different scientific researchers to study the role of the tropical Indian Ocean in the regional climate variability (e.g.

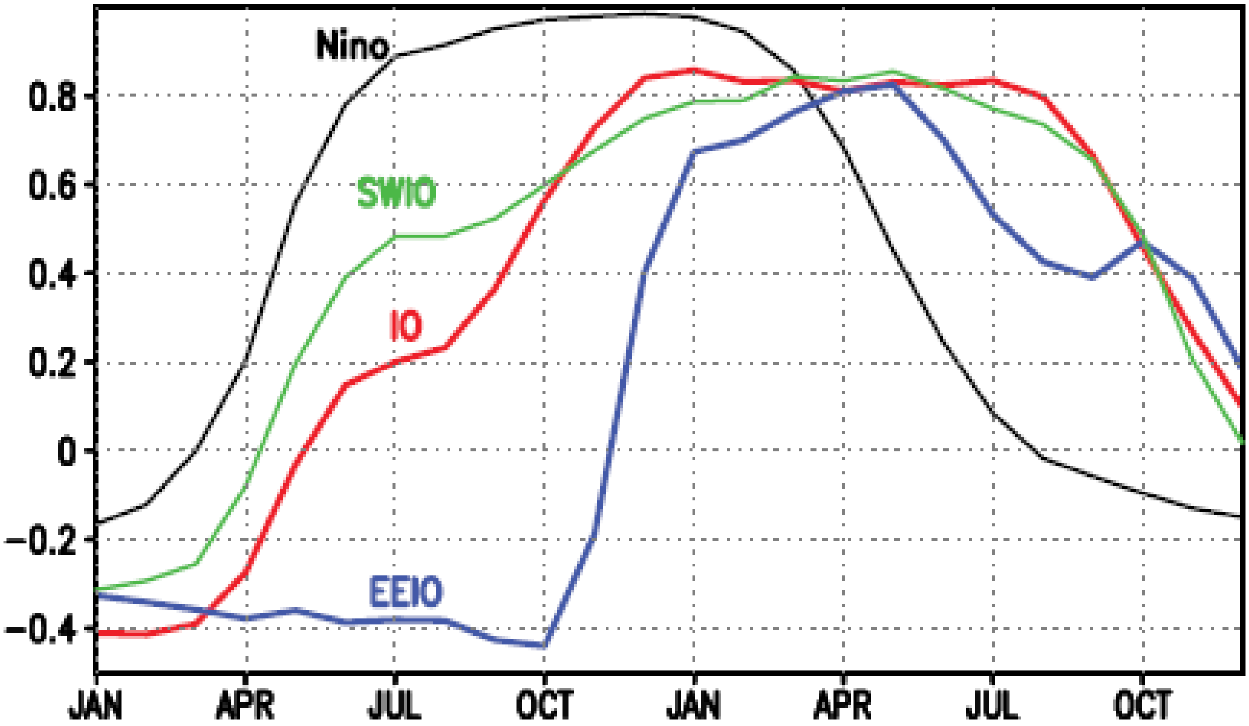

Figure 2.6: Niño SST correlation with SST averaged in the eastern equatorial Pacific (160–120^0 W, 5^{o}S–5^{o}N; black), the tropical IO (40–100^{o}E, 20^{o}S–20^{o}N; red), the southwest IO (50–70^{o}E, 15–5^{o}S; green), and the eastern equatorial IO (90–110^{o}E, 10^{o}S–0^o; blue) (Schott et al., 2009).

Saji et al., 1999; Webster et al., 1999). The studies concluded that the El Niño by itself was not sufficient to cause these tremendous climatic changes over the tropical Indian Ocean in 1997/1998. Thus, the co-occurrence of the El Niño event with the Indian Ocean Dipole Mode (IOD), which is a climatic mode originating within the Indian Ocean, was suggested as being the reason for the profound climatic variations in 1997/98. Therefore, the next section provides a literature review of the IOD.

2.2.2 Indian Ocean Dipole (IOD)

The IOD is an interannual climate mode of the Indian Ocean associated with anomalously warm and cold SST over the western and eastern tropical Indian Ocean basin during its positive phase, respectively (Saji et al, 1999; Webster et al, 1999). Saji et al. (1999) found a strong correlation (>0.7) of the SST anomalies in the tropical western Indian Ocean with a time series of the Indian

Ocean Dipole Mode Index (IODMI) derived from the SST averaged over a tropical western Indian Ocean box (50^oE-70^oE, 10^oS-10^oN) minus that over a tropical south-eastern Indian Ocean box (90^oE-110^oE, 108^oS-Equator). This is the positive phase of the IOD, and its reverse, which is almost an intensification of the normal state of the equatorial Indian Ocean, is known as a negative IOD phase (Vinayachandran et al., 2009). The positive phase of the IOD shows positive (negative) SST anomalies in the western (eastern) Indian Ocean basin, and its reverse is a negative phase (Figure 2.7).

Earlier atmospheric studies reported signatures of the zonal dipole in the atmospheric fields over the tropical Indian Ocean. In analysing observational meteorological parameters (1954–1976), Reverdin et al. (1986) explored an east-west cloudiness dipole that develops during October–November with zonal wind anomalies in the central ocean in the tropical Indian Ocean. They showed that the negative cloudiness anomalies in the equatorial eastern Indian Ocean (EEIO) co-occurred with cool SST suggesting that the cool SST suppresses atmospheric convection and drives easterly anomalies along the equator. Meyers (1996) noted a strong coupling between the SST cooling and shoaling thermocline off the south coast of Java in 1994 which now is considered as a part of IOD (Vinayachandran et al., 1999; Behera et al., 1999).

Much effort, especially after the 1997/1998 event, has been devoted to understand the evolution and mechanisms of IOD in the tropical Indian Ocean. The evolution of an IOD event is seasonally phase-locked; it begins in late austral autumn/early winter, peaks during September-November, and most of the SST anomalies disappear by January of the following year (Vinayachandran et al., 2009). This timing is supported by composite analysis of the recent extreme IOD events of 1961, 1967, 1972, 1982 and 1997 which shows that an IOD event establishes in early/peak austral winter, matures by September and weakens by December (Figure 2.8; Saji et al., 1999; Achuthavarier and Krishnamurthy, 2009). The coupled ocean-atmosphere processes, particularly Bjerknes feedback, in the equatorial eastern Indian Ocean play a vital role in the IOD mechanisms as reported by Hastenrath et al. (1993) and Vinayachandran et al. (1999). The Bjerknes feedback involves positive interaction loop of anomalies of wind stress, thermocline depth, upwelling strength and SST (Schott et al., 2009).

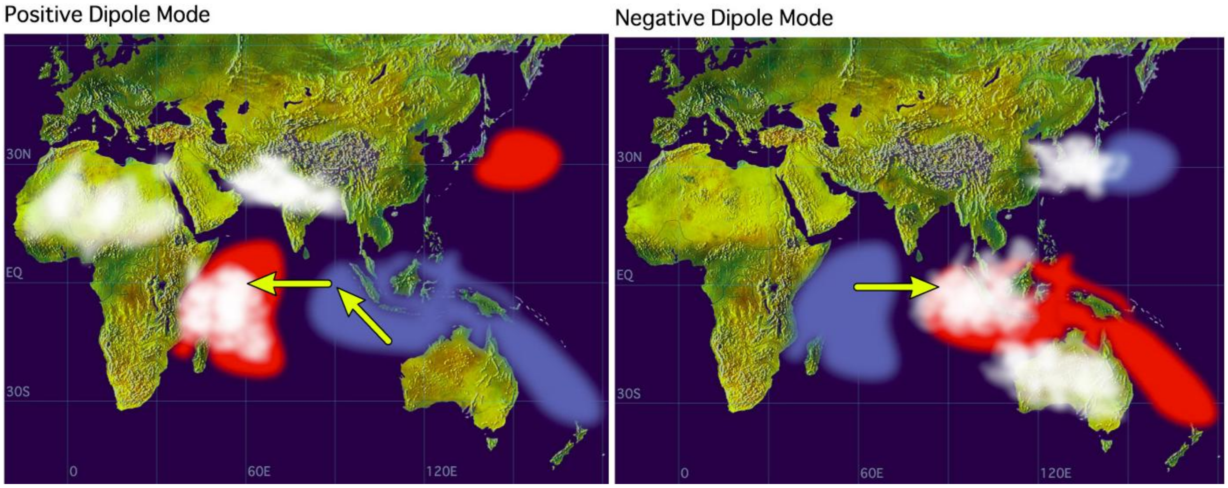

Figure 2.7: Schematic diagram for a positive (negative) Indian Ocean dipole to the right (left) [red shading denote warming; blue cooling, white patches for increased convection and arrows indicating wind direction; A. Suryachandra Rao, Institute for Global Change Research, Yokohama City, Japan].

The strong easterly winds along the equatorial Indian Ocean weaken or even reverse the Wyrtki Jets in initial stage of IOD, and consequently, decrease the eastward transport there. As a result, anomalous upwelling Kelvin waves are generated which are reflected as coastally trapped Kelvin and Rossby waves at the boundaries of the eastern equatorial Indian Ocean (EEIO). The combination of the weakened or reversed Wyrtki Jets and upwelling Kelvin waves lifts up the thermocline to the east during development and peak of IOD, favouring coastal upwelling by southeasterly wind anomalies off Sumatra and Java coasts. As results, strong easterly winds along the equator and strong southeasterly winds along Sumatra/Java coasts generate a strong anomalous anti-cyclonic wind stress curl in the southern tropical Indian Ocean that generates downwelling Rossby waves in the developing phase of IOD. The downwelling Rossby waves deepen the thermocline and warm the SST in the western tropical Indian Ocean (Murtugudde et al., 2000; Vinayachandran et al., 2009). As a result, anomalously warm SST occurs in the west and anomalously cold SST in the east of the Indian Ocean basin during positive IOD phase (Saji et al, 1999; Webster et al, 1999).

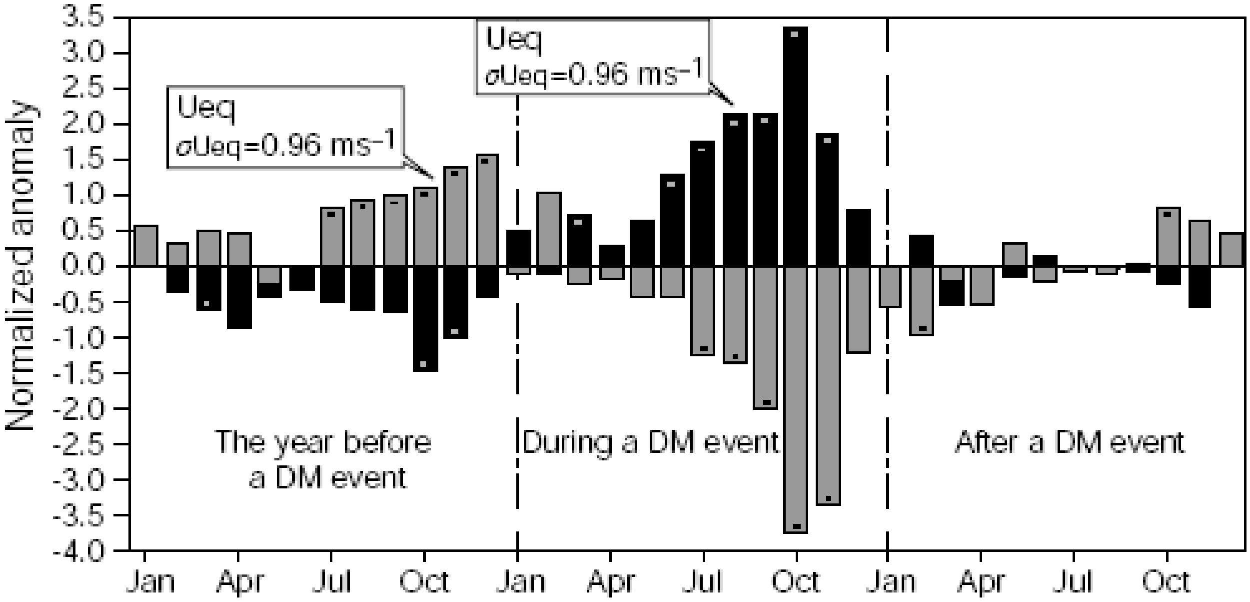

Figure 2.8: Time evolution of the dipole mode index defined as the SSTA difference between the western and eastern Indian Ocean (dark-shaded bar) and the zonal wind anomaly (light-shaded bar) (Saji et al., 1999).

Similar features/characteristics occur in all IOD events which may differ in timing and location of the peak anomalies as well as in phase evolution. The latter varies for every event over the eastern Indian Ocean due to influence of the coastal upwelling off Sumatra. For example, the peak anomalies of 1994 event took place about 2 months earlier in the year than that of 1997; the positive SSTA of 2006 event were located to the west of 50-70^{o}E; 10^{o}S-10^{o}N which is regarded as IOD box (Vinayachandran et al., 2007). Some studies, based on the satellite data, have examined the positive and negative IOD separately (e.g. Saji and Yamagata, 2003; Hong et al., 2008). Hong et al. (2008) found that positive and negative IODs have different evolution and structure. They stated that the positive IOD develops abruptly and quickly as its SSTA begin in May. In contrast, the negative IOD starts earlier, develops gradually and its SSTA begins earlier before March. Typically, both IOD phases terminate almost at the same time of year.

The east-west dipole of the SST anomalies associated with the IOD has great implications for the ocean and atmospheric fields over the tropical Indian Ocean. The warm SST increases cloud amounts over the tropical Indian Ocean which decreases the net downward shortwave radiation and cools SST (Li et al., 2003). Further, cooled SST decreases the atmospheric convection over the EEIO; consequently, an anomalous anti-cyclonic circulation occurs to the west of its center. The anti-cyclonic circulation generates downwelling Rossby waves in the western tropical Indian Ocean (Gill, 1980), and enhances both southeasterly and easterly winds over the southeastern Indian Ocean. As a result, wind-induced strong evaporative cooling occurs in the southeastern Indian Ocean in the austral winter (Vinayachandran et al., 2009). Moreover, the enhanced winds boost both coastal upwelling and vertical mixing, resulting in further cooling of SST over the southeastern tropical Indian Ocean. Through satellite monitoring, increased chlorophyll concentration was captured in 1997-1998 and 2006 events over the eastern equatorial Indian Ocean while that of the western Indian Ocean and along the coast of India appears to decrease (Wiggert et al., 2009; Iskandar et al., 2009). Using satellite altimetry measurements, Palastanga et al. (2006) found that the positive phase of the IOD (e.g. 1994 and 1997) weakens the SEC, NEMC, SEMC and EACC, and they are strengthened in negative phase (e.g. 1996 and 1998). They also found stronger southward flow and eddy activity in Mozambique Channel during positive IOD and weakens during negative IOD

IOD events are typically associated with large climate impacts on the regional and global scales. The east-west dipole of intensified anomalous coupled ocean-atmosphere parameters such as rainfall, surface pressure, outgoing long wave radiation and sea surface height anomalies, appears in the tropical Indian Ocean (Yamagata et al., 2003; 2004). As the IOD develops between September and November, an east-west dipole of anomalous rainfall is established over the tropical Indian Ocean, with precipitation increasing in the west because of the low-level convergence associated with the anomalous equatorial easterlies and vice versa in the east (Saji et al., 1999; Webster et al., 1999). A 40 years analysis from 1979 by Saji et al. (1999) and (2003) shows that in positive IOD events, equatorial East Africa typically experiences above average rainfall and severe droughts occur over Indonesia. Moderate climate impacts are observed over Sri Lanka (Lareef et al., 2003) and Australia (England et al., 2005). In short, East Africa tends to experience above average rainfall during October to December while Indonesia and Australia experience relatively dry conditions (Ashok et al., 2004). The most recent positive IOD years which are associated with the above average rainfall in East Africa are 1994, 1997 and 2006 (McPhaden et al., 2009). During a negative IOD phase, the SST pattern leads to drought and relative stability in the atmosphere over East Africa, whereas East Asia tends to experience heavy rainfall (Behera and Yamagata, 2001).

2.2.3 Relationship and Challenges between ENSO and IOD

The co-occurrence of ENSO and IOD has been studied by several authors in the climate research community within the last decade (e.g. Saji and Yamagata, 2003; Behera et al., 2006; Meyers et al., 2007; Achuthavarier and Krishnamurthy, 2009). In understanding the relationship between ENSO and IOD, some studies proposed that IOD events can exist without ENSO such as IOD events of 1961, 1967 and 1994 (e.g. Behera et al., 2006; Saji and Yamagata, 2003; Achuthavarier and Krishnamurthy, 2009). However, Krishnamurthy and Kirtman (2003), and Klein et al. (1999) suggested a linkage between ENSO and IOD based on analyses of seasonally observed SST (1870-1998) and numerical model simulation, respectively. Furthermore, Saji et al. (1999) and Webster et al. (1999) showed a weak correlation (<0.35) between ENSO and IOD. The observational analysis by Saji and Yamagata (2003) for 1958-1997 found 11 episodes out of 19 which were considered as moderate to strong IOD events that occurred independently of ENSO. Another observational analysis by Meyers et al. (2007) for 1876-1999 found about half IOD events occurred independently of ENSO during that period. Thus, the existing studies suggest that several ENSO events can co-occur with IOD events.

The co-occurrence of ENSO and IOD tends to depend on the ending month of the season following the ENSO events, and it is phase-orientated bringing strong changes in ocean-atmospheric fields. Based on the observed SST and National Centres for Environmental Prediction (NCEP) reanalysis, Nagura and Konda (2007) analysed the Indian Ocean SST anomalies associated with ENSO and IOD events. They found that the IOD development depends on the seasonal switch from neutral/La Niña conditions in the Pacific to El Niño. They concluded that if switching occurs from spring to summer, an IOD event will be likely to develop and otherwise, an IOD event will not occur. The co-occurrence of ENSO and IOD event mainly relies on their two different phases; a positive IOD normally co-occurs with El Niño and a negative IOD with La Niña (Alory et al., 2007; McPhaden et al., 2009; Schott et al., 2009). The highest warm SST, sea level and rainfall anomalies occur in the tropical western Indian Ocean when El Niño co-occurs with a positive IOD (e.g. 1997/1998). In contrast, the highest cool SST and sea level anomalies as well as severe drought occur in the tropical western Indian Ocean when La Niña co-occurs with a negative IOD. Yuan and Li (2008) suggested that since 1970, almost all El Niño (La Niña) events have been co-occurring with positive (negative) IOD; almost every positive (negative) IOD event occurs in an (a) El Niño (La Niña) event. They added that this behaviour may be related to a strong warming trend over the Maritime Continent in the Indo-Pacific Ocean after 1970 which increased the Walker circulation. Thus, there has been low-level convection and upper-level divergence in connection with the sea water between the eastern Indian Ocean and western Pacific Ocean (Yuan and Li, 2008). The anomalous Ekman pumping that forces the IOD-induced Rossby waves dominate to the north of 10^{o}S and that force ENSO-induced Rossby waves dominate to the south of 10^{o}S (Rao et al., 2005; Yu et al., 2005).

Despite all the research on ENSO and IOD, the climate community faces different challenges relating to the ENSO and IOD. For example, there is no scientific consensus on an accepted scientific definition and classification criteria of El Niño and La Niña events, or the best indices to capture ENSO. Some papers consider the 1994 year as El Niño and others not (Meyers et al., 2007). As a result, different years have been classified as El Niño, La Niña, negative or positive IOD events as shown in Table 2.1, 2.2, 2.3 and 2.4 by Rao et al. (2002), Yamagata et al. (2004), Meyers et al. (2007) and Ummenhofer et al. (2009), respectively. Based on the classification of Yamagata et al. (2004), Tozuka et al. (2010) defined 1961, 1967, 1977, and 1994 as pure positive IOD years; 1958, 1960,1989, 1992, and 1996 as pure negative IOD years; 1965, 1969, 1976, 1986, and 1991 as pure El Niño years; and 1967, 1971, 1973, 1975, and 1988 as pure La Niña years.

Table 2.1: Classification of strong IOD events; italic indicates positive (negative) IOD events co-occurred with strong El Niño (La Niña) in the Pacific. Bold indicates the negative IOD event that occurred along with El Niño (Rao et al., 2002).

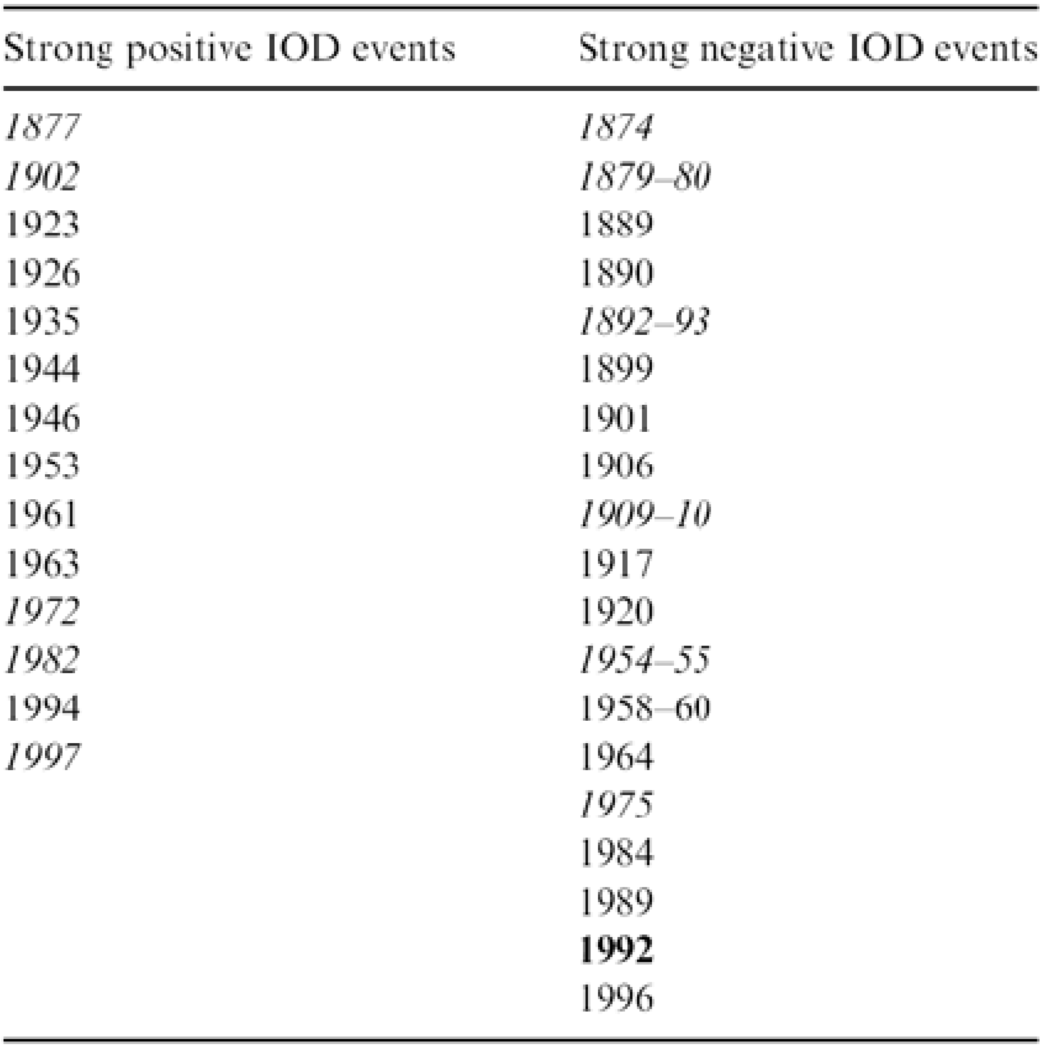

Strong positive IOD events	Strong negative IOD events
1877	*1874*
1902	*1879–80*
1923	1889
1926	1890
1935	*1892–93*
1944	1899
1946	1901
1953	1906
1961	*1909–10*
1963	1917
1972	1920
1982	*1954–55*
1994	1958–60
1997	1964
	1975
	1984
	1989
	1992
	1996

Table 2.2: Classification of IOD and ENSO events; the asterisk denotes pure events, i.e. no El Niño (La Niña) during a positive (negative) IOD event (Yamagata *et al.*, 2004).

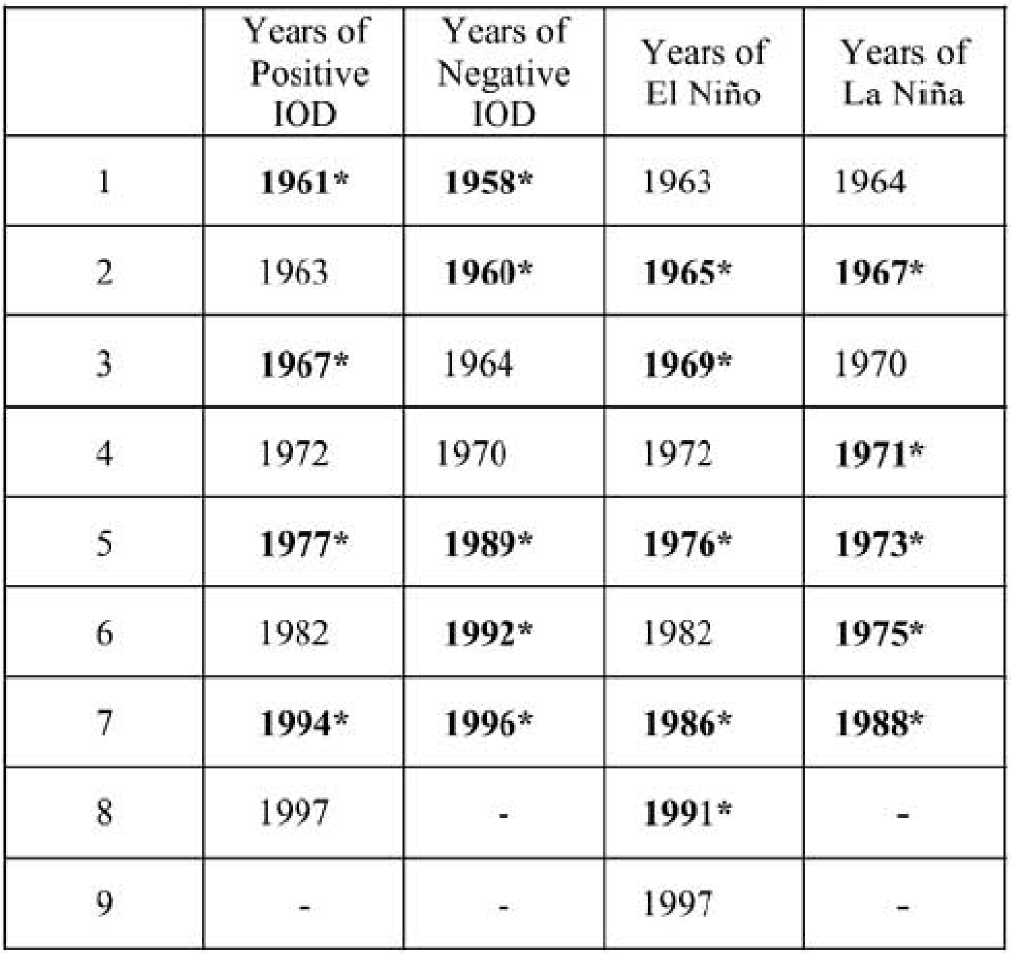

	Years of Positive IOD	Years of Negative IOD	Years of El Niño	Years of La Niña
1	**1961***	**1958***	1963	1964
2	1963	**1960***	**1965***	**1967***
3	**1967***	1964	**1969***	1970
4	1972	1970	1972	**1971***
5	**1977***	**1989***	**1976***	**1973***
6	1982	**1992***	1982	**1975***
7	**1994***	**1996***	**1986***	**1988***
8	1997	-	**1991***	-
9	-	-	1997	-

Table 2.3: Classification of positive/negative IOD events and El Niño/La Niña events. Boldface (lightface) indicates a higher (lower) level of certainty in the classification. A year is given a lower certainty if either the ENSO phenomenon or the IOD phenomenon is not clear (Meyers et al., 2007).

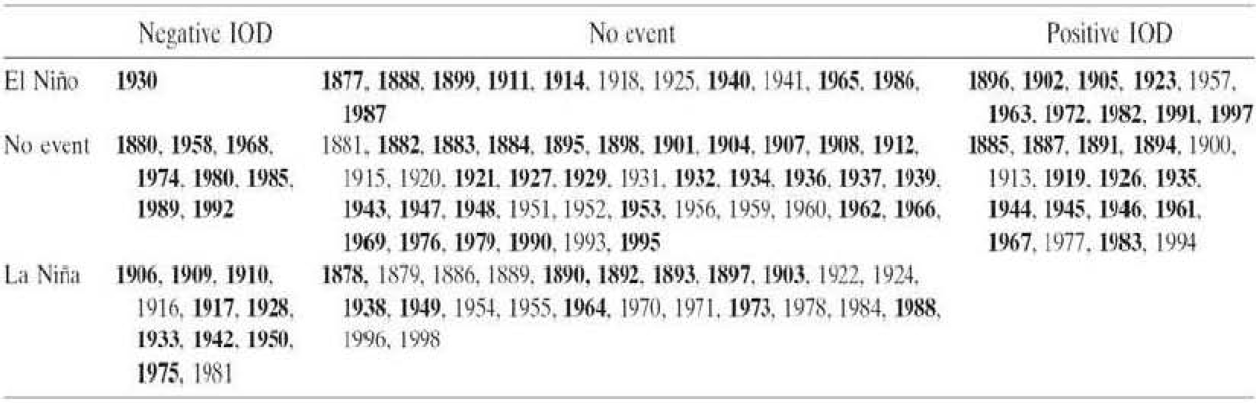

	Negative IOD	No event	Positive IOD
El Niño	**1930**	**1877**, **1888**, **1899**, **1911**, **1914**, 1918, 1925, **1940**, 1941, **1965**, **1986**, **1987**	**1896**, **1902**, **1905**, **1923**, 1957, **1963**, **1972**, **1982**, **1991**, **1997**
No event	**1880**, **1958**, **1968**, **1974**, **1980**, **1985**, **1989**, **1992**	1881, **1882**, **1883**, **1884**, **1895**, **1898**, **1901**, **1904**, **1907**, **1908**, **1912**, 1915, 1920, **1921**, **1927**, **1929**, 1931, **1932**, **1934**, **1936**, **1937**, **1939**, **1943**, **1947**, **1948**, 1951, 1952, **1953**, 1956, 1959, 1960, **1962**, **1966**, **1969**, **1976**, **1979**, **1990**, 1993, **1995**	**1885**, **1887**, **1891**, **1894**, 1900, 1913, **1919**, **1926**, **1935**, **1944**, **1945**, **1946**, **1961**, **1967**, 1977, **1983**, 1994
La Niña	**1906**, **1909**, **1910**, 1916, **1917**, **1928**, **1933**, **1942**, **1950**, **1975**, 1981	**1878**, 1879, 1886, 1889, **1890**, **1892**, **1893**, **1897**, **1903**, 1922, 1924, **1938**, **1949**, 1954, 1955, **1964**, 1970, 1971, **1973**, 1978, 1984, **1988**, 1996, 1998	

Table 2.4: Classification of years of positive/negative IOD and El Niño/La Niña events (Ummenhofer et al., 2009).

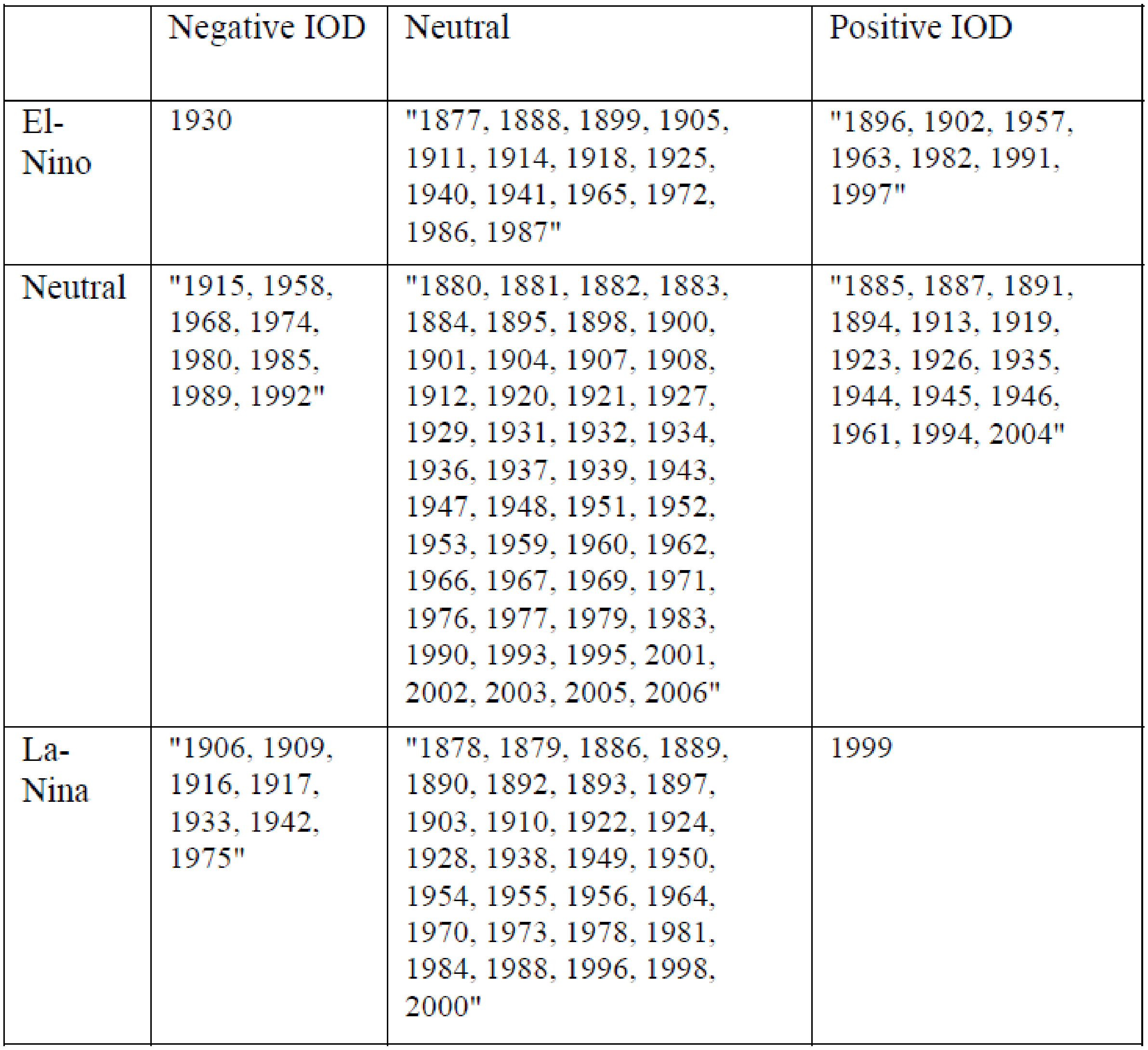

	Negative IOD	Neutral	Positive IOD
El-Nino	1930	"1877, 1888, 1899, 1905, 1911, 1914, 1918, 1925, 1940, 1941, 1965, 1972, 1986, 1987"	"1896, 1902, 1957, 1963, 1982, 1991, 1997"
Neutral	"1915, 1958, 1968, 1974, 1980, 1985, 1989, 1992"	"1880, 1881, 1882, 1883, 1884, 1895, 1898, 1900, 1901, 1904, 1907, 1908, 1912, 1920, 1921, 1927, 1929, 1931, 1932, 1934, 1936, 1937, 1939, 1943, 1947, 1948, 1951, 1952, 1953, 1959, 1960, 1962, 1966, 1967, 1969, 1971, 1976, 1977, 1979, 1983, 1990, 1993, 1995, 2001, 2002, 2003, 2005, 2006"	"1885, 1887, 1891, 1894, 1913, 1919, 1923, 1926, 1935, 1944, 1945, 1946, 1961, 1994, 2004"
La-Nina	"1906, 1909, 1916, 1917, 1933, 1942, 1975"	"1878, 1879, 1886, 1889, 1890, 1892, 1893, 1897, 1903, 1910, 1922, 1924, 1928, 1938, 1949, 1950, 1954, 1955, 1956, 1964, 1970, 1973, 1978, 1981, 1984, 1988, 1996, 1998, 2000"	1999

2.3 Summary

This literature review indicates strong seasonality of the atmospheric circulation fields such as surface winds and rainfall over the tropical western Indian Ocean, and their corresponding seasonal reversals of surface ocean circulation and ocean properties. Dry northeasterly winds blow towards the tropical western Indian Ocean during the North East monsoon and are channeled southward along the coast by the East African highlands. Consequently, the surface winds drive the southward Somali Current which confluences with the weakened EACC between 2 to 3^{o}S forming the SECC (Swallow et al., 1991; Schott et al., 2009). These surface winds also drive the SST cooling due to wind-induced evaporative heat loss. During the South West monsoon, the moist strong southeast winds blow towards the tropical western Indian Ocean and are channelled northward by the East African highlands. These surface winds become southwesterly towards India over the north of the tropical western Indian Ocean. The surface winds enhance the SEC, NEMC and EACC, and significantly cool the tropical western Indian Ocean. The EACC supplies the northward Somali Current in this period. The transition takes place during April-May and October-November when there is a strong westerly component along the equator. During the transitions, the surface winds weaken and the SST warm lagging about one month behind the ITCZ movement. The rainfall patterns migrate following the ITCZ. Thus, East African countries receive bimodal rainfall, March-May (MAM) and September to November (SON).

The ENSO and IOD are the prominent climate modes which significantly influence the interannual variability of the tropical western Indian Ocean. The tropical Indian Ocean basin warms gradually during El Niño and cools in La Niña, peaking in the spring of the following year. An IOD event warms the western tropical Indian Ocean during the positive phase and cools it during the negative phase. The El Niño and positive IOD phase are associated with heavy rainfall that causes floods in the tropical western Indian Ocean, especially over East African countries. The La Niña and negative IOD phase are associated with strong droughts in the tropical western Indian Ocean and East Africa. Co-occurrence of El Niño with a positive IOD phase or La Niña with a negative IOD phase may cause the strongest anomalies in the SST; consequently, the strongest precipitation anomalies occur in the tropical western Indian Ocean e.g. 1997/1998 El Niño/positive IOD phase event.

Rainfall is a climatic factor of great significance over East African countries because the livelihoods of most of their population rely on rain-fed agriculture and fisheries. Moreover, the variability of rainfall over East African countries affects socio-economic stability as drought is associated with shortages of food and energy (hydroelectric power), and flooding is associated with disease outbreak (e.g. malaria and cholera) as well as loss of life and property. To a large extent, the rainfall variability over East Africa is driven by the ocean properties, particularly SST, in the tropical western Indian Ocean. Therefore, a better understanding of the variability of the tropical western Indian Ocean could improve planning and the management of climate sensitive activities such as agriculture and water resources, hydroelectric power supply, prevention of disease outbreak and tourism in East African countries.

Chapter 3

Methodology and Datasets

3.0 Introduction

Existing studies on the oceanography of the Tanzanian shelf region focus more on observations than on numerical modeling. However, the observational studies are expensive, sparse and limited in time and to a few ocean variables. With regard to such observational limitations, small-scale oceanic processes and variability in the region are not well understood. On the other hand, numerical modeling is relatively cost effective with large spatial and temporal coverage of all variables. Furthermore, numerical simulations provide insight into variability at the surface and at the subsurface in a region. Thus, numerical simulations are alternative research tools to improve understanding of the ocean processes and variability in the region.

This thesis deploys numerical modeling to investigate the circulation in the Tanzanian shelf region and its variability. It uses a configuration of the Regional Ocean Modeling System (ROMS) validated by satellite and hydrographical data as well as in *situ* data around Chumbe Island in the Tanzanian shelf region. The study focuses on both the seasonal and the interannual variability. The model SST is validated using two SST satellite datasets, the Advanced Very High Radiometer Resolution (AVHRR) SST data and the Tropical Rainfall Measuring Mission Microwave Imager (TMI) SST data. Furthermore, the CSIRO Atlas of Regional Seas Version 2009 (CARS2009), the gridded Indian Ocean Hydrobase data and *in situ* SST data off Chumbe Island are used to validate the model SST. Data from Archiving, Validation and Interpretation of Satellite Oceanographic (AVISO) are compared with the model surface ocean currents and sea surface height, and the World Ocean Atlas 2009 (WOA2009) are compared with the model sea surface salinity (SSS) in the region.

This chapter describes the datasets used and the methods applied to investigate the variability in the Tanzanian shelf region. The descriptions of the physics and configurations of the ROMS model in the tropical western Indian Ocean are provided in the next section. Details for the satellite derived datasets from AVHRR, TMI and AVISO as well as the digitalized/gridded data from CARS2009/Hydrobase and direct *in situ* data around Chumbe Island over the model domain are provided in section 3.2. The third part deals with different techniques and tools used for statistical analysis (3.3) followed by details of some variables used in this study (3.4). The final section summarizes the datasets used and methodology applied in this research.

3.1 Regional Ocean Modeling System (ROMS)

ROMS is a modern ocean circulation model which has been applied in the western Indian Ocean (e.g. Mayorga-Adame, 2007; Penven et al., 2006; Hermes and Reason, 2008). It has been used extensively and successfully in a range of studies in the tropical western Indian Ocean; e.g., in the Zanzibar Channel by Mayorga-Adame (2007) and over the Southwest Indian Ocean by Penven et al. (2006) and the tropical Indian Ocean by Hermes and Reason (2008). It is a well known and established numerical tool for simulating ocean circulation in this region. Therefore, the ROMS model is a well-established tool for simulating Indian Ocean circulation and processes.

3.1.1 Model Description

The Regional Oceanic Modeling System (ROMS) is a numerical code originally developed at Rutgers University and at the University of California, Los Angeles, USA, as an improvement of the S-Coordinates Rutgers University Model (SCRUM). The version used here is the IRD version of the code (ROMS AGRIF), available from the Website "http://www.romsagrif.org" (Debreu et al., 2011). It is a free-surface, terrain-following ocean model which solves the three-dimensional hydrostatic primitive equations (Shchepetkin and McWilliams, 2003, 2005). It solves the equations using a split-explicit time-stepping scheme coupling between barotropic (fast) and baroclinic (low) modes. Thus, the ROMS model saves computational costs.

In the horizontal and vertical structure, the primitive equations are discretized according to orientation of coastal boundary and topography, respectively. Orthogonal curvilinear coordinates are applied on a staggered Arakawa C-grid. This involves Cartesian (constant metrics) and spherical (variable metrics) coordinates. Stretched, terrain-following coordinates are used in the vertical (Song and Haidvogel, 1994). It is a free-surface model with sigma vertical coordinates over variable topography. ROMS uses either the local closure scheme by Mellor and Yamada (1982) or the nonlocal closure scheme by Large et al., (1994) for the vertical mixing parameterization. The latter is based on K-profile scheme, and it has been expanded to include both surface and bottom oceanic boundary layers. By default, the ROMS model uses third-order advection scheme which is upstream biased with a velocity dependence on the hyper-diffusion dissipation (Shchepetkin and McWilliams, 1998). Second- and fourth-order differentiating are other options of the advection schemes.

The ROMS model is written in Fortran 90/95 with various software that support pre- and post-processing. Several physical and numerical options in the ROMS are activated by C-preprocessing. The model comprises different pre- and post-processing software for data preparation, analysis and displaying (Penven et al., 2007). The input and output data are in NetCDF format that allows data interchanges among different user community.

Equations of motion

Based on the Boussinesq and hydrostatic approximations for an incompressible ocean, the primitive equations of motion are discussed below using Cartesian coordinates:

$$\frac{\partial u}{\partial t} + \vec{v}.\nabla u - fv = -\frac{\partial \phi}{\partial x} + F_u + D_u \qquad (3.1)$$

$$\frac{\partial v}{\partial t} + \vec{v}.\nabla v + fu = -\frac{\partial \phi}{\partial y} + F_v + D_v \qquad (3.2)$$

$$\frac{\partial T}{\partial t} + \vec{v}.\nabla T = F_T + D_T \qquad (3.3)$$

$$\frac{\partial S}{\partial t} + \vec{v}.\nabla S = F_S + D_S \qquad (3.4)$$

$$\frac{\partial \phi}{\partial z} = -\frac{\rho g}{\partial x} \qquad (3.5)$$

$$\frac{\partial u}{\partial x} + \frac{\partial v}{\partial y} + \frac{\partial w}{\partial z} = 0 \qquad (3.6)$$

$$\rho = \rho(T,S,P) \tag{3.7}$$

The equations (3.1) and (3.2) express the horizontal momentum balance in the *x* and *y* directions, respectively. The equations (3.3) and (3.4) are for the advection/diffusion for potential temperature and salinity. The hydrostatic balance, mass balance and state for seawater are expressed by equations 3.5, 3.6 and 3.7, respectively.

Vertical boundary conditions

At the sea surface: $z = \xi(x,y,t)$

$$K_v \frac{\partial u}{\partial z} = \frac{\tau_s^x}{\rho_0}(x,y,t) \tag{3.8}$$

$$K_v \frac{\partial v}{\partial z} = \frac{\tau_s^y}{\rho_0}(x,y,t) \tag{3.9}$$

$$K_T \frac{\partial T}{\partial z} = \frac{Q_T}{\rho_0 cp} \tag{3.10}$$

$$K_S \frac{\partial S}{\partial z} = \frac{(E_v - P_r)S}{\rho_0} \tag{3.11}$$

$$\omega = \frac{\partial \xi}{\partial t} \tag{3.12}$$

At the sea bottom: $z = -H(x,y)$

$$K_v \frac{\partial u}{\partial z} = \frac{\tau_s^x}{\rho_0}(x,y,t) \tag{3.13}$$

$$K_v \frac{\partial v}{\partial z} = \frac{\tau_s^y}{\rho_0}(x,y,t) \tag{3.14}$$

$$K_T \frac{\partial T}{\partial z} = 0 \tag{3.15}$$

$$K_S \frac{\partial S}{\partial z} = 0 \tag{3.16}$$

$$-\omega + \vec{v}.\nabla H = 0 \tag{3.17}$$

The equations (3.8) and (3.9) express the horizontal momentum transferred into the ocean by the atmospheric wind stress at the surface, in x and y directions, respectively. The equations (3.10) and (3.11) represent the thermal and fresh-water fluxes, and the vertical velocities related to the sea surface are represented by equation (3.12). At the sea bottom, the equations (3.13) and (3.14) represent the momentum transfer into the ocean by friction at the sea bottom. The equations (3.15) and (3.16) express non-occurrences of a vertical thermal and salt flux at the seafloor. The non-crossing of the topography by the flow at the seafloor is expressed by equation 3.17.

$$\tau_s^x = \rho_{air} C_D \sqrt{u_{10}^2 + v_{10}^2} \cdot u_{10} \tag{3.18}$$

$$\tau_s^y = \rho_{air} C_D \sqrt{u_{10}^2 + v_{10}^2} \cdot v_{10} \tag{3.19}$$

The equations (3.18) and (3.19) represent the x and y components of the surface wind stress τ_s^x and τ_s^y, respectively. At the seafloor, $z = -H(x,y)$, equations (3.20) and (3.21) represent the components of the bottom friction τ_{bot}^x and τ_{bot}^y, respectively.

$$\tau_{bot}^x = (\gamma_1 + \gamma_2 \sqrt{u^2 + v^2})u \tag{3.20}$$

$$\tau_{bot}^y = (\gamma_1 + \gamma_2 \sqrt{u^2 + v^2})v \tag{3.21}$$

Where

- *x, y, z* - are the zonal, meridional and vertical directions *[m]* in the Cartesian coordinate system
- *u, v, w* - are the components of the vector velocity $\vec{v}$ $[m.s^{-1}]$ in *x, y, z*, respectively

- t - is the time in seconds *[s]*
- f - is the Coriolis parameter *[s^{-1}]*
- ϕ - is the dynamic pressure, $\phi = \dfrac{P}{\rho_0}$ *[m^2s^{-2}]*
- P - is the total pressure, $\dfrac{\partial P}{\partial z} = -\rho g$ *[Nm^{-2} or $kgm^{-1}s^{-2\cdot}$]*
- F_u, F_v, F_T, F_S - are the possible surface forcing terms
- D_u, D_v -are the lateral momentum dissipation from the advective terms
- D_T, D_S - are the terms for the diffusion of temperature and salinity
- T - is the potential temperature *[^oC]*
- S - is the salinity *[PSU]*
- $\vec{g}$ - is the acceleration of gravity, g *[ms^{-2}]*

ρ - is the seawater density, *[kgm^{-3}]*

- ρ_0 -is the mean seawater density, *[kgm^{-3}]*
- ξ - is the sea surface variation *[m]*
- τ_s^x and τ_s^y - are the surface wind stress *[Nm^{-2}]*, in x and y directions, respectively
- τ_{bot}^x and τ_{bot}^y -are the bottom stress *[Nm^{-2}]*, in x and y directions, respectively
- Q_T - is the surface heat flux *[Wm^{-2}]*
- K_v - is the coefficient of vertical eddy viscosity *[m^2s^{-1}]*
- K_T, K_S - are the coefficient of vertical eddy diffusivity *[m^2s^{-1}]*
- E_r - is the evaporation rate *[$cmday^{-1}$]*
- P_r - is the precipitation rate *[$cmday^{-1}$]*
- C_p - is the heat capacity of seawater *[$Jkg^{-1}.^oC^{-1}$]*
- H - is the total ocean depth *[m]*.

- u_{10}, v_{10} - are the horizontal components of the wind vector $[m.s^{-1}]$ measured at 10 m above sea level in x and y, respectively
- C_D - is non-dimensional wind-drag coefficient
- ρ_{air} - is the density of atmospheric air $[kgm^{-3}]$
- γ_1 - is the coefficient of linear bottom friction
- γ_2 - is the coefficient of quadratic bottom friction.

Surface Fluxes

The ROMS model is forced with wind stress, heat and fresh-water fluxes from gridded observational datasets at the sea surface. The surface heat flux in the ROMS model is based on the bulk parameterization at the air-sea interaction (Fairall et al., 1996) adapted from the COARE (Coupled Ocean-Atmosphere Response Experiment) algorithm. At the sea-air interface, the feedback of the sea surface temperature into the surface heat fluxes is sometimes considered to avoid the model drifting away from observations. This is done by introducing a correction term in the forcing formulation as a relaxation of the model to climatological SST as shown in equation 3.22 (Barnier et al., 1995). This correction is referred to as the restoring term. The restoring term is only applied and valid for the climatology (COADS) experiment which is not forced by the bulk but directly fluxes. The term $\frac{\partial Q}{\partial SST_{clim}}$ is introduced in the Bulk formula for a linearization of the effect of the SST on the heat flux (Q).

$$Q_T = Q + \frac{\partial Q}{\partial SST_{clim}}(SST_{model} - SST_{clim}) \tag{3.22}$$

The surface heat flux comprises the incoming shortwave radiation, the outgoing long-wave radiation, the latent heat flux and the sensible heat flux.

$$\frac{\partial Q}{\partial SST_{clim}} = -4\sigma T^3_{clim} - \rho_{air} C_p U - \rho_{air} C_e LU \times 2353 log_{10} q_s T^{-2}_{clim} \tag{3.23}$$

Surface salinity does not have a direct feedback on evaporation and precipitation. Owing to the poor quality of the net surface flux ($E_r - P_r$), a non-physical term is added to the equation (3.11); as a result salinity flux is expressed as:

$$K_s \frac{\partial S}{\partial z}\Big|_{z=0} = \frac{(E_r - P_r).SSS_{clim}}{\rho_0} + \frac{1}{\tau}(SSS_{clim} - SSS_{model}) \qquad (3.24)$$

Where

- Q_{net} -is the net heat flux *[Wm^{-2}]*
- $\frac{\partial Q}{\partial SST_{clim}}$ - is the relaxation coefficient (linearization of the reference of Q to SST)
- SST_{clim} - is the climatology sea surface temperature *[^{o}C]*
- SST_{model} - is the model derived sea surface temperature *[^{o}C]*
- $K_s \frac{\partial S}{\partial z}\Big|_{z=0}$ - is the salt flux at the sea surface *[PSU.cm.day^{-1}]*
- SSS_{clim} - is the climatology sea surface salinity SSS *[PSU]*
- SSS_{model} - is the model derived sea surface salinity SSS *[PSU]*
- σ -the Stefan-Boltzman constant *[5.6697x10^{-8} W.m^{-2}.^{o}C^{-4}]*
- U - is the wind speed at 10 m above sea level *[ms^{-1}]*
- C_h -is the sensible heat transfer coefficient *[0.66x10^{-3} W.m^{-2}.^{o}C^{-1}]*
- C_e -is the latent heat transfer coefficient *[1.15x10^{-3} W.m^{-2}.^{o}C^{-1}]*
- L-is the latent heat of evaporation *[J.kg^{-1}]*
- q_s -is the sea level specific humidity
- $\frac{1}{\tau}$ - is the relaxation constant (also called inverted time). It prevents the model SSS

from drifting too far away from its climatologic value. This term is usually kept equivalent to $\dfrac{\partial Q}{\partial SST_{c\,lim}}$ ~ 30 - 40 days.

Lateral boundary conditions

Lateral boundary conditions impose a restriction on the flow characteristics on the model boundary, and they influence the flow near and away from the boundary. Marchesiello et al., (2001) established that open-ocean boundary conditions are imposed accurately when an outward oblique radiation and adaptive nudging toward the external boundary conditions are applied together. The setting of the numerical boundary scheme should allow the inner solution to radiate through the boundary without reflection and information from the surrounding ocean to come into the model. Closed boundary conditions are defined as masked regions (i.e. land). The time step computation of variables over the masked region is set to zero at the end time step. However, the calculated velocity terms in the masked region are corrected for free or no slip conditions. The procedures are extensively described by Hedström (1997).

Marchesiello et al. (2001) implemented the active open boundary scheme in ROMS which estimates the two dimensional horizontal phase velocities in the vicinity of the boundary. For each model variable ϕ, following Raymond and Kuo (1984), the normal (c_x) and tangential (c_y) phase velocities are:

$$c_x = -\frac{\dfrac{\partial \phi}{\partial t}\dfrac{\partial \phi}{\partial x}}{\left(\dfrac{\partial \phi}{\partial x}\right)^2 + \left(\dfrac{\partial \phi}{\partial y}\right)^2} \tag{3.25}$$

$$c_y = -\frac{\dfrac{\partial \phi}{\partial t}\dfrac{\partial \phi}{\partial y}}{\left(\dfrac{\partial \phi}{\partial x}\right)^2 + \left(\dfrac{\partial \phi}{\partial y}\right)^2} \tag{3.26}$$

If the propagation is towards the open ocean, the features produced inside the model are evacuated following the wave equation:

$$\frac{\partial\phi}{\partial t}+c_x\frac{\partial\phi}{\partial x}+c_y\frac{\partial\phi}{\partial y}=\frac{\phi_{data}-\phi}{\tau_{out}} \qquad 3.27$$

If the propagation is towards the interior, the value at the boundary is nudged towards data:

$$\frac{\partial\phi}{\partial t}=\frac{\phi_{data-}\phi}{\tau_{in}} \qquad 3.28$$

The tangential and normal propagations are discretized in ROMS in an upstream biased fashion, where the normal component is treated implicitly. Thus, this scheme allows large time steps without loss of stability.

3.1.2 Model Configuration

In this study, two realistic ROMS simulations are configured in the tropical western Indian Ocean for the domain 37.5-60^{o}E and 4.85^{o}N-18^{o}S with its bathymetry derived from ETOPO2V2C (see www.ngdc.noaa.gov, Figure 3.1). The configurations are designed to study the influence of the upper ocean circulation on the properties in the Tanzanian shelf region, and the relationship between the Tanzanian shelf waters and offshore. Thus, the domain was largely extended in the tropical western Indian Ocean to encompass the dominant oceanographic features in the region like the Northeast Madagascar Current (NEMC) and the East African Coastal Current (EACC). The domain is also extended to accommodate the offshore region.

The two configurations of the ROMS model use a global topography dataset at 2' resolution processed by Smith and Sandwell (1997). The first simulation focuses on the annual cycle in the Tanzanian shelf region in the tropical western Indian Ocean. It is forced with the monthly mean Comprehensive Ocean and Atmosphere Data Sets (COADS) winds and heat fluxes (da Silva et al., 1994) for 10 years with a three year spin-up time. The initial and lateral boundary conditions for this simulation are extracted from World Ocean Atlas 2001 global dataset with monthly climatology 1^0 resolution, WOA2001 (Conkright et al., 2002). The restoring term is applied in this experiment. The second simulation investigates the interannual variability in the Tanzanian shelf region in the tropical Indian Ocean. It is forced from 1978 to 2007 by the National Center for Environmental Prediction (NCEP) reanalysis of winds and heat fluxes with two years spin-up

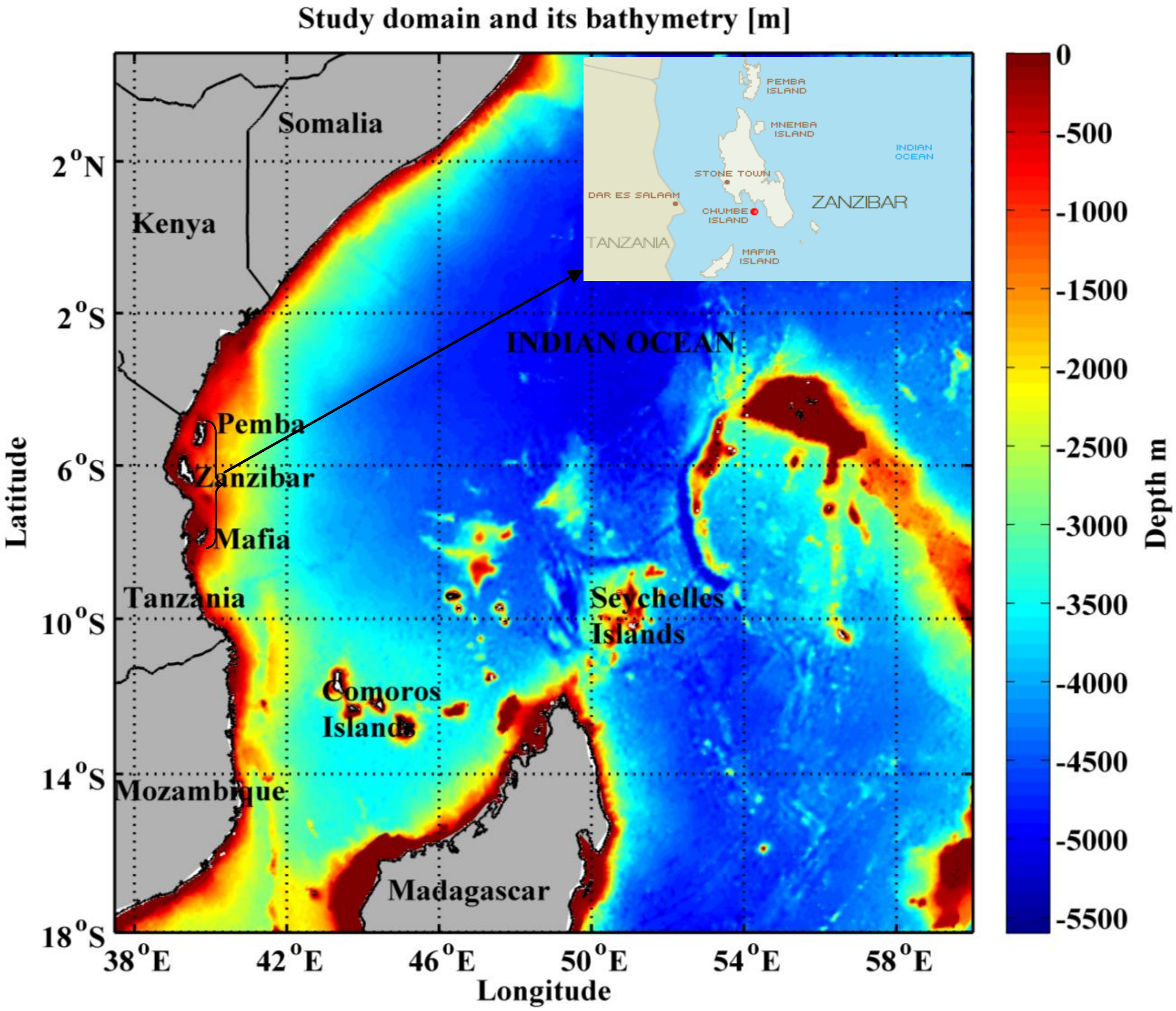

Figure 3.1: The study domain in the tropical western Indian Ocean and its bathymetry derived from ETOPO2V2C (www.ngdc.noaa.gov).

time. Its initial and lateral boundary conditions are extracted from the Ocean Global Circulations Models (OGCM), the Simple Ocean Data Assimilation 2.0.2-4 (SODA 2.0.2-4; Carton et al., 2008). The Monthly values are used to force the lateral open boundaries by means of a linear temporal interpolation. The lateral boundary conditions are based on a combination of active adaptive radiation conditions added to nudging (reaching a nudging time scale of 360 days) and sponge (reaching a viscosity/diffusivity value of 1000 m^2s^{-1}) layers 150 km wide (Marchesiello et al., 2001). In this experiment, no explicit restoring towards observed SST is used in the bulk formula. Both model simulations consist of 40 vertical levels with $1/6^0$ horizontal resolution and time steps of 1800 seconds.

The model outputs from the COADS run and the NCEP experiment are averaged every two model days which in turn are processed to calculate monthly and climatological data. The mean and climatological monthly output of different ocean fields from the COADS run and NCEP experiment are compared in order to get confidence of the accuracy and effectiveness of the ROMS model in the tropical western Indian Ocean. The monthly anomalies of the interannual model output are extracted by subtracting the monthly climatological mean calculated for 28 years (i.e. 1980-2007) of the model interpretation. The realistic NCEP model run is termed the reference experiment (EXP_REF).

The interannual NCEP run is used to perform experiments to investigate the sensitivity of the circulation over the domain to the local surface heat fluxes and lateral boundary conditions. These runs are conducted in order to understand the relative roles of the local surface heat fluxes and lateral boundary conditions on the evolution of the interannual variability in the tropical western Indian Ocean. The two sensitivity experiments are conducted with the same domain configuration of the EXP_REF experiment. In those experiments, the interannual surface heat fluxes or lateral boundary conditions are replaced by a climatological equivalent in order to assess the relative importance of those two forcings on the interannual variability (Table 3.1).

Table 3.1: The descriptions of the ROMS experiments in the tropical western Indian Ocean.

S/No	**ROMS SIMULATION NAME**	**ROMS CONFIGURATION DETAILS**		
		NCEP WIND STRESS	*NCEP SURFACE HEAT FLUX*	*SODA LATERAL BOUNDARY CONDITIONS*
1	EXP_REF	INTERANNUAL	INTERANNUAL	INTERANNUAL
2	EXP_CLIM_SODA	INTERANNUAL	INTERANNUAL	CLIMATOLOGY
3	EXP_CLIM_FLUX	INTERANNUAL	CLIMATOLOGY	INTERANNUAL

3.2 Description of Datasets

The ROMS model used to investigate the variability in the Tanzanian shelf region is validated by comparing different model oceanic variables with those from observations, satellite or digitalized/gridded data. However, due to the way the ROMS surface heat flux boundary condition is imposed, validating the model through the observed/satellite SST might not be a strong test of the model. A stronger test involves comparing the ROMS sea surface height (SSH) with altimeter data, or the sub-surface temperature/salinity with hydrographic data (e.g. Indian Ocean hydrobase) or currents with observed current meter data. Thus, the model SST, SSS, SSH and surface currents together are validated using observations, satellite or digitalized/gridded data as explained below.

In order to confidently use the ROMS simulations, satellite-derived and the digitalized/gridded SST data are used to validate the performance of the model SST simulations. The AVHRR Pathfinder version 5 SST project data (Pathfinder V5) at 4km horizontal resolution (see ftp://ftp.nodc.noaa.gov) and the TMI **S**ST measurements (see ftp://ftp.ssmi.com) at 0.25^o horizontal resolutions are used for validation of the model SST for the same region. In addition, the digitalized global climatology of the SST data from CARS2009 on a 0.5^o grid (see www.marine.csiro.au) and the gridded Indian Ocean Hydrobase SST data (see apdrc.soest.hawaii.edu) in the annual mean state are used for further validation of the model SST.

However, due to the way the ROMS surface heat flux boundary condition is imposed, although no explicit restoring towards observed SST is used in the bulk formula, validating the model through the observed/satellite SST might not be a strong test of the model. In the model, atmospheric properties from the NCEP reanalysis are used to force a bulk formula (Fairall et al., 1996). In this context, the model sea surface temperature is influenced by the NCEP atmospheric surface temperature, which is itself influenced by observed sea surface temperature. In this regard, although not directly forced, model SST is not totally independent to observed SST. Thus, a stronger test involves comparing the ROMS sea surface height (SSH) with altimeter data, SSS, or/and subsurface variables. The model SSS is validated using WOA2009 consisting of the global monthly climatology at 1^o grid resolution and interpolated to standard depth levels on both

1^o and 5^o grids (Antonov et al., 2010, see www.nodc.noaa.gov). Furthermore, the WOA2009 data was used to validate the subsurface temperature and salinity in the region. Validation of the ROMS model is provided by the altimeter sea surface height observations from Archiving, Validation and Interpretation of Satellite Oceanographic (AVISO). The altimeter sea surface height observations for AVISO are obtained for 1992 to 2007 at $1/3^o$ resolution (www.aviso.oceanobs.com). These are gridded data produced which combine altimeter measurements from different satellites by an interpolation mapping technique (Ducet et al., 2000). This study uses gridded maps of absolute dynamic topography. Owing to different absolute values of SSH in the ROMS simulation and the AVISO data due to their different reference level, the SSH deviations from their spatial mean are represented here.

This study benefits from the direct *in situ* measurements of the SST around Chumbe Island Coral Park in the Zanzibar Channel over the tropical western Indian Ocean. These *in situ* SST data were provided by Dr. Christopher Muhando of the Institute of Marine Sciences, University of Dar es Salaam (personal communication, March 1, 2011). The *in situ* SST data have been recorded from 1997 to 2007 using data loggers which were tied on acropora coral branches off Chumbe Island. However, data were missing sporadically due to the data logger detachment from the acropora coral branches by either strong currents or fish bites. In addition, premature expiry of the temperature logger batteries can be a source of data loss during several periods of time.

The influences of El Niño-Southern Oscillation (ENSO) and Indian Ocean Dipole (IOD) on the variability of the Tanzanian shelf region can be assessed through correlation using the Niño 3.4 index and the Dipole Model Index (DMI). The ENSO and IOD are prominent climate modes in the tropical Indian Ocean. The DMI is extracted from the Japan Agency for Marine-Earth Science and Technology (JAMSTEC). The DMI represents the difference of the monthly SST (HadISST dataset from 1958 to 2010) between two boxes on the west (50-70^oE, 10^oS-10^oN) and the east (90-110^oE 10^oS-0) of the tropical Indian Ocean (see www.jamstec.go.jp). The Niño 3.4 index is extracted from National Ocean and Atmosphere Agency (NOAA). The Niño3.4 index is the difference between monthly SST anomaly averaged over 5^oN-5^oS and 120-170^oW (see gcmd.nasa.gov).

3.3 Statistical Tools and Data Analysis Techniques

Statistical analysis of the ROMS model and satellite data in this study involves wavelet analysis, correlation analyses and Empirical Orthogonal Function (EOF) Analysis. The details of the wavelet and EOF analyses are provided below.

3.3.1 Empirical Orthogonal Function Analysis

Empirical Orthogonal Function (EOF) analysis is widely used in atmospheric and oceanic researches for identification of spatio-temporal physical leading modes of variability in a particular region (Dommenget and Latif, 2002). It reduces a time series of spatial data to a smaller number of spatial patterns which explain most of the variance in the data (Cheng et al., 1995; Hannachi et al., 2006; Tao et al., 2012). This is done by diagonalizing the covariance matrix data after removing the spatial or temporal mean from the data. The diagonalizing by removing the spatial mean from data is known as spatial EOF analysis. In the spatial EOF analysis, data are reduced to a few significant modes explaining fractions of spatial variance in the data. However, temporal EOF analysis or principal component analysis provides a set of modes explaining fractions of temporal variance in the data. Both spatial and temporal EOF analyses possess an orthogonality feature which reproduces uncorrelated modes. As a consequence, the EOF analysis produces unrelated features that can be interpreted physically.

In this research, the EOF analysis decomposition is applied in the Tanzanian shelf region on the monthly anomalies of the upper ocean temperature from 1980 to 2007. The EOF analysis for the SST variability is performed for the study domain ranging between 37.5-60^{o}E and 4.85^{o}N-18^{o}S. Thus, the EOF analysis is used to identify the leading modes of the SST in the region. This technique is also applied to the subsurface temperature (upper 200 m) in the region. It is performed on the temperature vertical transects from 38 to 60^{o}E averaged over 9-9.5^{o}S and 1-1.5^{o}S for the region with the lowest and highest SST variations in the study domain. The regions with the lowest and highest SST variations are located in the Tanzanian shelf region and further offshore, respectively. In both applications, the first leading modes that explain more than 10% of the total variance of the SST and subsurface temperature variability from the EOF analysis are retained.

3.3.2 Wavelet Analysis

Wavelet analysis is a mathematical tool with wide and extensive applications in meteorology and oceanography. It decomposes a time-series of a non-stationary signal into time-frequency space. Applications of wavelet analysis have grown considerably in the last two decades (Domingues, 2005). Wavelet analysis is useful because it represents the amplitude of a non-stationary signal within a time-series at a particular time. Most of the ocean or atmospheric signals are non-stationary. Therefore, their decomposition into frequency, time, period and intensity using this wavelet analysis is useful for studying and identifying the variability in these data.

In oceanographic applications, wavelet analysis has been successfully used in the tropical Indian Ocean and in the fields related to large scale modes (e.g. Torrence and Webster, 1999; Savoka et al., 2006; Collins et al., 2011). Wavelet analysis has been used to decompose time-series of different oceanic fields related to wave growth and breaking (Liu 1994) and ENSO (Torrence and Compo, 1998) as well as the ENSO-Monsoon system (Torrence and Webster, 1999). In the tropical Indian Ocean, wavelet analysis has been successfully used for analysis of different wind products (Collins et al., 2011) and low frequency variability (Savoka et al., 2006). Thus, it is an established technique for analysing ocean circulation and properties in the tropical western Indian Ocean.

In the current study, wavelet analysis has been performed on the first leading principal components of the SST EOF and on the time-series of the selected locations in the domain using the Morlet wavelet (Torrence and Compo, 1998). The principal components of the first leading modes of the SST EOF in the tropical western Indian Ocean are analysed using wavelet analysis. The analysis aims to determine the time, intensity and duration of dominant modes produced by the SST EOF from 1980 to 2007 in the region. Furthermore, wavelet analysis is performed on the normalized box-averaged monthly SST anomalies in the coastal ocean off Tanzania (40-42^{o}E, 8-10^{o}S) and further offshore (48-50^{o}E, 0-2^{o}S). The selected boxes are within regions of low and high standard deviations of the monthly SST anomalies in the coastal and open oceans, respectively.

3.4 Other Variables

Wind stress curl

Wind stress curl plays a significant dynamical role as a source of vorticity in the upper ocean surface. It is directly related to the Sverdrup balance for the volume transport. The z component of the wind stress curl vector is given by the following equation:

$$Curl_z \tau = \frac{\partial \tau y}{\partial x} - \frac{\partial \tau x}{\partial y} \tag{3.29}$$

where positive (negative) wind stress curl in the Northern Hemisphere is cyclonic (anti-cyclonic) and in the Southern Hemisphere is anti-cyclonic (cyclonic).

Ekman Pumping

Ekman pumping is generated by the wind stress curl as an open ocean upwelling and downwelling (Risien and Chelton, 2008). It is associated with Ekman velocities which are purely caused by frictional forces. Therefore, the Ekman pumping velocities are expressed as a function of the applied wind stress. It is given by equation:

$$We = \frac{1}{\rho f}\left(\frac{\partial \tau y}{\partial x} - \frac{\partial \tau x}{\partial y}\right) = \frac{1}{\rho f} Curl_z \tau \tag{3.30}$$

where **We** is the vertical Ekman velocity, ρ is the density of sea water, f is the Coriolis parameter, **f**=2.Ω.sin (θ) where 2. Ω =1.458 x 10^{-4}, and θ is latitude.

The upward (downward) vertical velocities due to the applied wind stress are usually referred to as Ekman pumping (suction) velocities.

Net Volume Transport

$$\mathbf{Net\_V\_Flux} = \sum_{i=1}^{m} |\mathbf{Vin}_i| - \sum_{j=1}^{n} |\mathbf{Vout}_j| \tag{3.31}$$

Where Net_V_Flux-Net volume flux in the boxes

$\mathbf{Vin}_i$ -Volume flux transported cross-shore or along-shore into the boxes through the specific line **i** and **i=1, 2, 3… m**

$\mathbf{Vout}_j$ -Volume flux transported cross-shore or along-shore out of the boxes through the specific line **j** and **j=1, 2, 3… n.**

Oceanic mixed layer heat budget

The temperature tendency equation for the mixed layer temperature is useful to investigate the forcing mechanisms in the ocean temperature variability. In this study, mixed layer temperature tendency has been divided into three parts, heat flux term, total advection and total mixing terms. The combination of the latter two terms forms the total mixed layer temperature tendency contributed by oceanic processes. Therefore, mixed layer temperature tendency (with space and time indices [**x, y, z, t**] omitted for simplicity) is shown below:

$$\frac{\partial \mathbf{T}}{\partial \mathbf{t}} = \underbrace{\frac{\mathbf{1}}{\rho \mathbf{C_p}}\partial\frac{(\mathbf{Qnet})}{\partial \mathbf{z}}}_{\mathbf{Heat\_Flux}} - \underbrace{\left(\mathbf{u}\frac{\partial \mathbf{T}}{\partial \mathbf{x}} + \mathbf{v}\frac{\partial \mathbf{T}}{\partial \mathbf{y}} + \mathbf{w}\frac{\partial \mathbf{T}}{\partial \mathbf{Z}}\right)}_{\mathbf{Total\_Advection}} + \underbrace{\left\{\frac{\partial}{\partial \mathbf{x}}\left(\mathbf{K_x}\frac{\partial \mathbf{T}}{\partial \mathbf{x}}\right) + \frac{\partial}{\partial \mathbf{y}}\left(\mathbf{K_y}\frac{\partial \mathbf{T}}{\partial \mathbf{y}}\right) + \frac{\partial}{\partial \mathbf{z}}\left(\mathbf{K_z}\frac{\partial \mathbf{T}}{\partial \mathbf{z}}\right)\right\}}_{\mathbf{Total\_Mixing}} \quad (3.32)$$

Where:

(**u, v, w**) are zonal, meridional, and vertical velocities;

$\mathbf{K_x}$ and $\mathbf{K_y}$ are the horizontal diffusivity coefficients and

$\mathbf{K_z}$ is the vertical diffusivity coefficient determined from the KPP parameterization;

ρ is density;

$\mathbf{C_p}$ is specific heat of seawater.

Qnet= Qsw+Qlw+Qsh+Qlh (3.33)

Qsw, Qlw, Qsh, and **Qlh** are correspondingly prescribed as short-wave radiation, long-wave radiation, sensible heat fluxes, and latent heat fluxes.

3.5 Summary

The methodology applied and the datasets used to investigate the variability in the Tanzanian shelf region have been discussed in this chapter. Two ROMS realistic simulations forced with COADS and NCEP as well as two sensitivity experiments forced with NCEP are performed for the domain 37.5-60^{o}E and 4.85^{o}N-18^{o}S. The sensitivity experiments aim to determine the relative effects of the local surface heat fluxes and lateral boundary conditions in the Tanzanian shelf region. The next chapter (Chapter 4) evaluates the ability of the ROMS model to reproduce the seasonal variability in the Tanzanian shelf region.

Chapter 4

Evaluation of the Model

4.0 Introduction

This chapter serves to assess the ability of the configured ROMS model to satisfactorily reproduce the ocean circulation and properties in the tropical western Indian Ocean. Although the ROMS model is a well established model tool in the western Indian Ocean (e.g. Mayorga-Adame, 2007; Penven et al., 2006; Hermes and Reason, 2008), evaluation of the configuration used in the thesis is necessary. Such assessment determines the confidence of the current ROMS model to represent the regional circulation and properties. The upper ocean properties in the region are validated by examining the spatial and temporal distribution of the sea surface temperature (SST), sea surface salinity (SSS), mixed layer, thermocline, and subsurface temperature and salinity. The model SST is compared with satellite data (AVHRR and TMI), *in situ* data around Chumbe Island in the Zanzibar Channel as well as digitalized data from CARS2009 and gridded data from the Indian Ocean Hydrobase database. Data from the World Ocean Atlas 2009 (WOA2009) are used to assess the model SSS patterns in the region as well the subsurface temperature and salinity. The spatial and temporal patterns of the model upper ocean circulation are assessed using the sea surface height (SSH) and estimated geostrophic currents from the AVISO data as well as volume transport from two different realistic simulations. In addition, the thermocline and mixed layers are validated by comparing the model outputs from the two realistic simulations in the region. Recall that the two realistic ROMS simulations are forced with NCEP and COADS, and they are termed Model_NCEP and Model_COADS in this chapter, respectively.

The chapter is organized in four main parts: The evaluation of the mean state of the upper ocean circulation and properties is discussed in the first section. The second section illustrates the assessment of the annual cycle of the upper ocean circulation and properties. The third part provides assessment for the interannual variability and the last section provides the summary of the chapter.

4.1 Mean State

The annual mean state in the tropical western Indian Ocean is examined through the upper ocean circulation and properties from the model, observational and satellite data. The assessment focuses on the mean state of the SST, SSS, SSH, current speeds, volume transport, mixed layer and thermocline as well as subsurface temperature and salinity for Model_NCEP and Model_COADS. The spatial patterns of the mean state of the above variables from the model simulations are compared with observations and satellite data as discussed below.

The tropical western Indian Ocean shows spatial distribution patterns of the ROMS SST in agreement with observations, hydrographical and satellite data in the annual mean state. The tropical western Indian Ocean is generally characterized by warm annual mean SST that ranges from 26.5 to 29.0^{o}C as evident by Model_COADS (Figure 4.1a) and Model_NCEP (Figure 4.1b) as well as in satellite data from AVHRR (Figure 4.1c) and TMI (Figure 4.1d). Such SST patterns are also illustrated by the digitized SST data from CARS2009 (Figure 4.1e) and by the gridded SST data from the Indian Ocean Hydrobase database (Figure 4.1f). The warmest SST (>28^{o}C) appears to the north of 10^{o}S, being confined to the open ocean. Relatively cool SST (~26.5^{o}C) occurs to the east of Madagascar with a tongue that extends towards the coast from the north of this island. The model SST in the domain is further validated by *in situ* data around Chumbe Island in the Zanzibar Channel (6^{0}16’S, 39^{0}10’E). The *in situ* data is compared with the spatially averaged SST over a box near Chumbe Island (39.5 to 40.5^{o}E, 7 to 6.5^{o}S) from Model_NCEP, AVHRR and TMI within the same period (1998 to 2007). The annual mean value of the SST around Chumbe Island, which is 27.5^{o}C, is comparable with 27.3^{o}C from Model_NCEP, 27.5^{o}C from AVHRR and 28.5^{o}C from TMI. The difference between the model results and observations products can be associated with differences in time periods and the nature of the observational products. Moreover, the difference between the two model simulations is related to the presence of a restoring term for Model_COADS which is absent in Model_NCEP.

The tropical western Indian Ocean shows north-south distribution patterns of the SSS in the ROMS model simulations and WOA2009. High SSS (>35.00 ppt) appears to the north of 7^{o}S, and relatively low SSS (<35.00 ppt) occurs to the south with the highest values being confined to further offshore (Figure 4.2a-c). The region with high SSS matches with strong evaporation

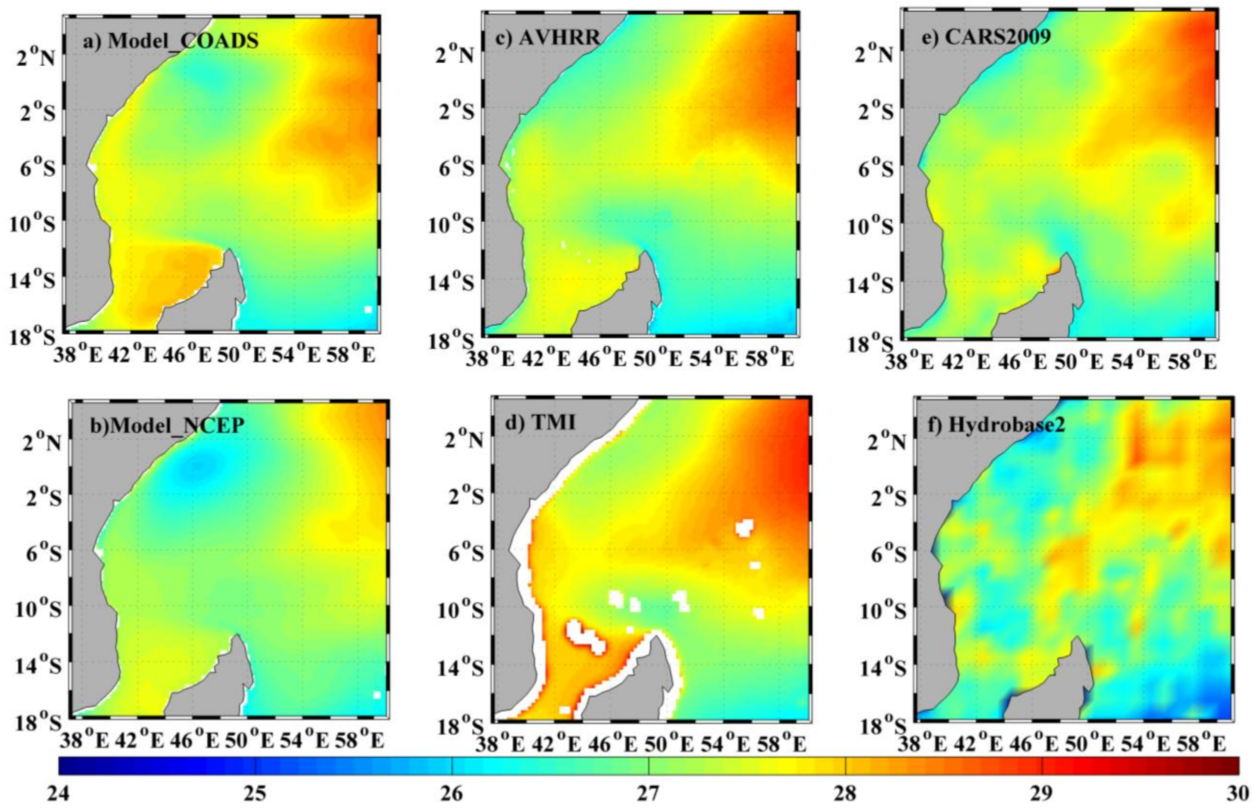

Figure 4.1: Annual mean sea surface temperature in the tropical western Indian Ocean for (a) Model_COADS, (b) Model_NCEP, (c) AVHRR, (d) TMI, (e) CARS2009, (f) the Indian Ocean Hydrobase2 database.

greater than 0.2 cm/day (Figure 4.2d), which may be the major contributor to the high SSS. Although Model_NCEP seems to underestimate the mean state of the SSS, the Model_COADS reproduces the SSS spatial patterns in the region fairly well compared to the WOA2009 SSS data. As for SST, this difference between the model results and observations products can be associated with differences in time periods and the nature of the observational products. In addition, the presence of a restoring term in Model_COADS that is not in Model_NCEP leads to SSS difference between the two model simulations.

The mean spatial distributions of the surface current speeds and sea surface height (SSH) from the model are compared to geostrophic currents and SSH estimated from the AVISO data. In the model simulations and the AVISO data, strong currents occur along the East African coast and to the north of Madagascar, reflecting the EACC and the NEMC, respectively (Figure 4.3, top panel). The NEMC, which flows northwestward past the north of Madagascar, has speeds ranging from 60 to 70 cms^{-1} in agreement with the observed 70 cms^{-1} reported by Schott et al. (2001). The NEMC bifurcates near the African coast between 10 and 12°S into the northward flowing EACC and a southward flow into the Mozambique Channel. The EACC shows its strongest current speeds which range from 100 to 120 cms^{-1} between 8°S and the equator for Model_COADS and Model_NCEP as well as for the AVISO data. The tropical western Indian Ocean indicates north-south SSH patterns in the mean state. High SSH appears to the south of

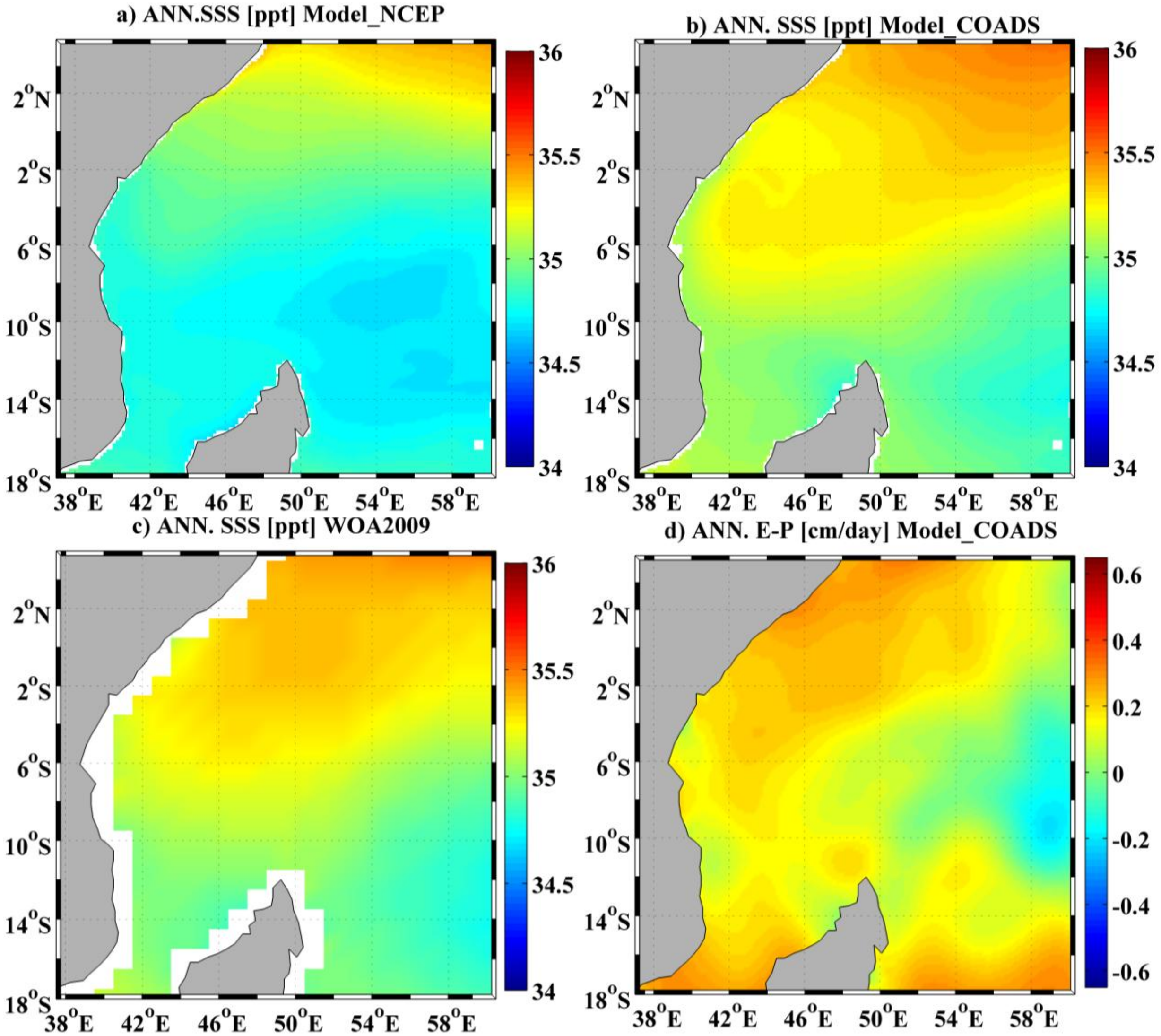

Figure 4.2: Annual mean sea surface salinity in the tropical western Indian Ocean for (a) Model_NCEP, (b) Model_COADS, (c) World Ocean Atlas 2009 (WOA2009), and (d) heat fresh water flux (net evaporation minus net precipitation) for Model_COADS.

10^{o}S being constricted to the African coast in the ROMS simulations and the AVISO data (Figure 4.3, bottom panel). The lowest surface height appears around 8^{o}S in the tropical western Indian Ocean between the SEC and SECC as cited by Hermes and Reason (2008) from Donguy and Meyers (1995).

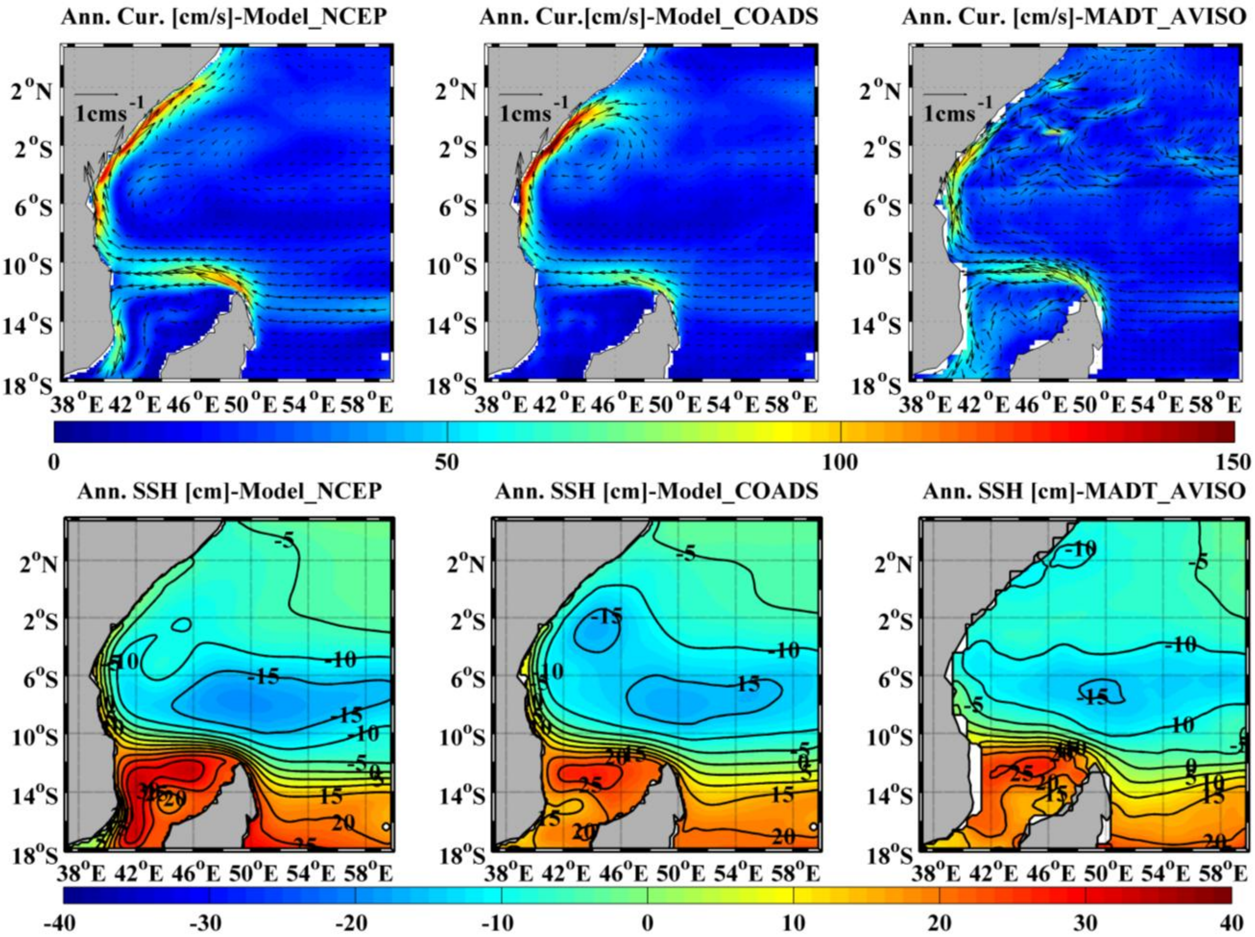

Figure 4.3: Annual mean of surface current speeds superimposed on the surface current speed (cms^{-1}) (1st row) and sea surface height (cm) in the tropical western Indian Ocean extracted from the ROMS model forced with NCEP (1st column) and COADS (2nd column), and MADT AVISO (3rd column).

The mean volume transport integrated in the upper 1500 m in the tropical western Indian Ocean from the model simulations is shown in Figure 4.4. A volume transport of about 35 Sv and 25 Sv occurs to the north of Madagascar for Model_NCEP and Model_COADS, respectively. These annual mean values to the north of Madagascar reflect the NEMC, and they agree reasonably

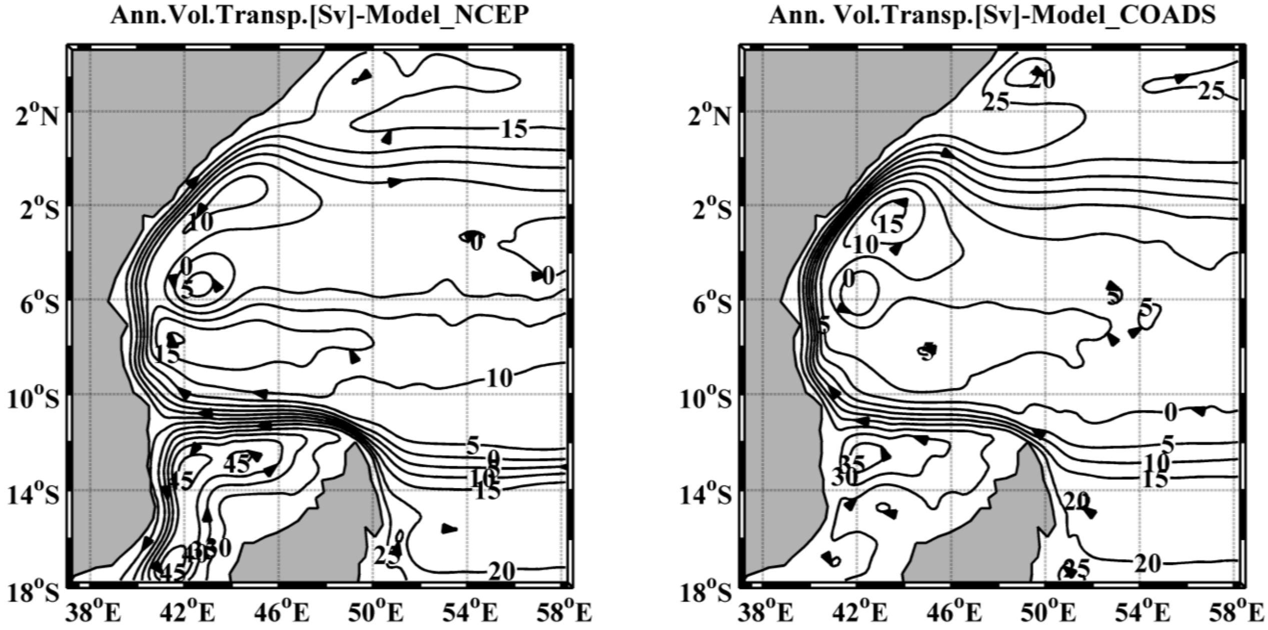

Figure 4.4: Annual mean upper-ocean volume transport integrated from the surface to 1500 m for Model_NCEP (left) and Model_COADS (right).

with the value of 29.60±8 Sv reported by Swallow et al. (1988) and Schott et al. (2009). The annual mean volume transported by the EACC appears to be 20 Sv in Model_NCEP and 25 Sv in Model_COADS. In fact, the mean model volume transport in the region depicts the basin-wide cyclonic tropical gyre which comprises the SEC to the south, the EACC to the west and an eastward flow to the north. The latter, which does not exist in austral winter, occurs as the SECC in austral summer and the Wyrtki Jets in transition seasons. The mean volume transport in the two model runs indicate differences in the centre of the basin, suggesting that the volume transport in the region is sensitive to different forcing. These discrepancies could be due to differences in the spatial and temporal resolutions and the initial and lateral boundary conditions for Model_NCEP and Model_COADS.

The spatial distributions of the annual mean mixed layer in the tropical western Indian Ocean for Model_NCEP and Model_COADS are shown in the first row of Figure 4.5. Mixed layers of about 35-40 m depth occur to the north and east of Madagascar, with shallow mixed layers of about 20 m depth between 10°S and the equator, being confined to the open ocean (Figure 4

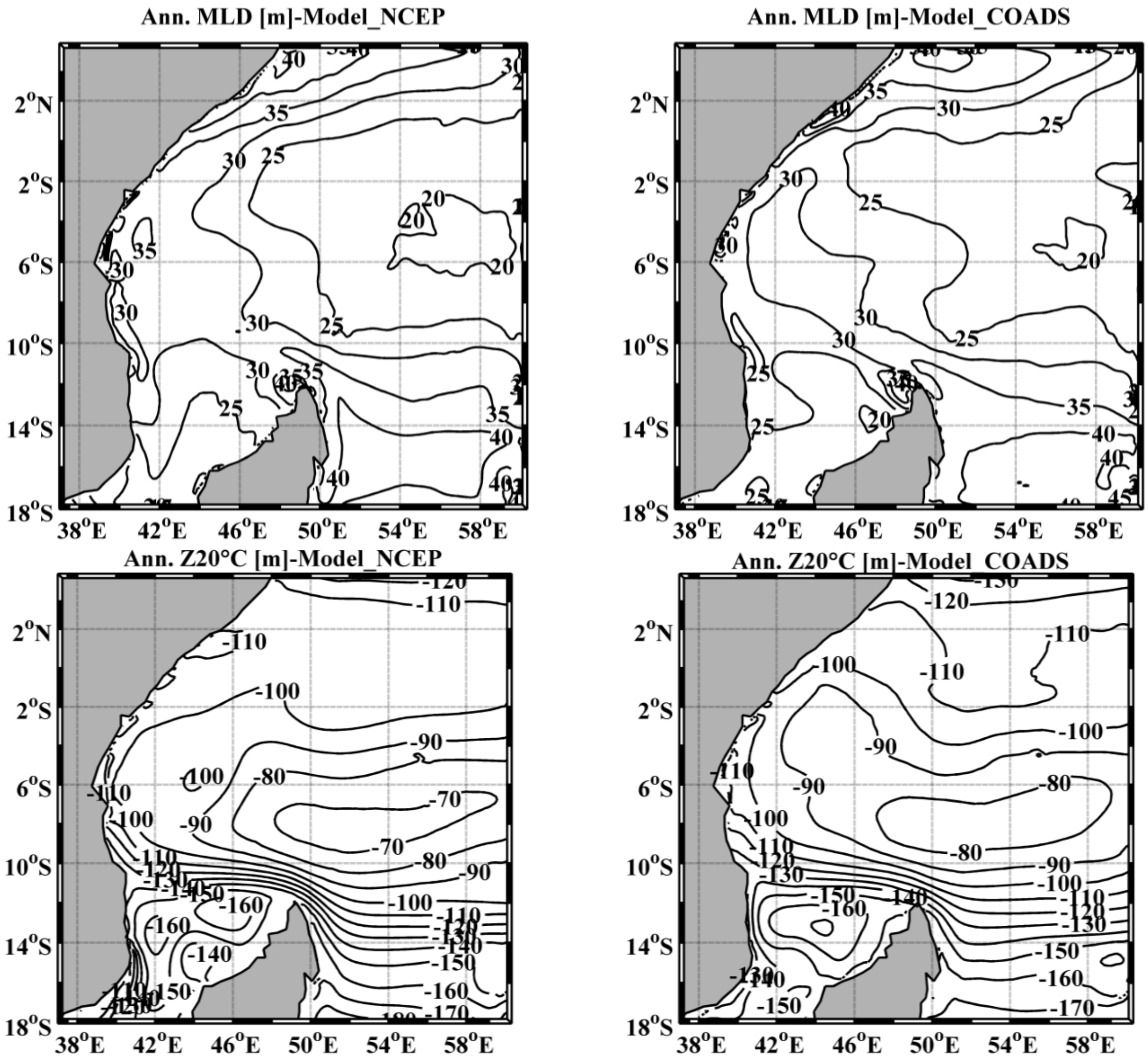

Figure 4.5: Annual mean mixed layer depth (1st panel) and thermocline depth at 20°C isotherms (2nd panel) from the ROMS model forced with NCEP (1st column) and COADS (2nd column).

.5, 1st panel). Shallow mixed layers appear between 10°S and the equator in the open ocean. This could be associated with the shallow thermocline feedback in the upwelling region over the open ocean that prevents excessive deepening of the mixed layer when winds are suddenly strengthened (Duvel et al., 2004).

The annual mean of the thermocline structure in the tropical western Indian Ocean from the model shows spatial distribution with a shallow thermocline in the centre of the open ocean of about 70-80 m (Figure 4.5, 2nd panel). It is the Seychelles-Chagos thermocline ridge (Hermes and Reason, 2008). The thermocline depths are computed as the depth of the 20°C isotherm in order to be consistent with the previous works (e.g. Masumoto and Meyers, 1995; Hermes and Reason, 2008). Deep thermocline depths ranging between 100 and 150 m occur to the north of Madagascar and along the Tanzanian coast which reflect the NEMC and EACC, respectively. Between 5-10°S and 45-60°E, however, minimum depth of about 70 m and 80 m occur in the Seychelles-Chagos thermocline ridge for Model_NCEP and Model_COADS, respectively. Similar thermocline depth in the region has been reported by Xie et al., (2002). These patterns are driven by the negative wind stress curl from the southeasterly trade winds and monsoonal westerly winds, divergence of the cyclonic circulation and the Rossby waves (Hermes and Reason, 2008; Yokoi et al., 2008).

The vertical structure of the annual mean temperature and salinity across the domain from 38 to 60°E, averaged over 10-10.5°S in the upper 250 m, is evaluated to understand the ability of the model to reproduce subsurface variability (Figure 4.6). Relatively warm temperature (>26°C) appears in the upper 50 m in Model_NCEP and Model_COADS as well as in the WOA2009 data (Figure 4.6a-c). Similar temperature patterns occur below 50 m with about 14°C isotherm laying around 250 m near the coast in the model simulations and the WOA2009 data. For salinity, the patterns from the WOA2009 salinity data appear to be much more similar to that from Model_COADS than that from Model_NCEP. Model_NCEP shows relatively fresh surface water (34.8 ppt) in the upper 50 m (Figure 4.6d). However, salty waters (>35.0 ppt) appear in the northeast of the domain for Model_COADS and in the WOA2009 data, being confined to the subsurface (Figure 4.6e, f). The salty waters (>35.0 ppt) appear below 100 m in Model_NCEP. Below this depth, the salty waters for the two ROMS simulations are similar with the WOA2009 data. In short, the model seems to reproduce the annual mean of the subsurface temperature and salinity in the tropical western Indian Ocean fairly well. The salinity difference between Model_NCEP and that for Model_COADS as well as that from the WOA2009 can be associated with the temporal coverage as mentioned earlier.

To summarize, the ROMS model simulates the annual mean state in the tropical western Indian Ocean reasonably well. This is shown by a good agreement of the mean state of the upper ocean properties and circulation from the model and that from observations, hydrographical and satellite data as well as *in situ* SST data from Chumbe Island in the Zanzibar channel. Due to strong seasonal variability in the region, it is also important to evaluate the annual cycle of the upper ocean properties and circulation in the region. Therefore, the next section deals with the assessment of the ROMS model performance on the annual cycle of the regional upper ocean.

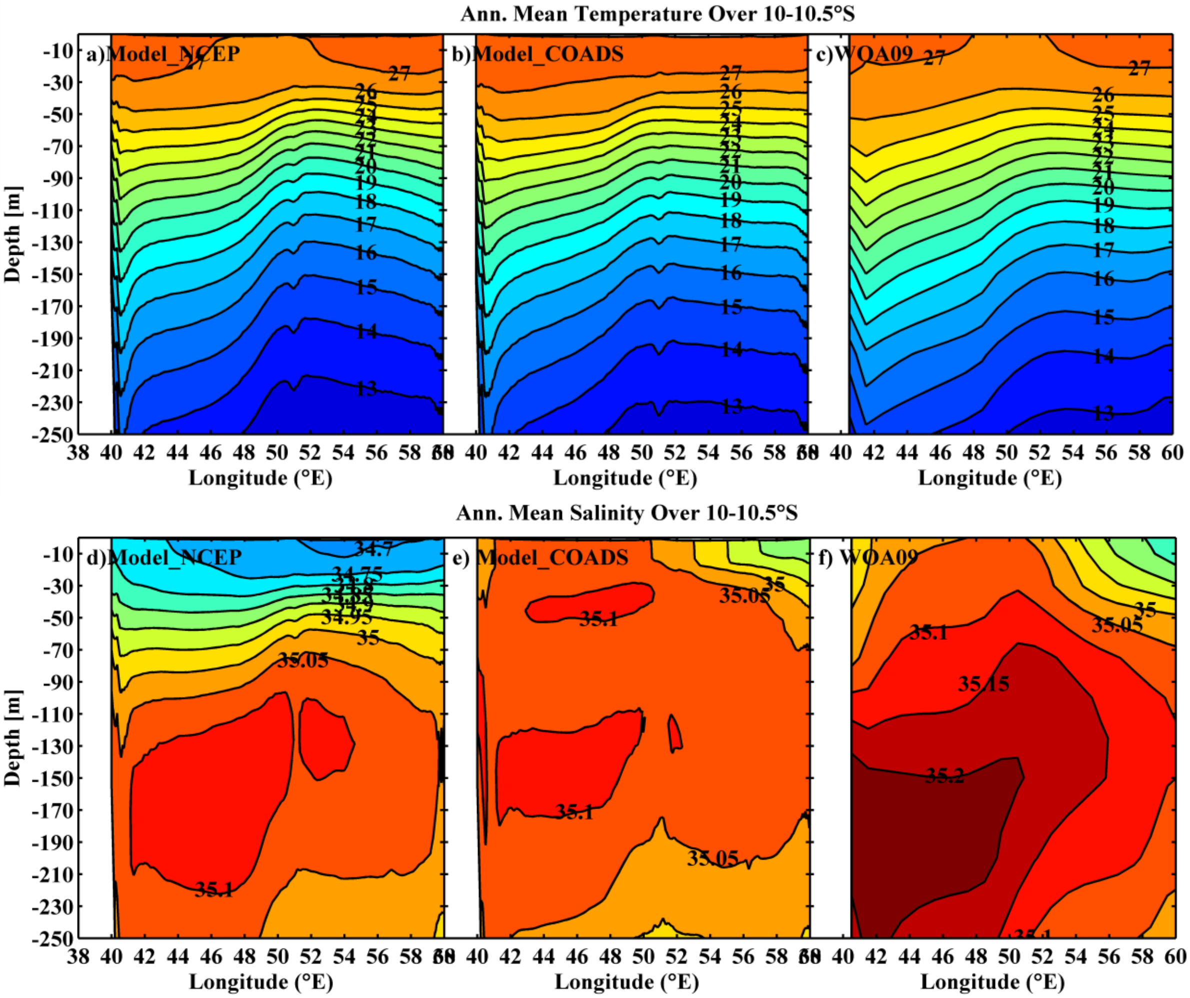

Figure 4.6: Annual mean of the vertical temperature in ^{o}C (1st panel) and salinity in ppt (2nd panel) for Model_NCEP (1st column) and Model_COADS (2nd column), and from WOA2009 (3rd column). The temperature and salinity are averaged over 10-10.5^{o}S from 38^{o}E to 60^{o}E with contour intervals of 1^{o}C and 0.05 ppt, respectively.

4.2 Annual Cycle

The annual cycle of the ROMS realistic simulations forced with NCEP (Model_NCEP) and with COADS (Model_COADS) is evaluated using satellite, hydrographic and observational data of the upper ocean circulation and properties. The SST, SSS, SSH, current speeds, volume transport, mixed layer and thermocline from the model are examined. Since the tropical western Indian Ocean experiences strong seasonality, it is useful to discuss its annual cycle starting with May, the monsoon transition season, then July, midway through the South West monsoon, followed by the seasonal monsoon transition (November) and then January, midway through the North East monsoon.

4.2.1 Sea Surface Temperature

The annual cycle of the SST in the tropical western Indian Ocean shows spatially and temporally asymmetric distribution patterns (Figure 4.7). In addition to cloud cover and the positions of the overhead sun and the Inter-tropical Convergence Zone (ITCZ), this asymmetry is caused by a strong seasonal reversal of winds during the South West and North East monsoons. The surface heat fluxes and mixed layer related to the surface winds during the monsoons play a great role in the SST distribution in the region. Therefore, it is useful to discuss the annual cycle of the SST in the tropical western Indian Ocean in relation to the net surface heat fluxes, wind stress and mixed layer.

In May, before the South West monsoon begins, the tropical western Indian Ocean appears to be warm. During this month, warm SST that ranges between 28 and 30^{o}C appears in a large area to the north of 10^{o}S for Model_NCEP, Model_COADS, AVHRR and TMI (Figure 4.7a). The warmest SST of about 30^{o}C occurs to the northeast of the domain, and relatively cool SST ranging between 27 and 28^{o}C appears to the east and north of Madagascar. The warm SST to the northeast of the domain is consistent with weak winds (Figure 4.8a) which reduce the wind-induced evaporative heat losses and vertical mixing. As a result, shallow mixed layer depths ranging between 20 and 40 m occur to the northeast of the domain (Figure 4.8a, 2nd and 3rd columns) which contributes to the warm SST. In addition, the eastward flowing Wyrtki Jets which develop during the monsoon transitions periods, carry warm waters from the west to the east. Thus, such warm waters can contribute to further warming of the SST to the northeast of the domain.

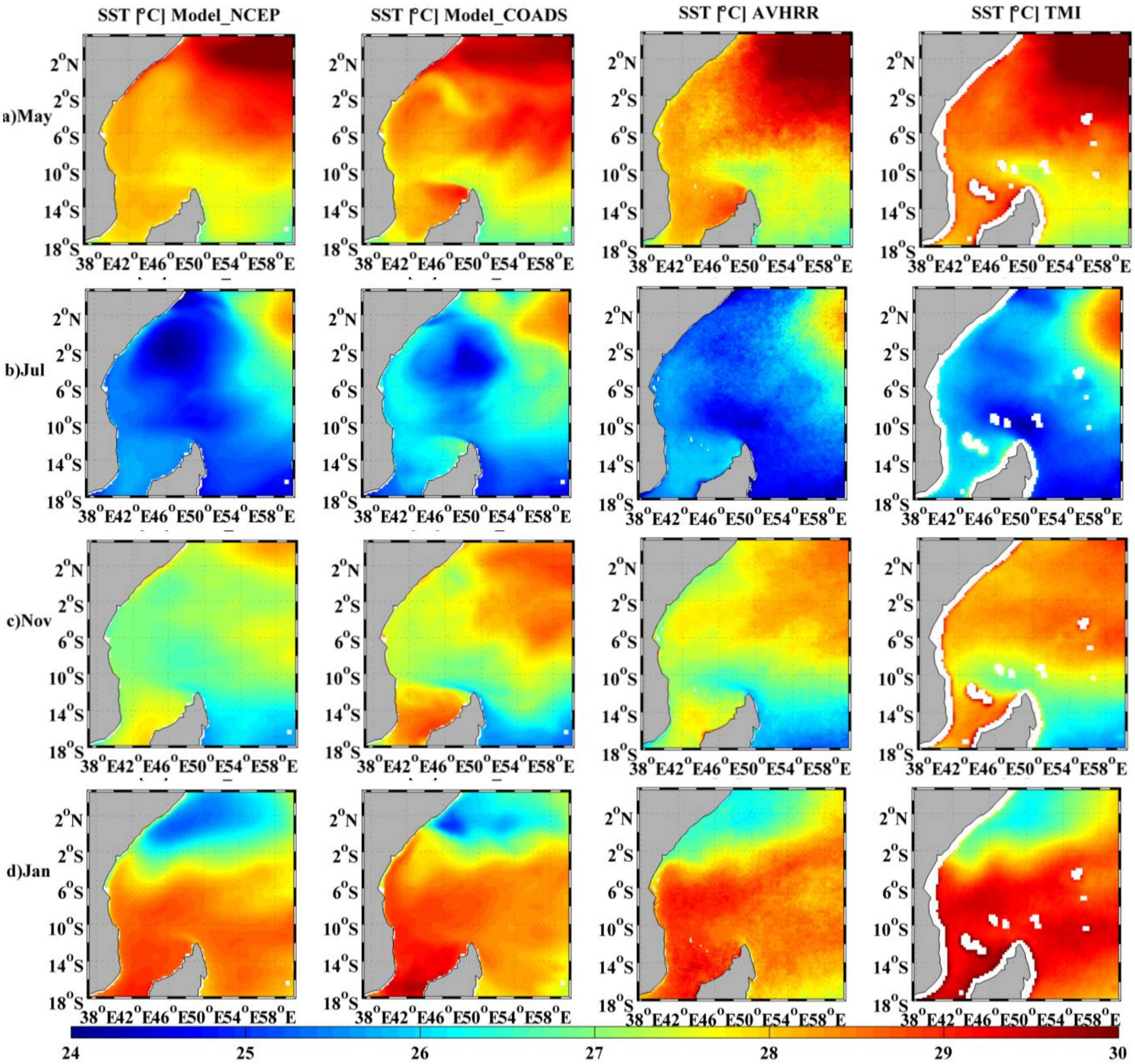

Figure 4.7: Annual cycle of the sea surface temperature [°C] over the tropical western Indian Ocean for Model_NCEP (1st column), Model_COADS (2nd column), AVHRR (3rd column) and TMI (4th column) in (a) May, (b) July, (c) November and (d) January.

As the South West monsoon strengthens in June, the tropical western Indian Ocean cools significantly by July when the South West monsoon is fully developed. The cool SST that ranges between 24 and 26^{o}C appears in a large area of the tropical western Indian Ocean except to the east of 54^{o}E near the equator in Model_NCEP, Model_COADS, AVHRR and TMI (Figure 4.7b). The coolest SST is attributed to the strongest and steadiest winds over the region which enhances both wind-induced evaporative cooling (Figure 4.8b, 1st column) and vertical mixing that deepens the mixed layer depth to about 30-70 m (Figure 4.8b, 2nd and 3rd columns). Moreover, the increased cloud cover which occurs in this period reduces the solar insolation (Figure 4.9); consequently, the net surface heat flux gain of the sun surface is reduced leading to further cooling of the SST. Relatively warm SST occurs to the east along the equator which increases towards the east and reflects the weak winds there. However, the upwelled cold-wedge off coasts of Somalia and northern Kenya reduces the latent heat losses along the coasts as the winds near coast are upwelling favourable (Figure 4.8b). The cloudy sky conditions during this season over the tropical western Indian Ocean reduce the solar shortwave radiation to the maximum value of 240 Wm^{-2} and are restricted off coasts of Somalia and northern Kenya (Figure 4.9). As a result, strong net surface heat flux gain occurs off the coasts of Somalia and northern Kenya (100-120 Wm^{-2}; Figure 4.8b).

During the transition period from the South West monsoon (November), the tropical western Indian Ocean shows relatively warm SST. The spatial patterns of the SST for Model_NCEP, Model_COADS, AVHRR and TMI appear to range from 27.7 to 29.0^{o}C (Figure 4.7c). Relatively warm SST (>27^{o}C) occurs to the north of 10^{o}S, reflecting relatively weak winds (Figure 4.8c, 1st column). The weakest winds occur in the northeast of the equatorial region (Figure 4.8c, 1st column) matching with shallow mixed layers (Figure 4.8c, 2nd and 3rd columns) and the warmest SST. The relatively warm SST during this period can also be associated with a strong net surface heat flux gain (domain average of about 95 Wm^{-2}; Figure 4.8c, 1st column). Such strong net surface flux gain could be mainly attributed to the weak wind-induced evaporative losses and the surface heat flux gain accumulated due to movement of the ITCZ from September. In October the ITCZ is at 2^{o}S moving southwards through November resulting in strong shortwave radiations over the region (Figure 4.9). Both strong net surface heat flux gain and shallow mixed

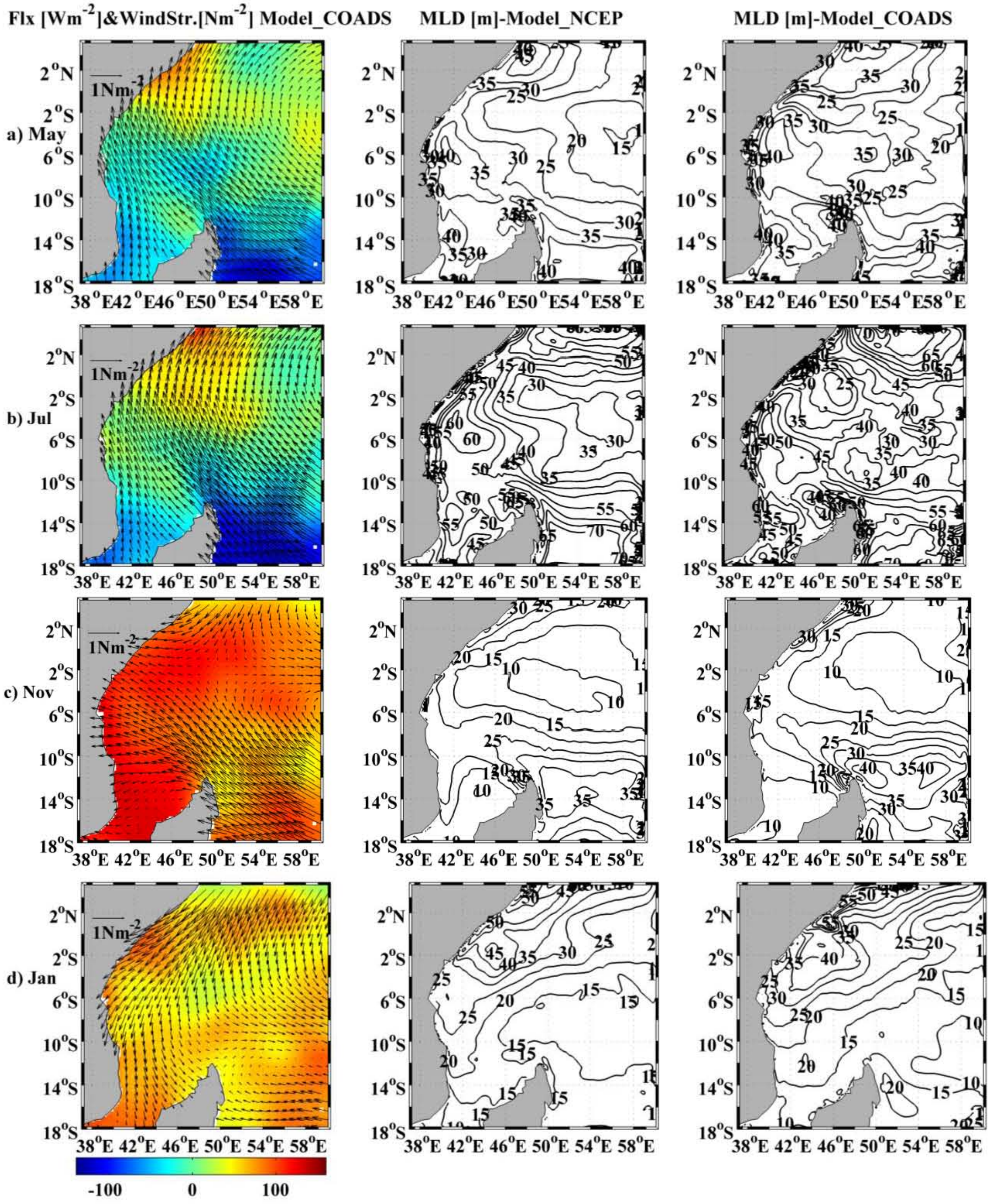

Figure 4.8: Annual cycle wind stress components overlay on the net surface heat fluxes for Model_COADS (Wm^{-2}; 1st column), and mixed layer depth (m) for Model_NCEP (2nd column) and Model_COADS (3rd column) in the tropical western Indian Ocean in (a) May, (b) July, (c) November and (d) January.

layer (Figure 4.8c, 2nd and 3rd columns) play a major role in warming the SST in this period. As a result, warmer SST occurs north of 10^{0}S over the eastern half of the domain where there are shallow mixed layers. Along and near the equator, there are moderate easterly winds near the coast and weak westerly winds further offshore. The strong net surface heat flux gain and mixed layer leads to warm SST offshore. Near the coast along the equator, cooler SST and deeper mixed layers occur. This east-west SST orientation along the equator can also be associated with the Wyrtki Jets which carry warm waters eastward.

During January when the North East monsoon peaks, the SST shows a distinct north-south distribution for Model_NCEP and Model_COADS as well as satellite data from AVHRR and TMI (Figure 4.7d). The zone of cooler waters of about 25-26^{o}C appears to the north of the equator which gradually warms up to 27^{o}C towards the east. Meanwhile, a zone with warmer waters of about 28-29^{o}C is observed to the south of equator, which cools down to 27-28^{o}C towards the east. Strong northeasterly winds from the Asian landmass appear over north of 10^{o}S in January, and they decrease the net heat flux gain accumulated in November (Figure 4.8d, 1st column). These winds deepen the surface mixed layer up to 50 m to the north of 10^{o}S near the coast (Figure 4.8d, 2nd and 3rd columns). Consequently, the decreased surface heat gain and deepened mixed layer cool the SST to the north in conjunction with the reduction in solar radiation that ranges between 230 and 260 Wm^{-2} (Figure 4.9). The warm SST matches with shallow mixed layer of about 15-25 m and weak winds (4.6d). In January, the great difference between the warmer and colder zone is in the mixed layer depth and winds. Thus, the mixed layer depth exerted by the winds in this month significantly determines the north-south distribution of the SST in the tropical western Indian Ocean. Furthermore, a marked SST gradient between the cooler and warmer zone can be associated with heat advection towards the northern cooler zone through the horizontal circulation that separates the north cooler water zone and the south warmer water zone.

The annual cycle in SST in both the model and satellite data show some spatial asymmetries. Relatively warm SST occurs during the North East monsoon (January) and both transition seasons (May and November). In this period, the regional SST ranges from 26 to 30^{o}C in the large part of the domain, except to the northwest in the North East monsoon and to the southeast in the transition seasons, respectively. The coolest SST that ranges between 24 and 26^{o}C occurs during the South West monsoon (July). Therefore, the ROMS model seems to simulate well the annual cycle of the SST in the tropical western Indian Ocean.

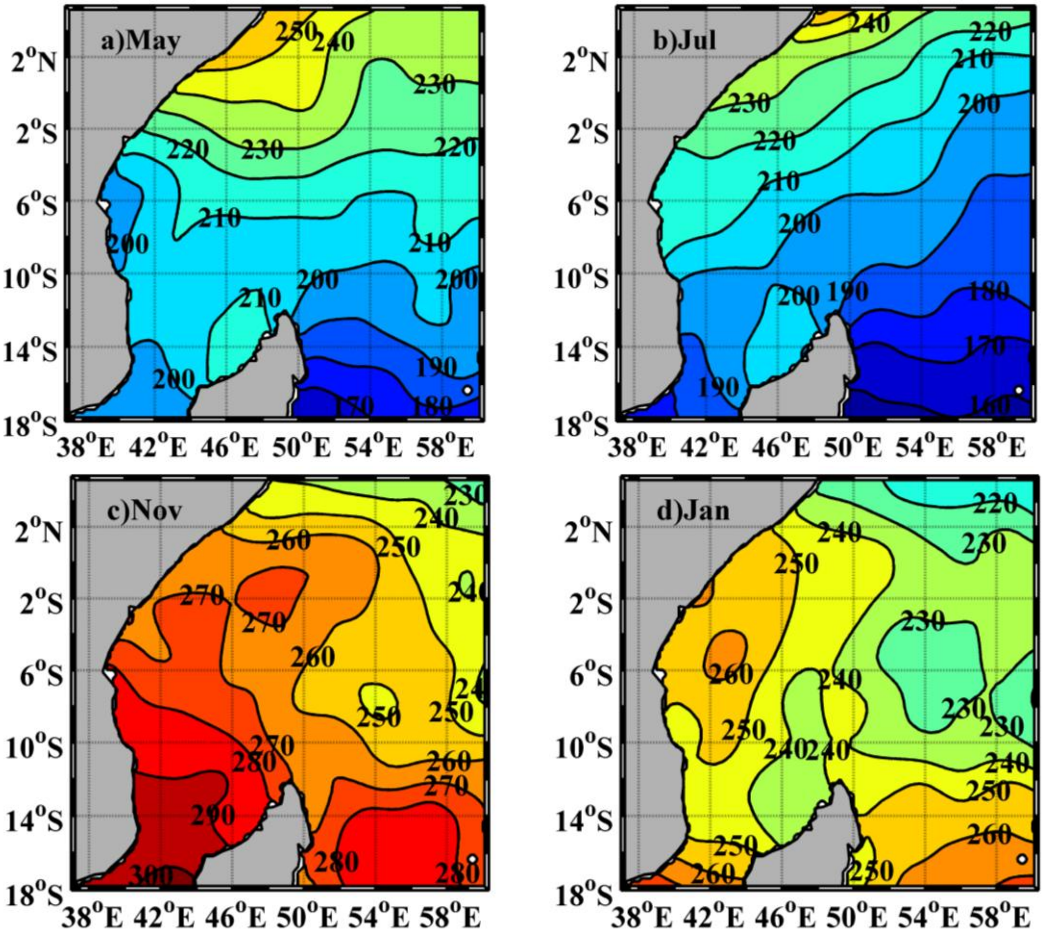

Figure 4.9: The annual cycle of the solar shortwave radiation [Wm^{-2}] in the tropical western India Ocean from Model_COADS for a) May, b) July, c) November and d) January.

4.2.2 Sea Surface Salinity

The annual cycle of the SSS for Model_NCEP and Model_COADS in the tropical western Indian Ocean is compared with that from the WOA2009 data (Figure 4.10, 1st to 3rd columns). In general, the annual cycle of the SSS for Model_NCEP seems to be lower than that from Model_COADS and WOA2009. As in the mean state, this SSS difference for Model_NCEP with that from Model_COADS and WOA2009 can be associated with difference in time periods and the nature of the observations. Furthermore, lack of a restoring term in Model_NCEP which is present in Model_COADS could be the cause of the SSS bias for Model_NCEP. All SSS data display seasonality. The evaluation of the annual cycle of the SSS patterns in the region is performed in conjunction with the net freshwater fluxes (net evaporation minus net precipitation) as the major contributor for this distribution (Figure 4.10, 4^{th} column).

The spatial distribution of the SSS and its corresponding net freshwater flux during the transition period towards and during the South West monsoon (May and July) is illustrated in Figure 4.10 (1^{st} and 2^{nd} rows). In May, relatively fresh water of about 34.6-34.8 ppt occurs to the south of 10^{o}S matching with strong net evaporation fluxes of more than 0.5 $cmday^{-1}$ (Figure 4.10a). Moreover, the fresh waters are confined to the coast to the north of the domain. The net precipitation flux near the Tanzanian coast between 0-10^{o}S reflects the March-May rainfall season (long rains) over East Africa. In this period, the salty waters (~35.6 ppt) appear to the north of the region in Model_NCEP, Model_COADS and WOA2009. The net evaporative flux is slightly enhanced in July resulting in relatively high SSS to the north of the domain (Figure 4.10b).

Figure 4.10 (3^{rd} and 4^{th} rows) displays the spatial patterns of the SSS and net freshwater fluxes during the transition period to and during the North East monsoon (November and January) in the region. The highest SSS in the region occurs in the transition period to the North East monsoon (November) as indicated in Figure 4.10c. In this period, relatively high SSS in the Tanzanian shelf region can be associated with high net precipitation in November (Figure 4.10c). This is a period with very weak winds that create shallow mixed layers especially to the northeast of 10^{o}S where it matches with high SSS ranging between 35.4 to 35.8 ppt (Figure 4.10c). High SSS is maintained to the northwest of the domain during January to the north of 10^{o}S matching with a strong net evaporation driven by cold dry north-easterly winds (~0.5 $cmday^{-1}$). This cooler salty zone matches with strong net evaporation to the north, and the warmer fresh zone matches with strong net precipitation to the south.

In general, the simulated SSS in the tropical western Indian Ocean reasonably agrees well with that from the WOA2009 data particularly with that form Model_COADS. Fresh and salty water occur to the south and south of the domain, respectively. A longer interannual simulation and absence of a restoring term in Model_NCEP could be the reason for relatively fresher waters in the annual cycle SSS for Model_NCEP than in Model_COADS and WOA2009. As a result, the Model_NCEP has more opportunity to drift away from observations than in the climatological run (Model_COADS).

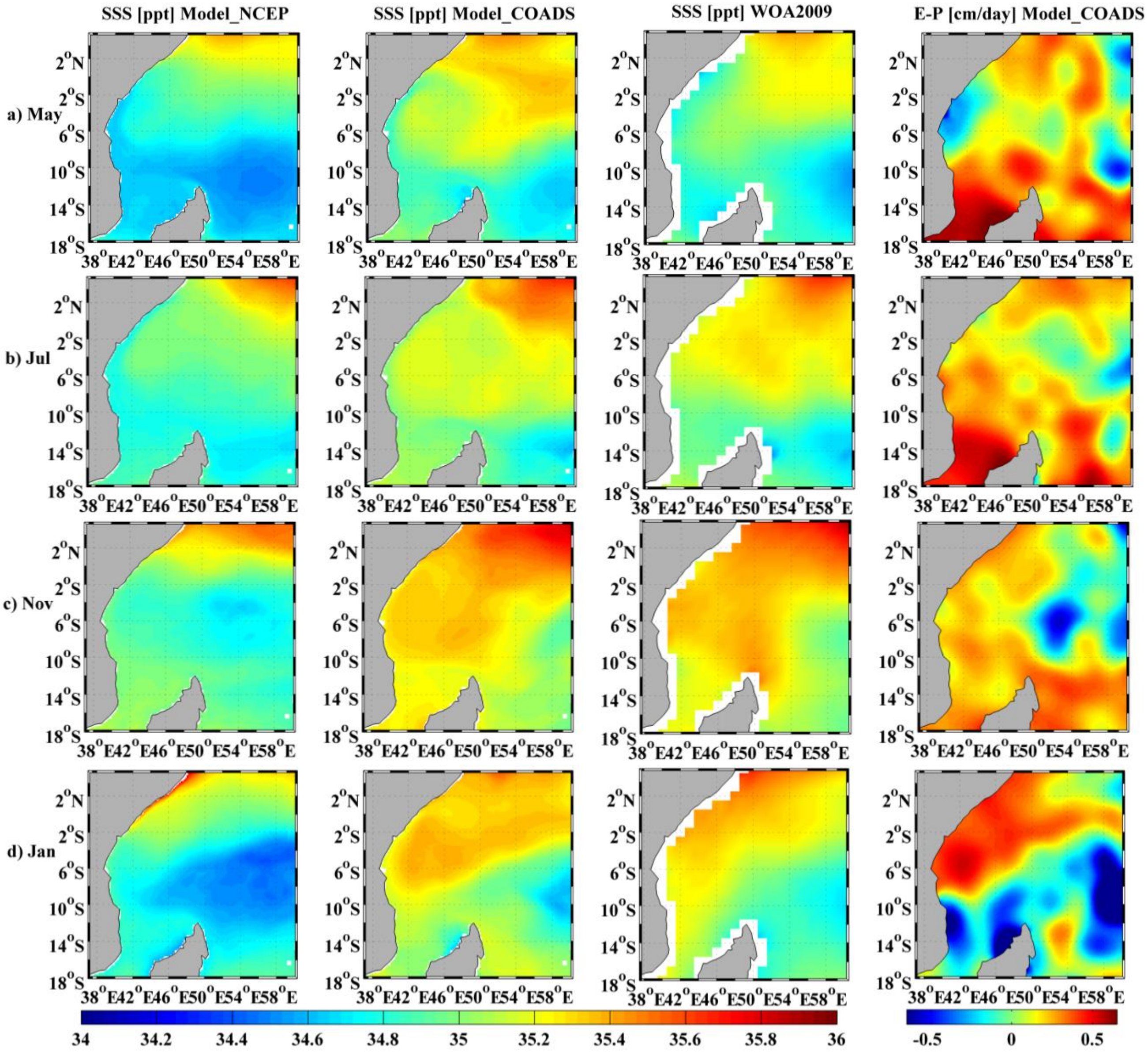

Figure 4.10: Annual cycle sea surface salinity for Model_NCEP (1st column), Model_COADS (2nd column), WOA2009 (3rd column) and (d) freshwater flux (net evaporation minus net precipitation) for Model_COADS (4th column) over the tropical western Indian Ocean in (a) May, (b) July, (c) November and (d) January.

4.2.3 Upper Ocean Circulation

The annual cycle of the upper ocean circulation in the tropical western Indian Ocean from the ROMS simulations, Model_NCEP and Model_COADS as well as the AVISO data is evaluated using the SSH, surface ocean currents and volume transport (Figure 4.11, 4.12 and 4.13). The annual cycle of the SSH indicates a north-south distribution in the region with seasonal variation in both model simulations and AVISO. High SSH occurs to the south of 10^{o}S and along the Tanzanian coast associated with the subtropical gyre and the EACC exceptionally occur during all months. The SSH difference between high and low sea levels in the domain is higher than 40 cm throughout the year, implying a dynamically active region in the year round. Along with the SSH, which is a key variable commonly used for the dynamical analysis of the ocean circulation, surface ocean currents and volume transport are evaluated. The sea surface currents and volume transport in the tropical western Indian Ocean also show seasonal variations.

During the transition period to the South West monsoon (May), the sea surface currents, SSH and volume transport in the tropical western Indian Ocean reflect the basin-wide cyclonic tropical gyre in the model and satellite data. The gyre comprises the SEC and the NEMC to the south, the EACC to the west and the eastward flowing Wyrtki Jets to the north in Model_NCEP, Model_COADS and the AVISO data (Figure 4.11a). The Wyrtki Jets are the eastward flowing currents which develop during both monsoon transition periods along the equator (Wyrtki, 1973). These jets appear in the surface currents between 2^{o}N and 2^{o}S, and they are strong and clearly visible in the open ocean to the east of 54^{o}E. High SSH patterns in the model simulations and AVISO align with the SEC and the NEMC to the south, the EACC to the west and the eastward flowing Wyrtki Jets to the north (Figure 4.12a). The lowest negative SSH in the model simulations and the AVISO data occurs from the southern Tanzanian waters to the open ocean between 5 and 12^{o}S. It is elongated and centred at 8^{o}S, 52^{o}E in the model simulations and further east in the AVISO data. The volume transport also marks the jets between 2^{o}N and 4^{o}S, which are clearly visible in Model_COADS (Figure 4.13a). In this period, the NEMC is strong at the north tip of Madagascar (about 100 cms^{-1}) moving north-westwards towards the Tanzanian coast. This current transports about 35 Sv in Model_NCEP and about 25 Sv in Model_COADS between the tip of the north Madagascar and 10^{o}S (Figure 4.13a). Moreover, the NEMC supplies

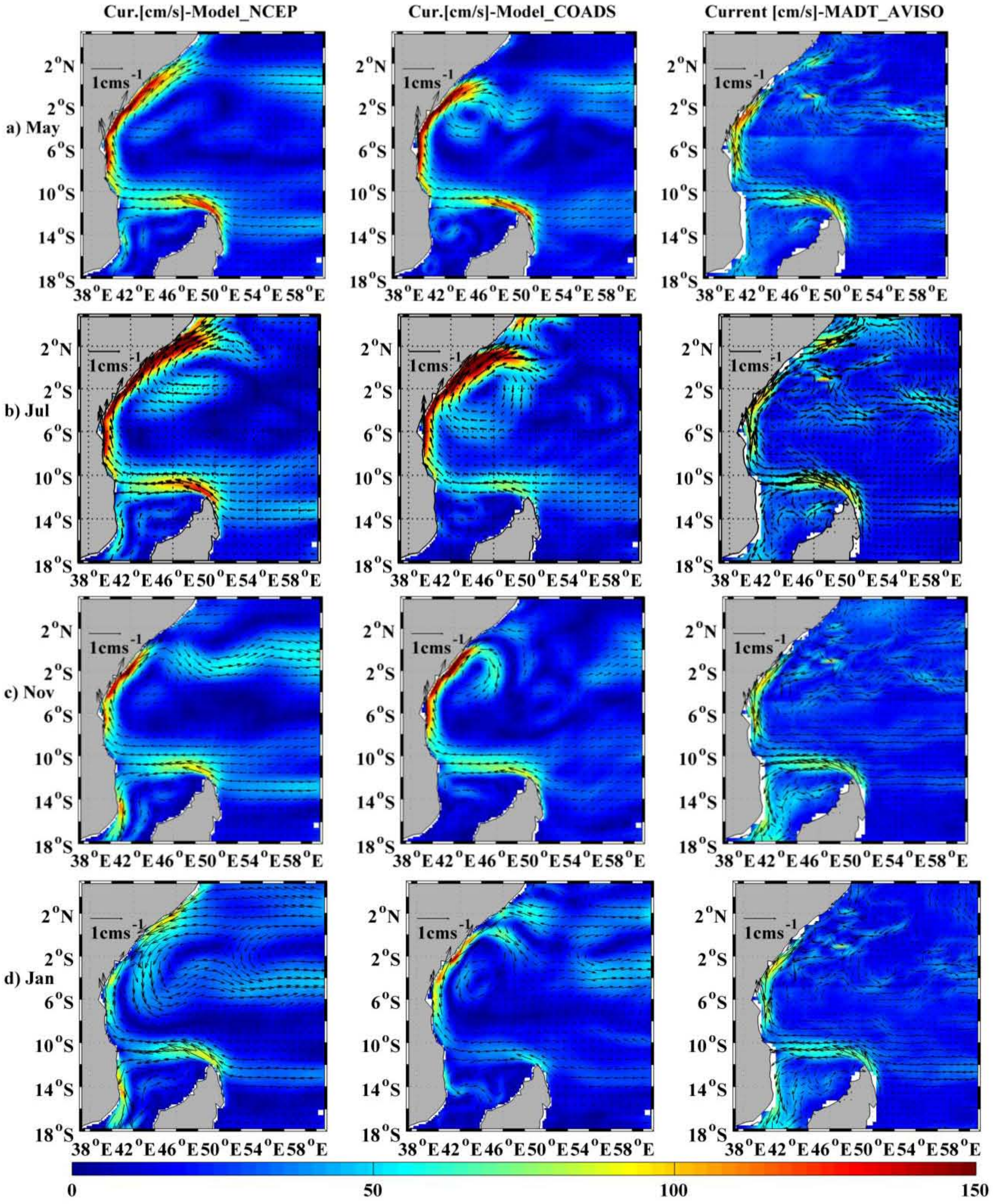

Figure 4.11: Annual cycle of surface current components superimposed on the surface current (cms^{-1}) in the tropical western Indian Ocean for Model_NCEP (1st column), Model_COADS (2nd column), and MADT-AVISO (3rd column) in (a) May, (b) July, (c) November and (d) January.

the northward flowing EACC near the African coast, the speeds which reach up to 120 cms^{-1} in this month with about 25 Sv volume transport into the southern Tanzanian waters in Model_NCEP and Model_COADS.

As the South West monsoon peaks in July, the tropical western Indian Ocean shows the strongest near-surface current speeds, SSH and volume transport in Model_NCEP, Model_COADS and AVISO (Figure 4.11b, 4.12b, 4.13b). The SEC and the NEMC appear to be located further northward as suggested by Schott et al. (2009) in the supply of the EACC. The speeds of the EACC reach up to greater than 150 cms^{-1} in this period, feeding the northward flowing Somali Current. After crossing the equator, part of the Somali Current turns offshore where it recirculates forming the Southern Gyre between 1^{o}N and 6^{o}S. The Southern Gyre, which is completely closed, appears to extend further north and south in Model_COADS than Model_NCEP. High SSH patterns in Model_NCEP, Model_COADS and AVISO which align with the SEC and the NEMC to the south as well as with the EACC to the west are maintained. The most negative SSH in the model simulations and AVISO between 5 and 12^{o}S is focused westward and centered at 8^{o}S, 50^{o}E. Similarly, the Southern Gyre also appears in the volume transport as the Somali Current which recirculates near the equator (Figure 4.13b). The cross equator Somali Current transports about 5 Sv and 20 Sv in Model_COADS and Model_NCEP, respectively.

During the transition period to the North East monsoon (November), the surface currents, SSH and the upper ocean volume transport reflect the basin-wide cyclonic tropical gyre. As in May, the basin is bounded by the SEC and the NEMC to the south, the EACC to the west and the Wyrtki Jets to the north in the model runs and AVISO (Figure 4.11c, 4.12c, 4.13c). The near-surface currents in the region are weaker than in the previous season due to weaker winds blowing over the region. The Wyrtki Jets tend to be stronger (about 80 cms^{-1}) than those in May (50-60 cms^{-1}), as suggested by Han et al. (1999). The jets reflect volume transport of about 20-25 Sv flowing eastward as shown in Model_NCEP and Model_COADS. The SEC and the NEMC are now located further south with weak speeds that feed the EACC. The EACC has speeds ranging between 80 and 120 cms^{-1}. High SSH patterns in the model simulations and AVISO align with the SEC and the NEMC to the south, the EACC to the west and the eastward flowing Wyrtki Jets to the north. Regions of negative SSH in the model and AVISO data occur between 2

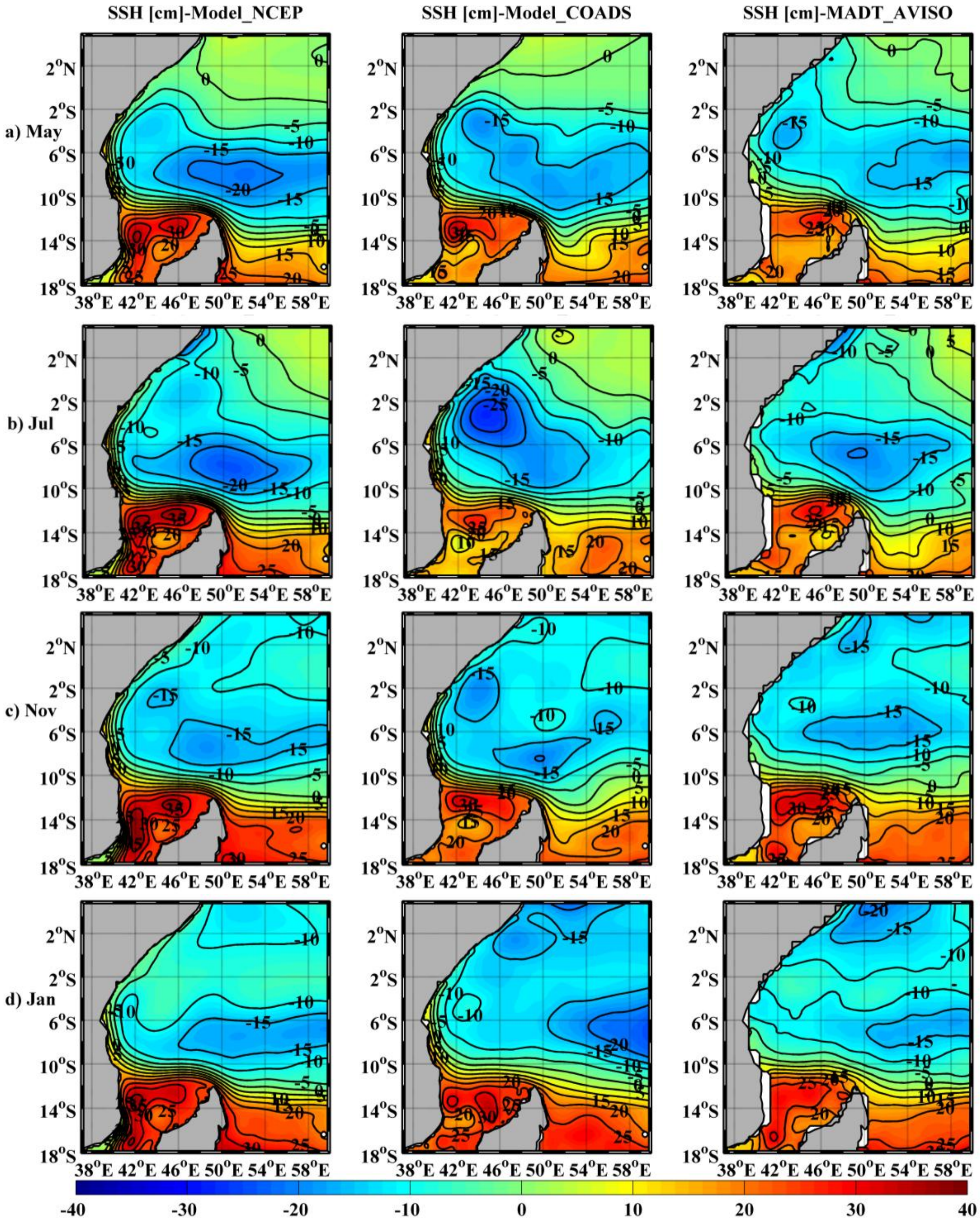

Figure 4.12: Annual cycle of the SSH (cm) in the tropical western Indian Ocean for Model_NCEP (1st column), Model_COADS (2nd column), and MADT-AVISO (3rd column) in (a) May, (b) July, (c) November and (d) January.

and 12^{o}S with the largest to the south. The southern region of negative SSH is defined in Model_COADS compared to the other two datasets. The volume transport integrated in the upper ocean to a depth of 1500 m indicates that the NEMC transports about 35 Sv at the tip of Madagascar and supplies about 25 Sv to the EACC.

During January when the North East monsoon is fully developed, weak surface ocean currents, SSH and volume transport occur in the region in the Model_NCEP, Model_COADS and AVISO. In this period, a reversal of the Somali Current occurs to the north of 2^{o}S, and there is a weakened EACC to the south of 2^{o}S in the model experiments and AVISO (Figure 4.12d). This is attributed to the northeasterly winds which blow towards and along the East African coast that drive the southward Somali Current which crosses the equator. The southward flowing Somali Current confluences with the EACC between 1^{o}S and 4^{o}S forming the SECC which is clearly visible to the east of 54^{o}E in the model results and AVISO (Figure 4.12d). The confluence zone between the EACC and Somali Current occurs in the current speeds and volume transported around 2^{o}S in Model_NCEP and AVISO data, and at the Equator in Model_COADS. The SEC, the NEMC and the EACC are weaker in this season with the current speeds less than 40 cms^{-1}, about 70 cms^{-1} at the tip of Madagascar and less than 50 cms^{-1} along the East African coast, respectively. This is attributed to the southward Somali Current and the northeasterly winds which oppose the NEMC and the EACC. The SECC forms the northern boundary of the basin-wide cyclonic tropical gyre during this period which is located further south and wider than Wyrtki Jets in the transition periods. Large SSH values in the model simulations and AVISO align with the SEC and the NEMC to the south, the EACC to the west and the eastward SECC to the north. Negative values of SSH in Model_NCEP, Model_COADS and the AVISO data is elongated toward the open ocean between 5 and 10^{o}S.

In general, the evaluation of the annual cycle of the upper ocean circulation in the tropical western Indian Ocean shows good consensus between the model simulations and the AVISO data. The near-surface current speeds, SSH and the volume transport integrated in the upper 1500 m in the tropical western Indian Ocean mark the basin-wide cyclonic tropical gyre during all seasons except in the South West monsoon.

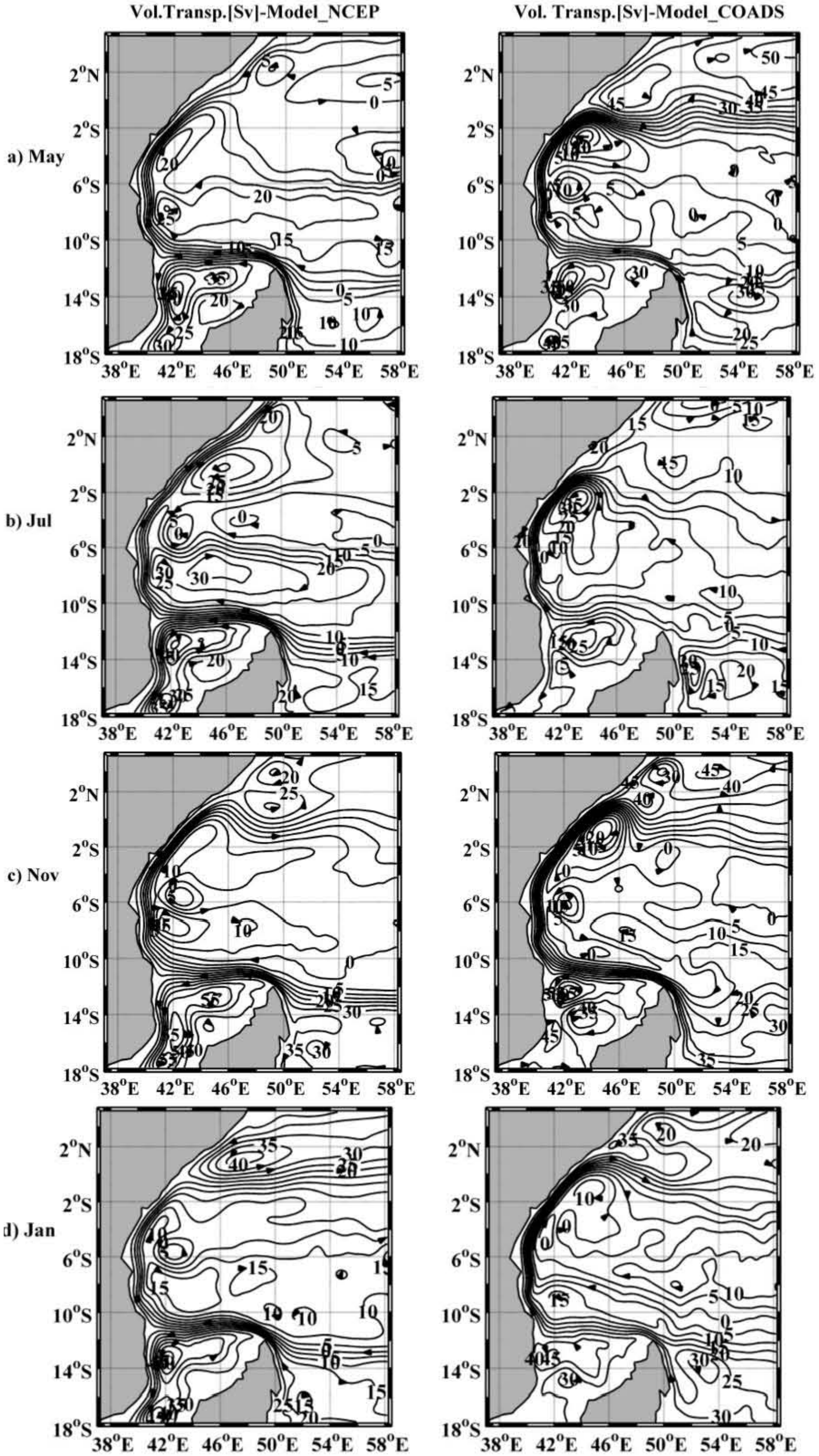

Figure 4.13: Volume transport in the upper 1500 m (Sv) in the tropical western Indian Ocean for Model_NCEP (1st column) and Model_COADS (2nd column) in (a) May, (b) July, (c) November and (d) January.

4.2.4 Thermocline Structure

The annual cycle of the thermocline structure in the tropical western Indian Ocean is described by using the model outputs from Model_NCEP with that from Model_COADS (Figure 4.14). In both simulations, the thermocline is determined from the depth of the 20°C isotherm. Deeper thermoclines often align with the dominant currents in the region, the SEC, NEMC and EACC, throughout the year. Shallow thermoclines, however, occur in the 5-12°S latitudinal zone in the year round. These minimum thermocline depths reflect the main upwelling region in the open ocean near the Republic of Seychelles (45-60°E) termed by Hermes and Reason (2008) as the Seychelles-Chagos thermocline ridge. However, the secondary upwelling region which occurs near Chagos (75-80°E), is beyond the domain of this study. These two regions link with each other during the austral summer to form a ridge like feature in the southwest Indian Ocean (Hermes and Reason, 2008). The position and shape of the ridge and thermocline structure in the tropical western Indian Ocean show seasonality, as discussed below.

During the transition monsoon to the South West monsoon (May), the thermocline depth reflects the basin-wide cyclonic tropical gyre in both model simulations, Model_NCEP and Model_COADS. By this time, the tropical gyre comprises the SEC and NEMC to the south, the EACC to the west and the Wyrtki Jets to the north with the thermocline ridge in its centre (Figure 4.14a). Deeper thermoclines that range between 100 and 160 m align with the SEC, and the strongest meridional gradient lies to the north of Madagascar reflecting the NEMC. In the southern Tanzanian waters, the EACC appears to align with thermoclines of 90-110 m depth. In the centre of the tropical gyre, there are minimum thermocline depths of 70 m between 5 and 12°S, and centred at 54°E, 8°S. This minimum thermocline reflects the main open ocean upwelling region near the Seychelles. Such open ocean upwelling results from weak negative wind stress curl caused by the southeast trades and monsoon westerlies, the divergence of the tropical cyclonic gyre and Rossby waves excited in the tropical southeastern Indian Ocean (McCreary et al., 1993; Xie et al., 2002; Hermes and Reason, 2008).

In July when the South West monsoon is fully developed, the strongest and steadiest winds together with the Rossby waves are responsible for the existence and structure of the thermocline distribution in the region. Although region of deep thermocline depths (90-150 m) align with the SEC, NEMC and EACC, the main upwelling region of the Seychelles-Chagos thermocline ridge is contracted and more elevated to about 60 m from the surface. Furthermore, the centre of the thermocline region is located further west with its peak centred at 50^{o}E, 9^{o}S. A strong thermocline gradient appears at the tip of the northern Madagascar (100-170 m) and at 10^{o}S near the Tanzanian coast (90-130 m) in both ROMS simulations (Figure 4.14b).

In the monsoon transition to the North East monsoon (November), the thermocline ridge is elongated with a weaker slope near the tip of the north Madagascar (Figure 4.14c). The thermocline ridge (70-80 m) is elongated and located towards the open ocean. The minimum thermocline is elongated, eastward suggesting it to be linked with the secondary ridge near Chagos.

The tropical western Indian Ocean shows a deeper thermocline with a much wider zone of the ridge during the North East monsoon. In January the region is characterized by thermoclines that range from 70 to 180 m for Model_NCEP and Model_COADS (Figure 4.14d). The thermocline orientation shows a weaker slope from the north of Madagascar towards the East African coast than in the other season.

In general, the spatial patterns of the thermocline indicate that the deep thermocline regions align with the dominant currents that form the tropical cyclonic gyre, and the minimum thermocline depths from the ridge near 5-10^{o}S which occurs throughout the year. Deep thermocline depths ranging between 100 and 180 m occur to the east and north of Madagascar, and extended towards the southern Tanzanian waters, signifying the NEMC and the EACC. The thermocline ridge in the open ocean shows both an annual and semiannual signals. It is elongated and compressed during the austral spring/summer and austral autumn/winter, respectively. However, the minimum values (about 60 m) of the thermocline occur during austral winter (July) and summer (January), while the maximum depth of the ridge about 70-80 m occurs during the monsoon transitions (May and November).The annual and semi-annual signals are discussed further in Hermes and Reason (2008) and Yokoi et al. (2008).

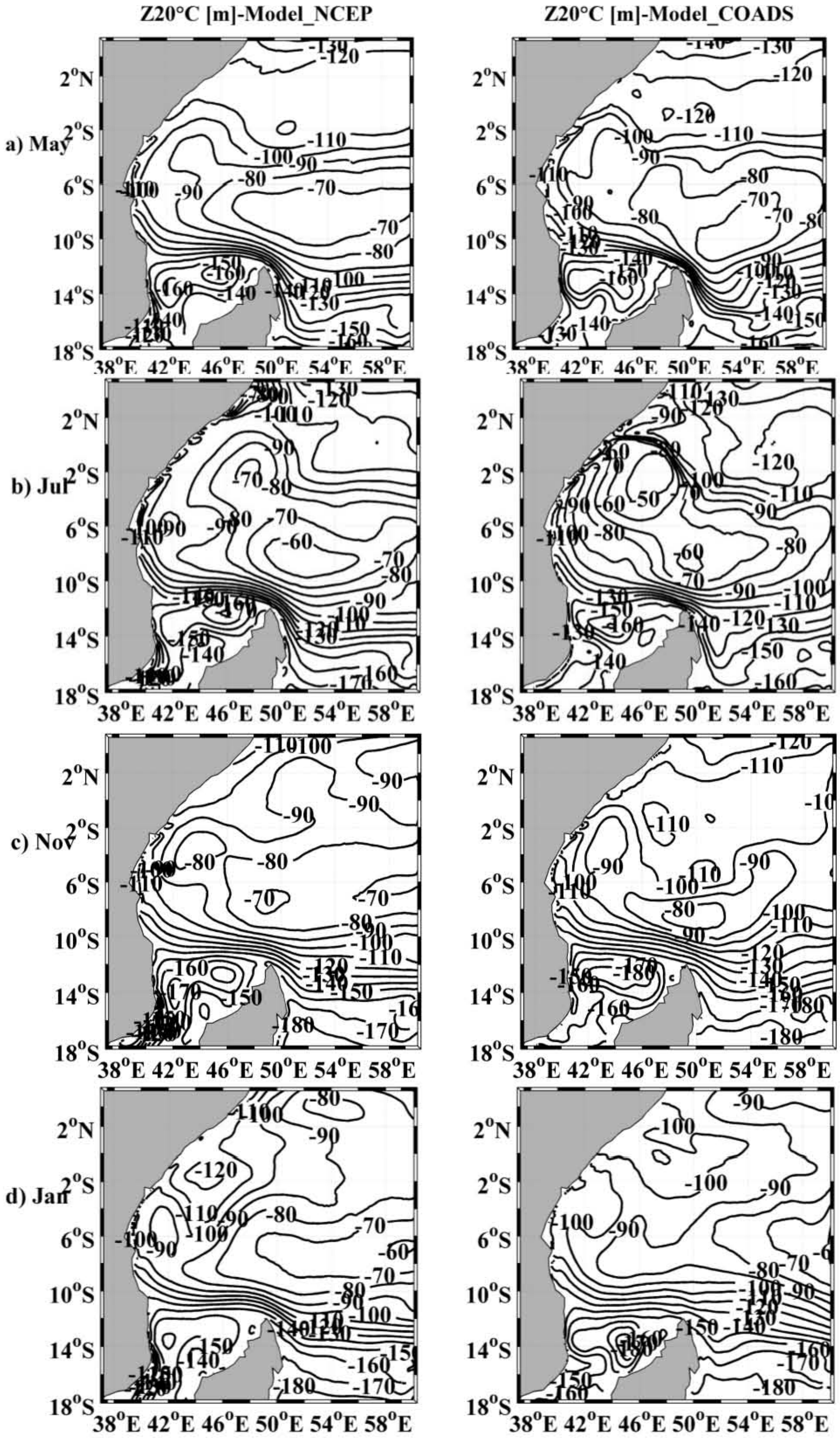

Figure 4.14: Thermocline depth (m) in the tropical western Indian Ocean for Model_NCEP (1st column) and Model_COADS (2nd column) in (a) May, (b) July, (c) November and (d) January.

4.3 Interannual Variability

The interannual variability of SST in the tropical western Indian Ocean is considered below using ROMS model (Model_NCEP), AVHRR, TMI, and in *situ* measurements. The interannual variations of the model SST in the region were compared with those for the AVHRR and TMI SST data as well as *in situ* measurements around Chumbe Island, in the Zanzibar Channel. The SST data corresponding to the region around Chumbe Island ($6^0$16'S, $39^0$10'E; Figure 3.1) are extracted between 39.5 to 40.5^{o}E and 6 to 7^{o}S from the model and satellite SST data. The time coverage of the model output is from 1980 to 2007, 1982 to 2007 for AVHRR, 1998 to 2007 for TMI and 1997 to 2007 for *in situ* data. The time series of the averaged monthly SST and SST anomalies from the model are compared against the AVHRR, TMI, and *in situ* SST data around Chumbe Island (Figure 4.15), and they are in good agreement.

The interannual variations of the SST for the model, AVHRR, TMI and *in situ* measurements off Chumbe Island in the tropical western Indian Ocean capture signals of the large scale climate modes such as El Niño-Southern Oscillation (ENSO) and the Indian Ocean Dipole (IOD). The model shows the El Niño/positive IOD events of 1982/1983, 1987/1988 and 1997/1998 and the La Niña/negative IOD events of 1984/1985, 1989 and 1999 in agreement with the satellite data (Figure 4.15b). The largest El Niño/positive IOD event of 1997/1998 appears in all datasets with positive SST anomalies greater than 0.5^{o}C. However, there are sometimes large differences between the temperature collected at the Chumbe Island Coral Park and the other products, probably caused by the coastal position of the station. Furthermore, the difference could be caused by different temporal coverage used to generate the climatology. In general, the difference between ROMS and the observations is comparable to the difference between the different SST products.

In general, the ROMS model forced with NCEP (Model_NCEP) seems to reproduce fairly well the interannual variability in the tropical western Indian Ocean. It agrees with the *in situ*, AVHRR and TMI data one interannual time scales. This suggests that the ROMS model, which is forced with NCEP from 1978 to 2007, realistically simulated the interannual variability in the tropical western Indian Ocean. Thus, the ROMS model can be used to study interannual SST variability and investigate possible mechanisms responsible for the variability in the region.

(a) Monthly SST off Chumbe Island 6-7°S, 40.5-39.5°E

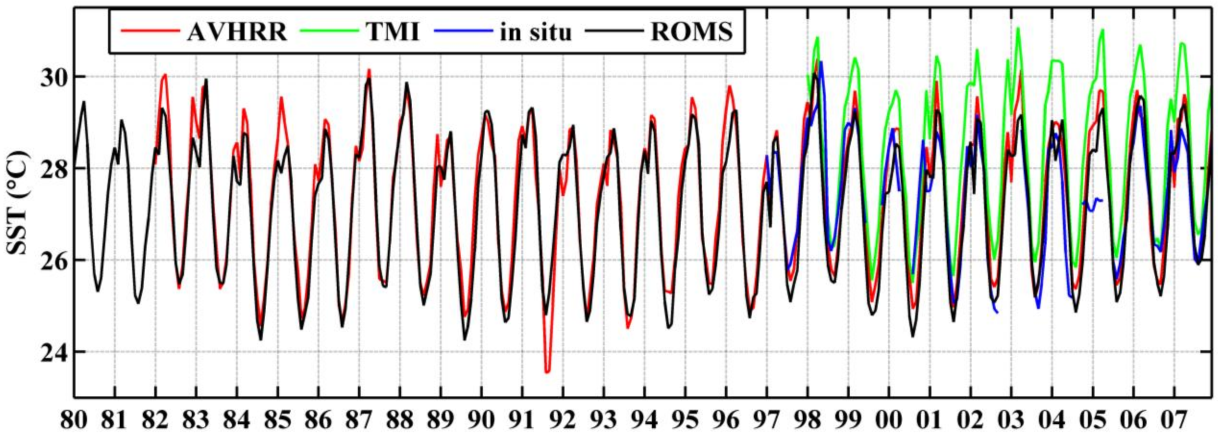

(b) SST Anom off Chumbe Island 6-7°S, 40.5-39.5°E

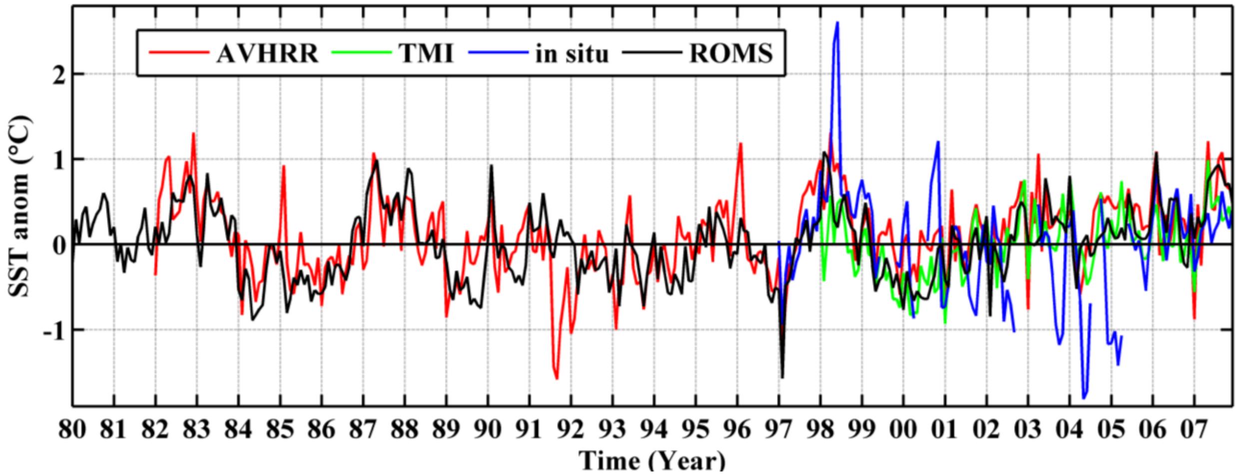

Figure 4.15: Time series for ROMS model (1980-2007), AVHRR (1982-2007), TMI (1998-2007) and *in situ* data around the Chumbe Island Coral Park in Zanzibar Channel (a) monthly SST and (b) monthly SST anomalies.

.

4.4 Summary

The ability of the ROMS model to reproduce variability in the tropical western Indian Ocean is evaluated using observations, hydrographic and satellite data. The ROMS models realistically simulated the regional variability at the mean state, the annual cycle and interannual variability. The model outputs from the realistic simulations forced with NCEP (Model_NCEP) and with COADS (Model_COADS) are in good agreement with observations, hydrographic and satellite data. Furthermore, the interannual variations of the model SST for Model_NCEP around

Chumbe Island are consistent with the AVHRR and TMI SST data as well as *in situ* measurements. This provides confidence in the accuracy and effectiveness of the ROMS model to simulate the regional variability. Therefore, the ROMS model forced with NCEP may be used to investigate variability and perform meaningful sensitivity experiments on the upper ocean circulation in the Tanzanian shelf region. The next chapter deals with the seasonal impacts of the of the upper ocean circulation in the Tanzanian shelf region.

Chapter 5

Influences of Seasonal Ocean Circulation on Coastal Waters

5.0 Introduction

This chapter provides an analysis of the influences of the upper ocean circulation in the Tanzanian shelf region at seasonal time scale. The analysis focuses on gaining an understanding of how ocean flow in the Tanzanian shelf region responds to the flow in the north of Madagascar, and how these changes influence the sea temperature and salinity. The dominant flow in the Tanzanian shelf region is the East African Coastal Current (EACC) which is supplied by the Northeast Madagascar Current (NEMC) to the north of Madagascar. Moreover, the EACC supplies the northward flowing Somali Current during the South West monsoon. During the North East monsoon, the EACC meets and confluences with the southward flowing Somali Current to form the eastward flowing South Equatorial Counter-Current (SECC). Thus, the seasonal variability of the EACC, SECC and Somali Current might have influences on the upper ocean properties in the Tanzanian shelf region. The impacts of these currents on the upper ocean properties in the Tanzanian shelf region are the subject of this chapter. Using the Regional Ocean Modeling System (ROMS) forced with reanalysed winds and heat fluxes from the National Center for Environmental Prediction (NCEP), this objective is achieved by addressing the following questions:

How does the Northeast Madagascar Current (NEMC) contribute to the volume, heat and salt transport and budgets in the coastal waters of Tanzania?

i. What is the mean flow and seasonality of the Northeast Madagascar Current in the north of Madagascar? Is this seasonality in phase with the East African Coastal Current (EACC) in the Tanzania shelf region?

ii. How does advection from the NEMC influence on the heat content of the upper ocean in the Tanzanian shelf waters?

iii. How does advection from the NEMC influence on the salinity in the Tanzanian shelf waters?

The chapter is outlined as follows: The introductory section is followed by the mean state of the upper ocean in the Tanzanian shelf in relation to the north of Madagascar and offshore. The seasonal variability in the upper ocean between the Tanzanian shelf region and offshore is provided in Section 5.2. The third section (5.3) provides a summary of the chapter.

5.1 Mean State

The distributions of the surface circulation and properties in the Tanzanian shelf region and to the north of Madagascar in the model are shown by the near-surface currents, sea surface temperature (SST) and sea surface salinity (SSS) in Figure 5.1. The simulated surface currents show the northwestward flowing NEMC which branches into the northward flowing EACC and a southward flow in the Mozambique Channel (Figure 5.1a). Mean current speeds stronger than 100 cm/s occur at the tip of the north of Madagascar as well as between 8°S and 2°N along the East African coast. The annual mean SST and SSS indicate a tongue of relatively cool freshwaters (~27°C, <34.8 ppt) extending from the north of Madagascar towards the Tanzanian waters. The relatively cool freshwaters get warmer and saltier along the Tanzanian coast to about 2°S. Such SST and SSS distributions suggest influences of the EACC and the NEMC in the Tanzanian shelf region.

To investigate influences of the upper ocean currents on the properties in the Tanzanian shelf region, two boxes are considered in the south and north of the Tanzanian shelf region. The first box A (38-49°E, 7-13°S) is bounded by lines L1 (49°E, 7-13°S) as the NEMC entrance, line L2 (13°S, 38-49°E) as an exit of the flow through the Mozambique Channel and line L3 (7°S, 38-49°E) as the southern entrance of the EACC in the shelf. The box is used to assess exchange of properties between the north of Madagascar and the southern Tanzanian waters. The second subregion is box B in the northern Tanzanian shelf region (38-49°E, 1-7°S) being bounded by line L3 (7°S, 38-49°E) as the southern entrance of the EACC, line L4 (1°S, 38-49°E) as the southward/northward Somali Current in the South West monsoon/North East monsoon. Line L5 (49°E, 1-7°S) serves as an exit of the SECC in the North East monsoon, and the Wyrtki Jets in the transition seasons. In these regions, the volume transport is integrated in the upper 1500 m.

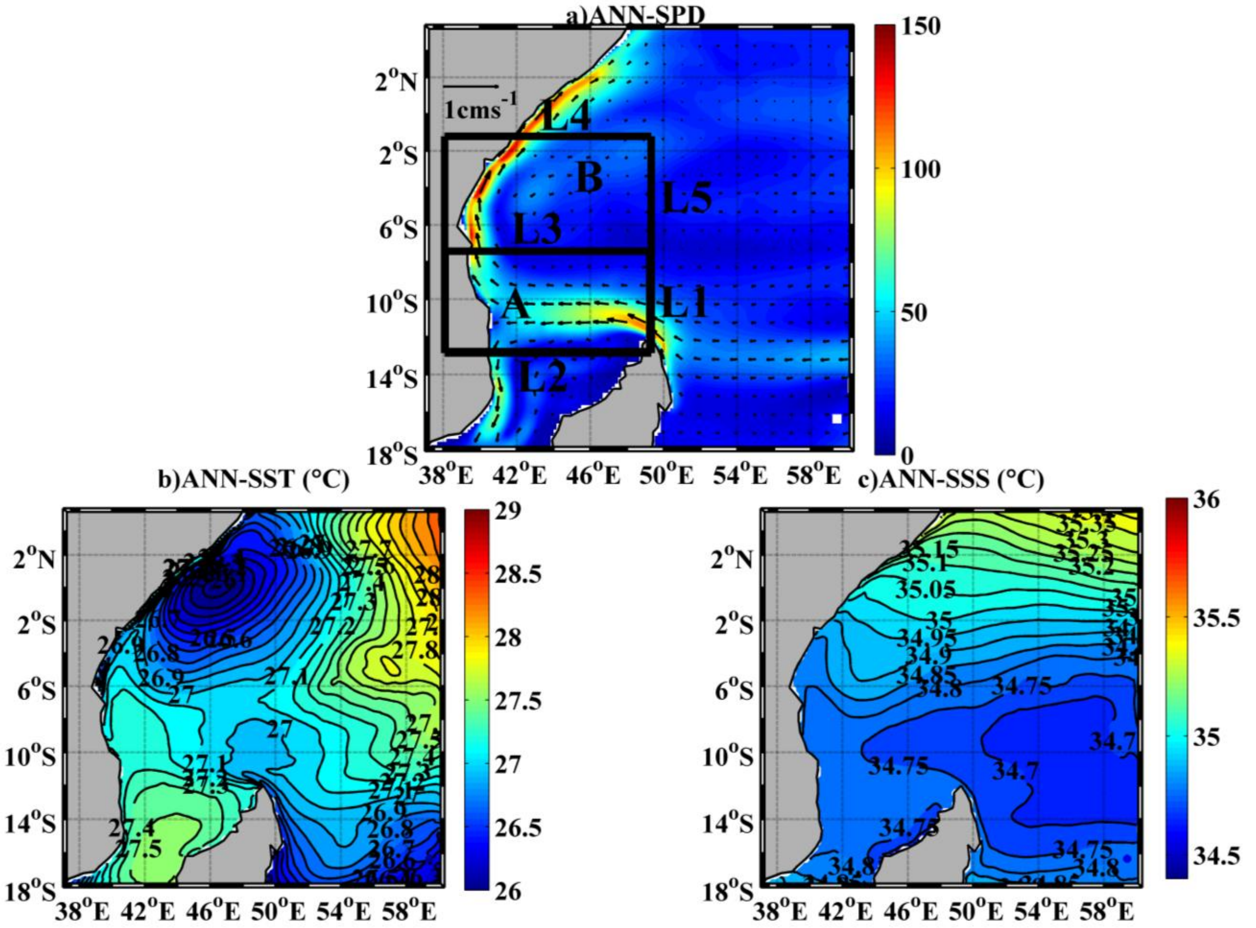

Figure 5.1: Annual mean for (a) surface currents in cm/s, (b) sea surface temperature in °C and (c) sea surface salinity in ppt. Box A represents (38-49°E, 7-13°S) and B represents (38-49°E, 1-7°S); lines L1 (49°E, 7-13°S), L2 (13°S, 38-49°E), L3 (7°S, 38-49°E), L4 (1°S, 38-49°E) and L5 (49°E, 1-7°S).

The southern Tanzanian waters, which extend to the north of Madagascar (box A), show a net volume flux gain in the annual mean which can be associated with a small downwelling. The volume flux of about 47.0 Sv, integrated in the upper 1500 m, crosses L1 into the subregion A with the major contribution from the NEMC in the north of Madagascar (Table 5.1). This volume is higher than the NEMC annual mean transport of about 29.60±8Sv reported by Swallow et al. (1988) and Schott et al. (2009) in the upper 1000 m. The difference may be associated with the difference in area-depth coverage. This research considered only the cross-shore current component in the upper 1500 m from 7 to 13°S which is deeper and wider than the reported one by Swallow et al. (1988) and Schott et al. (2009). Of the outgoing 47 Sv, about 12.5 Sv and 34.0 Sv are transported out southward and northward of the southern Tanzanian region (subregion A) across L2 through the Mozambique Channel and via L3 through the EACC, respectively. Thus, there is an extra of incoming volume of about 0.5 Sv into the subregion which can be associated with a weak downwelling.

The subregion between the southern Tanzanian waters and north of Madagascar indicates different mean ocean properties. There is a large mean sea surface height which matches with surface currents of about ~34.1 cm/s and mixed layer of about 23.9 m as well as relatively deep thermocline of about 118.2 m (Table 5.2). Furthermore, the subregion shows warm SST of about 27.2^{o}C and relatively low salinity of about 34.8 ppt. This warm water can be related to the horizontal advective warming (~14.9^{o}C/month) and atmospheric surface warming (~1.9^{o}C/month), which collectively act to balance the cooling from vertical surface processes (~-16.8^{o}C/month) in the mixed layer (Table 5.2). Warming from horizontal advection can be associated with the NEMC to the north of Madagascar and the EACC in the Tanzanian shelf waters.

The subregion over the northern Tanzanian shelf waters and offshore (box B) shows an annual mean of net volume flux loss of about 4.2 Sv suggesting the presence of upwelling. The volume flux of about 34.0 Sv in the upper 1500 m crosses L3 in the middle of the Tanzanian shelf waters with the EACC dominating near the coast (Table 5.1). Nevertheless, an annual mean of about 21.9 Sv and 16.3 Sv respectively appears to be transported out of the subregion across L4 to the north as the northward flowing Somali Current and eastward flow through L5. Moreover, the eastward flow is either the SECC during the North East monsoon or the Wyrtki Jets in the transition seasons. Thus, there is an extra of 4.2 Sv transported out which can be associated with upwelling.

The subregion between the northern Tanzanian shelf region and offshore (box B) shows relatively low sea surface heights which match with weaker surface currents (about 31.1 cm/s) than in the south (Table 5.2). This subregion is characterized by a relatively shallow mixed layer (23.7 m), a thermocline depth (106.8 m) and mixed layer cooling by the horizontal advection (3.3^{o}C/month) (Table 5.2). The sea surface temperature of about 27.0^{o}C and sea surface salinity of about 34.8 ppt occur in the subregion which are almost the same as the southern Tanzanian shelf region. Horizontal advection cooling in the subregion is balanced by the warming from the atmosphere (1.9^{o}C/month) and vertical processes (1.4^{o}C/month) in the mixed layer (Table 5.2).

Table 5.1: Annual mean for the volume transport integrated in the upper 1500 m (Sv) acrosses line L1 (49^{o}E, 7-13^{o}S), L2 (13^{o}S, 38-49^{o}E), L3 (7^{o}S, 38-49^{o}E), L4 (1^{o}S, 38-49^{o}E) and L5 (49^{o}E, 1-7^{o}S).

Variable	**LINE**				
	L1	**L2**	**L3**	**L4**	**L5**
Volomu transport (Sv)	-47.0	-12.5	34.0	21.9	16.3

Positive (negative) indicates northward and eastward (southward and westward) volume transport.

Table 5.2: Annual mean sea surface current (SSC, in cm/s), sea surface height (SSH, in cm), mixed layer depth (MLD, in m), thermocline depth (Z20^{o}C, in m), sea surface temperature (SST, in ^{o}C) and sea surface salinity (SSS, in ppt) spatially averaged over boxes A (38-49^{o}E, 7-13^{o}S) and B (38-49^{o}E, 1-7^{o}S) in the tropical western Indian Ocean.

VARIABLE	**BOXES**	
	A	**B**
Net. Volu (Sv)	0.5	-4.2
SSC (cm/s)	34.1	31.1
SSH (cm)	45.0	38.5
MLD (m)	23.9	23.7
Z20^{o}C (m)	-118.2	-106.8
SST (^{o}C)	27.2	27.0
SSS (ppt)	34.8	34.8
Net_MLT (^{o}C/mon)	-0.0002	0.0019
Atms (^{o}C/mon)	1.9	1.9
Horz. Adv.(^{o}C/mon)	14.9	-3.3
Vert. Proc. (^{o}C/mon)	-16.8	1.4

Note: Positive and negative net volume flux indicates downwelled and upwelled water volume in the boxes, respectively.

In general, the Tanzanian shelf region experiences different upper ocean circulation and properties at the mean states between the north and south. Net volume flux gain occurs in the southern shelf waters which can be associated with a weak downwelling. However, the net volume flux loss is observed in the northern Tanzanian shelf which can be associated with a considerable upwelling from below the 1500 m depth. It is noteworthy that the Tanzanian shelf region experiences strong seasonality which impacts the regional variability. Thus, it is useful to analyse the seasonality of the ocean properties and circulation patterns in the shelf region.

5.2 Seasonality

Analyses of the seasonal climatology of the vertical temperature structure and volume transport are conducted to investigate the relationship of the flow in the Tanzanian shelf region and to the north of Madagascar. The vertical climatology for the transects in the upper 250 m of the zonal and meridional currents as well as temperature and salinity are computed along L1+L5 and L3 as defined above. Additionally, the climatological time series of the cross-shore volume transport for the NEMC (L1) and alongshore volume transport for the EACC (L3) is also computed. Owing to strong seasonality in the region, the transect in May represents the transition period to the South West monsoon, July for the South West monsoon, November for the transition from the South West monsoon and January represents the North East monsoon for brevity.

5.2.1 Meridional Transect Averaged Over 49-49.5^{o}E (L1+L5) from 1 to 13^{o}S (Offshore Transect)

Figure 5.2 displays the vertical structure of the cross-shore currents, temperature and salinity for the transect from the north coast of Madagascar at 13^{o}S to the north offshore at 1^{o}S, averaged between 49 and 49.5^{o}E from each of the four months. Common to all variables is a strong downward gradient near the north coast of Madagascar between 11 and 13^{o}S throughout the year. In the cross-shore currents, this region indicates a core of intense westward flow which is broadened at the surface, reflecting the westward flowing NEMC (Figure 5.2a-d). The temperature and salinity also show strong variability over the mentioned region throughout the year with the deepened warm isotherms (Figure 5.2e-h) and freshwater isohalines (Figure 5.2i-l), respectively. Along with the wind stress and the surface heat fluxes over the region, these upper ocean patterns suggest that the westward flowing NEMC plays a role in the temperature and salinity distributions. As the warm isotherms are vertically displaced downward (negatively sloped) towards the offshore waters in the region, the NEMC possibly carries warm waters westwards into the Tanzanian shelf region. The shape, intensity and position of the contour lines in the core intense of the cross-shore currents, temperature and salinity vary monthly, suggesting seasonal variations.

In May, the onset of the South West monsoon, relatively strong cross-shore currents related to change in temperature and salinity occur near the coast to the north of Madagascar (Figure 5.2a, e, i). Current speeds of greater than 70 cm/s occur in the upper 150 m to the north of Madagascar, between 11^{o}S and 13^{o}S, reflecting the NEMC. This period is characterized by moderate winds that reduce the wind-induced evaporative heat loss and vertical mixing. As a result, warm surface temperature of about 27-28^{o}C occurs in the upper 50 m (Figure 5.2e). This elevated temperature could drive an enhanced vertical convection in the atmosphere and precipitation to the south of 8^{o}S, resulting to the freshwater of about 34.7 ppt in the surface waters within 50 m (Figure 5.2i). The surface waters in the upper 40 m are characterized by 28^{o}C isotherms intersecting the surface, being displaced vertically upward around 10^{o}S. Such patterns occur with the eastward flowing cross-shore currents that reflect the Wyrtki Jets near the equator which develop during the transition periods (Wyrtki, 1973) around 5^{o}S at 50 m depth. The isotherms and isohalines below 50 m show downward slopes around 10^{o}S in the region with strong cross-shore currents. This is indicative of the westward flowing NEMC that is about 50 cm/s at the 60 m depth. The deepening of the warm isotherms and fresh isohalines between 7 and 12^{o}S suggest that the westward NEMC plays a significant role in this distribution, possibly by either carrying warm and fresh waters or by interrupting the flow of water upwelling over the open ocean (Hermes and Reason, 2008; Yokoi et al., 2008). Between 100 and 200 m, the region displays isotherms and isohalines ranging from 14 to 22^{o}C and 35.1 ppt, respectively. In this period, the volume transported into the southern Tanzanian shelf region (box A) across the north of Madagascar, L1, increases from ~45.0 Sv in April to ~47.2 Sv in May (Figure 5.3).

During July, when the South West monsoon is fully developed, the offshore transect indicates enhanced current speeds with relatively cool and salty surface waters (Figure 5.2b, f, j). The cross-shore current speeds are strengthened to greater than 70 cm/s at 150 m between 11 and 12°S to the north of Madagascar marking the NEMC (Figure 5.2b). This region matches with relatively cool and salty surface waters (~24-25°C, ~34.8-34.9 ppt) in the upper 75 m with cool waters (~25°C) laying adjacent the northern coast of Madagascar. The cross-shore currents in the upper 250 m off the northern coast of Madagascar broaden from May to July (Figure 5.2b). This may be due to the strong winds over the tropical western Indian Ocean that enhances both the wind-induced evaporative cooling and the vertical mixing. Moreover, the sky is covered by clouds which reduce the solar insolation, and thus, decrease the net surface heat flux gain, leading to further cooling of the surface temperature. Compared with May, the warm isotherms and fresh isohalines in this period are slightly deeper in July. For example, the depth of 20°C isotherm is located at about 150 m in July compared with about 140 m in May. The bottom doming of the isothermal and isohaline structures between 5 and 10°S is maintained with slight changes in their gradients compared with that in May. The westward volume transport across the north of Madagascar peaks in June and July for about 52.3 Sv followed by relatively small volume transport of about 45 Sv in August and September (Figure 5.3).

In November, the transition period to the North East monsoon, the offshore transect indicates relatively weak cross-shore currents and salty warm surface waters with strong current speeds being confined to the subsurface waters (Figure 5.2c, g, k). The weakened cross-shore currents near the northern coast of Madagascar reflect the NEMC. The upper surface temperature ranges between 26 and 27°C in the upper 50 m depth, and the 27°C isotherms of surface waters are more confined to the south. The entire transect indicates high salinity that ranges between 34.8 and 35.1 ppt from the surface to 250 m. Similar to May and July, the deepening of the warm isotherms and fresh isohalines appear between 11 and 13°S suggesting that the westward NEMC plays a significant role in this process. This is possibly because the NEMC either carries warm salty waters towards the Tanzanian shelf or by interrupts the flow of upwelled waters onto the north of Madagascar shelf from the Seychelles-Chagos thermocline ridge that occurs throughout the year. The westward volume transport across the north of Madagascar is about 50 Sv in October and November (Figure 5.3).

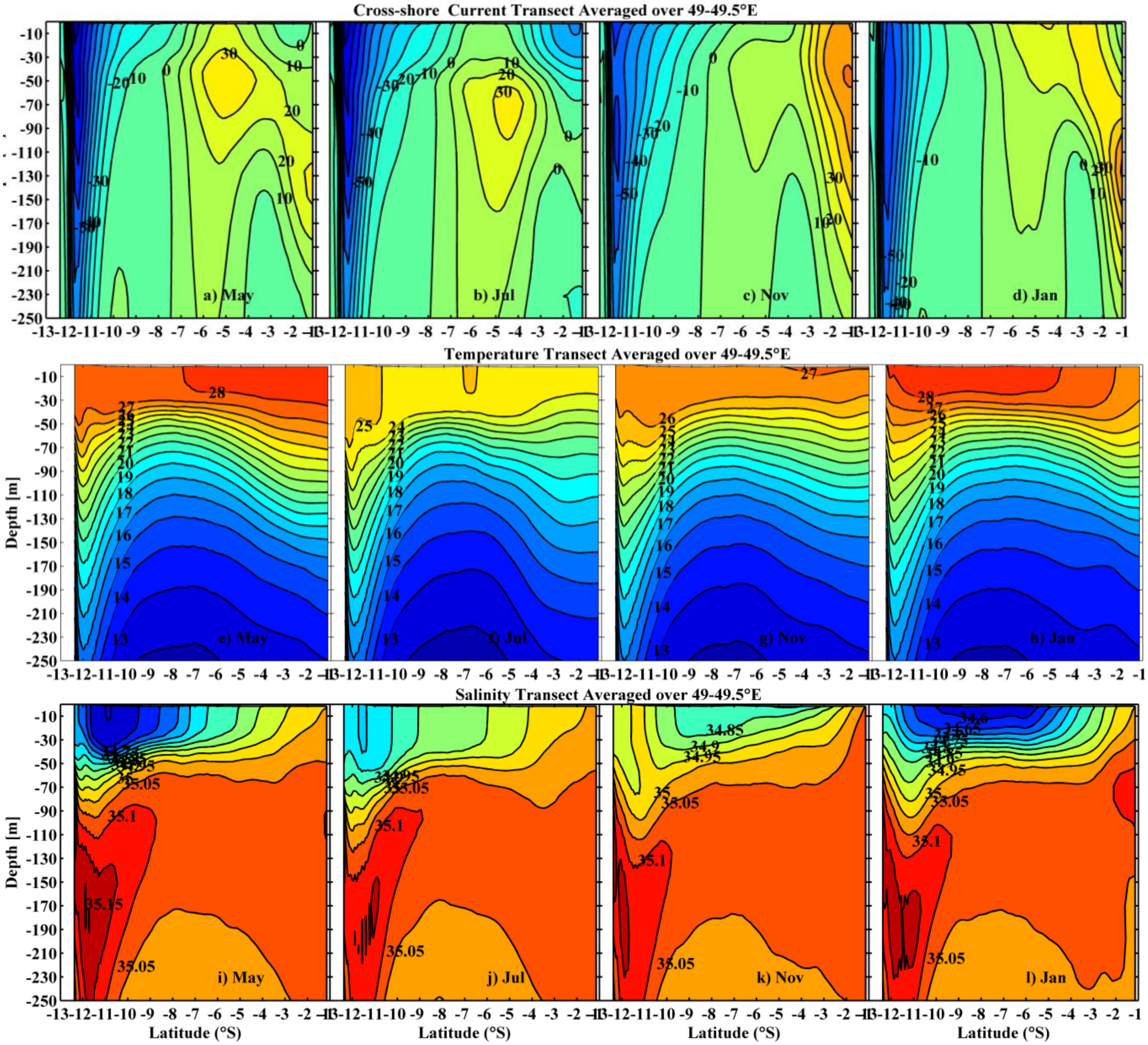

Figure 5.2: Vertical sections of (a, b, c, d) cross-shore current component in cm/s with 10 cm/s contour intervals, (e, f, g, h) temperature in ^{o}C with 1^{o}C contour intervals and (i, j, k, l) salinity in ppt with 0.05 ppt contour intervals averaged over 49-49.5^{o}E from 1^{o}S to 13^{o}S along L1+L5.

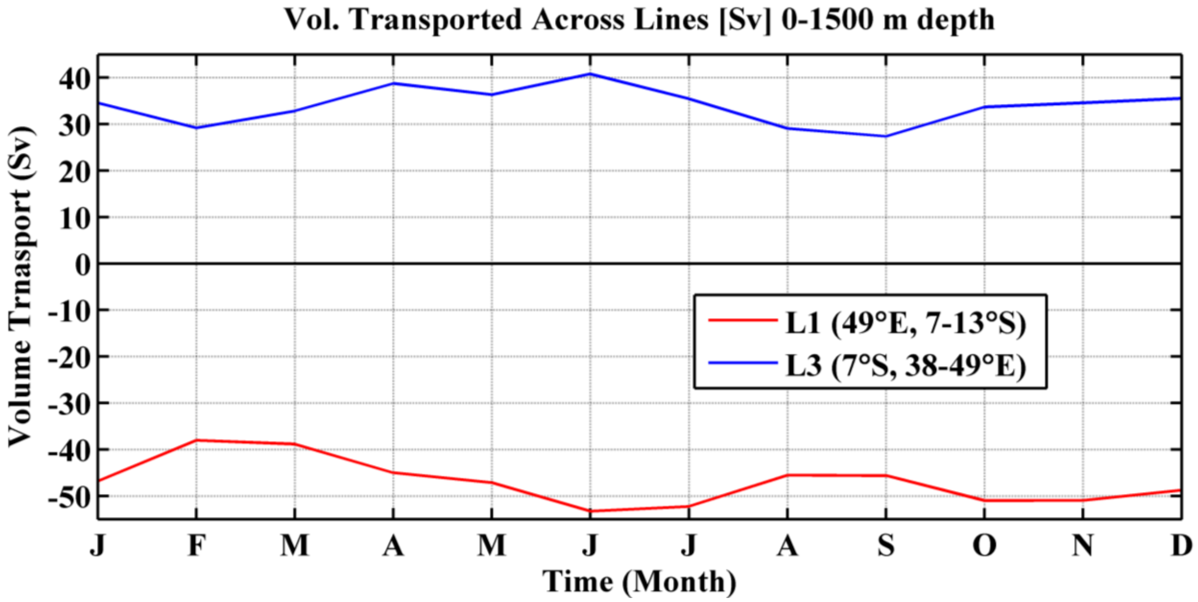

Figure 5.3: Climatology of the volume transport integrated between surface and 1500 m (Sv) acrosses lines L1 (49°E, 7-13°S) in red in the north of Madagascar and L3 (7°S, 38-49°E) in blue in the southern Tanzanian shelf region.

During January, when the North East monsoon is fully developed, the offshore transect shows relatively weak cross-shore currents and warm fresh waters at the middle of the transect (Figure 5.2d, h, l). The NEMC appears in the region between 11 and 13°S and dominates the westward cross-shore currents. The region is characterized by the upward displacement of the warm isotherms and salty isohalines towards the surface and to the northern coast of Madagascar. Such patterns can be associated with the westward NEMC by either carrying warm and salty waters or by interrupting the flow of water upwelled onto the north Madagascar shelf from the open ocean region. Warm temperatures of about 28°C and low salinity of about 34.7 ppt appear at the surface of this transect in the depth of 40 m in the middle of the transect. The warm temperature and relatively low salinity in the middle of the transect can be associated with the position of the ITCZ which is at 12°S by the end of December before it starts moving northwards in January. North of 8°S is dominated by the eastward cross-shore currents reflecting the SECC. The westward volume transport across the north of Madagascar decreases to the minimum value of about 38 Sv in February and March (Figure 5.3).

Generally, there is a relation between the NEMC patterns and the distributions of the temperature and salinity in the vertical structure in the Tanzanian shelf region. The cross-shore currents show a core of intense flow for the westward NEMC near the northern coast of Madagascar between 11^{o}S and 13^{o}S throughout the year. The effect of the NEMC on the temperature and salinity distributions in the transect is by interrupting the cold isotherms and salty isohalines in the region. Along with the wind stress and surface heat flux over this region, the patterns of the upper ocean circulation and properties suggest that the westward NEMC plays a strong role in the temperature and salinity distributions. The NEMC possibly carries warm surface waters toward the Tanzanian shelf region during November, January and May, and cold waters in July. Furthermore, the NEMC carries freshwater in May and July and salty waters in November to January as shown near the north coast of Madagascar. Next section presents the zonal transects for the alongshore currents, temperature and salinity across the coastal waters in the middle of the Tanzanian shelf region for comparison with that in the north of Madagascar.

5.2.2 Zonal Transect Averaged Over 7-7.5^{o}S from 38^{o}E to 49^{o}E (L3)

Strong upper ocean currents that influence the temperature and salinity distribution occur in the middle of the Tanzanian shelf waters (Figure 5.4). The transect averaged between 7 and 7.5^{o}S from the coast of Tanzania at 38^{o}E to offshore at 49^{o}E indicates strong northward ocean currents with some seasonal variation. The strong northward along-shore current speeds are confined to the Tanzanian coast and reflect the northward flowing EACC. The seasonal variation of the EACC in the Tanzanian shelf region matches with variations in temperature and salinity in the upper 50 m and weaker changes occur below this depth.

The transect presents that the northward flowing EACC influence the upper ocean temperature and salinity during May (Figure 5.4a, e, i) and July (Figure 5.4b, f, j). In May, the surface waters in the upper 50 m are warmer than 27^{o}C and fresher than 34.6 ppt, with isotherms and isohalines being displaced vertically upward near the Tanzanian coast. This is indicative of the equatorward flowing EACC which possibly influences the vertical temperature and salinity distributions by interrupting the weak downwelling flow of waters near the coast. During April and May, the volume transport across L3 ranges between 36 and 38 Sv (Figure 5.3). In July, the 25^{o}C isotherm and 34.8 ppt isohaline appear to be displaced vertically upward offshore and deepened near the coast in the upper 50 m. Such patterns suggest that the broadened northward flowing EACC carries the cool and relatively high salinity waters northwards. Moreover, the EACC probably interrupts the strong mixing and downwelling along the coast in this period. This is due to the presence of the strongest and steadiest southerly to southwesterly winds over the region. As a result, the winds can cause considerable downwelling along the Tanzanian shelf region and enhance both wind-induced evaporative cooling and vertical mixing leading to cool surface waters. The volume transported across L3 peaks in July to about 40 Sv followed by relatively small volume transport of about 28-30 Sv in August and September (Figure 5.3).

The middle transect of the Tanzanian shelf waters shows relatively weak ocean currents which influence the warm and salty waters near the coast during November (Figure 5.4c, g, k) and January (Figure 5.4d, h, l). In these months, the EACC is fairly weak with the strongest values being confined to the subsurface (Figure 5.4c and d). In November, the surface waters have constant temperature, whereas the isohalines of about 34.8-35.0 ppt are vertically displaced towards the surface and coast. The surface temperature appears to be about 26^{o}C within the upper 50 m. This period is characterized by weak winds that reduce the wind-induced evaporative heat losses and vertical mixing resulting in the warm surface temperature of about 26^{o}C and salty waters of about 35.0 ppt. Furthermore, moderate volume transport of about 35 Sv across L3 during October and November (Figure 5.3). In January, the EACC is weakened, especially at the surface with strong speeds located in the subsurface waters. The vertical temperature and salinity distributions show warm and fresh surface waters with near horizontal isotherms and isohalines, except near the coast where they are vertically displaced upward. The warmer waters of about 28^{o}C isotherm appear at the surface, being vertically displaced upward over the shelf near the coast. Moreover, the warmer waters are displaced upward from about 100 m depth being associated with weak upwelling of warm waters due to the northerly/northeasterly wind component along the coast of Tanzania. The effects of upwelling along the Tanzanian shelf waters are more apparent in the vertical structure of salinity than in temperature in January. This is shown by the salty waters (about 34.9 ppt) being vertically displaced upward towards the shelf and surface near the coast from 50 m depth in November and January. The northward volume transport across the middle of the Tanzanian shelf region decreases to the minimum value of about 30-33 Sv in February and March (Figure 5.3).

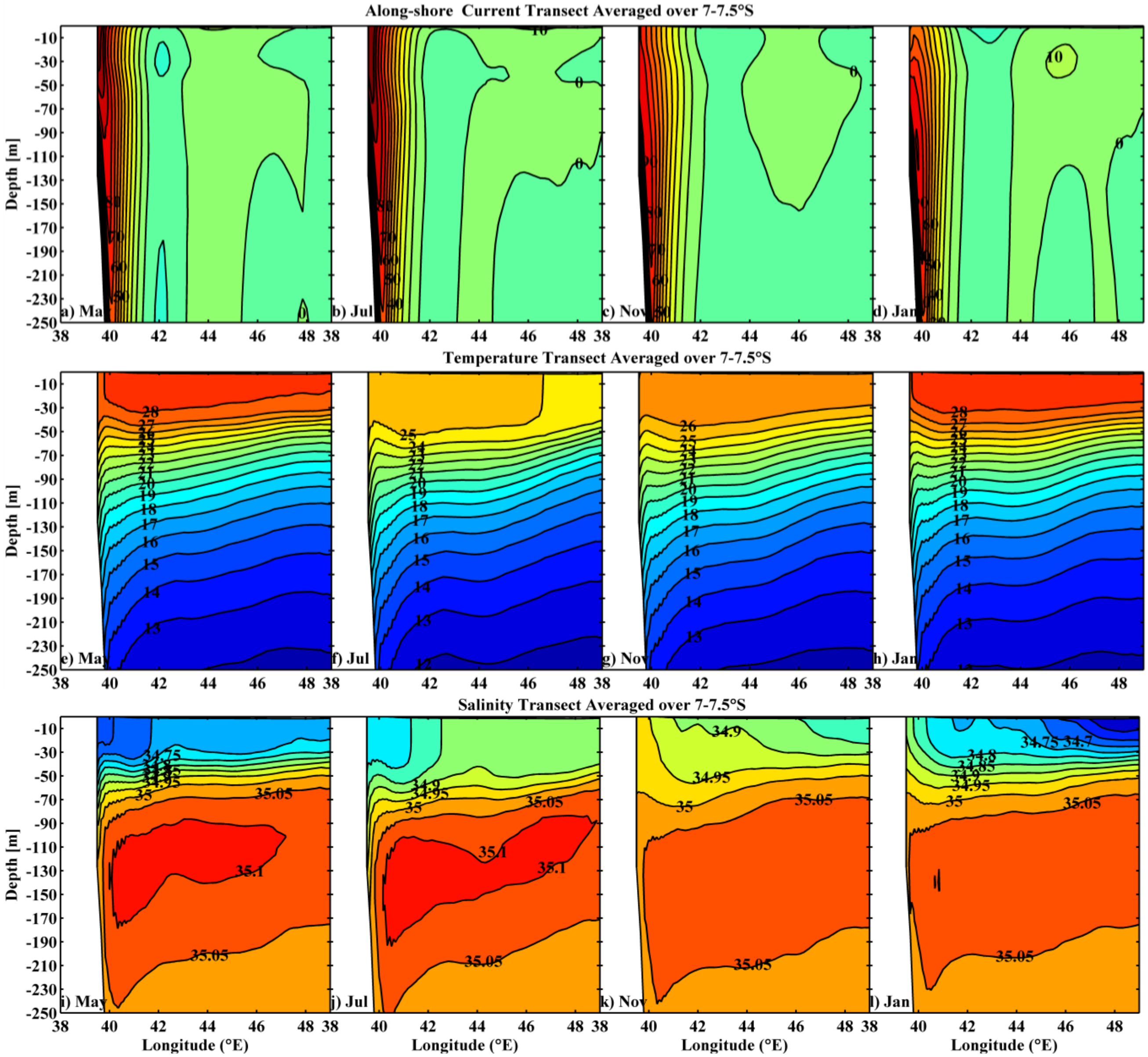

Figure 5.4: Vertical sections of (a, b, c, d) alongshore current component in cm/s with 10 cm/s contour intervals, (e, f, g, h) temperature in ^{o}C with 1^{o}C contour interval and (i, j, k, l) salinity in ppt with 0.05 ppt contour intervals averaged over 7-7.5^{o}S from 38 to 49^{o}E along L3.

Below 50 m depth, the vertical structure of the temperature and salinity in the transect shows the horizontal isotherms and isohalines which are deepened towards the Tanzanian coast (Figure 5.4). The isotherms below 50 m depth are uplifted near the coast (between 11 and 13^{o}S) matching with the strong equatorward EACC. Such pattern indicates that the equatorward EACC influences the SST distribution over this region throughout the year.

Generally, it is observed that the surface waters are warmer during the transition periods and in the North East monsoon (October through May) with an average of surface temperature warmer than 27^{o}C in May, November and January. In contrast, during the South West monsoon (June to September), surface temperatures are cooler with an average surface temperature of about 25^{o}C in January. The vertical salinity distribution shows relatively low values (34.5-34.7 ppt) in January and May and relatively high salinity (34.8-34.9 ppt) in July and November. Common to all months are the isothermal ridges near the coast which are deepened further near the coast. The EACC is in phase with the NEMC throughout the year with the volume transport that peak in June through July. Both currents show significant correlation of about 0.7 above the 95% level when the NEMC lags behind the EACC by two months. The EACC in the Tanzanian shelf region carries warm surface waters northwards during May, November and January, and cold waters in July as the NEMC. Furthermore, the EACC respectively carries the lowest and highest surface salinity waters northwards as the NEMC near the north coast of Madagascar in May and November.

5.3 Summary

The relationship between the upper ocean circulation and properties in the Tanzanian shelf region and offshore has been studied for both the annual mean and for each monsoonal season. The region between the southern Tanzanian shelf region and north of Madagascar indicates weak downwelling and the strong westward flowing NEMC in the mean state. The warming effect of the horizontal advection from the NEMC, in conjunction with the deep thermocline and shallow mixed layer matches with warm SST and relative high salinity. On the annual average in the northern Tanzanian shelf region and offshore, there is upwelling and weak cooling in the mixed layer from the horizontal advection. Furthermore, the region is characterized by relatively weak surface currents which match with relatively high sea surface temperature and low salinity. The influence of the NEMC on the temperature and salinity are evident in the strong downward orientated along the path of the westward flowing NEMC. The EACC also impacts the temperature and salinity by advection or by interrupting the vertically transported waters. This knowledge of the mean and seasonal distributions of the upper ocean circulation and properties improves our understanding of their relationship in the region. The next chapter, therefore, deals with the interannual variability in the region.

Chapter 6

Interannual Variability of Sea Surface Temperature

6.0 Introduction

This chapter focuses on interannual variability of the SST between the Tanzanian shelf waters and offshore, and the possible mechanisms and relationships of the variability from 1980 to 2007. The chapter attempts to address the following questions:

How large is the interannual variability of the sea surface temperature in the tropical western Indian Ocean compared to the annual cycle? What drives this inter-annual variability?

i. How large are the seasonal variations in the tropical western Indian Ocean compared with the interannual variations?
ii. Does the SST variability in the Tanzanian shelf waters differ from offshore?
iii. Does the Northeast Madagascar Current (NEMC) contribute to the SST variability in coastal waters in the Tanzanian shelf region?
iv. How sensitive is the SST interannual variability to the local surface heat fluxes and to lateral remote influences?

This chapter begins with analysis of the spatial and temporal patterns of the interannual SST variations in the region (section 6.1). It is followed by determination of the spatial patterns of the leading modes of the SST in the entire domain, and their linkage to the global large-scale modes of climate variability. Section 6.3 deals with sensitivity experiments of the interannual SST variability in the region. The last section (section 6.4) of this chapter summarizes the main results.

6.1 The Spatial Patterns and Temporal Variations

6.1.1 The Spatial Patterns Analysis

Figure 6.1 displays the spatial variance of the SST over the tropical western Indian Ocean for the ROMS model and AVHRR for 25 years (1982-2007). The period is chosen for the common temporal coverage comparisons due to the fact that AVHRR SST temporal coverage is available from 1982 to now whereas, the ROMS model data are from 1980 to 2007. The seasonality in the region tends to explain most of the regional SST variability (explained variance >80%) except near the equator, particularly over the east of the domain where the explained variance is <50% (Figure 6.1). This suggests higher interannual variability relatively to seasonal cycle in the SST near the equator than the rest of the domain.

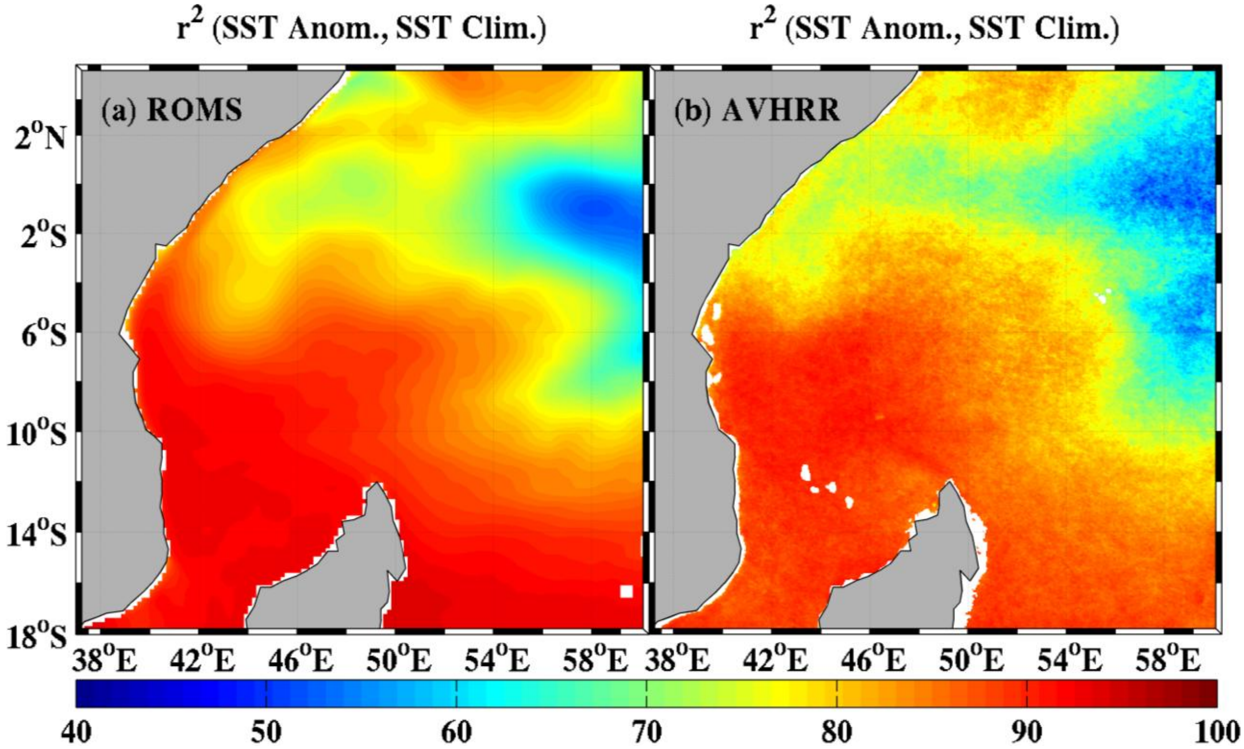

Figure 6.1: Variance (%) of monthly SST anomalies explained by the monthly climatology extracted from (a) the ROMS model and (b) AVHRR from 1982 to 2007.

Figure 6.2 shows the standard deviation and variance of the monthly SST anomalies in the Tanzanian shelf waters and the open ocean for the ROMS model and AVHRR data for 25 years (1982-2007). The smallest interannual SST variations are restricted along the coast up to 2°S and occur to the south of the domain in both ROMS (standard deviation less than 0.4°C) and AVHRR (standard deviation around 0.5-0.6°C). Thus, coastal variance is lower for ROMS and shows more spatial coherence than for AVHRR. Along with the differences in spatial and temporal resolution, this could be related to the local surface forcing as well as to coastal instability processes which are not resolved by the model. The weakest variability in the Tanzanian shelf region links to that near Madagascar, marking the NEMC and the northward flowing EACC. The highest interannual variations of the SST in the region (standard deviation greater than 0.8°C) are located offshore to the north of 6°S and are tilted to the northeast. Similar spatial patterns and magnitude in the interannual SST variations in the tropical western Indian Ocean also appear in the TMI dataset (not shown). Such spatial patterns and magnitude in the monthly SST anomalies justify the analysis of the difference of the interannual SST variability between the Tanzanian shelf waters and those in the open ocean (offshore) in the tropical western Indian Ocean. To investigate the origin of the interannual SST variability in the Tanzanian shelf region and in the open ocean, time series (Figure 6.3) of the spatially-averaged monthly SST anomalies were extracted for 40-42°E, 8-10°S (box A) and 48-50°E, 0-2°S (box B) as shown in Figures 6.2a and b, respectively.

To check the origin of the weakest interannual variations of the SST in the Tanzanian shelf region, shared variance is established between the waters in the Tanzanian shelf and those in the rest of the domain. The shared variance of the coastal waters off Tanzania for box A with the rest of the tropical western Indian Ocean is presented in Figure 6.2c and d for the ROMS model and AVHRR data, respectively. Although the broad patterns are similar, there are a few differences in the maps between ROMS and AVHRR. In general, there is more fine-scale structure in the AVHRR map which may result from its 4km horizontal resolution (see ftp://ftp.nodc.noaa.gov) which is substantially higher than the roughly 16 km or 1/6° horizontal resolution of the ROMS simulation. In both maps, the interannual SST variability in the Tanzanian shelf region appears to be shared with that to the north of Madagascar. The shared variance is evident on the path of the Northeast Madagascar Current (NEMC) and the East African Coastal Current (EACC). This

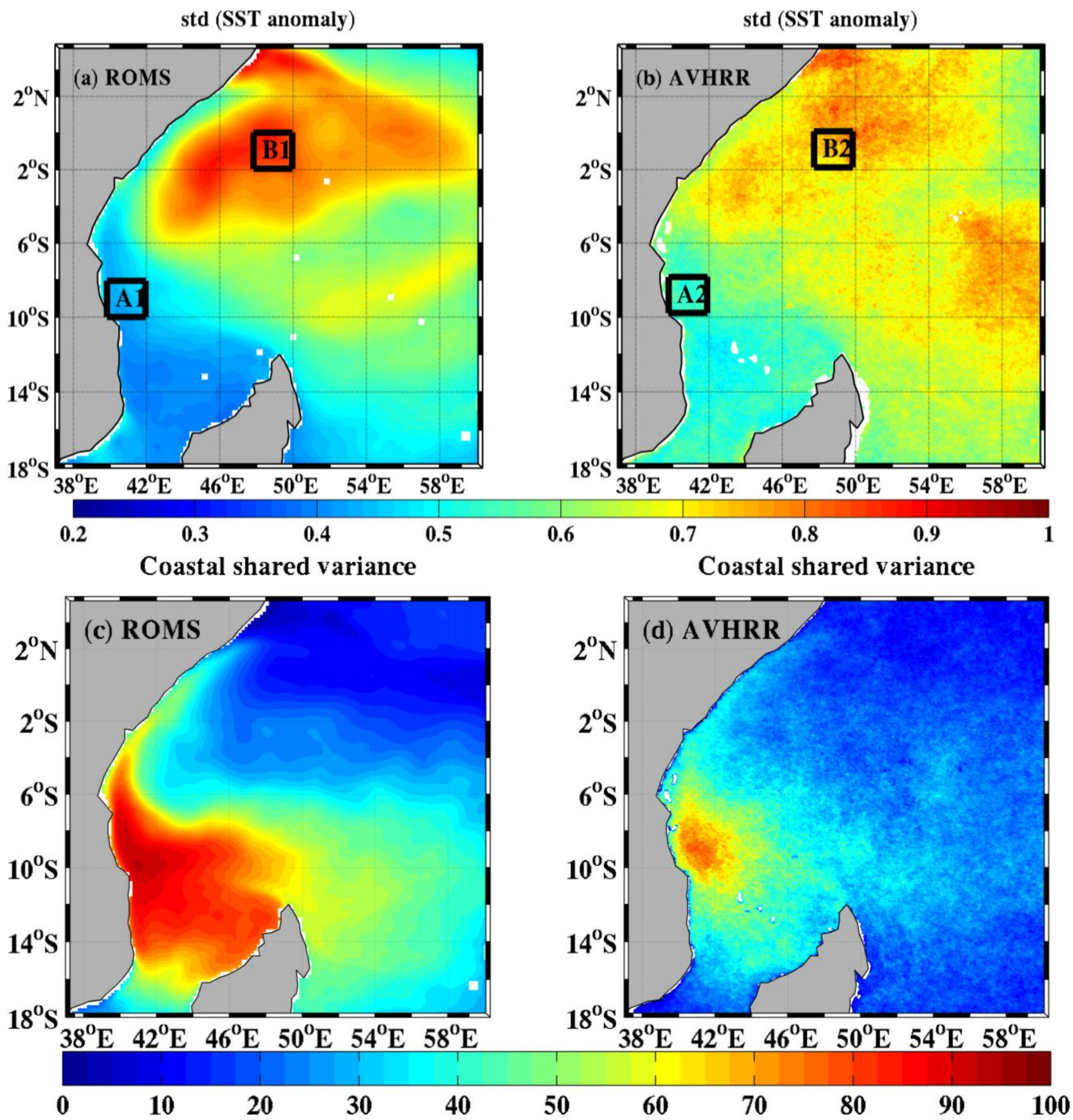

Figure 6.2: Standard deviation of the monthly SST anomalies (top panel, a and b). Boxes A1 and A2 represent coastal waters in the Tanzanian shelf region (40-45°E, 8-11°S) and B1 and B2 represent further offshore (48-54°E, 1°N-2°S). Variance (%) of the monthly SST anomalies in the entire domain shared with the monthly SST anomalies averaged over coastal ocean indicated by A1 and A2 black boxes (Figure 6.2c-d).

suggests that local SST anomalies could be advected by the mean flow from the NEMC, north of Madagascar, towards the Tanzanian waters. On the other hand, the interannual variability in the Tanzania shelf waters indicates no obvious link with that in the open ocean, especially to the north of 8^{o}S. Such difference leads to further analyses of the interannual SST variability in the Tanzanian shelf region and offshore using time series and wavelet analysis. These analyses assess the differences in time and frequency-time space of the SST variability between the Tanzanian shelf waters and the open ocean, respectively.

6.1.2 Time Series and Wavelet Analysis

The time series of the interannual SST variations in the Tanzanian shelf waters and offshore from the model and AVHRR are displayed together with the Niño3.4 index and the DMI in Figure 6.3. The analysis of the variability of these time series is performed by filtering the monthly anomalies of the SST and indices with a seven months running mean to remove high frequency variability. ROMS and AVHRR coastal time series show a reasonably good correspondence for the long term signals while there are more differences for the higher frequencies. Such difference as that in the SST amplitude mentioned in Figure 6.2 could be related to the local surface forcing as well as to coastal instability processes which are not resolved by the model. This could be tested using other surface forcing, which is beyond the scope of this paper as it is focusing at the interannual variability, and the difference seems mostly at higher frequencies.

Warm SST anomalies greater than 0.5^{o}C in the model and AVHRR data occur for both the coastal and offshore region during 1982/1983, 1987/1988, 1997/1998. These periods match with the positive anomalies in the DMI and the Niño3.4 index (Figure 6.3), consistent with these being El Niño and positive IOD years. In addition to the warm years above, only the offshore region indicates warm model SST anomalies greater than 0.5^{o}C in 1980, 1991 and 2002/2003. The positive anomalies in 1980 and 2002/2003 occur together with negative and positive

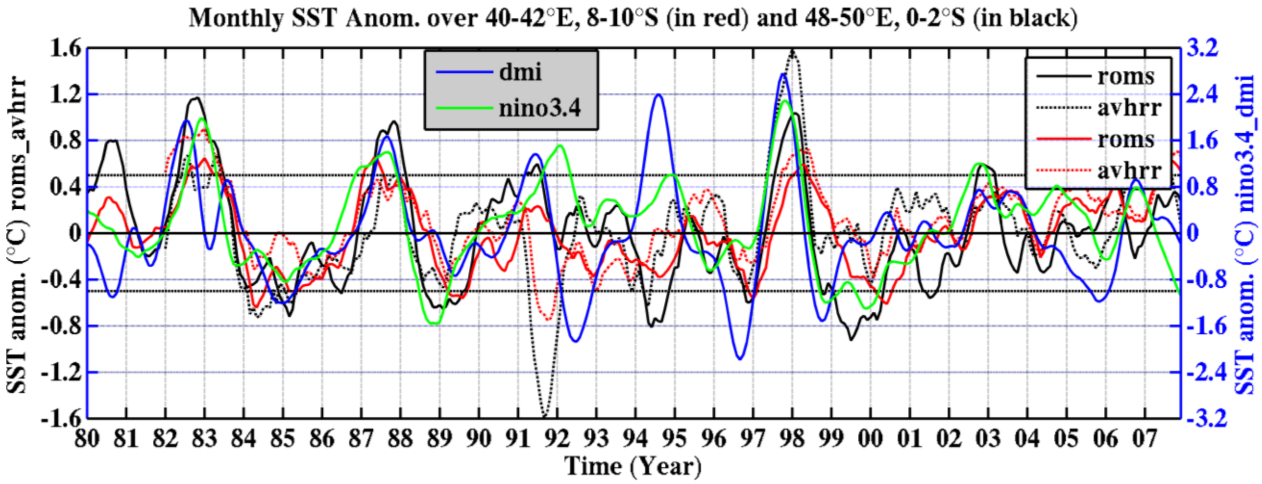

Figure 6.3: Time series of the box-averaged monthly SST anomalies at near-shore ocean (in red, box A) and open ocean (in black, box B) filtered with a seven months running mean filter to remove any seasonal high frequency variability. The solid line is for the ROMS model and the dotted line is for the AVHRR SST data. The DMI (in blue) and Niño3.4 index (in green) are added to the time series.

anomalies in the both large scale indices, respectively. Thus, the warming in 1980 does not relate to both large scale indices as it is out of phase, whereas the warming in 2002/2003 may relate to the large scale indices as it is in phase with them. The model shows a large discrepancy in 1991 when the positive anomalies in the model SST, the DMI and the Niño3.4 index in both the shelf waters and offshore occur at the same time as negative AVHRR SST anomalies. Moreover, in 1994 there was a greater positive anomaly in the DMI than in other indices. The 1991 and 1994 years are suggested by Tozuka et al. (2010) to be pure positive IOD and El Niño, respectively. In short, the Tanzanian shelf region and the open ocean in the tropical western Indian Ocean show commonality in the strong warm years (>0.5^{o}C) in 1982/1983, 1987/1988, and 1997/1998.

Strong SST cool anomalies (<-0.5^{o}C) occur in 1984/1985, 1988/1989, 1996 and 1999/2000 in both the coastal and offshore regions. Although these negative anomalies match with the negative anomalies of the DMI and the Niño3.4 index, the 1996 event is most strongly evident in the DMI. The 1992 and 1996 years were suggested to be pure negative IOD events (Tozuka et al., 2010). However, the 1996 year seems to be La Niña as there are at least five conservative over-lapping seasons with SST <-0.5^{o}C from August-October 1995 to February-March, 1996 (www.cpc.ncep.noaa.gov). The cold anomalies in 1984/1985, 1988/1989 and 1999/2000 are consistent with La Niña and negative IOD years. In addition to the cold years above, only the offshore region indicates cold model SST anomalies greater than 0.5^{o}C in 1994 and 2001. The negative anomalies in 1994 appear also in the AVHRR data, and correspond with the positive anomalies greater than 0.5^{o}C in the DMI and the Niño3.4 index. However, the negative anomalies in 2001 are not captured in AVHRR; instead, there are positive anomalies with weak anomalies from the large scale indices. In short, the Tanzanian coastal waters and the offshore region show commonality in the strong cold years (<-0.5^{o}C) in 1984/1985, 1988/1989, 1996, and 1999/2000.

Wavelet analysis was performed on the time-series of the coastal and offshore SST boxes in the tropical western Indian Ocean for the model and AVHRR (Figure 6.4). Signals near a 64 month period appear in the coastal waters from 1982 to 1992 and 1997 to 1999 in the model SST. Similar signals also occur in the open ocean from 1984 to 1990 in the model SST. In the open ocean, a 32 month signal is also significant, whereas, in the coastal waters, only signals near 64 month period are significant. The difference in interannual variations between the Tanzanian shelf region and offshore suggests either different forcing mechanisms or else the same forcing mechanisms over the regions but where the SST in the two regions is modified differently by the same mechanisms.

In the Tanzanian shelf region, interannual variations of the mixed layer temperature tendency significantly correlate with only the local surface heat fluxes (r=~0.38) at the 95% significant level, and is driven mainly by anomalous shortwave radiation (Figure 6.5a and b). In the shelf region, anomalies of shortwave radiation and latent heat fluxes are out phase (Figure 6.5b). This implies that enhanced latent heat loss (negative latent heat anomalies) occurs at the same time as positive anomalies of shortwave radiation (like in 1987/1988, 1997/1998, 2003 and 2005), whereas the reduced latent heat loss (positive latent heat anomalies) relates to negative anomalies of shortwave radiation (such as in 1984/1985, 1988/1989 and 1994-1996). The positive anomalies of the shortwave radiation over the Tanzanian shelf region can be associated with strong winds over the shelf and to the north of Madagascar which carry away moisture and cloud during warm years, leaving the region in mainly clear sky conditions. The opposite occurs during cold years in the Tanzanian shelf region. Figure 6.6a shows anomalies of the mixed layer

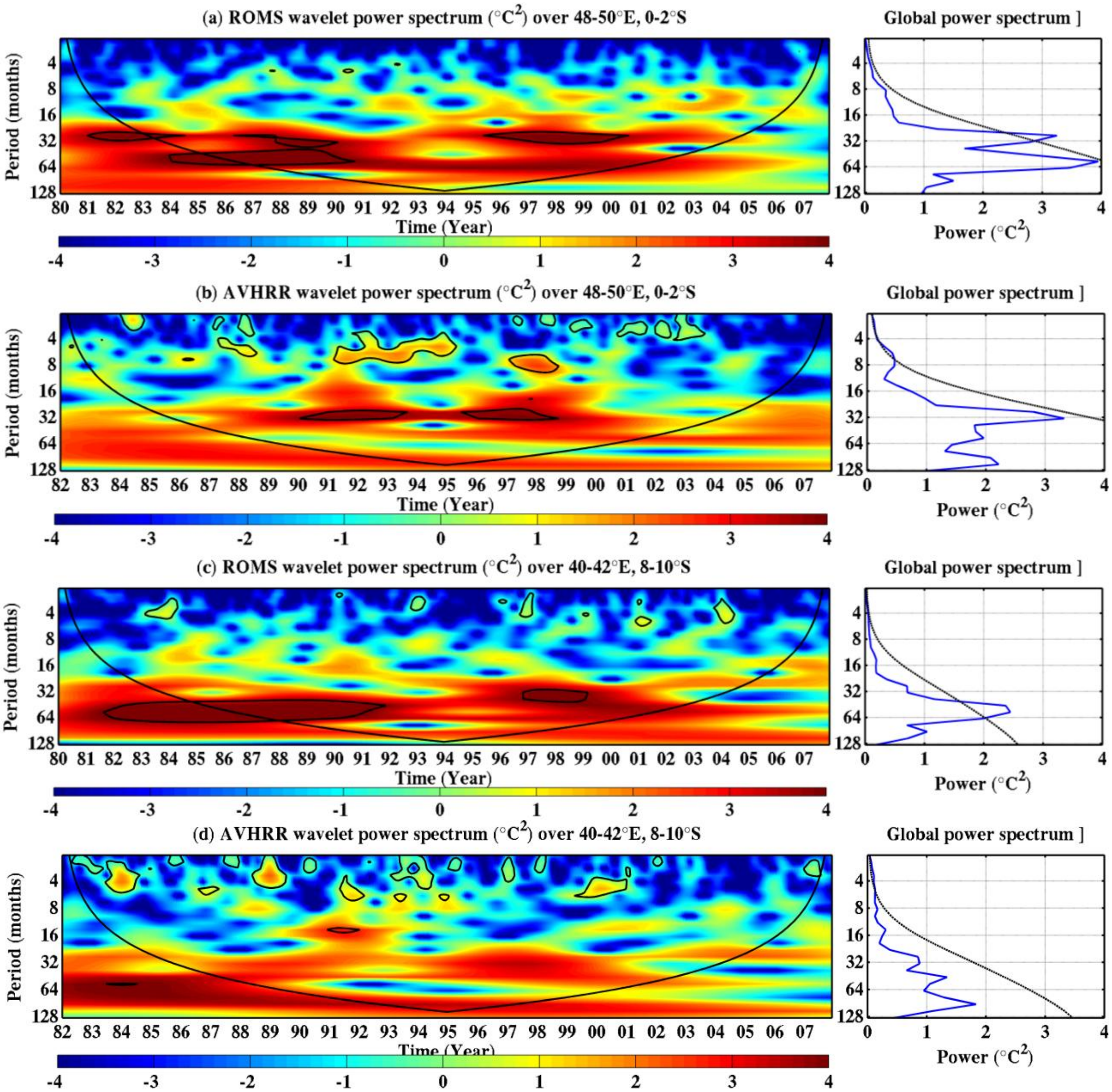

Figure 6.4: Wavelet power spectrum and power of the wavelet analysis of the box-averaged monthly SST anomalies in the open ocean (box A) from (a) the model and (b) AVHRR and in the coastal waters in the Tanzanian shelf region (box B) from (c) the model and (d) AVHRR. The cone of influence (COI) is indicated by the thin black line, and the thick black contours indicate the 95% significance levels. Significance in the global wavelet spectrum is indicated by the black dashed line.

temperature tendency which are negatively related to anomalies of the mixed layer depths (r=~-0.29) and wind stress (r=~-0.33) at the 95% significant level with a small contribution of the wind stress curl (Figure 6.7). The local SST anomalies are then advected by the mean flow Northeast Madagascar Current (NEMC) as implied by Figure 6.2.

The deepened and elevated thermocline depths occur during strong warm and cool events in the offshore region, respectively (Figure 6.5c-d). A significant correlation (r=-0.38 at the 95% significant level) of the interannual variations of the mixed layer temperature tendency with the thermocline depths occurs in this region. The deepest thermocline depth (~35 m) occurs in 1997/1998, the year with the greatest positive SST anomalies in the region. Furthermore, strong negative anomalies of wind stress and mixed layer occur in the offshore region (Figure 6.6b) which results in negative wind stress curl (Figure 6.7) during 1997/1998. Thus, Ekman pumping from local wind stress curl partly drives vertical transport in the offshore region which then causes variations of thermocline depths.

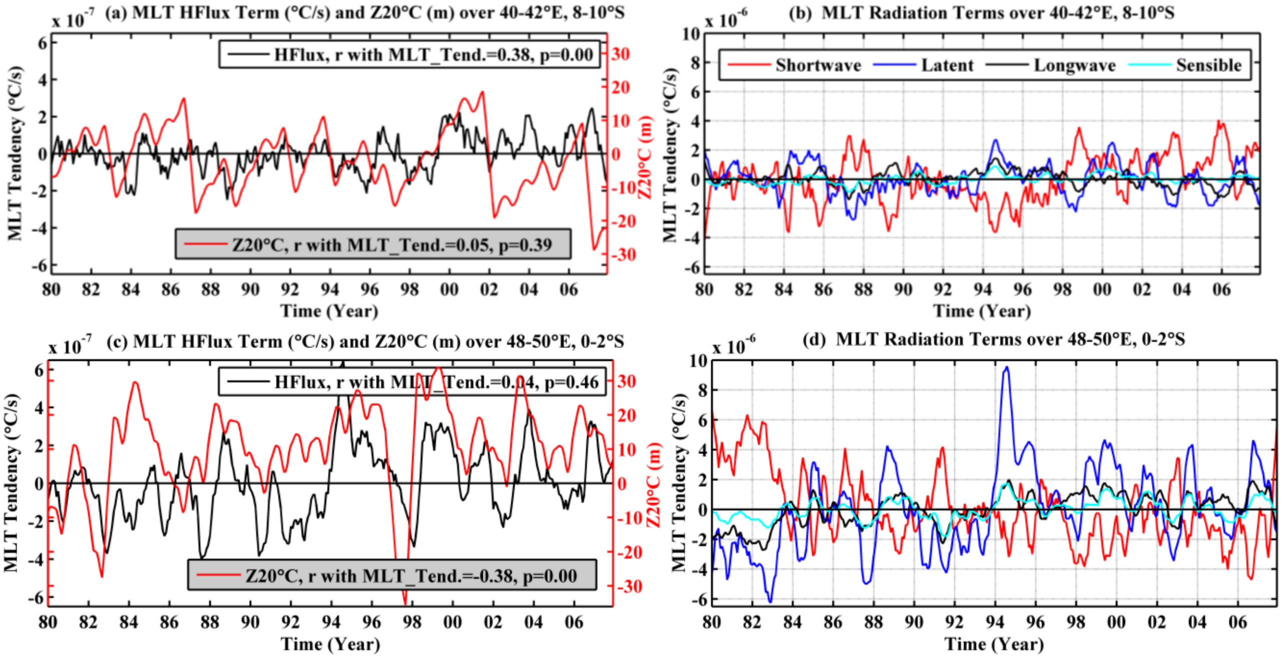

Figure 6.5: Time-series of anomalies for the mixed-layer temperature tendency and thermocline depth over the inshore box A (a and c) and offshore box B (b and d) from the ROMS model (smoothed by seven months running mean). Positive and negative anomalies indicate lifted up and deepened thermocline depth, respectively.

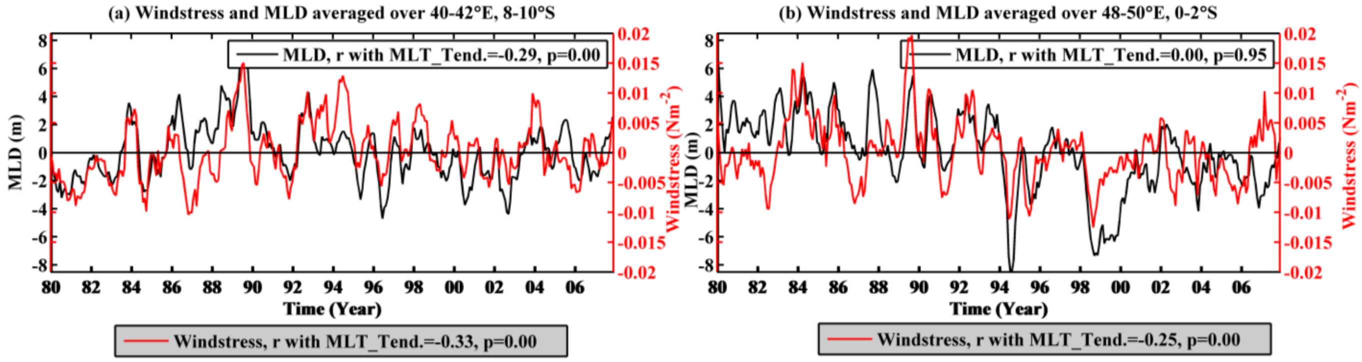

Figure 6.6: Time-series of anomalies for the mixed layer depths and wind stress over the inshore box A (a) and offshore box B (b) from the ROMS model (smoothed by seven months running mean).

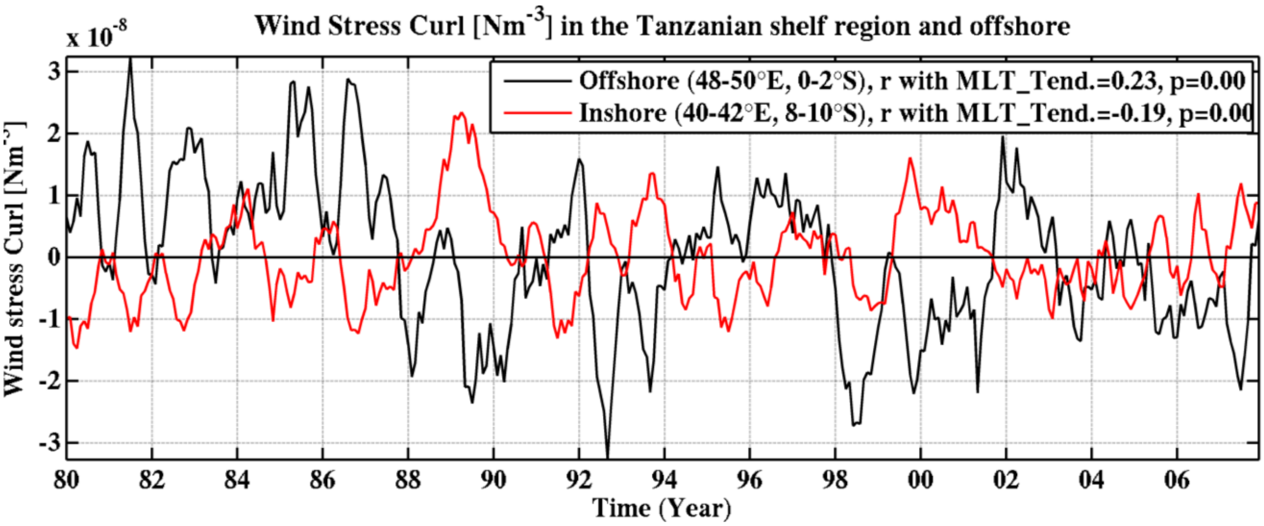

Figure 6.7: Time-series of anomalies for wind stress curl over the Tanzanian shelf region (40-42^{o}E, 8-10^{o}S) in black and in the offshore region (48-50^{o}E, 0-2^{o}S) in red from the ROMS model (smoothed by seven months running mean).

To further investigate the variability of the SST and mechanisms responsible for the SST variability, Empirical Orthogonal Function (EOF) analysis is applied in the next section. Such analysis determines the spatial patterns of the leading modes of the SST in the entire domain and their linkage to the global large-scale modes of climate variability as shown below.

6.2 The Leading SST Modes and their Linkage to Large-scale Climate Variability Modes

An Empirical Orthogonal Function (EOF) analysis is used for the identification of the leading modes of spatial and temporal interannual variability of the SST in the tropical western Indian Ocean. It is performed on the monthly SST anomalies over the study domain for the ROMS model and AVHRR (Figure 6.8). The first two leading modes which explain about 61% of the total variance are retained.

The first mode explains about 48% of the total variance with a near homogeneous spatial pattern (Figure 6.8a). Strong spatial loading patterns occur between 2^{o}N and 6^{o}S, the region with strong standard deviation in the open ocean. The first principal component time-series (PC1) of the SST EOF significantly correlates with the Niño3.4 index and DMI with the values of 0.54 and 0.35 at 95% significant levels, respectively. Similar patterns are shown in the first EOF of the AVHRR SST data explaining about 40% of the total variance (Figure 6.8b). Such difference in the total explained variance could be explained by the differences in spatial and temporal resolutions between the model and AVHRR data. The first spatial pattern mode and its principal component time series may also be related to the ENSO and the IOD signals. The principal component time series of the first EOF for ROMS and AVHRR are significantly correlated with r=~0.73 at 95% significant levels.

The second mode explains about 13% of the total variance with a north-south oriented dipole spatial pattern (Figure 6.8c). The same spatial structure is displayed in the second SST EOF of the AVHRR, and it explains about 8% of the total variance. The first two leading modes of the EOF SST in AVHRR data collectively explain about 48% of the total variance. The principal component time series of second EOF for ROMS and AVHRR are significantly correlated with r=~0.64 at 95% significant levels. The second principal component time series (PC2) in the model is not correlated with either the ENSO or the IOD. It shows a strong warming signal in the

Tanzanian shelf region and cooling in the offshore region in 1987.The former region shows deepened thermocline as a dominant forcing as shown in Figure 6.5c.

Figure 6.9a-b shows that signals near 64 months (5.3 years) and 32 months (2.7 years) are significant in the model PC1. The 64 months signal can be seen in the AVHRR PC1, but it is mostly outside the cone of influence (Figure 6.9b). The difference could be associated with the finer temporal and spatial resolution of the AVHRR data. Figure 6.9c-d indicates that the PC2 presents a dominant signal around the 32 months period for both ROMS and AVHRR. The periods of 5.3 and 2.7 years reflect interannual variability of the ENSO or the IOD, the prominent modes in the tropical Indian Ocean. Figure 6.10a & b suggest that there was strong propagation via Rossby waves of positive anomalies of the SST and SSH from the east which influence the coastal waters particularly from 1987 to 1988, 1997 to 1998 and 2002 to 2003. The strongest propagation of the positive SST and SSH occurs in 1997/1998. Strong propagation of positive anomalies of the SST and SSH from the east with slightly influence on the coastal waters appear from 1997 to 1998, indicating influences of Rossby wave propagation (Figure 6.10a & b). During the 1997-1998 event, local Ekman pumping partly plays a role in the thermocline anomaly as suggested by Tozuka et al. (2010) in addition to Rossby waves. Further Rossby wave influences appear through the westward propagation of the positive anomalies of the SST and SSH through the offshore region in 1982/1983 and 1997/1998 (Figure 6.10c & d). Thus, the 1997/1998 period shows one of the stronger Rossby wave signals and local Ekman pumping during the studied period. These waves are generated by wind anomalies in the eastern Indian Ocean during ENSO and IOD events.

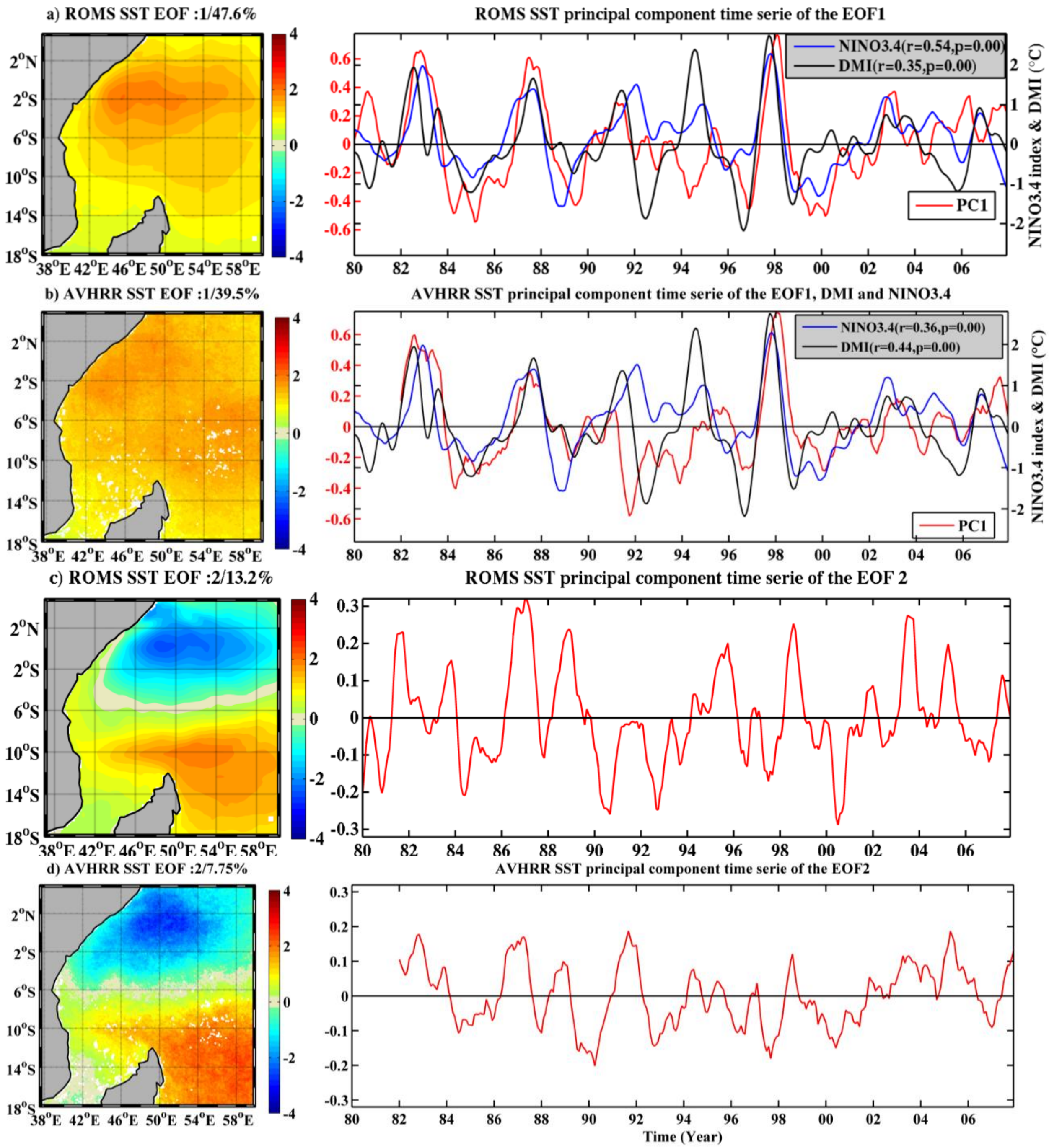

Figure 6.8: The first two EOF modes (°C) for EXP_REF in the tropical western Indian Ocean and their corresponding principal component time series (in red). DMI (in black) and Niño3.4 index (in blue) are added (smoothed by a seven month running mean); (a) ROMS 1st EOF, (b) AVHRR 1st EOF (c) ROMS 2nd EOF and (d) AVHRR 2nd EOF.

a) ROMS wavelet power spectrum ($^{\circ}C^2$) for PC01

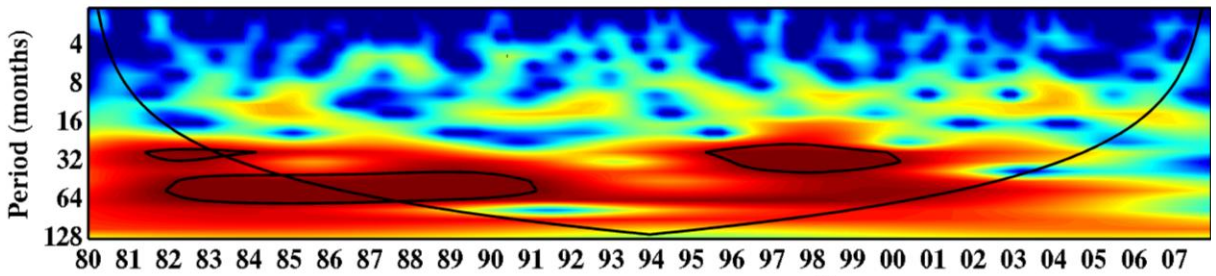

b) AVHRR wavelet power spectrum ($^{\circ}C^2$) for PC01

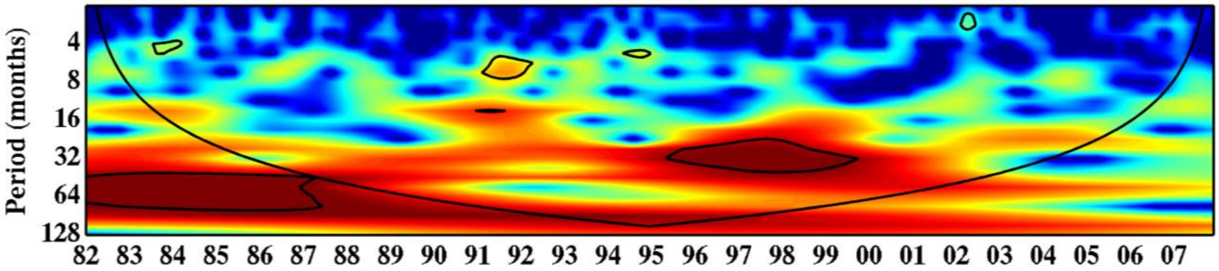

(c) ROMS wavelet power spectrum ($^{\circ}C^2$) for PC02

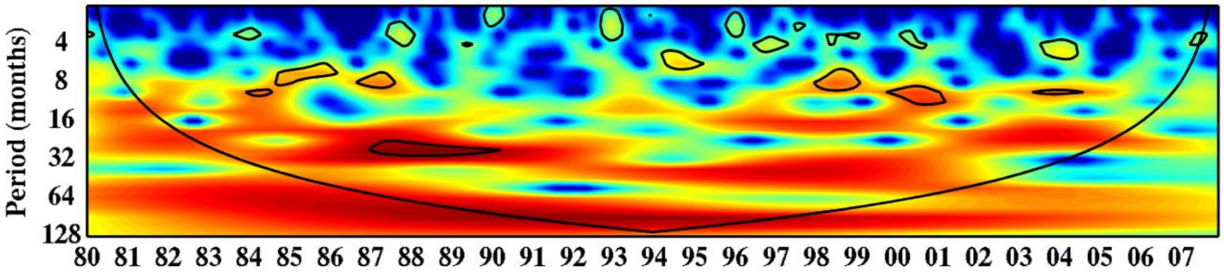

d) AVHRR wavelet power spectrum ($^{\circ}C^2$) for PC02

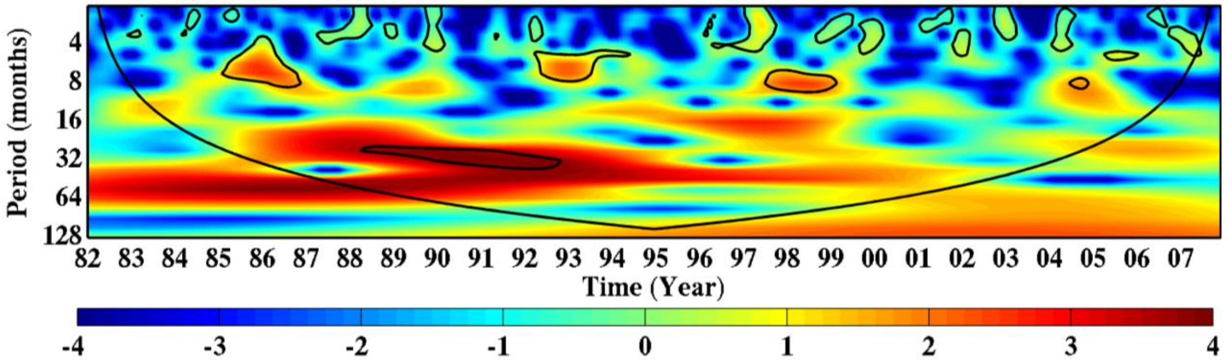

Figure 6.9: Wavelet power spectrum of the wavelet analysis of the SST PC01 from (a) the model and (b) AVHRR and PC02 from (c) the model and (d) AVHRR. The cone of influence (COI) is indicated by the thin black line, and the thick black contours indicate 95% significance levels.

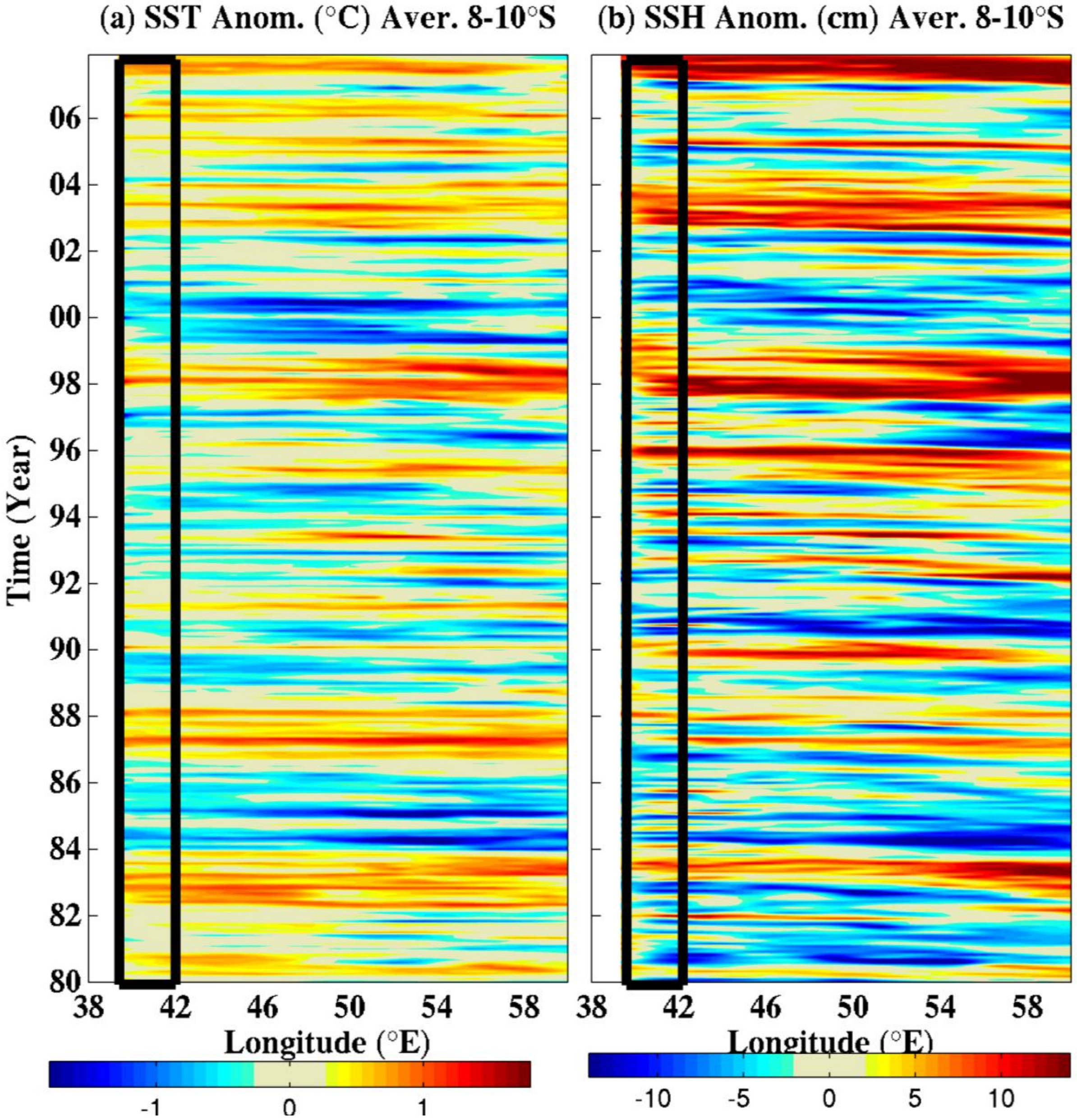

Figure 6.10 (a-b): Hovmöller plots for REF_EXP in the tropical western Indian Ocean from the coast 38°E to 60°E for monthly anomalies averaged over 8–10°S of (a) SST and (b) SSH. The black rectangle shows the coastal location A.

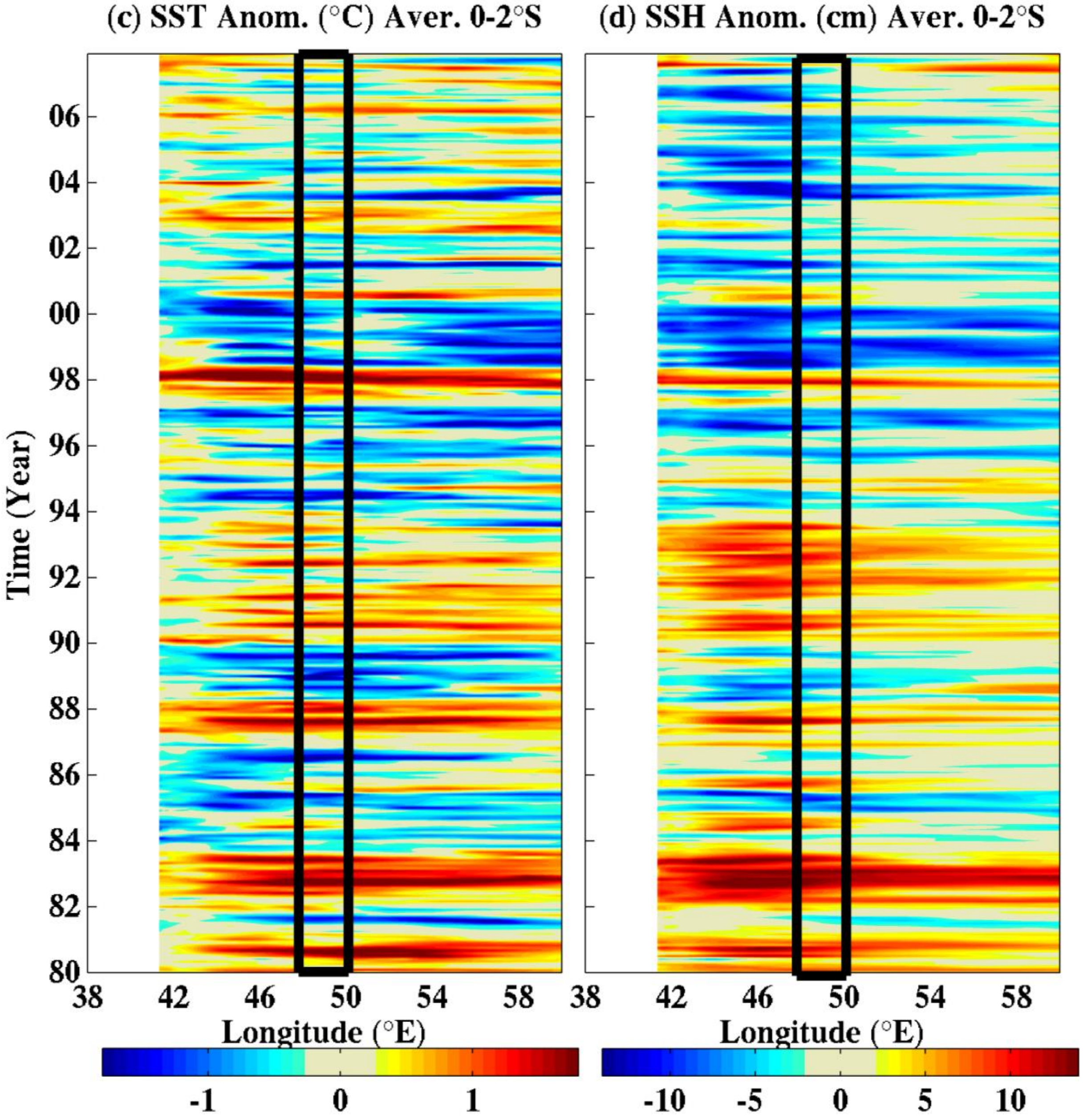

Figure 6.10 (c-d): As Figure 16a-b but averaged over 0-2^{o}S of (c) SST and (d) SSH. The black rectangle shows the offshore location B.

Strong variations of the interannual SST in the tropical western Indian Ocean and their relation with the ENSO and IOD signals can be obtained by stratifying the SST data and their correlation with Niño3.4 index and DMI in calendar months. This is due to the fact that the influences of the ENSO and IOD in the tropical Indian basin are locked to the seasonal cycle. Figure 6.11 displays monthly standard deviation of the PC1 for the model and AVHRR SST EOF. The PC time series of the SST EOF develops from November (standard deviation >0.3^{o}C), peaking in February when the North East monsoon is fully developed and the influence of the ENSO event in the tropical Indian Ocean basin peaks. The SST for the PC1 in the region mostly correlates with Niño3.4 index (0.64 in the ROMS model and 0.46 in AVHRR SST data at 95% significant levels) when the Niño3.4 index lags behind the first SST PC by 3-4 months (Figure 6.12). The SST from the PC1 in the region correlates with the DMI with values of 0.41 and 0.45 at 95% significant levels when the DMI lags behind the PC1 SST by 2-3 months in the model and by 1-2 months in the AVHRR data, respectively (Figure 6.12). Monthly correlations between the principal component of the first SST EOF and DMI indicate significant correlation during August to January peaking in November (about r=0.61) (Figure 6.13a and b). The Niño3.4 index and the PC1 show a significant correlation during the whole year with high values in October through January (Figure 6.13c and d). Thus, strong variations of the interannual SST variations in the tropical western Indian Ocean relate to the local surface forcing as well as remote forcing induced by ENSO and the IOD.

a) ROMS SST PCs Standard Deviation

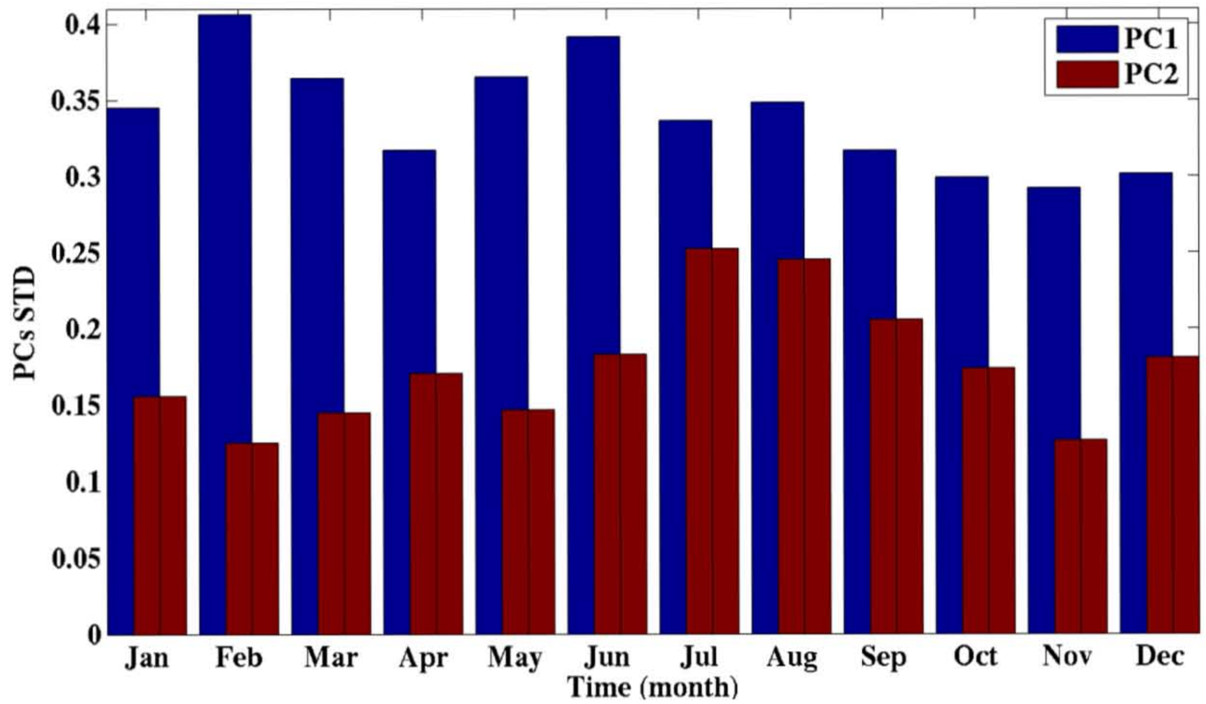

b) AVHRR SST PCs Standard Deviation

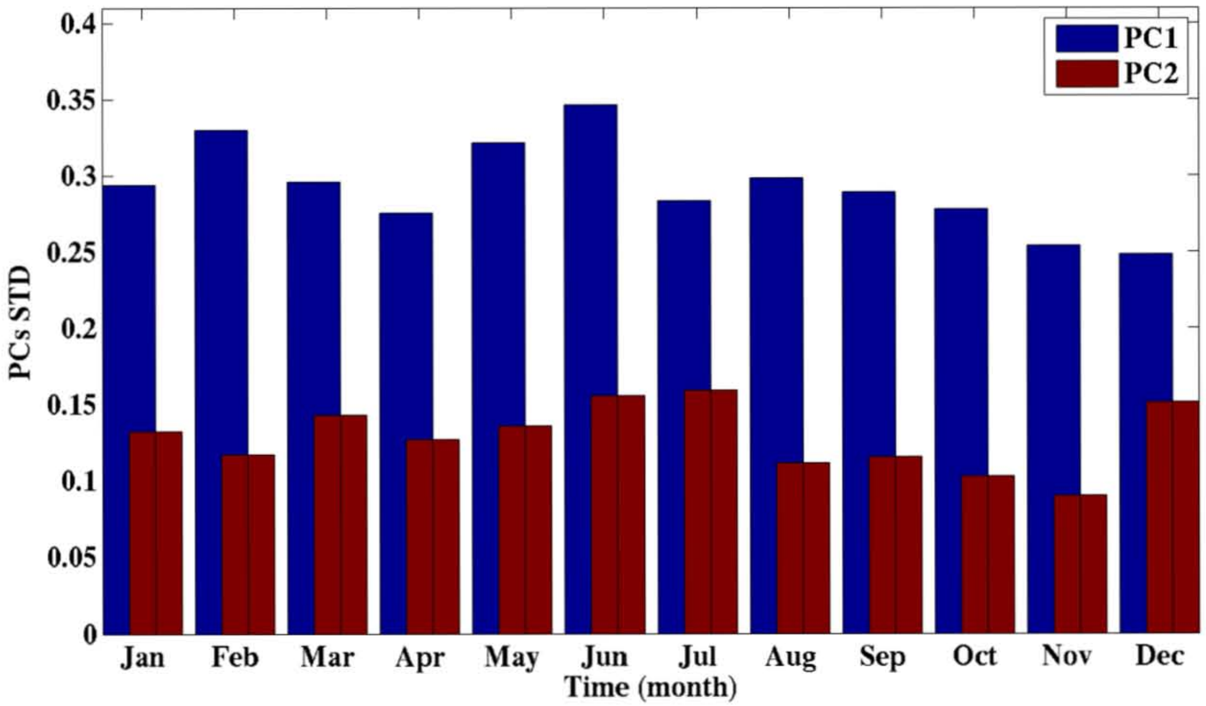

Figure 6.11: Monthly standard deviation of the principal component time series (PCs) with EOF1 (*in blue*) and EOF2 (*in brown*) of the SST for (a) ROMS model and (b) AVHRR.

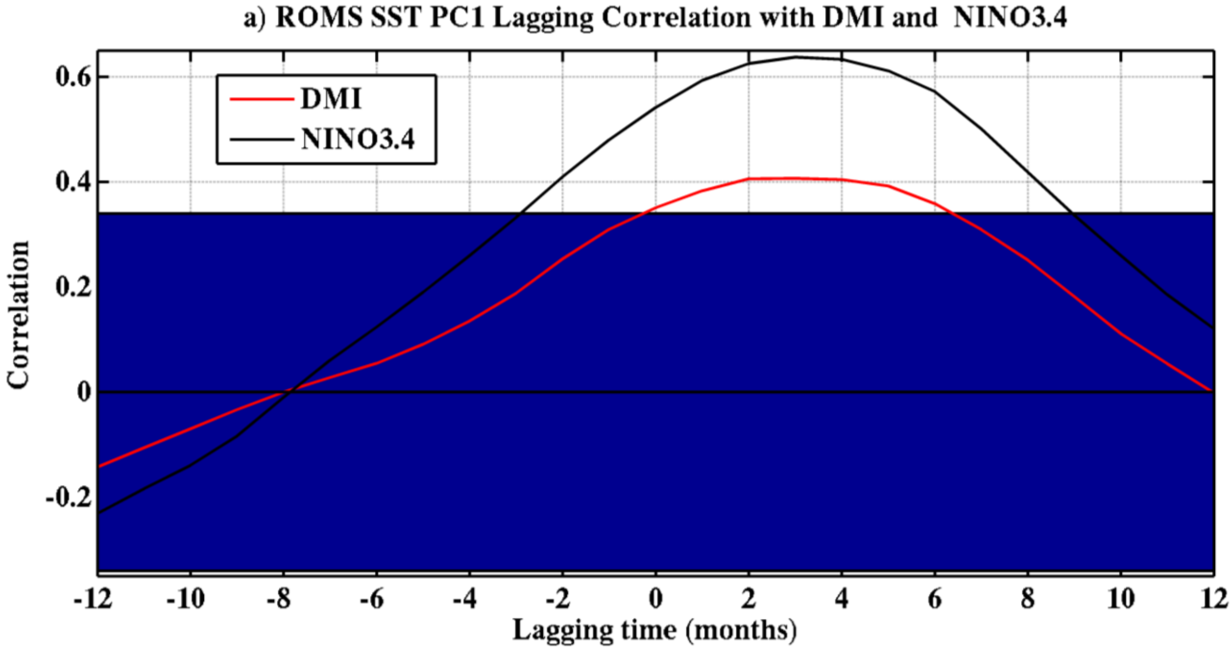
a) ROMS SST PC1 Lagging Correlation with DMI and NINO3.4

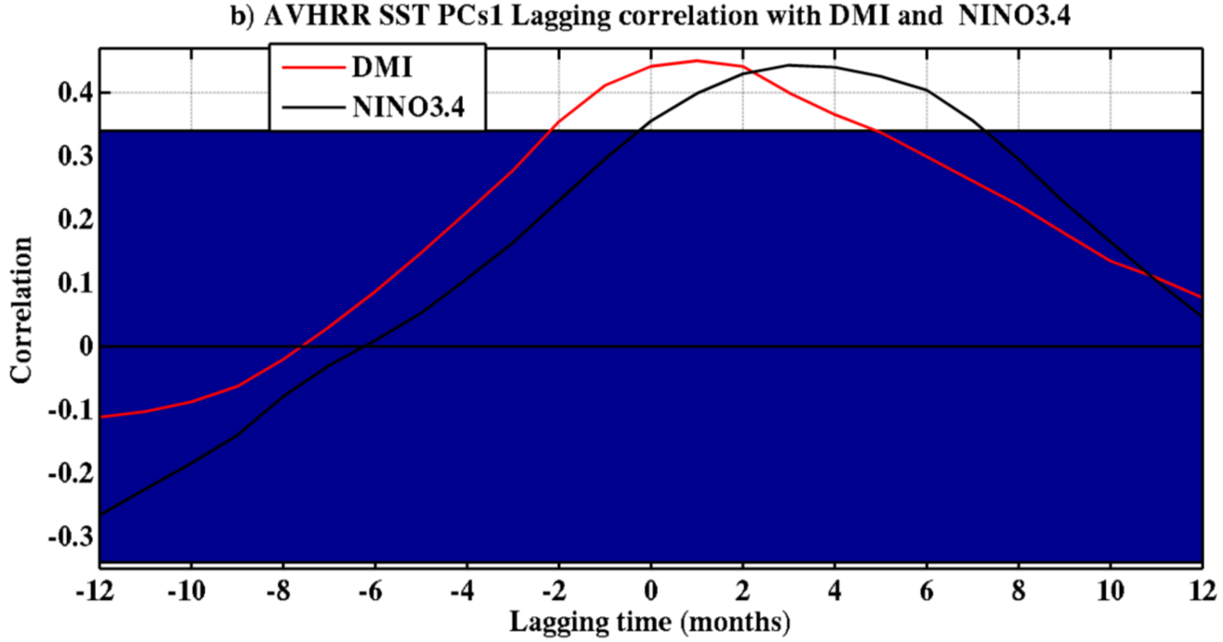
b) AVHRR SST PCs1 Lagging correlation with DMI and NINO3.4

Figure 6.12: Lag correlation of monthly anomaly Niño3.4 index (black) and monthly anomaly dipole mode index (DMI, red) with the first principal component of the EOF of the SST for (a) ROMS model and (b) AVHRR. The unshaded regions indicate statistical significant correlation at 95% significant levels (p<=0.05).

.

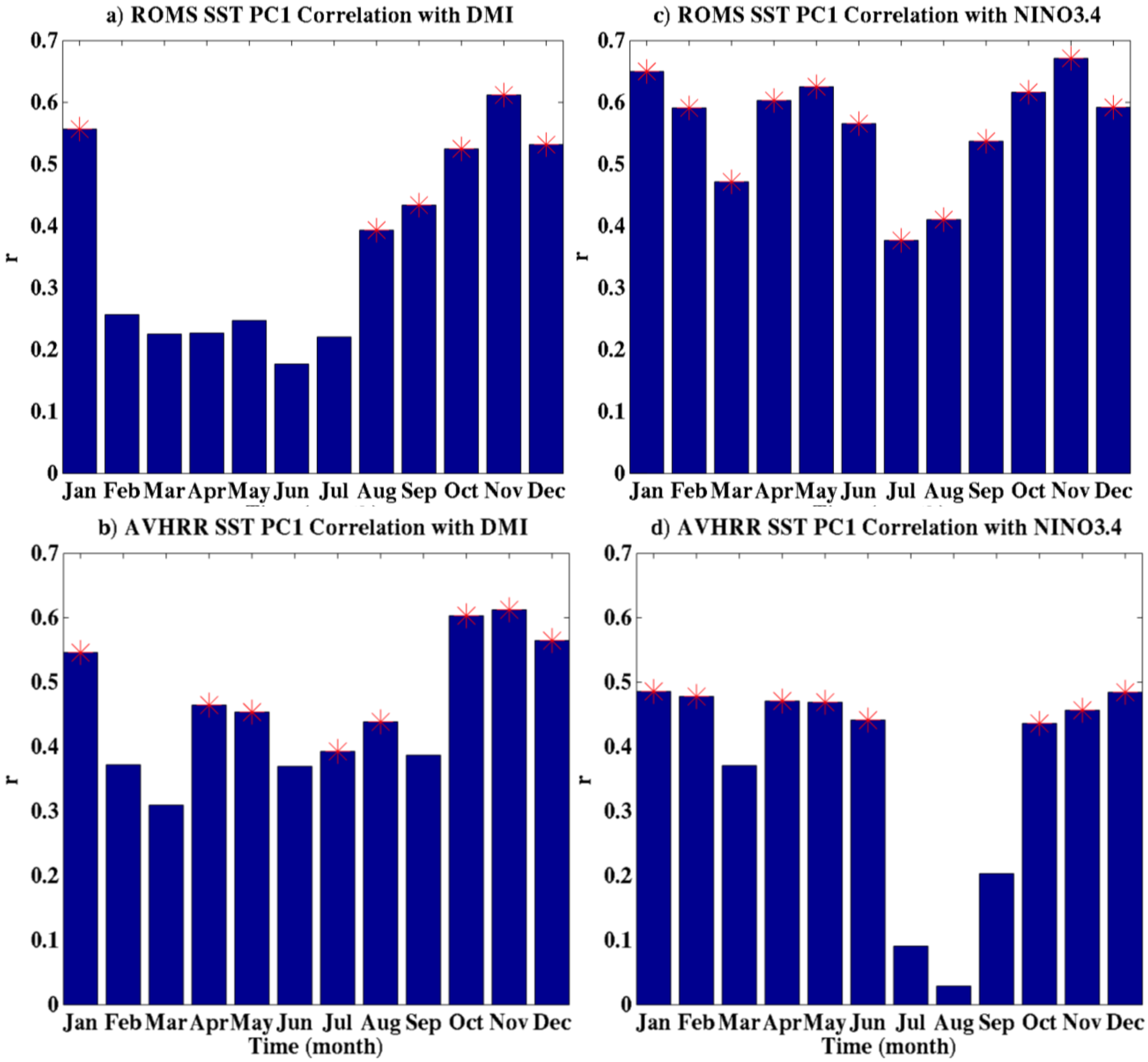

Figure 6.13: Bar diagram of the monthly correlation coefficients between the first principal component of the EOF of the SST with DMI index (left) and Niño3.4 index (right) for (a and b). the ROMS model (c and d) AVHRR. The red star indicates a statistical significant correlation at 95% significant levels (p<=0.05).

To summarize, the Tanzanian shelf region shows weaker interannual SST variability than the offshore region. Such difference suggests different SST forcings in these two regions. Variability in the surface heat fluxes and thermocline appear to be associated with the interannual SST variability in the Tanzanian shelf region and offshore, respectively. Thus, it is useful to investigate their relative contributions. The next section deals with the sensitivity experiments in the region to investigate the relative contributions of the local surface heat fluxes and lateral boundary conditions.

6.3 Sensitivity experiments

In order to gain more insight into the relative roles of the local surface heat fluxes and lateral boundary conditions on the variability in the tropical western Indian Ocean, sensitivity experiments are conducted in the region. The monthly SST anomalies from the control experiment (EXP_REF) are compared with the monthly SST fluctuations from the sensitivity experiments. The surface forcings are kept as a climatology in EXP_CLIM_FLUX, and the lateral boundary conditions are kept as a climatology in EXP_CLIM_SODA.

6.3.1 Sensitivity Experiments on Interannual Variability

Figure 6.14a shows the reduced magnitude of the monthly SST anomalies to less than $\pm 0.2^{o}$C in EXP_CLIM_FLUX throughout the whole period (1980-2007), and is much smaller than in the control and EXP_CLIM_SODA experiments in the Tanzanian shelf region. However, the monthly SST anomalies from EXP_CLIM_SODA are very similar to that for EXP_REF except during 1998-2000. A strong reduction of the SST anomalies in EXP_CLIM_FLUX in the shelf waters appears also in the first EOF analysis of the SST anomalies (Figure 6.15). Values close to zero appear in the Tanzanian shelf region in the first EOF for EXP_CLIM_FLUX. Such patterns suggest a strong relationship between the surface heat fluxes and the SST anomalies in the Tanzanian shelf region. The EOF analysis of the monthly SST anomalies for EXP_CLIM_SODA in the Tanzanian shelf waters reflects that of the control experiment with smaller values ($<1^{o}$C) in the spatial patterns (Figure 6.16). In general, the sensitivity experiments demonstrate that the surface heat fluxes is the dominant forcing of the weaker SST interannual variability in the Tanzanian shelf region.

In the offshore region, the monthly SST anomalies from EXP_CLIM_FLUX and EXP_CLIM_SODA show that the local surface forcing and lateral boundary conditions both exert notable influence (Figure 6.14b). Since the mixed layer temperature tendency shows no significant relationship with the surface latent heat fluxes, the influences of the surface forcing can be associated mainly with the local Ekman pumping from wind stress curl. The monthly SST anomalies for EXP_CLIM_FLUX are reduced to about 50% in 1982-83 and 1987, whereas such anomalies are very similar to that for EXP_REF in 1997-1998. The monthly SST anomalies for EXP_CLIM_SODA are also reduced to about 50% in 1982-1983 and 1997-1998, whereas these anomalies are very comparable to that for EXP_REF in 1987. Therefore, these SST anomalies suggest relatively equal contributions from the local surface forcing and remote forcing. The first EOF analysis of the SST anomalies for EXP_CLIM_FLUX shows increased signals in the offshore region (Figure 6.15) showing the influence of the lateral boundary conditions on the variability in the North-East of the model domain. The spatial patterns of the EOF SST anomalies for EXP_REF and EXP_CLIM_SODA are similar with a smaller amplitude for the first EOF in EXP_CLIM_SODA (Figure 6.16). This shows that secondary mode of variability in the tropical Western Indian Ocean shown in Figure 6.8 responds to local forcing while the dominant mode is influenced by both large scale and local processes. The first EOF of the monthly SST anomalies for EXP_CLIM_SODA significantly correlates with the Niño3.4 index (r=0.3) and DMI (r=0.4) at 95% significant levels. In short, the sensitivity experiments demonstrate the influence of both local forcing and remote forcing in the interannual SST variability in the offshore region.

To summarize, local surface heat fluxes and lateral remote influences play different roles in the interannual SST variability in the tropical western Indian Ocean. The local surface fluxes play a significant role in the interannual SST variability in the coastal waters in the Tanzanian shelf region. The remote influences play a dominant role in the offshore region. To further understanding on the relative contributions of the local surface heat fluxes and remote forcing, analysis of the SST characteristics for the control and sensitivity experiments during strong warm and cold years is performed.

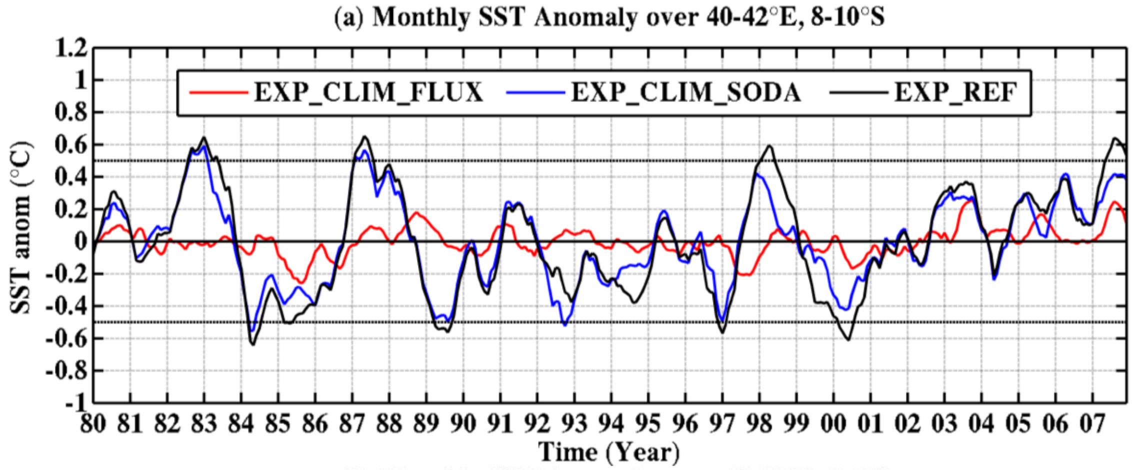

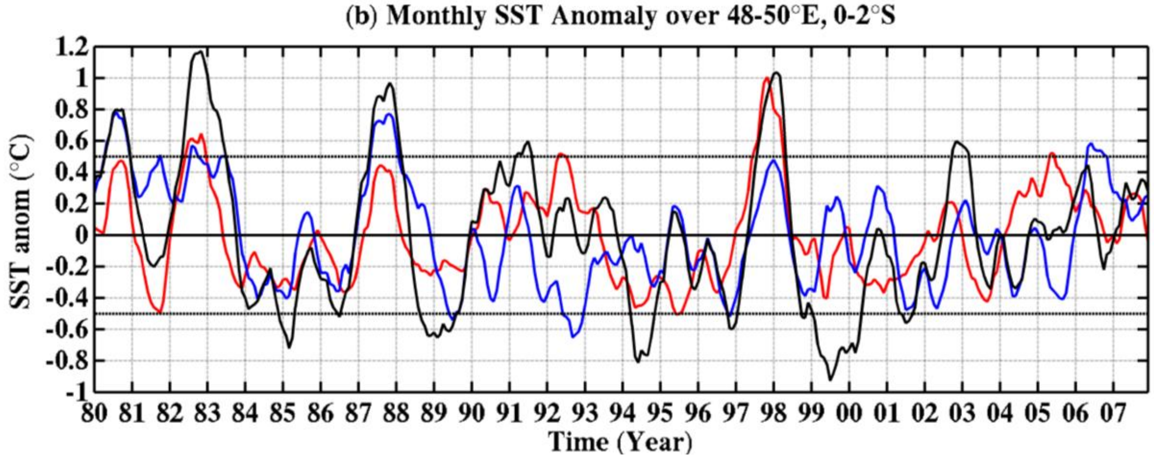

Figure 6.14: SST fluctuations from the ROMS model averaged over (a) Box A and (b) Box B for EXP_REF (black), EXP_CLIM_FLUX (red) and EXP_CLIM_SODA (blue).

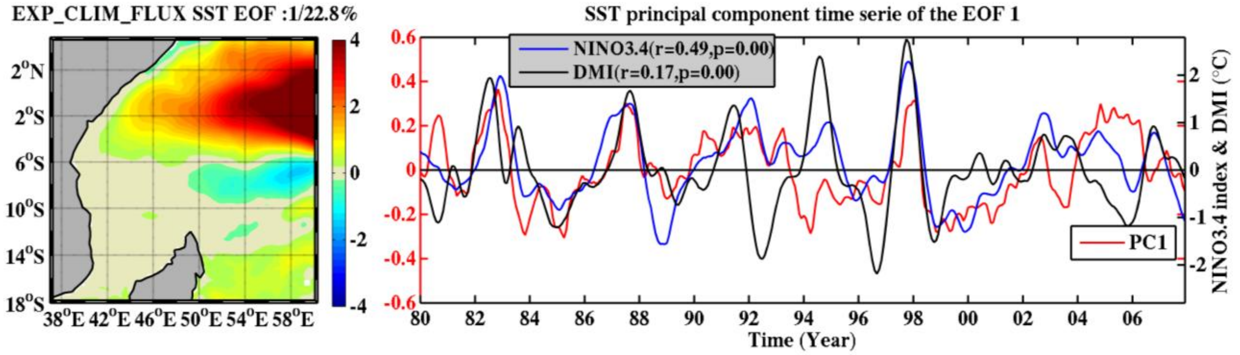

Figure 6.15: The first EOF mode (^{o}C) for EXP_CLIM_FLUX and its corresponding principal component time series (in red). The DMI (in black) and the Niño3.4 index (in blue) are added (The time series are smoothed by seven months running mean).

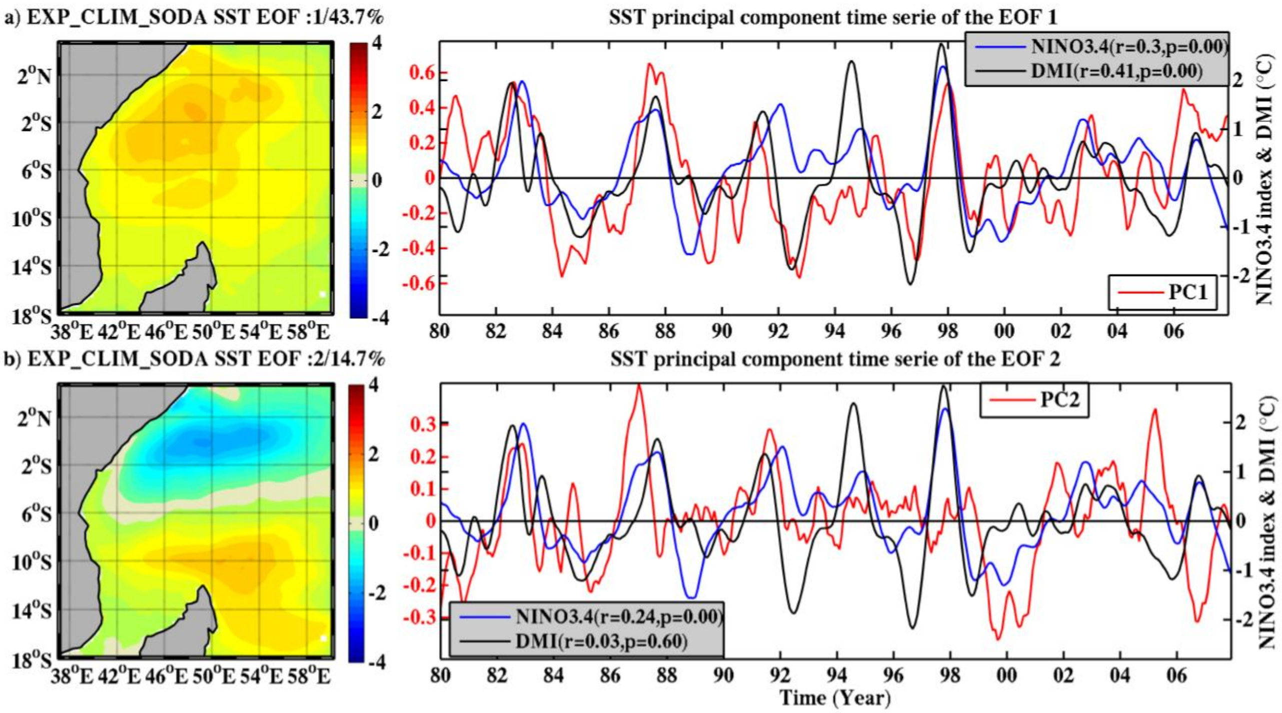

Figure 6.16: The first two EOF modes (°C) for EXP_CLIM_SODA and their corresponding principal component time series (in red). The DMI (in black) and the Niño3.4 index (in blue) are added (The time series are smoothed by seven months running mean); (a) ROMS 1st EOF, (b) ROMS 2nd EOF.

.

6.3.2 Sensitivity Experiments during Warm and Cold Events

The SST variations for the control and sensitivity experiments during the warm and cold events are analysed in the Tanzanian shelf region and offshore as shown in Figure 6.17. Composite analysis of the SST variations during warm and cold events is conducted for EXP_REF, EXP_CLIM_FLUX and EXP_CLIM_SODA. The common warm years (>0.5°C) are 1982/1983, 1987/1988, 1997/1998 and the common cold years (<-0.5°C) are 1984/1985, 1988/1989, 1999/2000 in both the Tanzanian shelf waters and offshore.

Warm Event

Figure 6.17a-b shows the SST characteristics during the warm events in the Tanzanian shelf region and offshore for EXP_REF, EXP_CLIM_FLUX and EXP_CLIM_SODA. The Tanzanian shelf waters are relatively cooler than in the offshore region during the warm year and the following year. In this period, large warm SST differences between the coastal waters and the open ocean occur from June of the warm year through February following the warm year. The prominent differences in the warm SST anomalies between the two regions occur from May of the warm year through March following the warm year. In these months, warm SST anomalies of about 0.4-0.8^{o}C occur in the coastal waters and 0.6-1.2^{o}C in the open ocean. The warm SST anomalies over the open ocean peak in September of the warm year (~1.1^{o}C), meanwhile that in the coastal waters peak in March of the year following the warm event (~0.8^{o}C). The warm SST anomalies start cooling from January/February following the warm year through the rest of the months in the following year in both regions. The cooling is stronger and quicker in the open ocean than in the coastal waters.

During a warm year, the evolution of the warm SST anomaly seems to be weaker in the Tanzanian shelf region than offshore in the realistic and sensitivity experiments (Figure 6.17a-b). In the coastal waters, the boundary condition does not have any significant influence on the SST during the warm year and the following year with an exception in May-August of the following year (Figure 6.17a). However, the warm SST anomalies from EXP_CLIM_FLUX in the coastal waters are much reduced during the warm event (Figure 6.17a). This suggests the dominance of local surface heat fluxes in the evolution of the model SST anomalies. Warm SST anomalies for EXP_CLIM_SODA are reduced to about 50% of the SST anomalies from EXP_REF from June of the warm year through April of the following year in the offshore region (Figure 6.17b). The reduction of the warm SST anomalies in this period is close to that from EXP_CLIM_FLUX except from August to October when the warm SST anomalies from EXP_CLIM_FLUX abruptly rise and drop, peaking in September of the warm year. This suggests that remote influences play a significant role in warming the SST in the offshore region from June in the warm year through April of the following year in conjunction with the local surface forcing except in September of the warm year.

Cold Event

Figure 6.17c-d shows the SST anomalies during the cold event in the Tanzanian shelf region and offshore for the control and sensitivity experiments. In EXP_REF, negative SST anomalies occur in the cold years and the following year, except in January through March in the coastal waters and except in January in the open ocean of the cold years. During this period, the SST anomalies in the open ocean are stronger than the coastal waters from January of the cold years to June of the following year. This is in contrast to July through December of the years following the cold events. The prominent differences of the cold SST anomalies between the coastal waters in the Tanzanian shelf region and the open ocean occur from May of the cold years through March of the following year. The coolest SST in the open ocean and in the coastal waters occurs in January-February (~-0.8^{o}C) and in March (~-0.7^{o}C) of the cold years, respectively. Both the coastal waters and the open ocean experience two periods of maximum SST cooling; the first one in April-May of the cold years, and the second one in January-March of the following year. In cold events, the offshore region is cooler than the Tanzanian shelf waters, suggesting different forcing characteristics between the two regions.

During the cold events, there are different responses of the coastal waters in the Tanzanian shelf and the open ocean to the local surface heat fluxes and lateral boundary conditions. The SST anomalies from EXP_CLIM_FLUX in the coastal waters are much reduced during the cold event (Figure 6.17c). This suggests the dominance of the surface heat fluxes in the evolution of the model SST anomalies in the cold event in the coastal waters. Offshore, the cold SST anomalies from EXP_CLIM_SODA are reduced to at least 50% of the SST anomalies from EXP_REF from May of the warm year through June of the following year (Figure 6.17d). The reduction of the cold SST anomalies in EXP_CLIM_SODA in this period is close to that from EXP_CLIM_FLUX except from July to September when the warm SST anomalies from EXP_CLIM_FLUX abruptly rise and drop, peaking in August of the cold year (Figure 6.17d). This suggests that the lateral remote influences play a significant role in cooling the SST anomalies offshore from June in the cold year through May of the following year in conjunction with the surface heat fluxes except in August of the cold year.

To summarize, local surface heat fluxes and lateral remote influences play different roles in the interannual SST variability in the tropical western Indian Ocean. The local surface fluxes play a significant role in the interannual SST variability in the coastal waters in the Tanzanian shelf region. The remote influences play a dominant role in the offshore region. During the warm (cold) year, the lateral remote influences warm (cool) the SST anomalies offshore from June in the warm (cold) years through April of the following year in conjunction with the surface heat fluxes except in September (August) of the warm (cold) year.

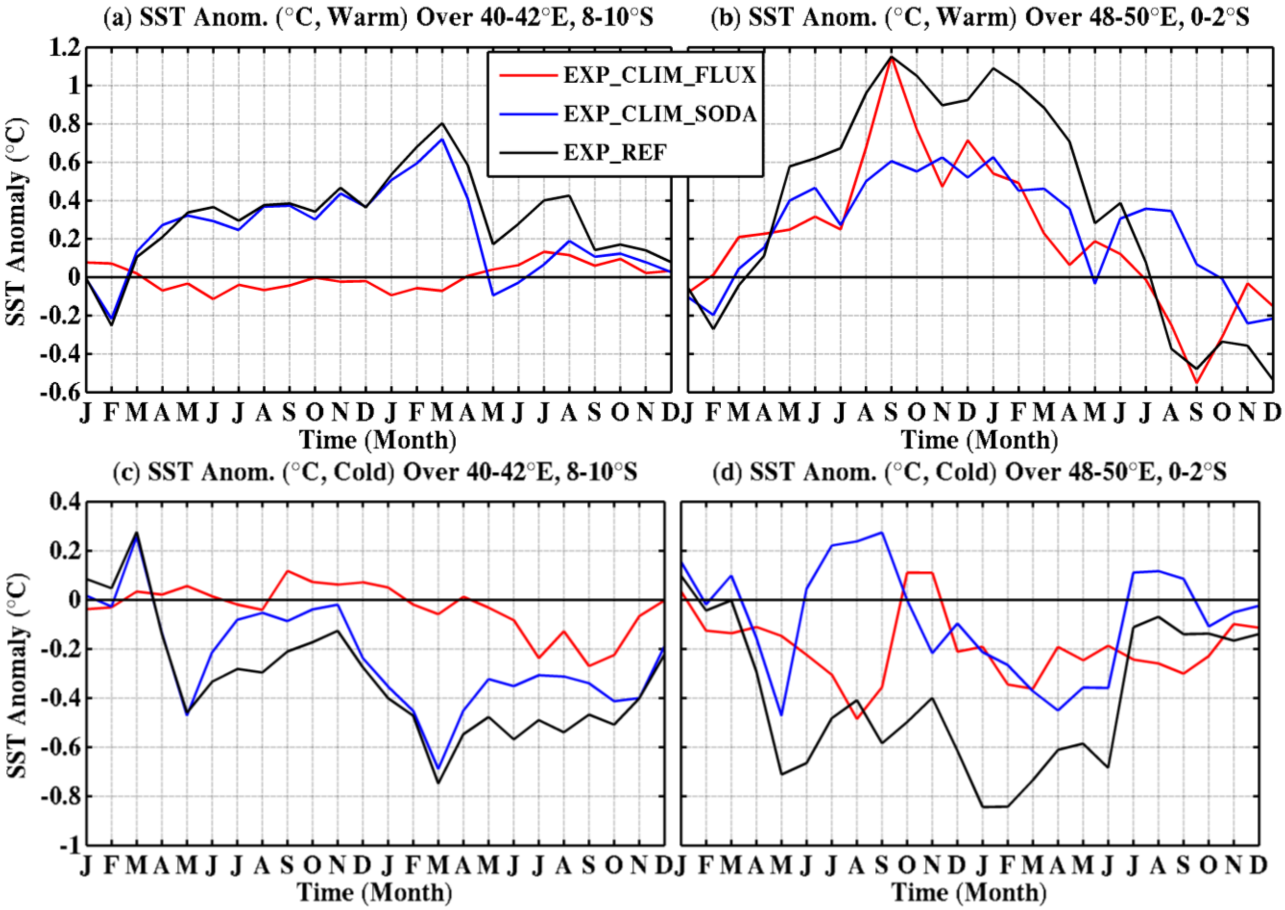

Figure 6.17: SST fluctuations from the ROMS model averaged over box A (left column) and box B (right column) during the warm event in the top panel (a and b) and cold event in the bottom panel (c and d) for EXP_REF (black), EXP_CLIM_FLUX (red) and EXP_CLIM_SODA (blue).

6.4 Summary

The Tanzanian shelf region, linked to the north of Madagascar, experiences weaker interannual variations than the offshore region. Waters in the Tanzanian shelf region are dominated by the surface heat fluxes and in the offshore region by the thermocline variations mainly driven by remote forcing and local surface forcing. With this knowledge of the interannual SST, it is useful to study interannual variability of the subsurface temperature in the Tanzanian shelf region and offshore. This will lead to a better understanding of the interannual subsurface variability in comparison to the SST in the region in the Tanzanian shelf region and further offshore.

Relationships between interannual subsurface and surface temperature variability in the two regions is discussed in the next chapter.

Chapter 7

Interannual Variability of Subsurface Temperatures

7.0 Introduction

The previous chapter showed the difference in the interannual variability of sea surface temperature (SST) between the Tanzanian shelf region and offshore in the tropical western Indian Ocean. This chapter examines the relationship between the subsurface temperature in the Tanzanian shelf region and offshore at the interannual timescales. The chapter addresses the following questions:

How does the upper ocean temperature vary in the Tanzanian shelf region and offshore in the tropical western Indian Ocean in relation to the SST? How sensitive is it to the local surface heat flux or lateral remote forcing?

i. What are the characteristics of the upper ocean temperature in the Tanzanian shelf region compared to offshore in the tropical western Indian Ocean?

ii. Does the temperature near and below the thermocline in the region vary in the same way as the SST in the Tanzanian shelf region and offshore?

iii. How does the upper ocean temperature in the Tanzanian shelf region and offshore respond to the local surface heat fluxes?

iv. How does the upper ocean temperature in the Tanzanian shelf region and offshore respond to the lateral boundary conditions?

This chapter is outlined as follows: The first section deals with the vertical structure of the interannual variability of the upper ocean temperature (7.1). The second section (7.2) deals with indentifying dominant modes of the interannual variability of the upper ocean temperature and their linkage to large-scale climate variability modes. The third section (7.3) deals with sensitivity experiments on the upper ocean temperature. The last section (7.4) provides a summary.

7.1 Vertical Structure of the Interannual Variability of the Upper Ocean Temperature

Figure 7.1 displays standard deviation of vertical temperature anomalies and the annual mean thermocline depth in red line (1st panel) as well as variance (%) of monthly vertical temperature anomalies explained by the monthly climatology for the upper 200 m (2nd panel). The vertical transects of the standard temperature anomalies are extracted from the coast at 38 to 60°E, and averaged between 1 and 1.5°S for Figure 7.1 (a and c) and between 9 and 9.5°S for Figure 7.1 (b and d) from 1980 to 2007. The former transect crosses through the offshore region, and the latter one goes through the inshore region as shown in Figure 7.1, the regions with the strongest and weakest interannual variability of the SST, respectively.

The temperature transect that crosses through the offshore region shows strong interannual temperature variations (standard deviation of about 2-3°C) in the subsurface waters between 30 and 130 m (Figure 7.1a). The transect displays very deep thermocline depth at the annual mean ranging from 100 to 130 m (Figure 7.1a). The highest interannual variations of the vertical temperature are confined to the subsurface waters near the offshore region where the annual thermocline depth is relatively elevated. Relatively weak interannual variations of the upper ocean temperature (standard deviation <1°C) occur in the upper 30 m and below 130 m. The 130 m depth is the annual mean thermocline depth in the offshore region. The variations of the temperature in the upper 30 m in the transect can be mainly explained by seasonality (explained variance >65%), and they are confined to the coast, where they reach below 200 m (Figure 7.1c). The offshore region corresponds to strong interannual variations in the thermocline depth with standard deviation which ranges from 18 m at 50°E to 24 m at 48°E (Figure 7.2). Thus, variations in the thermocline depth are associated with strong variations in the upper temperature in the offshore region.

The vertical temperature transect through the coastal waters in the Tanzanian shelf region shows weak interannual variations (standard deviation <0.5°C) in the upper 200 m (Figure 7.1b). The annual mean of the thermocline depth ranges from 70-80 m in the Seychelles-Chagos thermocline ridge as reported by Hermes and Reason (2008) and Yokoi et al. (2008) to the deepest value (130 m) in the Tanzanian shelf region. In this transect, strong seasonality is present in the upper 40 m (explained variance >80%), and it is confined to the coast where it reaches below 200 m. High subsurface temperature variations (standard deviations of about 1.5-2.0°C) occur between 30 and 80 m to the east of the transect which seems to advect towards the Tanzanian shelf region. This high variability is located between 48 and 60°E. The region

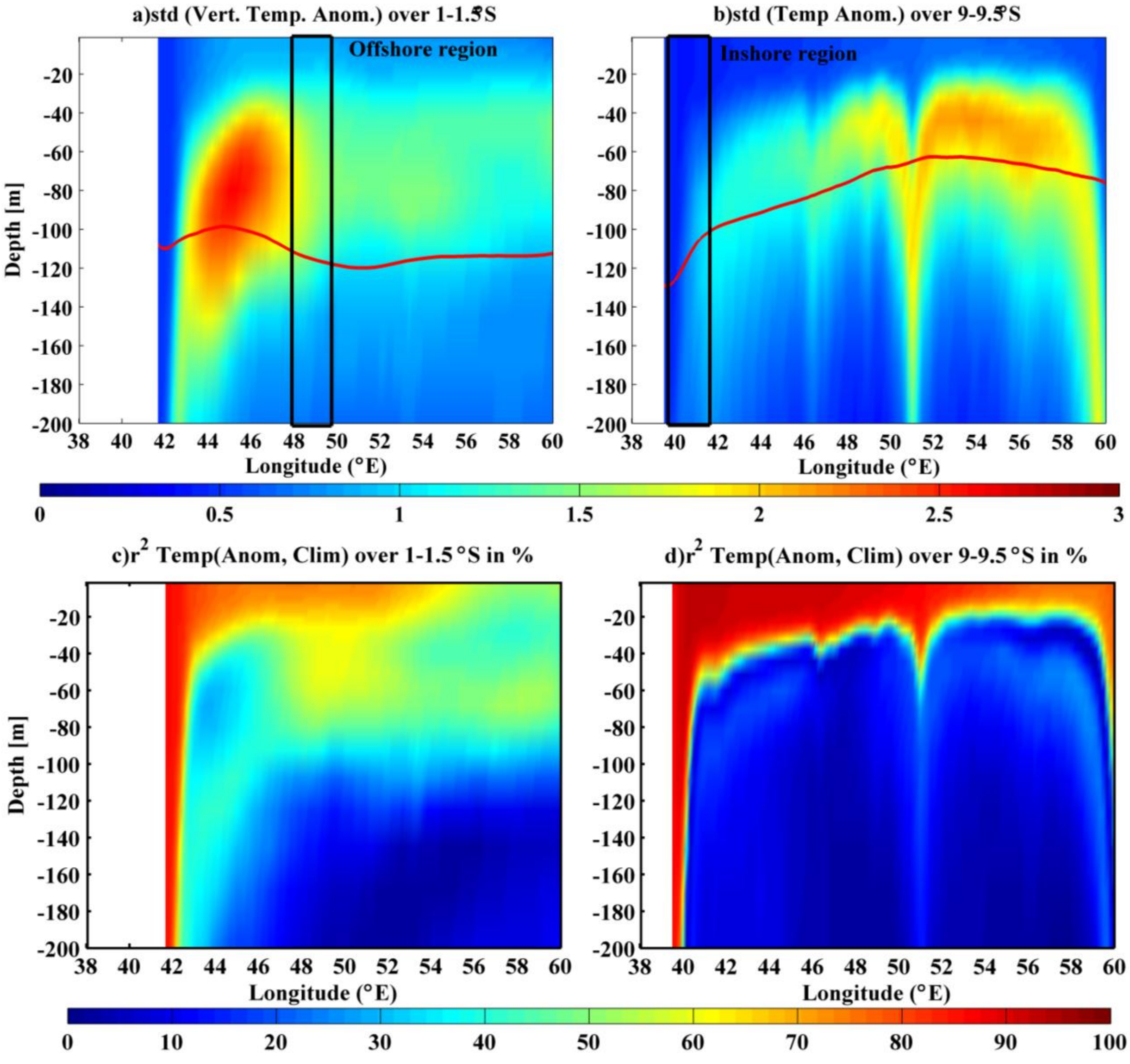

Figure 7.1: Standard deviation of the vertical temperature anomaly and the annual thermocline depth in red line (1st panel) and variance (%) of monthly SST anomalies explained by the monthly climatology (2nd panel) from 38°E to 60°E averaged over (a, c) 1-1.5°S and (b, d) 9-9.5°S from 1980 to 2007 in the upper 200 m depth.

corresponds with relatively high standard deviation of the thermocline depth (>13 m) which becomes higher than that in the offshore region towards the east of 52°E (>15 m). Thus, uniformly weak variations of the temperature in the upper 200 m occur in the Tanzanian shelf region which is mainly dominated by the seasonality and some contribution from advection from the region with high variations to the East in the subsurface waters.

In general, the region with the highest SST variability in the offshore region lies over strong subsurface temperature variations located between 30 and 130 m. Moreover, the region corresponds with strong variations in the thermocline depth. The weakest SST variations in the Tanzanian shelf waters lie over the subsurface waters with the smallest temperature variations in the upper 200 m. It matches with weak variations in the thermocline depth. The highest regional variability of the subsurface temperature is more explained by interannual variability. Additionally, both regions with strong variations in the subsurface temperature are related to strong thermocline variations. Thus, the next section deals with relationships between the vertical structure of the upper ocean temperature and large-scale climate modes.

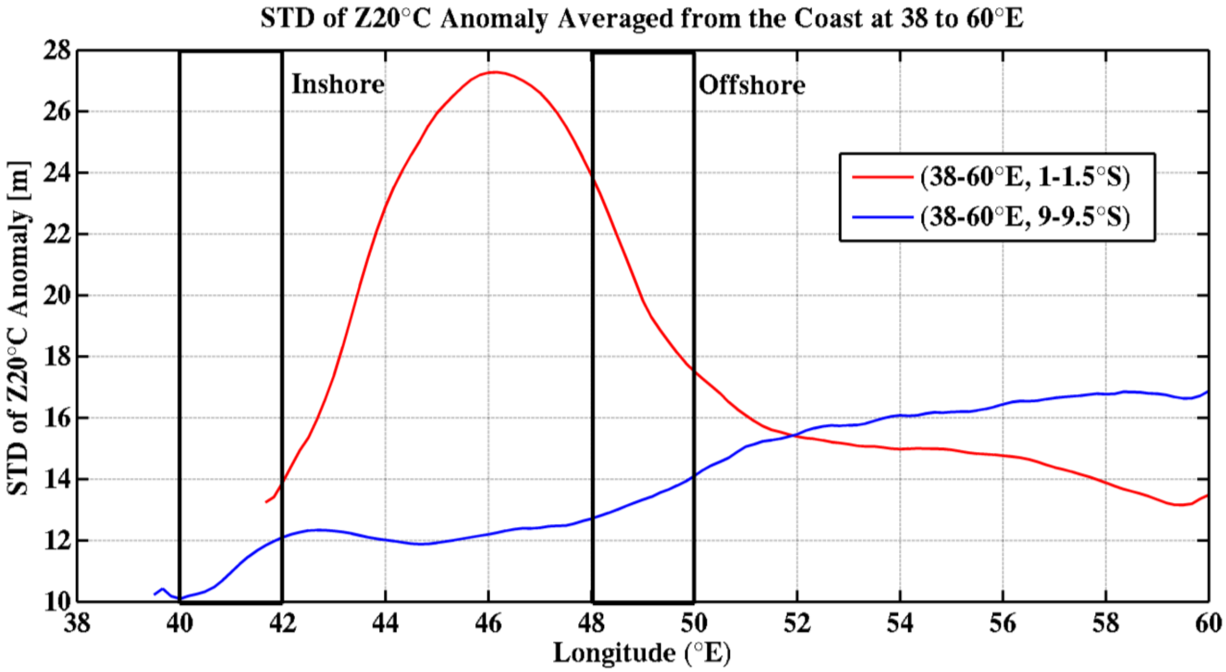

Figure 7.2: Standard deviation of the thermocline anomalies from the ROMS model in the tropical western Indian Ocean averaged from the coast at 38 to 60°E over 1-1.5°S (red) and 9-9.5°S (blue).

7.2 Vertical Structure of the Upper Ocean Temperature and Large Scale Climate Variability Modes

An EOF analysis is applied to the upper ocean temperature (0-200 m) in the vertical transects through the Tanzanian shelf region and offshore in the tropical western Indian Ocean. It is performed on the monthly vertical temperature anomalies to determine the dominant modes of variability.

7.2.1 Vertical Interannual Temperature Variability Averaged over 9-9.5^{o}S from 38 to 60^{o}E

The EOF analysis in the transect through the Tanzanian shelf waters is performed on the monthly vertical temperature anomalies from 38 to 60^{o}E averaged between 9 and 9.5^{o}S (Figure 7.3). The first two leading modes of the vertical temperature anomalies in the upper 200 m of the EOF, which collectively explain about 64% of the total variance, are retained.

The first mode explains about 51% of the total variance with the same sign everywhere in the transect (Figure 7.3a). The weakest loadings are in the Tanzanian shelf region reflecting the weakest temperature variations. However, strong spatial loading patterns occur to the east between 48 and 60^{o}E in the subsurface waters between 20 to 140 m where they match with strong standard deviation in the vertical temperature anomalies. The principal component time series of the first EOF (PC1) of the anomalies in the upper temperature correlate with the Niño3.4 index and the DMI with values of 0.31 and 0.12 at 95% significant levels, respectively.

The second mode of the EOF explains about 14% of the total variance with an east-west dipole spatial pattern in the subsurface waters (Figure 7.3b). The lowest values close to zero occur in the upper 30 m being confined to the Tanzanian shelf region. The PC2 shows correlation with the Niño3.4 index and the DMI with values of about 0.24 and 0.18 at 95% significant levels, respectively.

The first two modes of the monthly vertical temperature anomalies through the Tanzanian shelf waters show correlation with ENSO and IOD signals. Very low and relatively high values of correlation between the large-scale indices (the Niño3.4 index and the DMI) occur with the upper temperature occur in the Tanzanian shelf region and offshore, respectively. However, significantly small values of correlation of the PC1 and PC2 with the Niño3.4 index and the DMI could be associated with strong seasonality of the indices. Thus, stratification of the PC1 and PC2 as well as their correlation with the Niño3.4 index and the DMI in calendar months can provide strong correlation in seasonal variations.

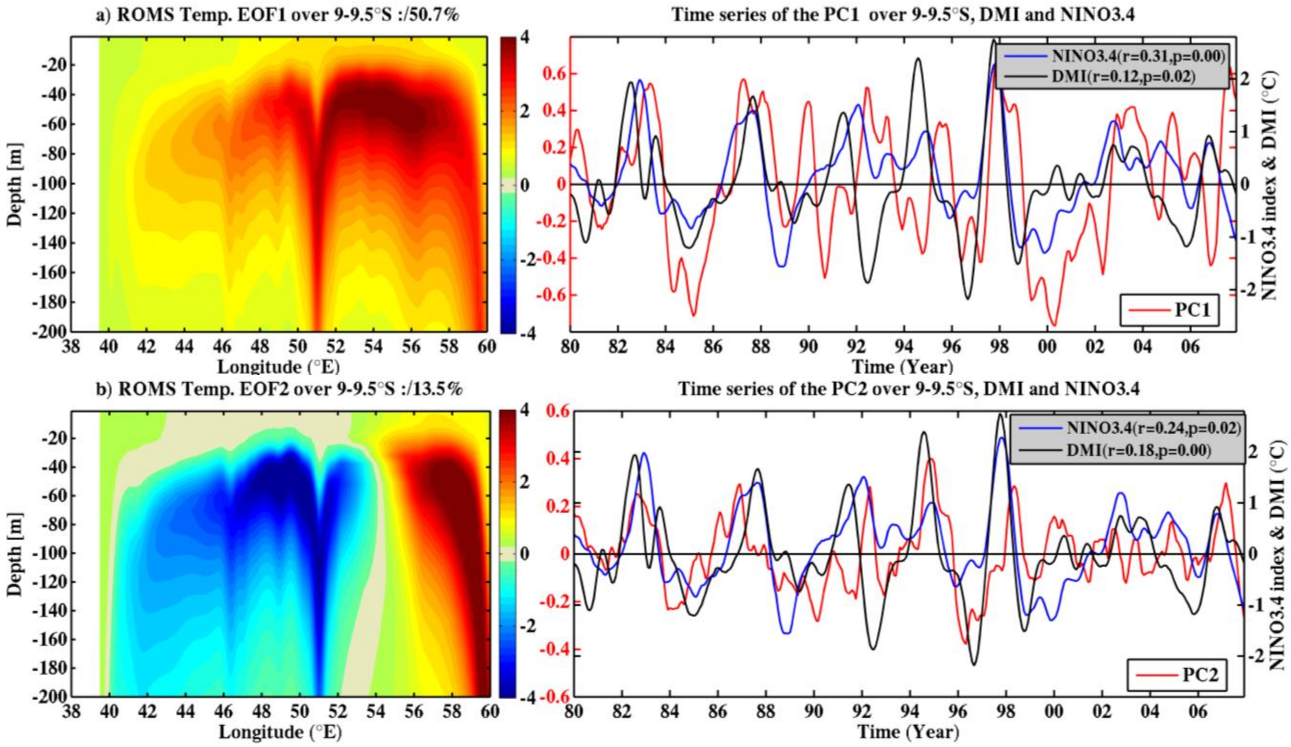

Figure 7.3: The first two EOF modes for the upper ocean temperature (0-200 m) from 38 to 60°E averaged over 9-9.5°S in the tropical western Indian Ocean and their corresponding principal component time series (in red). The DMI (in black) and the Niño3.4 index (in blue) are added (The time series are smoothed by seven months running mean). (a) 1st EOF, (b) 2nd EOF.

To understand the seasonal variations of the vertical temperature anomalies in the Tanzanian shelf region and their relation to the ENSO and IOD signals, the principal component time series of the first two leading modes and their correlation with the Niño3.4 index and the DMI are stratified by calendar months. The PC of the first two leading modes of the vertical temperature anomalies show semi-annual signals. The PC1 displays relatively strong standard deviation which peaks in April (~0.5°C) and in November (~0.4°C), while the standard deviation of the PC2 peaks in October and December at about 0.25°C (Figure 7.4). The PC1 of the vertical temperature anomalies in the region mostly correlate with the Niño3.4 index (r>0.6) at 95% significant level when the Niño3.4 index lags behind the PC1 by 3-7 months (Figure 7.5a).

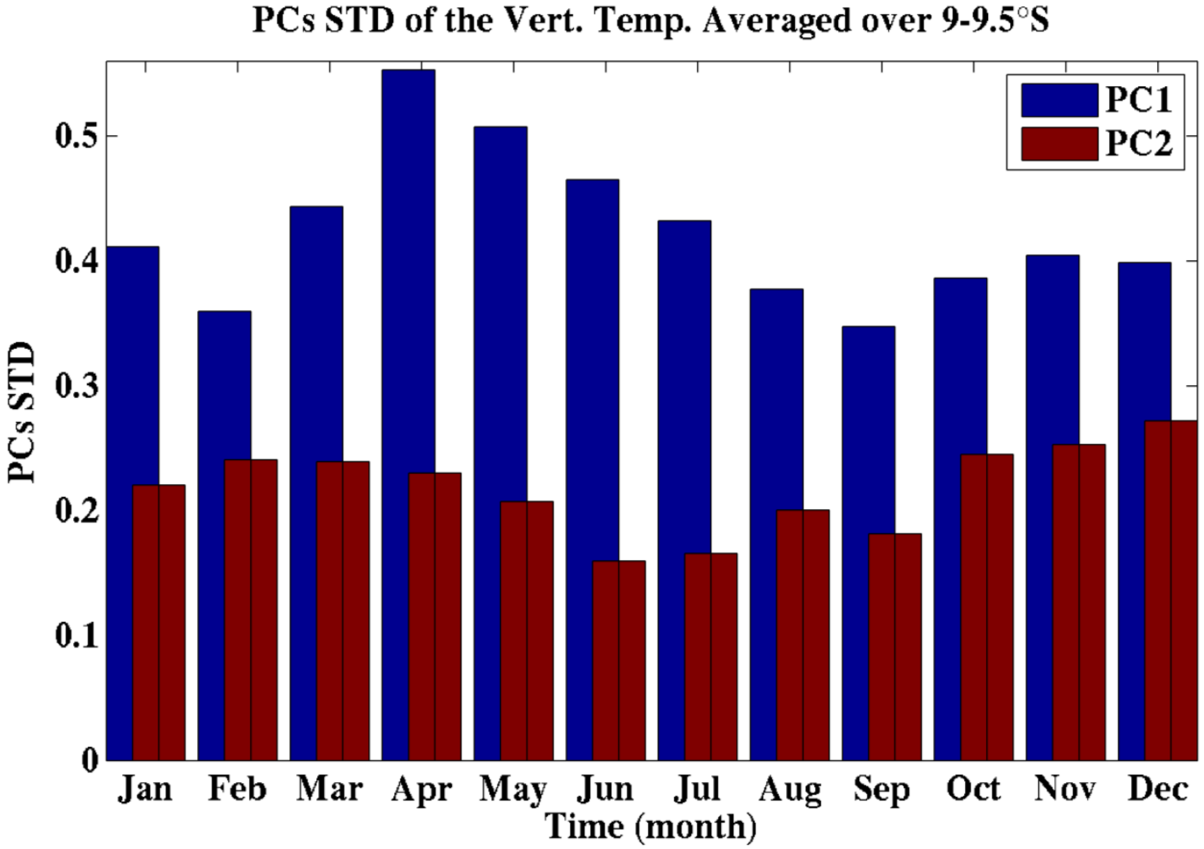

Figure 7.4: Monthly standard deviation of the principal component time series with the EOF1 (*in blue*) and the EOF2 (*in brown*) of the vertical temperature anomaly in the upper 200 m depth from 38 to 60^{o}E averaged over 9-9.5^{o}S.

However, the correlation between the PC1 of the vertical temperature anomalies with the DMI is very weak. Furthermore, no significant monthly correlation exists between PC1 of the vertical temperature anomalies and the DMI (Figure 7.5b). On the other hand, the Niño3.4 index and the PC1 of the vertical temperature anomalies show a strong correlation from January to April, peaking in March-April at about 0.7 (Figure 7.5c). Weak signals of the ENSO and IOD appear in the PC2 of the vertical temperature anomalies which are mostly correlated (r~=0.3) when the Niño3.4 index and the DMI lags behind the PC2 by 2-3 and 5 months, respectively (Figure 7.6a). No significant monthly correlation of the PC2 with the DMI exists except in only October (r~=0.4; Figure 7.6b), and with the Niño3.4 index, except in March to May (Figure 7.6b). The significant correlation for the latter tends to peak at about 0.5 in April. These results suggest strong variations of the interannual vertical temperature anomalies around 9-9.5^{o}S in the tropical western Indian Ocean are more associated with ENSO signals than IOD signals as was previously reported by Rao et al. (2005) and Yu et al. (2005).

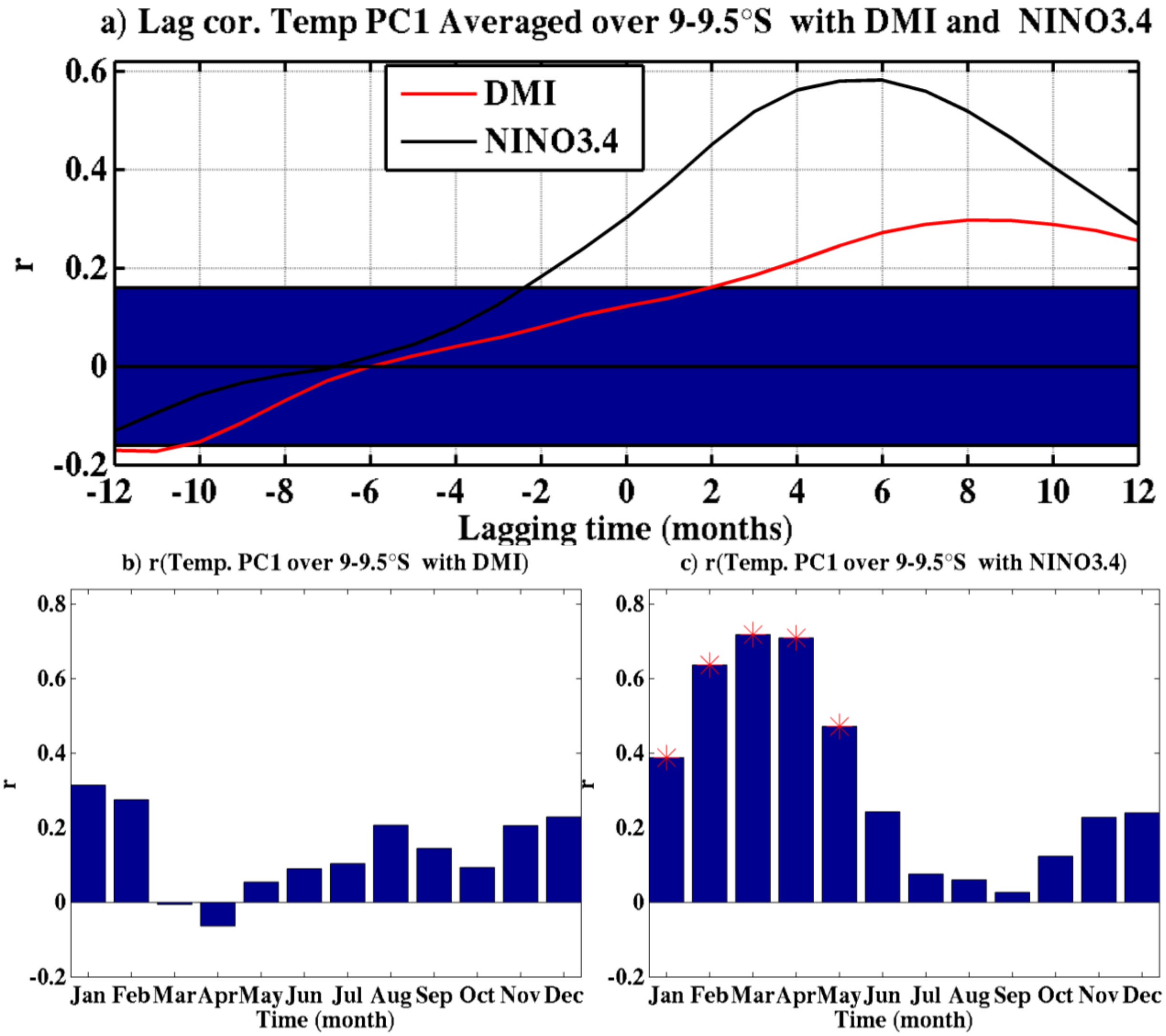

Figure 7.5: (a) Lag correlation of the Niño3.4 index (black) and the DMI (red) with the PC1 of the vertical temperature EOF from 38 to 60^{o}E averaged over 9-9.5^{o}S in the upper 200 m. Bar diagrams of the monthly correlation coefficients between the PC1 with (b) the DMI (left) and (c) the Niño3.4 index (right). The unshaded region in (a) and the red stars in (b and c) indicate statistical significant correlation at 95% significant levels (p<=0.05).

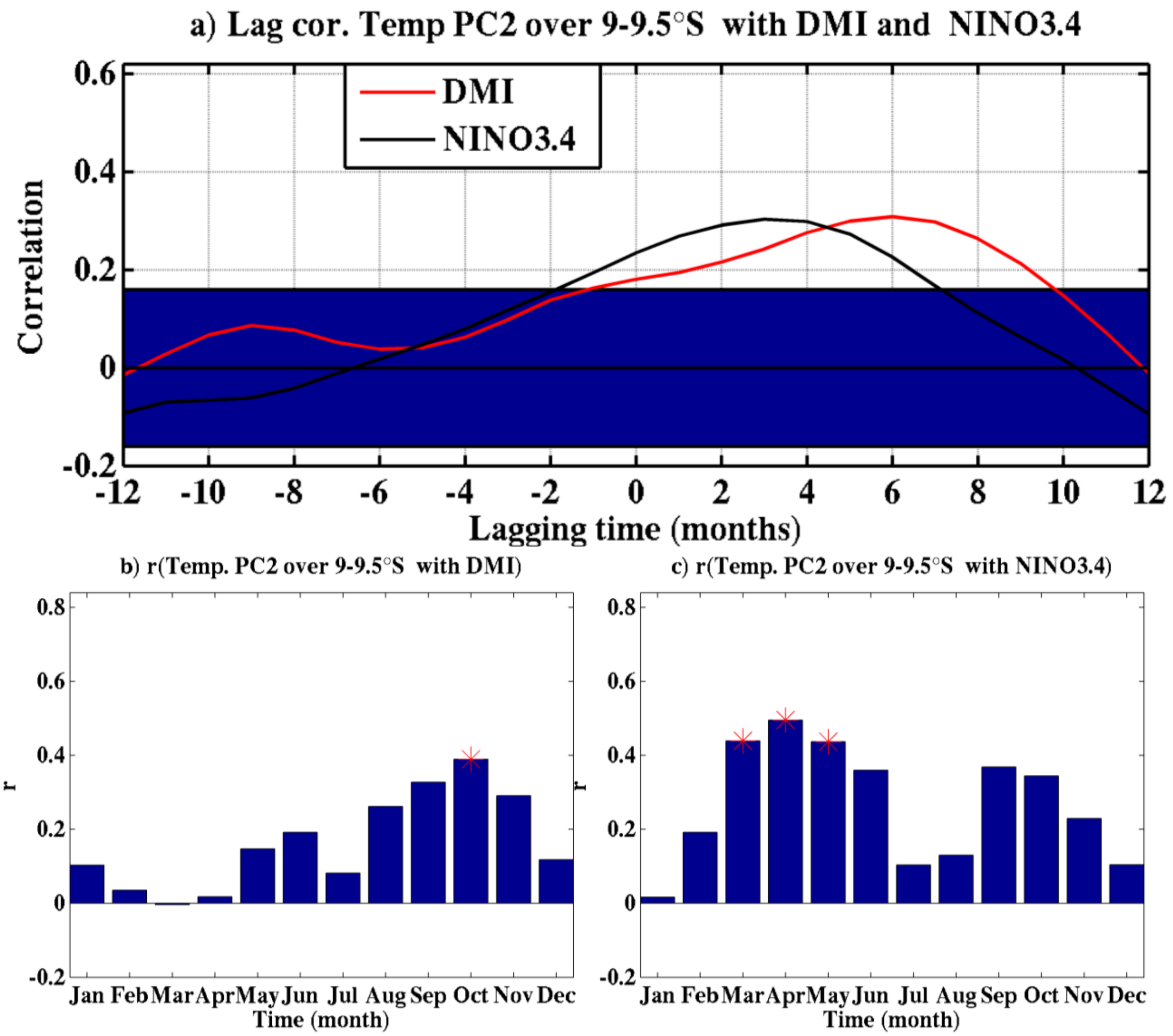

Figure 7.6: As Figure 7.5 but for the PC2.

7.2.2 Vertical Interannual Temperature Variability Averaged over 1-1.5^{o}S from 38 to 60^{o}E

The monthly temperature anomalies of the vertical transect through the offshore region are used to compute the EOFs in the region from 38 to 60^{o}E averaged between 1 and 1.5^{o}S (Figure 7.7). The first leading mode of the vertical temperature of the EOF which explains about 52% of the total variance with homogeneous sign of the spatial pattern is retained (Figure 7.7). Strong spatial loading patterns occur between 20 and 160 m depth matching with the strong variations

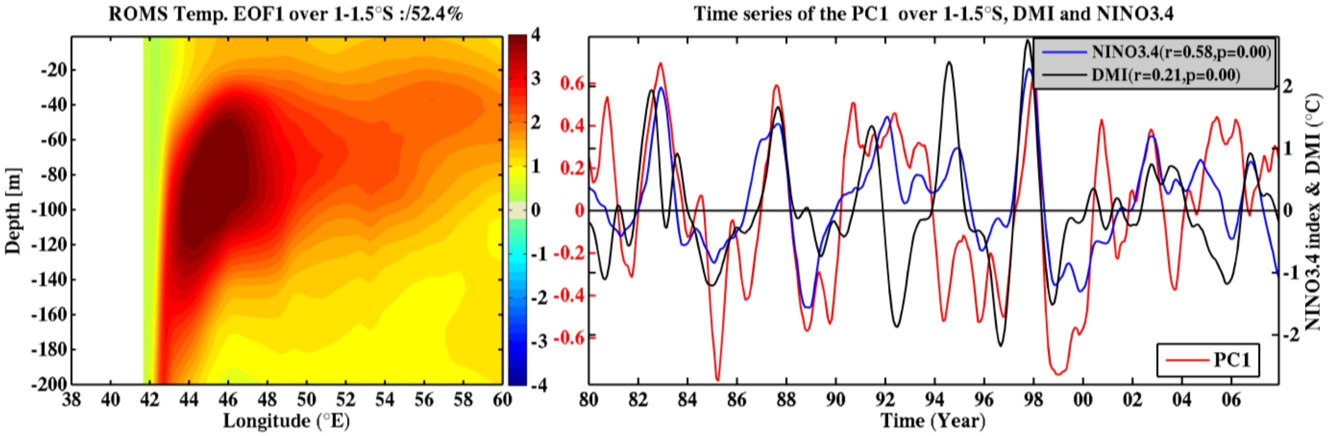

Figure 7.7: The first EOF mode for the upper ocean temperature (in 200 m depth) from 38 to 60°E averaged over 1-1.5°S in tropical western Indian Ocean and their corresponding principal component time series (in red). The DMI (in black) and the Niño3.4 index (in blue) are added (The time series are smoothed by seven months running mean).

of the temperature. The offshore region appears to the east of the strongest loadings in this EOF with upward advection toward the surface waters. The PC1 of the upper temperature anomalies correlate with the Niño3.4 index and the DMI with values of 0.58 and 0.21 significant at the 95% level, respectively. Therefore, the vertical temperature anomalies in the offshore region between 48 and 50°E and nearby are associated with the ENSO and the IOD. Moreover, significant correlation of the PC1 with the Niño3.4 index and DMI could be obtained if they are stratified in calendar months owing to that the ENSO and IOD signals in the tropical Indian Ocean are annually phase-locked.

Figure 7.8 displays standard deviation of the monthly PC1 through the offshore region from 38 to 60°E averaged between 1 and 1.5°S for the vertical temperature anomalies stratified in calendar months. The PC1 shows relatively strong standard deviation from August to December which peaks in December at about 0.4°C. The vertical temperature anomalies in this region mostly correlate with the Niño3.4 index (r=~0.6) at 95% significant level when the Niño3.4 index lags behind the PC1 by 1-3 months. Moreover, the correlation between the PC1 of the vertical temperature anomalies in the region with the DMI peaks at 2-4 lag months. Monthly correlation of about 0.42 appears between the PC1 of the vertical temperature anomalies and the DMI in only December at the 95% significant level (Figure 7.9b). However, the Niño3.4 index and the PC1 of the vertical temperature anomalies show significantly strong correlation throughout the year, except in August, and the correlation peaks in January at about 0.8 (Figure 7.9c). Therefore, strong variations of the interannual temperature in the upper 200 m which are related to the thermocline variation in the offshore region can be associated mainly with the ENSO and IOD signals.

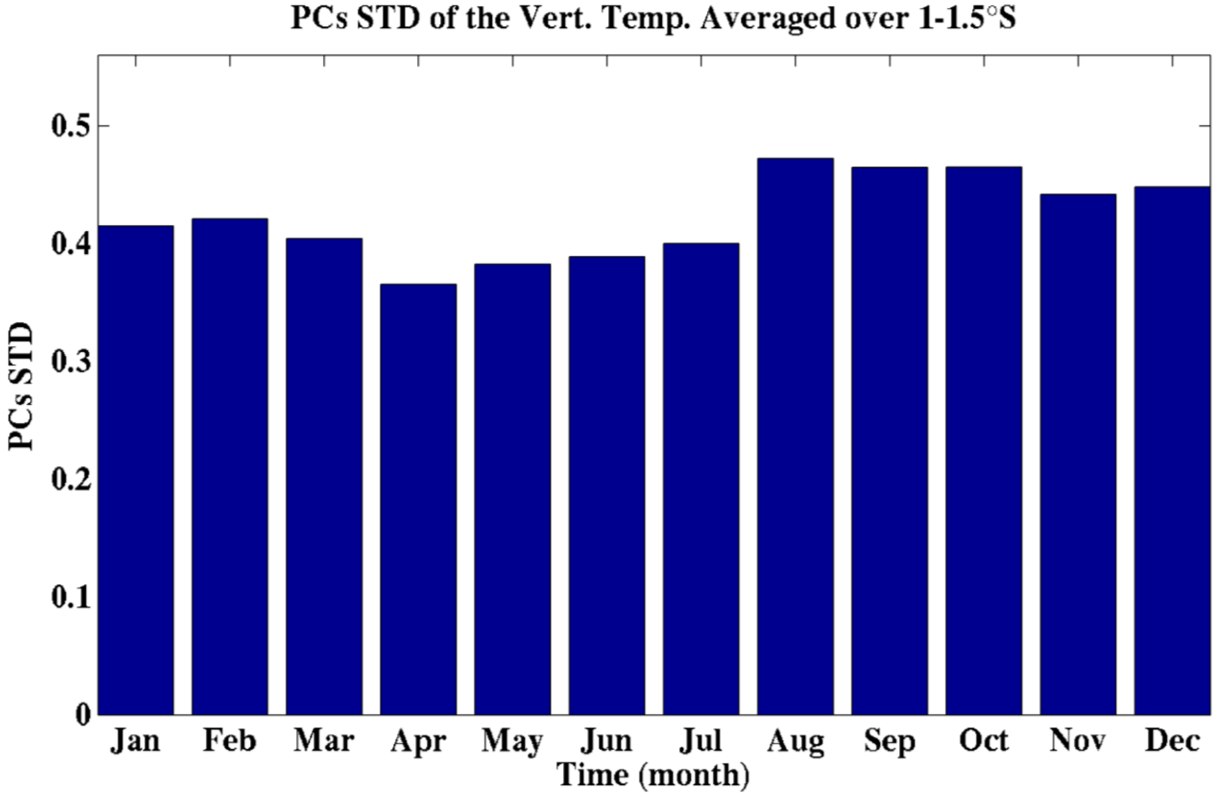

Figure 7.8: Monthly standard deviation of the principal component time series with EOF1 of the vertical temperature anomaly in upper 200 m depth from 38 to 60^{o}E averaged over 1-1.5^{o}S.

To summarize, the upper ocean temperature in the tropical western Indian Ocean shows spatial and temporal variability. The offshore region around 48-50^{o}E averaged between 1 and 1.5^{o}S shows high interannual temperature variability in the upper 200 m. The highest temperature variations are confined to the subsurface, and they match with anomalous thermocline depths. Moreover, the subsurface temperature variations in the offshore region strongly relate to the ENSO and IOD. The Tanzanian shelf region indicates weak temperature variations in the upper 200 m with weak influences of ENSO and the IOD. The next section deals with the sensitivity experiments in the region to investigate the relative contributions of the local surface heat fluxes and lateral remote influences on the subsurface temperature and SST variability.

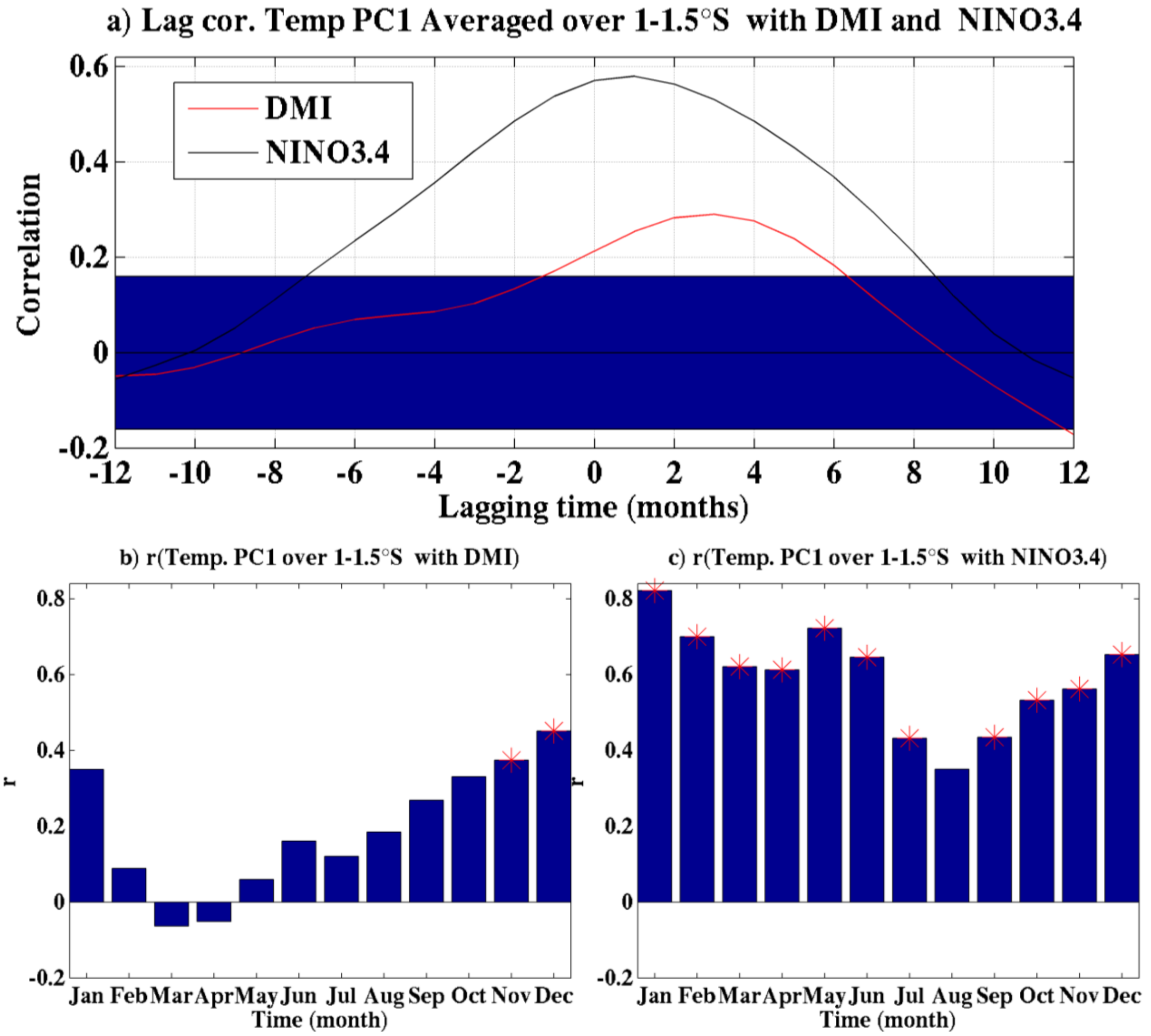

Figure 7.9: As Figure 7.5 but for the PC1 of the vertical temperature anomalies from 38 to 60°E averaged over 1-1.5°S.

7.3 Sensitivity Experiments on the Upper Temperature Variability

Sensitivity experiments are conducted in the tropical western Indian Ocean in order to understand the relative roles of the surface heat fluxes and lateral boundary conditions on the upper ocean temperature variability in the region. Two sensitivity experiments are performed, one with climatological surface heat fluxes (EXP_CLIM_FLUX) and the other with climatological SODA boundary conditions (EXP_CLIM_SODA). The experiments aim to understand the responses of the interannual temperature variability in the upper ocean to the local surface and remote forcings in the Tanzanian shelf region and offshore.

7.3.1 Sensitivity Experiments on the Local Surface Forcing

Figure 7.10 displays standard deviation of the vertical temperature anomalies (1st panel) and variance (%) of monthly vertical temperature anomalies explained by the monthly climatology (2nd panel) in the upper 200 m for EXP_CLIM_FLUX. The vertical transects of the temperatures are obtained from 38 to 60^{o}E being averaged between 1 and 1.5^{o}S in Figure 7.10 (a, c) and between 9 and 9.5^{o}S in Figure 7.10 (b, d) from 1980 to 2007. The experiment aims to understand the sensitivity of the vertical temperature anomalies in the Tanzanian shelf and offshore to the local surface heat fluxes.

In the temperature transect through the offshore region, the strong interannual temperature variations (standard deviation ~2-3^{o}C) between 40 and 160 m depth in EXP_REF are reduced to less than 1.7^{o}C in EXP_CLIM_FLUX (Figure 7.10a). The patterns of the highest interannual variations of the vertical temperature continue to be confined to the offshore subsurface waters between 42 and 48^{o}E. Furthermore, in this region, higher seasonality than that in EXP_REF tends to explain the temperature variability in the upper 40 m (explained variance >80%) being confined to the coast where it reaches below 200 m (Figure 7.10c). Since the mixed layer temperature tendency shows no significant relationship with the surface latent heat fluxes in the offshore region, the influences of the surface forcing can be associated with the local Ekman pumping from wind stress curl. Anomalous local Ekman downwelling and upwelling leads to region of deepened and elevated thermocline, which results in warm and cool temperature in the region, respectively.

Figure 7.10b displays the standard deviation of the vertical temperature anomalies through the Tanzanian shelf region. The variability of the subsurface temperature is reduced (standard deviation <1.5°C) in the transect through the Tanzanian shelf region for EXP_CLIM_FLUX Such high temperature variations are located further east between 30 and 80 m depth from 48 to 60°E. In this region, stronger seasonality than that from EXP_REF tends to explain the temperature variability to deeper depth, in the upper 80 m (explained variance >90%) being confined to the coast where it reaches below 200 m (Figure 7.10d). A distinct separation between the influences of the seasonality and interannual variability appears also in the transect through the Tanzanian shelf region in EXP_CLIM_FLUX.

In general, the local surface forcing plays a role in the interannual temperature variability further offshore and near the coast in the transects of the upper ocean temperature (0-200 m depth) through the region of the lowest and highest SST variations in the tropical western Indian Ocean, respectively. The highest interannual variations of the vertical temperature are reduced to about half of EXP_REF. Also, the regional variability explained by the seasonality is increased and deepened in both transects. Thus, the local surface forcing explains the interannual variability in the near surface. The next section deals with the lateral remote influences on the vertical structure of the upper ocean temperature in the tropical western Indian Ocean.

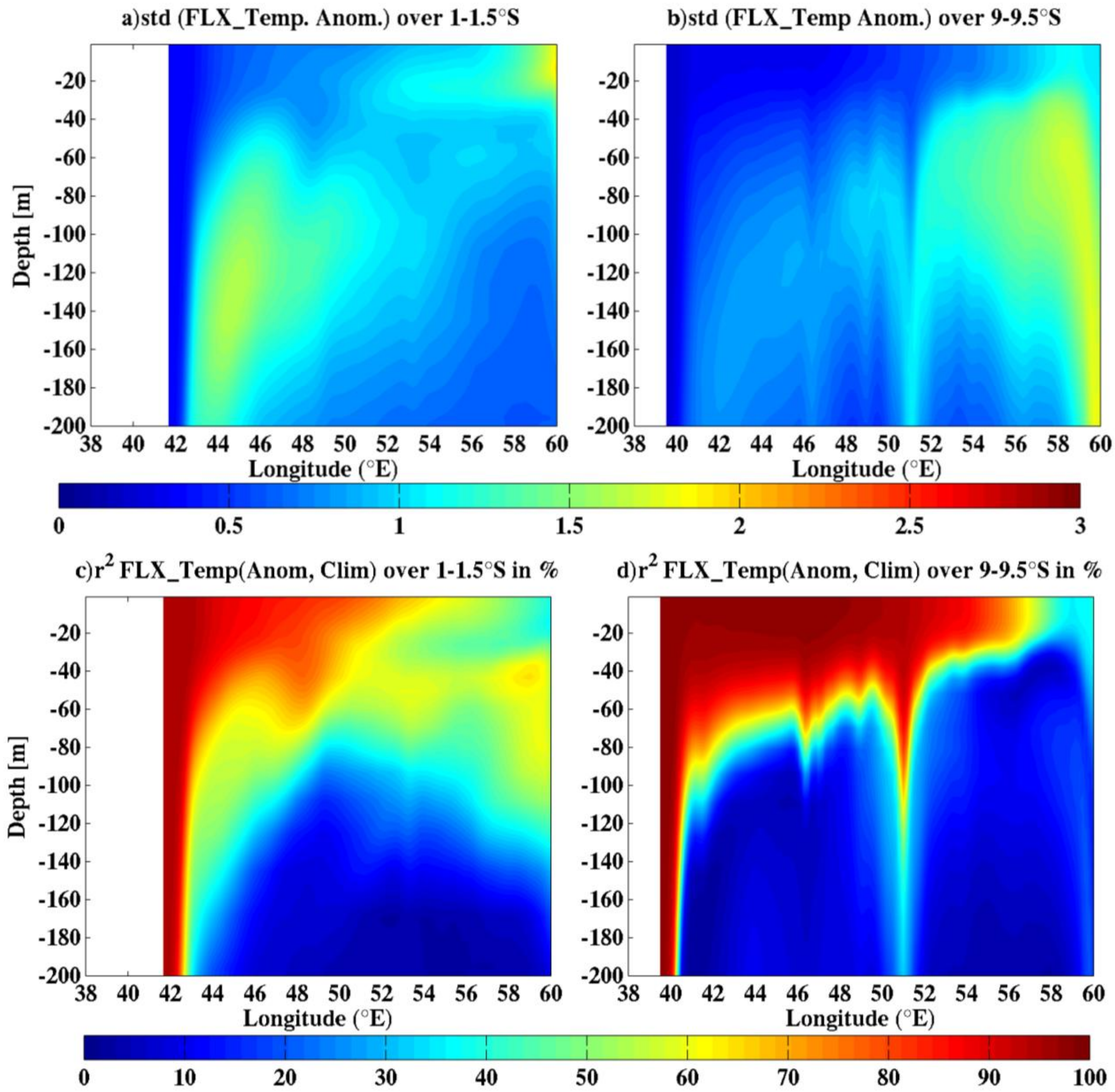

Figure 7.10: Standard deviation from EXP_CLIM_FLUX for the vertical temperature anomaly (1st panel) and variance (%) of monthly SST anomalies explained by the monthly climatology (2nd panel) from 38°E to 60°E averaged over (a, c) 1-1.5°S and (b, d) 9-9.5°S from 1980 to 2007 in the upper 200 m.

7.3.2 Sensitivity Experiments on the Lateral Boundary Conditions

Figure 7.11 displays standard deviation of the vertical temperature anomalies (1st Panel) and variance (%) of monthly vertical temperature anomalies explained by the monthly climatology (2nd Panel) for EXP_CLIM_SODA from 1980 to 2007. The vertical transects are extracted from 38°E to 60°E averaged between 1 and 1.5°S through the offshore region for Figure 7.10 (a, c) through the Tanzanian shelf waters averaged between and between 9 and 9.5°S for Figure 7.10 (b, d) in the upper 200 m.

The vertical structure of the temperature transects through the regions with the lowest and highest SST variations in the Tanzanian shelf region and further offshore indicates different spatial patterns, respectively. In the temperature transect through the offshore region, high interannual temperature variations (standard deviations 2-3°C) in EXP_REF between 40 and 160 m depth are reduced to less than 2.5°C. The patterns of the highest interannual variations of the vertical temperature continue to be confined to the offshore subsurface waters between 42 and 48°E. Furthermore, in this region, similar seasonality to EXP_REF tends to explain the temperature variability in upper 40 m depth (explained variance >65%) being confined to the coast where it reaches below 200 m. Anomalous downwelling and upwelling Rossby waves generated during ENSO and IOD events respectively lead to deepened and elevated thermocline and hence in warming and cooling temperature in the region. On the other hand, high variability of the subsurface temperature is reduced (standard deviation <1.5°C) in the transect through the Tanzanian shelf region. It appears further offshore between 30 and 80 m, being located between 48 and 60°E. In this region, the stronger seasonality than that from EXP_REF tends to explain the temperature variability in upper 60 m depth (explained variance >90%) being confined to the coast where it reaches below 200 m depth. A distinct separation between the influences of seasonality and interannual variability appears in the transect through the Tanzanian shelf region.

In general, lateral remote influences play a role in the interannual vertical temperature variability in the tropical western Indian Ocean particularly further offshore in the transect of the upper ocean temperature (in 200 m depth). The highest interannual variations of the vertical temperature are reduced to about half of EXP_REF. Also, the regional variability which is explained by the seasonality are increased and deepened in both transects. Thus, lateral remote influences explain the interannual variability on the surface.

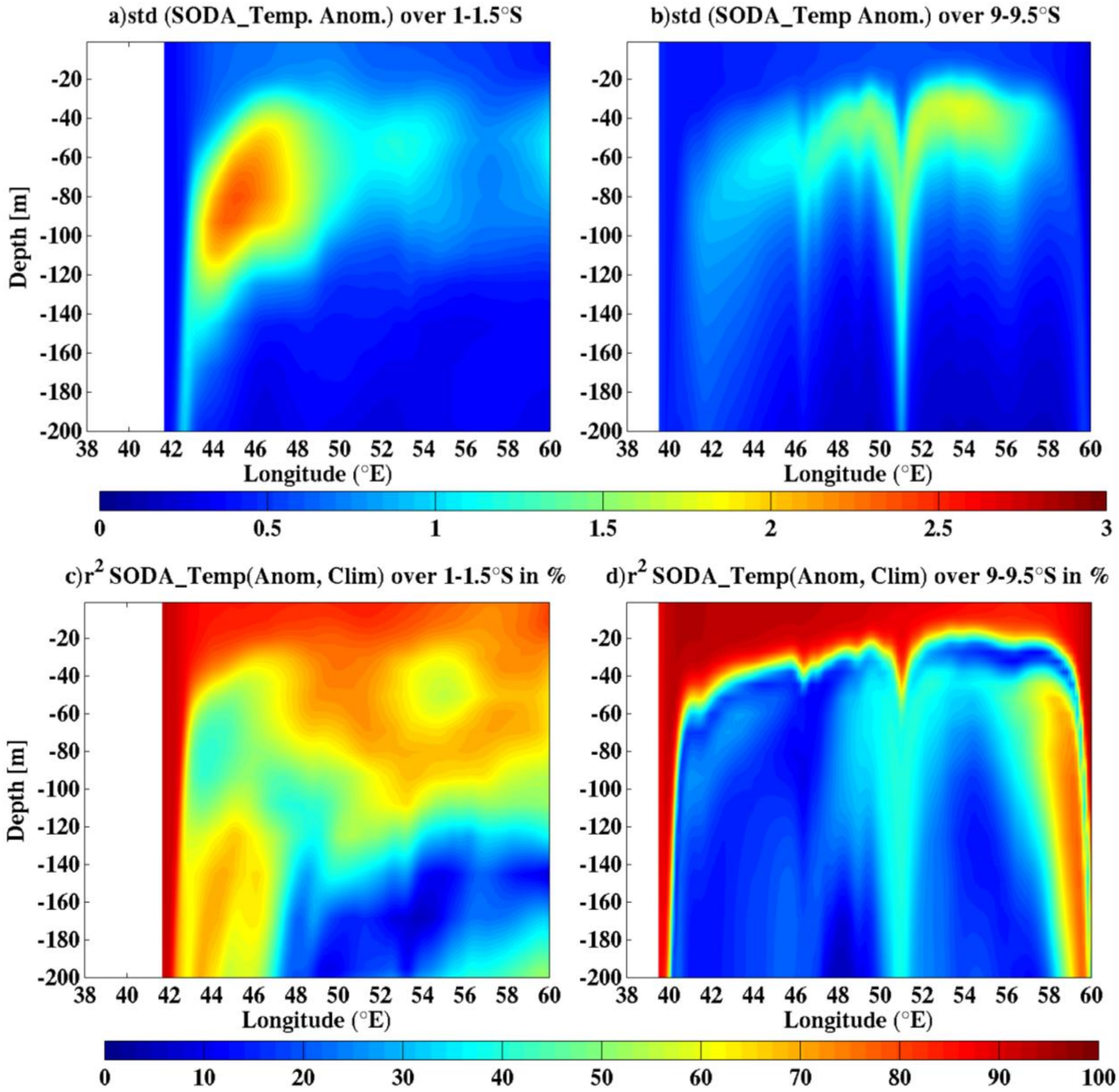

Figure 7.11: Standard deviation from EXP_CLIM_SODA for the vertical temperature anomaly (1st panel) and variance (%) of monthly SST anomalies explained by the monthly climatology (2nd panel) from 38°E to 60°E averaged over (a, c) 1-1.5°S and (b, d) 9-9.5°S from 1980 to 2007 in the upper 200 m.

7.4 Summary

The Tanzanian shelf region and offshore open ocean region shows different variability between the sea surface and subsurface temperature at interannual timescales. Weak interannual variations of the vertical temperature anomalies occur in the Tanzanian shelf region in the upper 200 m. The region experiences weak interannual variations in the thermocline suggesting that local forcing are responsible for the variability. However, strong variability in the thermocline to the east of the Tanzanian shelf waters leads to strong subsurface interannual variability which its advection could influence the Tanzanian shelf region at that depth. The offshore region experiences strong interannual variability in the vertical temperature with the highest variability between 30 and 130 m depth. The regional variability of the subsurface temperature cannot be explained by the seasonality, and thus, they are related to modes of interannual variability. Strong interannual variability in the thermocline depth associated with the local surface forcing and the remote forcing from ENSO and the IOD is responsible for the strong interannual variability in the region. The strongest interannual variability in the mid depth between 40 and 130 m seems to be upwelled towards the surface. Therefore, surface and subsurface temperatures in Tanzanian shelf region vary in the same way with weak interannual variability. However, stronger interannual variability of the temperature occurs in the subsurface waters than in the SST in the offshore region. The strong variability in the offshore region is related to strong interannual variability in the thermocline associated with ENSO and the IOD.

Chapter 8

Conclusion and Recommendations

8.0 Introduction

In this thesis, a model of the tropical western Indian Ocean has been designed to investigate variability in the Tanzanian shelf region and offshore. A realistic simulation of the Regional Oceanic Modeling System (ROMS) was conducted in the region to investigate the processes associated with the variability. The model was forced from 1978 to 2007 by National Centers for Environmental Prediction (NCEP) reanalysis winds and heat fluxes with a two year spin-up time. This experiment was named reference experiment (EXP_REF). In addition to that, two sensitivity experiments were conducted with the same domain configuration of the EXP_REF experiment. The surface forcings were kept as a climatology for EXP_CLIM_FLUX, and the lateral boundary conditions were kept as a climatology for EXP_CLIM_SODA. The ability of the model to reproduce variability in the region was extensively evaluated using observations, hydrographic and satellite data. Furthermore, another realistic experiment forced with the monthly mean Comprehensive Ocean and Atmosphere Data Sets (COADS) winds and heat fluxes (da Silva et al., 1994) for 10 years with a 3 year spin-up time was performed for evaluation of the mean and annual cycle of the model.

The ROMS model seems to reproduce the mean state, annual cycle and interannual variability in the tropical western Indian Ocean fairly well. The model SST from experiments forced with NCEP and COADS agrees with that from CARS2009 and Indian Ocean Hydrobase database in the annual mean and seasonal cycle as well as with in *situ* data around Chumbe Island, AVHRR and TMI. The last three datasets were also used for seasonal and interannual SST validation, and they are in good agreement. The simulated sea surface salinity (SSS) reasonably agrees with that from the WOA2009 in the tropical western Indian Ocean for the annual mean and for the annual cycle. The SSS from the model forced with the NCEP is relatively fresher than that from the COADS run and WOA2009. This deviation could be due to differences in the spatial and temporal resolutions as well as initial and lateral boundary conditions of the models forced with COADS and NCEP as well as the WOA2009 data. Moreover, the difference between the two model simulations is related to the presence of a restoring term for the COADS run which is absent for the NCEP experiment. Along with the good agreement between the volume transports for the two realistic models, the model surface currents and sea surface height are estimated well with the estimated geostrophical currents and sea surface height from AVISO, respectively. The annual mean and the annual cycles of thermocline structure match with previous studies with minimum depth of about 70-80 m between 5-10^{o}S and 45-60^{o}E as reported by Xie et al. (2002) and Hermes and Reason (2008). The vertical structure of the annual mean temperature and salinity from 38 to 60^{o}E, averaged over 10-10.5^{o}S is also in good agreement. The interannual variations of the SST for EXP_REF, AVHRR, TMI and *in situ* measurements off Chumbe Island in the tropical western Indian Ocean capture signals of the large-scale climate variability modes. EXP_REF captures the El Niño/positive IOD events of 1982/1983, 1987/1988 and 1997/1998, and the La Niña/negative IOD events of 1984/1985, 1989 and 1999 in agreement with the satellite data. Thus, the ROMS model forced with NCEP realistically simulated the variability in the tropical western Indian Ocean. Therefore, using the model, the key questions raised in Chapter 1 (introductory chapter), highlighted in bold, are summarized one by one in the following sections:

8.1 How does the Northeast Madagascar Current (NEMC) contribute to the volume, heat and salt transport and budgets in the coastal waters of Tanzania?

The annual mean state of the upper ocean circulation displays the Northeast Madagascar Current (NEMC) corresponding with relatively cool and fresh waters focused to the Tanzanian shelf region. The annual mean speeds of the NEMC are stronger than 100 cm/s at the northern tip of Madagascar as for the East African Coast Current (EACC) to the north of 8^{o}S in the Tanzanian shelf region. A tongue of relatively cool (SST ~27^{o}C) and fresh water (SSS <34.8 ppt) extends from the north of Madagascar towards the Tanzanian water in the annual mean. Such SST and SSS distributions suggest influences of the NEMC in the Tanzanian shelf region. The relatively warm and fresh waters in the southern Tanzanian shelf region are related to warming from horizontal advection from the NEMC and surface heat fluxes as well as from a small downwelling in the region.

Seasonality in the upper ocean circulation and properties occurs between the Tanzanian shelf waters and that to the north of Madagascar, where the NEMC and the EACC are in phase throughout the year. The volume transport of the NEMC and the EACC peaks in June through July. Throughout the year, the ocean currents, temperature and salinity show strong variability in the north of Madagascar on the path of the NEMC. This suggests that the westward NEMC plays a role in the process of the temperature and salinity distributions to the north of Madagascar towards the Tanzanian shelf region. Such distribution may be attributed to the advection or to interruption of the upwelled water from the Seychelles-Chagos ridge reported by Hermes and Reason (2008) and Yokoi et al. (2008). The variability of the volume transport, the ocean currents, temperature and salinity in the north of Madagascar on the path of the NEMC mirrors those in the middle Tanzanian on the path of the EACC throughout the year.

The cross-shore currents show a core of intense flow for the westward NEMC near the northern coast of Madagascar between 11^{o}S and 13^{o}S throughout the year. The effect of the NEMC on the temperature and salinity distributions in the transect is by interrupting the cold isotherms and salty isohalines in the region. Along with the wind stress and surface heat flux over this region, the patterns of the upper ocean circulation and properties suggest that the westward NEMC plays a strong role in the temperature and salinity distributions. The NEMC possibly carries warm surface waters toward the Tanzanian shelf region during November, January and May, and cold waters in July. Furthermore, the NEMC carries freshwater in May and July and salty waters in November to January as shown near the north coast of Madagascar. Similar seasonal distribution of the sea temperature and salinity occur in the equatorward EACC. When the NEMC lags behind the EACC by two months, the EACC correlates with the NEMC (r=~0.7) at the 95% significant level. The EACC in the Tanzanian shelf region carries warm surface waters northwards during May, November and January, and cold waters in July as the NEMC. Furthermore, the EACC respectively carries the lowest and highest surface salinity waters northwards as the NEMC near the north coast of Madagascar in May and November.

The influences of the NEMC in terms of volume, heat and salt budget in the coastal waters of Tanzania are investigated. The NEMC seems to influence the water masses with cooler and low salinity water, and warmer and salty water in the southern summer and winter, respectively. However, the freshwater flux through the ocean surface interface (between the ocean and the atmosphere) and river run-off contributions to the water budget in the region are not explicitly considered and their influences cannot be neglected completely. The modelling results found that there are strong seasonal variations in the upper ocean circulation and properties of the Tanzanian shelf and to the north of Madagascar, and that the NEMC and the EACC are in phase throughout the year. However, it is possible that there may be a lag between the circulation and properties in these two regions which may have been missed due to averaging over long periods and large areas.

8.2 How large is the interannual variability of the sea surface temperature in the tropical western Indian Ocean compared to the annual cycle?

The tropical western Indian Ocean indicates differences in the variability of the SST between the Tanzanian shelf region and offshore. The seasonality in the region tends to explain most of the regional SST variability, except along the equator, particularly in the open ocean. This suggests higher interannual variability in the SST along the equator than the rest of the tropical western Indian Ocean.

The Tanzanian shelf region, linked to the north of Madagascar, experiences weaker interannual variations than the offshore region. The Tanzanian shelf region and that extending to the north of Madagascar experiences the weakest interannual variations of the SST and these are only significant at about a five year period. However, the strongest interannual variations of the SST occur in the offshore region with two significant periods, near a period at about 2.7 and 5 years. These periods reflect the interannual variability of the ENSO and IOD with strong influences on the offshore region. The strongest impacts of the ENSO and IOD signals appear at two to four months lagging behind the SST in the region. This is in agreement with Klein et al. (1999) and Reason et al. (2000) who suggested that the tropical Indian Ocean warms one season after peak in the SST anomalies in the equatorial Pacific. The strongest spatial influence of these large-scale modes appears in the offshore region. Thus, these climate modes might induce strong influences on the interannual SST variations through the local surface forcing or remote forcing in the region.

The interannual variability of the SST is dominantly influenced by the surface heat fluxes related to the shortwave radiation in conjunction with the NEMC advection in the Tanzanian shelf region. Strong trade winds in the Tanzanian shelf region and to the north of Madagascar carry away moisture and cloud, leaving the region free from cloud in warm years. This could be a reason for the positive anomalies in shortwave radiation in 1987/1988 and 1998, and negative anomalies in 1984, 1985, and 1994-1996. The positive and negative anomalies of the shortwave radiation slightly precede the enhanced and decreased anomalous latent heat fluxes, respectively. The positive and negative shortwave radiation anomalies warm and cool the SST anomalies in the region and oppose the effect of the anomalous latent heat fluxes, respectively. The local SST anomalies are then advected by the NEMC mean flow. As a result, weak SST anomalies occur in the Tanzanian shelf region and to the north of Madagascar from the NEMC.

The thermocline depth is closely related to the mixed layer temperature tendency and SST in the offshore region. Thus, the thermocline interannual variations are most important to the strong interannual variability of the SST in the offshore region. In this region, the deepened and elevated thermocline depths respectively occur during strong warm events in 1982/1983, 1987/1988, and 1997/1998, and cool events in 1984/1985, 1988/1989, 1996 and 1999/2000. The thermocline variations are induced by local Ekman pumping from local wind stress curl, and by remote forcing from large-scale variability modes. The remote forcing is related to the ENSO and IOD signals in the offshore region as there is strong correlation between the mixed layer tendency and SST with the Niño3.4 index and the DMI. Thus, anomalous local downwelling (upwelling) Ekman and downwelling (upwelling) Rossby waves from large-scale climate modes (ENSO and the IOD) correspondingly lead changes in thermocline depth which then results in changes in temperature in the region.

8.3 How does the upper ocean temperature vary in the tropical western Indian Ocean in relation to the SST?

The region with the strongest SST variability in the offshore region lies over high subsurface temperature variations located between 30 and 130 m. Such a region corresponds with strong variations in the thermocline depth. The lowest SST variations in the Tanzanian shelf waters lie over the subsurface waters with the smallest temperature variations in the upper 200 m. It matches with weak variations in the thermocline depth. The highest regional variability of the subsurface temperature is more explained by interannual variability. Additionally, both regions with strong variations in the subsurface temperature are related to strong thermocline variations. Thus, thermocline variations can be associated with local Ekman pumping and/or remote influence from the large-scale climate modes.

Different influences of the surface forcing and lateral boundary conditions appear in the Tanzanian shelf region and offshore. In the Tanzanian shelf region, the upper temperature is influenced mainly by the local surface forcing. In the offshore region, both lateral boundary conditions and surface forcing influence the upper temperatures. As shown in the interannual variability in the SST, anomalous local downwelling (upwelling) and downwelling (upwelling) Rossby waves generated during ENSO and IOD events lead to anomalies in the thermocline depth and hence in subsurface temperature.

8.4 Summary and recommendations

The tropical western Indian Ocean shows variability in seasonal cycle and interannual time scale. The NEMC and EACC are in phase throughout the year with strong correlation of about r=~0.7 at the 95% significant level when the NEMC lags behind the EACC by two months. The NEMC contributes warm and fresh surface waters toward the Tanzanian shelf region during May, and cold and salty waters in November. The weakest interannual SST variations, which lie over the weak subsurface waters variations, occur in the Tanzanian shelf region. The strongest interannual SST variations, which lie over the strongest subsurface temperature variations, occur offshore. The interannual variability is asccocated with El Niño-Southern Oscillation (ENSO) and Indian

Ocean Dipole (IOD) events, which induce changes in the thermocline and surface forcing in the region. Local surface heat flux exchanges driven by the anomalous shortwave radiation dominate the weakest interannual SST variability in the Tanzanian shelf region, with some contribution by the advection of heat anomalies from the NEMC. Further offshore, the strongest interannual variability of the SST is dominated by the thermocline variations induced by local Ekman pumping from local wind stress curl and by remote forcing from large-scale climate modes.

Owing to marine and coastal contributions to the socio-economic development of Tanzania and its neighbouring countries, a better understanding of interannual SST variability in the tropical western Indian Ocean is crucial. Such understanding will improve planning and management of climate-sensitive activities in the East African marine ecosystem region as well as marine and coastal shipping activities in the Tanzanian shelf region. Thus, further investigation into the variability in the region is needed. Several studies accompanied by the numerical modeling, especially coupled ocean-atmosphere models should be conducted in the region in order to ascertain the knowledge of the regional variability. These studies should focus on different timescales in the region to enhance our understanding on the coupled ocean-atmosphere from mesoscale to large-scale.

References

Achuthavarier, D., and V. Krishnamurthy, 2009: The Leading Mode of Variability in the Indian Monsoon Region in the Absence of ENSO Variability in the NCEP CFS. COLA Technical Report 288.

Alexander, M. A., I. Blade´, M. Newman, J. R. Lanzante, N. C. Lau, and J. D. Scott, 2002: The atmospheric bridge: The influence of ENSO teleconnections on air-sea interaction over the global oceans. *Journal of Climate,* **15,** 2205–2231.

Alory, G., S. Wijffels and G. Meyers, 2007: Observed temperature trends in the Indian Ocean over 1960-1999 and associated mechanisms. *Geophysical Research Letters*, **34**, L02606, doi: 10.1029/2006GL028044.

Alusa, A., and M. Mushi, 1973: A study of the onset, duration and cessation of the rains in East Africa. Proceedings of the Fifth Specialist Meeting on Applied Meteorology in East Africa, Nairobi, Kenya, pp 133-140.

Anderson, D. L. T., and D. J. Carrington, 1993: Modeling interannual variability in the Indian Ocean using momentum fluxes from the operational weather analyses of the United Kingdom Meteorological Office and European Centre for Medium Range Weather Forecasts. *Journal of Geophysical Research,* **98,** 12483–12499.

Annamalai, H., and R. Murtugudde, 2004: The role of the Indian Ocean in regional climate variability. *Ocean-Atmosphere Interaction and Climate Variability, Geophysical Monograph series,* **147,** *American Geophysical Union*, 210–250.

Ashok, K., W. L. Chan, T. Motoi, and T. Yamagata, 2004: Decadal variability of the Indian Ocean dipole. *Geophysical Research Lett*ers, **31**, L24207, doi: 10.1029/2004GL021345.

Barnier, B., L. Siedfridt, and P. Marchesiello, 1995: Thermal forcing for a global ocean circulation model using three-year climatology of ECMWF analyses. *Journal of Marine Systems*, **6,** 363–380.

Behera, S. K., and T. Yamagata, 2001: Subtropical SST dipole events in the southern Indian Ocean. *Geophysical Research Letters*, **28**, 327–330.

Behera, S. K., J. J. Luo, S. Masson, S. A. Rao, H. Sakuma, and T. Yamagata, 2006: A CGCM study on the interaction between IOD and ENSO. *Journal of Climate*, **19,** 1688–1705.

Behera, S. K., P. S. Salvekar, and T. Yamagata, 2000: Simulation of interannual SST variability in the tropical Indian Ocean. *Journal of Climate*, **13,** 3487–3499.

Behera, S. K., R. Krishnan, and T. Yamagata, 1999: Unusual ocean-atmosphere conditions in the tropical Indian Ocean during 1994. *Geophysical Research Letters*, **26**, 3001–3004, doi: 10.1029/1999GL010434.

Bryceson, I., 1982: Seasonality of oceanographic conditions and phytoplankton in Dar es Salaam waters. *University Science Journal (Dar es Salaam University),* **8**, 66-76.

Carton, J. A., and B. S. Giese, 2008: A Reanalysis of Ocean Climate Using Simple Ocean Data Assimilation (SODA), *Monthly Weather Review*, **136**, 2999-3017

Chambers, D. P., B. D. Tapley, and R. H. Stewart, 1999: Anomalous warming in the Indian Ocean coincident with El Niño. *Journal of Geophysical Research*, **104(C2),** 3035–3047, doi: 10.1029/1998JC900085.

Cheng, X., G. Nitsche, and J. M. Wallace, 1995: Robustness of low-frequency circulation patterns derived from EOF and rotated EOF analyses. *Journal of Climate*, **8**, 1709–1713.

Chirokova, G., and P. J. Webster, 2006: Interannual Variability of Indian Ocean Heat Transport. *Journal of Climate*, **19**, 1013–1031, doi: http://dx.doi.org/10.1175/JCLI3676.1.

Collins, C., C. J. C. Reason, and J. C. Hermes, 2012: Scatterometer and reanalysis wind products over the western tropical Indian Ocean. *Journal of Geophysical Research*, **117**, C03045, doi: 10.1029/2011JC007531.

Conkright, M. E., R. A. Locarnini, H. E. Garcia, T. D. O'Brien, T. P. Boyer, C. Stephens, and J. I. Antonov, 2002: World Ocean Atlas 2001: Objective analyses, data statistics, and figures, CD-ROM documentation. Technical report, National Oceanographic Data Center, Silver Spring, MD.

Cutler, A. N., and J. C. Swallow, 1984: Surface currents of the Indian Ocean. (To 25°S, 100°E). I. O. S. Technical Report 187.

da Silva, A. M., C. C. Young, and S. Levitus, 1994: Atlas of Surface Marine Data 1994, Volume 1: Algorithms and Procedures. Technical report 6, United States Department of Commerce, NOAA, NESDIS.

de Ruijter, W. P. M., H. M. van Aken, E. J. Beier, J. R. E. Lutjeharms, R. P. Matano, and M. W. Schouten, 2004: Eddies and dipoles around south Madagascar: Formation, pathways and large-scale impact. *Deep Sea Research*, Part I, **51,** 383– 400.

de Ruijter, W. P. M., H. Ridderinkhof, J. R. E. Lutjeharms, M. W. Schouten, and C. Veth, 2002: Observations of the flow in the Mozambique Channel. *Geophysical Research Letters*, **29(10),** 1502, doi: 10.1029/2001GL013714.

Debreu, L., P. Marchesiello, P. Penven, and G. Cambon, 2011: Two-way nesting in split-explicit ocean models: algorithms, implementation and validation. *Ocean Modelling*, 49-50, 1-21.

Domingues, M. O., O. Mendes, and A. Mendes da Costa, 2005: On wavelet techniques in atmospheric sciences. *Advances in Space Research*, **35,** 831–842.

Dommenget, D., and M. Latif, 2002: A cautionary note on the interpretation of EOFs. *Journal of Climate*, **15**, 216–225.

Donohue, K. A., and J. M. Toole, 2003: A near-synoptic survey of the southwest Indian Ocean. *Deep Sea Research*, Part II, **50,** 1893-1931.

Dubi, A. M., 2000: Coastal erosion. In: Ngusaru, A.S. (Ed). The present state of knowledge of marine science in Tanzania: synthesis report. Tanzania Coastal Management Partnership, Science and Technical Working Group.

Ducet, N., P. Y. Le Traon, and G. Reverdin, 2000: Global high-resolution mapping of ocean circulation from TOPEX/Poseidon and ERS-1 and -2. *Journal of Geophysical Research*, **105**, 19477–19498.

Düing, W., and F. Schott, 1978: Measurements in the source region of the Somali current during monsoon reversal. *Journal of Physical Oceanography*, **8,** 278-289.

East African Meteorological Department, E.A.M.D., 1963a: Climatic seasons of East Africa. East African Meteorological Departmental Report No.8, 4pp.

East African Meteorological Department, E.A.M.D., 1963b: The weather of East Africa, East African Meteorological Department. Pamphlet series No.7, 13pp.

England, M. H., and F. Huang, 2005: On the interannual variability of the Indonesian Throughflow and its linkage with ENSO. *Journal of Climate*, 18, 1435–1444.

Fairall, C. W., E. F. Bradley, D. P. Rogers, J. B. Edson, and G. S. Young, 1996: Bulk parameterization of air-sea fluxes for TOGA COARE. *Journal of Geophysical Research,* **101**, 3747-3764.

Findlater, J., 1969: A major low-level air current near the Indian Ocean during the northern summer. *Quarterly Journal of Royal Meteorological Society,* **95,** 362–380.

Findlater, J., 1978: Observational aspects of the low-level cross-equatorial jet stream. Monsoon Dynamics, T. N. Krishnamurti, Ed., *Birkhauser Verlag*, 1251–1262.

Foltz, G. R., J. Vialard, B. Praveen Kumar, M. J. McPhaden, 2010: Seasonal mixed layer heat balance of the southwestern tropical Indian Ocean. *Journal of Climate*, **23**, 947-965.

Francis, J., S. Mahongo, and A. Semesi, 2000: The coastal environment. In: Eastern Africa atlas of coastal resources of Tanzania. UNEP. Nairobi, Kenya.

Gadgil, S., 2003: The Indian monsoon and its variability. *Annual Reviews of Earth and Planetary Sciences,* ***31*****,** 429–67.

Ganachaud, A., C. Wunsch, J. Marotzke, and J. Toole, 2000: The meridional overturning and large scale circulation of the Indian Ocean. *Journal of Geophysical Research,* **105 (C11)**, 26117-26134.

Gill, A. E., 1980: Some simple solutions for heat-induced tropical circulation. *Quarterly Journal of the Royal Meteorological Society,* **106,** 447– 462.

Godfrey, J. S., A. Alexiou, A. G. Ilahude, D. M. Legler, M. E. Luther, J. P. McCreary, Jr., G. A. Meyers, K. Mizumo, R. R. Rao, S. R. Shetye, J. H. Toole, and S. Wacongne, 1995: The Role of the Indian Ocean in the Global Climate System: Recommendations Regarding the Global Ocean Observing System. *Report of the Ocean Observing System Development Panel, Texas A&M University, College Station, Tex, USA.89pp.*

Gordon, G. L., and J. L. McClean, 1999: Thermohaline stratification of the Indonesian Seas: model and observations. *Journal of Physical Oceanography*, **29**, 198–216.

Griffiths, J., 1959: The variability of annual rainfall in East Africa. *Bulletin of America Society*, **44,** 361-362.

Halley, E., 1686: An historical account of the trade winds and monsoons observable in the seas between and near the tropical with an attempt to assign a physical cause of the said winds. *Philosophical Transactions of the Royal Society*, London, **16**,153-68.

Han, W., and J. P. McCreary, 2001: Modelling salinity distributions in the Indian Ocean. *Journal of Geophysical Research*, **106,** 859–877.

Han, W., J. P. McCreary, Jr., D. L. T. Anderson, and A. J. Mariano, 1999: On the dynamics of the eastward surface jets in the equatorial Indian Ocean. *Journal of Physical Oceanography*, **29**, 2191–2209.

Hannachi A., I. T. Jolliffe, D. B. Stephenson, and N. Trendafilov, 2006: In search of simple structures in climate: simplifying EOFs. *International Journal of Climatology*, **26**, 7–28.

Hastenrath, S., A. Nicklis, and L. Greischar, 1993: Atmospheric-hydrospheric mechanisms of climate anomalies in the western equatorial Indian Ocean. *Journal of Geophysical Research*, **98**, 20219–20235.

Hedström, K., 1997: Users manual for an s-coordinate primitive equation ocean circulation model (SCRUM) version 3.0. Technical report, Institute of Marine and Coastal Sciences, Rutgers University.

Hermes, J. C., and C. J. Reason, 2008: Annual cycle of the South Indian Ocean (Seychelles-Chagos) thermocline ridge in a regional ocean model. *Journal of Geophysical Research*, **113**, C04035, doi: 10.1029/2007JC004363.

Hermes, J. C., and C. J. Reason, 2009: The sensitivity of the Seychelles-Chagos thermocline ridge to large-scale wind anomalies. *ICES Journal of Marine Science*, **66**, 1455-1466.

Hong, C. C., M. M. Lu, and M. Kanamitsu, 2008: Temporal and spatial characteristics of positive and negative Indian Ocean dipole with and without ENSO. *Journal of Geophysical Research*, **113**, D08107, doi: 10.1029/2007JD009151.

Iskandar, I., S. Rao, and T. Tozuka, 2009: Chlorophyll-a bloom along the southern coasts of Java and Sumatra during 2006. *International Journal of Remote Sensing,* **30,** 663–671.

Izumo, T., C. de Boyer Monte´gut, J. J. Luo, S. K. Behera, S. Masson, and T. Yamagata, 2008: The role of the westernArabian Sea upwelling in Indian monsoon rainfall variability. *Journal of Climate*, **21**, 5603–5623.

Jensen, T. G., 1991: Modeling the seasonal undercurrents in the Somali Current system. *Journal of Geophysical Research*, **96**, 22151–22167.

Jensen, T. G., 1993: Equatorial variability and resonance in a wind-driven Indian Ocean Model. *Journal of Geophysical Research*, **98**, 22533–22552.

Jensen, T. G., 2003: Cross-equatorial pathways of salt and tracers from the northern Indian Ocean: Modelling results. *Deep Sea Research, Part II,* **50,** 2111–2128.

Jiddawi, N. S., M.C. Öhman, 2002: Marine fisheries in Tanzania. *Ambio,* **31**: 518-527.

Johnson, D. R., M. Mutua and E. J. Kimani, 1982: Response to annually reversing monsoon winds at the southern boundary of the Somali Current. *Deep Sea Research,* **29**:1217-1227.

Julius, A., 2005: Monitoring programme for resource condition, environmental and biological parameters for Mnazi Bay Ruvuma estuary marine park (MBREMP) Tanzania, Final Project, Fisheries Training Programme, The United Nations University, Iceland.

Kabanova. J. G., 1968: Primary production in the northern part of the Indian Ocean. *Oceanology,* **8**, 214-255.

Keerthi, M. G., M. Lengaigne, J. Vialard, C. de Boyer Montégut, and P. M. Muraleedharan, 2012: Interannual variability of the Tropical Indian Ocean mixed layer depth. *Climate Dynamics,* doi: 10.1007/s00382-012-1295-2.

Klein, S. A., B. J. Soden, and N. C. Lau, 1999: Remote sea surface temperature variations during ENSO: Evidence for a tropical atmospheric bridge. *Journal of Climate*, **12**, 917–932.

Knox, R., 1976: On a long series of measurements of Indian Ocean equatorial currents near Addu Atoll. *Deep Sea Research,* **23**, 211–221.

Krishnamurthy, V., and B. P. Kirtman, 2003: Variability of the Indian Ocean: Relation to monsoon and ENSO. *Quarterly Journal of the Royal Meteorological Society*, **129**, 1623-1646.

Krishnamurti, T., 1996: Monsoons. *Encyclopedia of Climate and Weather*, **2,** 512-515. Oxford University Press, New York.

Krishnamurti, T. N., 1971a: Observational study of the tropical upper tropospheric motion field during the northern hemisphere summer. *Journal of Applied Meteorology*, 1**0**, 1066-1096.

Krishnamurti, T. N., 1971b: Tropical east-west circulation during the northern summer. *Journal of Atmospheric Science*, **28**, 1342-1347.

Lareef, Z., A. S. Rao, and T. Yamagata, 2003: Modulation of Sri Lankan Maha rainfall by the Indian Ocean dipole. *Geophysical Research Letters*, **30**, doi: 10.1029/2002GL015639.

Large, W.G., J. C. McWilliams, and S. C. Doney, 1994: Oceanic vertical mixing: a review and a model with a non-local boundary layer parameterization. *Reviews of Geophysics*, **32**, 363-403.

Leetmaa, A., and H. Stommel, 1980: Equatorial current observations in the western Indian Ocean during 1975 and 1976. *Journal of Physical Oceanography*, **10**, 258–269.

Leetmaa, A., D. R. Quadfasel, and D. Wilson, 1982: Development of the flow field during the onset of the Somali current, 1979. *Journal of Physical Oceanog*raphy, **12**, 1325-1342.

Li, C., and M. Yanai, 1996: The onset and interannual variability of the Asian summer monsoon in relation to land-sea thermal contrast. *Journal of Climatology*, **9,** 358– 375.

Li, T., B. Wang, C. P. Chang, and Y. Zang, 2003: A theory for the Indian Ocean dipole-zonal mode. *Journal of Atmospheric Sciences*, **60,** 2119– 2135.

Liu, P. C., 1994: Wavelet spectrum analysis and ocean wind waves. *Wavelets in Geophysics,* E. Foufoula-Georgiou and P. Kumar, Eds., *Academic Press*, 151–166.

Liu, Z., and M. Alexander, 2007: Atmospheric bridge, oceanic tunnel, and global climatic teleconnections. *Reviews of Geophysics,* **45,** RG2005, doi: 10.1029/2005RG000172.

Mahongo, S. B., 1999: The Tanzanian Sea Level Network. Draft report submitted to IOC, 16pp.

Maltrud, M. E., A. J. Semtner, and R. C. Malone, 1998: Global eddy-resolving ocean simulation driven by 1985–1995 atmospheric winds. *Journal of Geophysical Research*, **103**, 30825–30853.

Mapande, A. T., and C. J. C. Reason, 2005: Interannual rainfall variability over western Tanzania. *International Journal of Climatology*, **25,** 1355-1368.

Marchant, R., C. Mumbi, S. Behera, and T. Yamagata, 2006: The Indian Ocean dipole – the unsung driver of climatic variability in East Africa. *Blackwell Publishing Limited, African Journal of Ecology,* **45,** 4–16..

Marchesiello, P., J. C. McWilliams, and A. Shchepetkin, 2001: Open boundary conditions for long-term integration of regional oceanic models. *Ocean Modeling,* **3,** 1–20.

Mayorga-Adame, C. G., 2007: Ocean circulation of the Zanzibar Channel: A Modeling Approach. Technical report, Theiss Research, La Jolla, California, USA. http://www.theissresearch.org/zanzibar/

McClanahan, T. R., 1988: Seasonality in East Africa’s coastal waters. *Marine Ecology-Progress Series*, **44**, 191-199.

McCreary, J. P., Jr., P. K. Kundu, and R. L. Molinari, 1993: A numerical investigation of dynamics, thermodynamics and mixed-layer processes in the Indian Ocean. *Progress in Oceanography,* **31**, 181–244.

McGill, D. A., 1973: Light and nutrients in the Indian Ocean. In: Zeitschel, B., Gerlach, S. A. (Eds.). *The biology of the Indian Ocean*, **3,** Springer-Verlag, Berlin, p 53-102

McPhaden, M. J., G. Meyers, K. Ando, Y. Masumoto, V. S. N. Murty, M. Ravichandran, F. Syamsudin, J. Vialard, L. Yu, and W. Yul, 2009: RAMA: The Research Moored Array for African-Asian-Australian Monsoon Analysis and Prediction. *Bulletin of the American Meteorological Society,* **90**, 459-480, http://dx.doi.org/10.1175/2008BAMS2608.1.

Meyers, G., 1996: Variation of Indonesian throughflow and the El Niño–Southern Oscillation. *Journal of Geophysical Research,* **101** (C5), 12 255–12 263.

Meyers, G., P. McIntosh, L. Pigot, and M. Pook, 2007: The Years of El Niño, La Niña, and Interactions with the Tropical Indian Ocean. *Journal of Climate,* **20,** 2872-2880, doi:10.1175/JCL14152.1.

Morrow, R., and F. Birol, 1998: Variability in the southeast Indian Ocean from altimetry: Forcing mechanism for the Leeuwin Current. *Journal of Geophysical Research*, **103**, 18529–18544.

Mpeta, E. J., 1997: Intra-seasonal convection dynamics over southwest and northeast Tanzania: An observational study. MSc. Thesis, University of Cape Town, South Africa.

Murtugudde, R., and A. J. Busalacchi, 1999: Interannual variability of the dynamics and thermodynamics, and mixed layer processes in the Indian Ocean. *Journal of Climate,* **12,** 2300–2326.

Murtugudde, R., J. P. McCreary, and A. J. Busalacchi, 2000: Oceanic processes associated with anomalous events in the Indian Ocean with relevance to 1997–1998. *Journal of Geophysical Research,* **105,** 3295–3306.

Mutai, C. C., and M. N. Ward, 2000: East African rainfall and the tropical circulation/convection on intraseasonal to interannual timescales. *Journal of Climate,* **13**, 3915–3939.

Nagura, M., and M. Konda, 2007: The seasonal development of an SST anomaly in the Indian Ocean and its relationship to ENSO. *Journal of Climate,* **20**, 38–52.

Newell, B. S., 1957: A preliminary survey of the hydrography of the British East African Coastal waters. *Fishery Publications Number* 9. Her Majesty's Stationery Office, London, 21 pp.

Newell, B. S., 1959: The hydrography of British East African coastal waters. II. *Fishery Publications,* London, **12**, 1-18.

Ngusaru, A., and S. Mohammed, 2002: Water, salt and stoichiometrically linked nutrient budgets for Chwaka Bay, Tanzania. Western Indian Ocean Journal of Marine Sciences, **1,** 97-106.

Nyandwi, N., and A. Dubi, 2001: Episodic atmospheric changes and their impact on the hydrography of coastal waters in Tanzania. *Climate Research,* **18**, 157 – 162.

O'Brien, J. J., and H. E. Hurlburt, 1974: An equatorial jet in the Indian Ocean theory. *Science,* **184**, 1075–1077.

Obura, D., L. Celliers, H. Machano, S. Mangubhai, M. Mohammed, H. Motta, C. Muhando, N. Muthiga, M. Pereira, and M. Schleyer, 2002. Status of Coral reefs in Eastern Africa: Kenya, Tanzania, Mozambique and South Africa. In: Wilkinson C (ed) Status of Coral Reefs of the World, 2002. Global Coral Reef Monitoring Network (GCRMN). Australian Institute of Marine Science, Townsville, Australia, pp. 63-78.

Ogallo, L. J., 1989: The spatial and temporal patterns of East African seasonal rainfall derived from principle component analysis. *International Journal of Climatology,* **9**, 145-167.

Ogallo, L. J., J. F. Janowiak, and M. S. Halpert, 1988: Teleconnection between seasonal rainfall over East Africa and global sea surface temperature anomalies. *Journal of the Meteorological Society of Japan,* **66**, 807–822.

Palastanga, V., P. J. van Leeuwen, and W. P. M. de Ruijter, 2006: A link between low-frequency mesoscale eddy variability around Madagascar and the large-scale Indian Ocean variability. *Journal of Geophysical Research,* **111**, C09029, doi: 10.1029/2005JC003081.

Penven, P., J. R. E. Lutjeharms, and P. Florenchie, 2006: Madagascar: A pacemaker for the Agulhas Current system? *Geophysical Research Letters*, **33,** L17609, doi: 10.1029/2006GL026854.

Penven, P., P. Marchesiello, L. Debreu, and J. Lefèvre, 2008: Software tools for pre- and post-processing of oceanic regional simulations. *Environmental Modelling & Software*, **23(5),** 660-662.

Pickard, G. L., and W. J. Emery, 1990: Descriptive Physical Oceanography. 5th edition, Pergamon Press, Oxford, UK.

PrasannaKumar, S., and J. Narverkar, 2005: Seasonal variability of the mixed layer in the central Arabian Sea and its implication on nutrients and primary productivity. *Deep Sea Research Part II: Topical Studies in Oceanography,* **52**, 14-15, pp 1848-1861.

Quartly, G. D., and M. A. Srokosz, 2004: Eddies in the Southern Mozambique Channel. *Deep Sea Research, Part II,* **51**, 69– 83.

Rao, G.L.V., and S. P. Ram, 2005: Upper ocean physical processes in the Tropical Indian Ocean, National institute of Oceanography, Goa, India, 68 pp.

Rao, R. R., and R. Sivakumar, 2000: Seasonal variability of near-surface thermal structure and heat budget of the mixed layer of the tropical India n Ocean from a new global ocean temperature climatology. *Journal of Geophysical Res*earch, **105(C1),** 995-1015.

Rao, R. R., R. L. Molinari, and J. F. Festa, 1989: Evolution of the climatological near-surface thermal structure of the tropical Indian Ocean. 1. Description of mean monthly mixed-layer depth, and sea surface temperature, surface current, and surface meteorological fields. *Journal of Geophysical Research*, **94**, 10801-10815.

Rao, S. A., and S. K. Behera, 2005: Subsurface influence on SST in the tropical Indian Ocean: Structure and interannual variability, *Dynamics of Atmospheres and Oceans*, **39**, 103–135.

Rao, S. A., S. K. Behera, Y. Masumoto, and T. Yamagata, 2002: Interannual variability in the subsurface tropical Indian Ocean, *Deep-Sea Research II*, **49,** 1549–1572.

Raymond, W. H., and H. L. Kuo, 1984: A radiation boundary for multi-dimensional flows. *Quarterly Journal of Royal Meteorological Society*, **110,**535-551.

Rayner, N. A., P. Brohan, D. E. Parker, C. K. Folland, J. J. Kennedy, M. Vanicek, T. Ansell, and S. F. B. Tett, 2006: Improved analyses of changes and uncertainties in sea surface temperature measured in situ since the mid-nineteenth century: The HadSST2 data set. *Journal of Climate*, **19,** 446–469.

Reason, C., R. Allan, J. Lindesay, and T. Ansell, 2000: ENSO and Climatic Signals across the Indian Ocean basin in the global context: Part 1, Interannual Composite Patterns. *International Journal of Climatology,* **20**, 1285-1327.

Reppin, J., F. A. Schott, J. Fischer, and D. Quadfasel, 1999: Equatorial currents and transports in the upper central Indian Ocean: annual cycle and interannual variability. *Journal of Geophysical Research*, **104**, 15495–15514.

Reverdin, G., D. Cadel, and D. Gutzler, 1986: Interannual displacements of convection and surface circulation over the equatorial Indian Ocean. *Quarterly Journal of the Royal Meteorological Society*, **112**, 43–67.

Saji, N. H., and T. Yamagata, 2003: Structure of SST and surface wind variability during Indian Ocean Dipole mode events: COADS observations. *Journal of Climate*, **16**, 2735–2751.

Saji, N. H., B. N. Goswami, P. N. Vinayachandran, and T. Yamagata, 1999: A dipole mode in the tropical Indian Ocean. *Nature,* **401,** 360-363.

Sakova, I., G. Meyers, and R. Coleman, 2006: Interannual variability in the Indian Ocean using altimeter and IX1-expendable bathy-thermograph (XBT) data: does the 18-month signal exist? *Geophysical Research Letters*, **33**, L20603, doi: 10.1029/ 2066GL027117.

Schott, F. A., J. P. McCreary, and G. C. Johnson, 2004: Shallow overturning circulations of the tropical-subtropical oceans, in Earth Climate: The Ocean-Atmosphere Interaction, *Geophysical Monograph series,* **147,** edited by C. Wang, S. P. Xie, and J. A. Carton, *pp.* 261–304, *American Geophysical Union,* Washington, D. C.

Schott, F. A., S. P. Xie, and J. P. McCreary, Jr., 2009: Indian Ocean circulation and climate variability. *Reviews of Geophysics*, **47**, RG1002, doi: 10.1029/2007RG000245..

Schott, F., and J. P. McCreary, 2001: The monsoon circulation of the Indian Ocean. *Progress in Oceanography*, **51**, 1-123.

Schott, F., J. C. Swallow, and M. Fieux, 1990: The Somali Current at the equator: annual cycle of currents and transports in the upper 1000 m and connection to neighboring latitudes. *Deep-Sea Research*, **37**, 1825–1848.

Shaghude, Y. W., 2003: Coastal impacts of water abstraction and impoundment in Africa: The case of Rufiji River. Framework of the African River Catchments (AfriCat). Electronic version, December 2005. (http://iodeweb1.vliz.be/odin/bitstream/1834/187/1/coastal.pdf)

Shchepetkin, A., and J. C. McWilliams, 1998: Quasi-monotone advection schemes based on explicit locally adaptive dissipation. *Monthly Weather Review,* **126,** 1541–1580.

Shchepetkin, A., and J. McWilliams, 2003: A method for computing horizontal pressure-gradient force in an ocean model with a non-aligned vertical coordinate. *Journal of Geophysical Research*, **108**, 35.1-35.34.

Shchepetkin, A., and J. McWilliams, 2005: The Regional Oceanic Modelling system (ROMS): A split-explicit, free-surface, topography following coordinate oceanic model. *Ocean modelling*, **9,** 347-404.

Shenoi, S. S. C., P. K. Saji, and A. M. Almeida, 1999: Near-surface circulation and kinetic energy in the tropical Indian Ocean derived from Lagrangian drifters. *Journal of Marine Research*, **57**, 885–907.

Smith, S. L., and L. A. Codispoti, 1980: Southwest monsoon of 1979: chemical and biological response of Somali coastal waters. *Science,* **209**, 597-600.

Smith, W. H. F., and D.T. Sandwell, 1997: Global seafloor topography from satellite altimetry and ship depth soundings. *Science,* **277**, 1957-1962.

Song, Q., A. L. Gordon, and M. Visbeck, 2004: Spreading of the Indonesian Throughflow in the Indian Ocean. *Journal of Physical Oceanography,* **34,** 772–792.

Song, Y., and D.B. Haidvogel, 1994: A semi-implicit ocean circulation model using a generalized topography-following coordinate system. *Journal of Computational Physics*, **115 (1),** 228-244.

Sreenivas, P., K. V. Patnaik, and K. V. S. R. Prasad, 2008: Monthly Variability of Mixed Layer over Arabian Sea Using ARGO Data. *Marine Geodesy*, **31**, 1, pp 17-38, **doi:** 10.1080/01490410701812311.

Subrahmanyam, B., V. S. N. Murty, and D.M. Heffner, 2011: Sea Surface Variability in the Tropical Indian Ocean. *Remote Sense Environment,* **115**, 3, 944-956.

Swallow J. C., F. Schott, and M. Fieux, 1991: Structure and transport of the East African Coastal Current. *Journal of Geophysical Research*, ***96***, 22254–22267.

Swallow, J. C., M. Fieux, and F. Schott, 1988: The boundary currents east and north of Madagascar, Part I: Geostrophic currents and transports. *Journal of Geophysical Research*, **93**, 4951–4962.

Swallow, J., 1967: The equatorial undercurrent in the western Indian Ocean in 1964. *Studies in Tropical Oceanography*, **5**, 15–36.

Taft, B. A., 1967: Equatorial undercurrent of the Indian Ocean, 1963. *Studies in Tropical Oceanography*, **40**, 3–14.10.1029/2001GL014098.

Tao, L., and C. Dake, 2012: An Evaluation of Rotated EOF Analysis and Its Application to Tropical Pacific SST Variability. *Journal of Climate*, **25,** 5361-5373, doi:10.1175/JCLI-D-11-00663.1.

Tomczak, M., and J. S. Godfrey, 1994: Regional Oceanography, An introduction. Pergamon, Oxford, UK.

Torrence, C., and P. J. Webster, 1999: Interdecadal changes in the ENSO-Monsoon System. *Journal of Climate*, **12**, 2679-2690.

Torrence, C., and G. P. Compo, 1998: A practical guide to wavelet analysis. *Bullet of the American Metrological Society*, **79,** 61–78.

Tozuka, T., T. Yokoi, and T. Yamagata, 2010: A modeling study of interannual variations of the Seychelles Dome, *Journal of Geophysical Research*, **115**, C04005, doi: 10.1029/2009JC005547.

Udaya Bhaskar, T. V. S., D. Swain, and M. Ravichandran, 2006: Inferring mixed-layer depth variability from Argo observations in the western Indian Ocean. *Journal of Marine Research,* **64 (3),** pp. 393-406.

Udaya Bhaskar, T. V. S., D. Swain, and M. Ravichandran, 2007: Mixed layer variability in Northern Arabian Sea as detected by an Argo float. *Ocean Science Journal*, **42(4),** ISSN 2005-7172.

Ummenhofer, C. C., M. H. England, P. C. McIntosh, G. A. Meyers, M. J. Pook, J. S. Risbey, A. Sen Gupta, and A. S. Taschetto, 2009: What causes southeast Australia's worst droughts? *Geophysical Research Letter,* **36,** L04706, doi: 10.1029/2008GL036801.

Unite Nations Environment Programme, UNEP, 1985: Implications of climate change in the East African coastal region. UNEP Regional Seas Reports and Studies Number 149.

Vinayachandran, P. N., J. Kurian, and C. P. Neema, 2007: Indian Ocean response to anomalous conditions in 2006. *Geophysical Research Letters*, **34**, L15602, doi: 10.1029/2007GL030194.

Vinayachandran, P. N., N. H. Saji, and T. Yamagata, 1999: Response of the equatorial Indian Ocean to an unusual wind event during 1994. *Geophysical Research Letters*, **26(11),** 1613–1616, doi:10.1029/1999GL900179.

Vinayachandran, P. N., P. A. Francis, and S. A. Rao, 2009: Indian Ocean Dipole: Processes and impacts. Current Trends in Science, Platinum Jubilee Special, Indian Academy of Sciences, pp 569-589.

Vissa, N. K, A. N. V. Satyanarayana, B. Prasad Kumar, 2013. Comparison of Mixed Layer Depth and Barrier Layer Thickness for the Indian Ocean using two different Climatologies. *International Journal of Climatology*, **33**, 2855-2870.

Webster, P. J., 1987: The elementary monsoon. In Monsoons, J. S. Fein, P. L. Stephens, (Eds.), pp. 3–32. New York.

Webster, P. J., A. Moore, J. Loschnigg, and R. Leben, 1999: Coupled ocean-atmosphere dynamics in the Indian Ocean during 1997–98. *Nature*, **401**, 356–360.

Wiggert, J. D., J. Vialard, and M. J. Behrenfeld, 2009: Basinwide modification of dynamical and biogeochemical processes by the positive phase of the Indian Ocean Dipole during the SeaWiFS era, in: Indian Ocean Biogeochemical Processes and Ecological Variability, vol. 185, J. D. Wiggert, R. R. Hood, S. Wajih, A. Naqvi, K. H. Brink, and S. L. Smith (Eds.), p. 350.

Wyrtki, K., 1973: An equatorial jet in the Indian Ocean. *Science*, **181**, 262–264.

Xie, S. P., H. Annamalai, F. A. Schott, and J. P. McCreary, 2002: Structure and mechanism of South Indian Ocean climate variability, *Journal of Climate*, **15**, 864–878.

Yamagata, T., S. K. Behera, J. J. Luo, S. Masson, M. R. Jury, and S. A. Rao, 2004: Coupled ocean–atmosphere variability in the tropical Indian Ocean. *Ocean–Atmosphere Interaction and Climate Variability, American Geophysical Union*, **147**,189–212.

Yamagata, T., S. K. Behera, S. A. Rao, Z. Guan, K. Ashok, and H. N. Saji, 2003: Comments on 'Dipoles, temperature gradient, and tropical climate anomalies'. *Bulletin of the American Meteorological Society,* **84,** 1418–1422.

Yamagata, T., S. K. Behera, J. J. Luo, S. Masson, M. R. Jury, and S. A. Rao, 2004: Coupled Ocean-Atmosphere variability in the Tropical Indian Ocean. *Earth's climate*, **147**, 1029/147GM12.

Yokoi, T., T. Tozuka, and T. Yamagata, 2008: Seasonal variation of the Seychelles Dome. *Journal of Climate*, **21**, 3740- 3754.

Yu, W., B. Xiang, L. Liu, and N. Liu, 2005: Understanding the origins of interannual thermocline variations in the tropical Indian Ocean. *Geophysical Research Letter,* **32**, L24706, doi: 10.1029/2005GL024327.

Yuan, D., and W. Han, 2006: Roles of equatorial waves and western boundary reflection in the seasonal circulation of the equatorial Indian Ocean. *Journal of Physical Oceanography*, **36**, 930–944.

Yuan, Y., and C. Li, 2008: Decadal variability of the IOD-ENSO relationship. *Chinese Science Bulletin,* **53**:11, 1745-1752.